The W boson spin density matrix at OPAL

by

Ian Richard Bailey
M.Sci., Cambridge University, 1997.

A Dissertation Submitted in Partial Fulfillment of the
Requirements for the Degree of

DOCTOR OF PHILOSOPHY

in the Department of Physics and Astronomy.

Supervisor: Dr. R. Keeler

Abstract

The spin states of W bosons in $e^+e^- \to W^+W^- \to q\bar{q}'\ell\nu_\ell$ events recorded by the OPAL detector at LEP are determined by an analysis of the angular distributions of their decay products. This information is used to calculate polarised differential cross-sections and to search for CP-violating effects. Results are presented for W bosons produced in e^+e^- collisions with centre-of-mass energies between 183 GeV and 209 GeV. The average percentage of longitudinally polarised W bosons measured from the data is found to be $(23.9 \pm 2.1 \pm 1.1)\%$ compared to a Standard Model prediction of $(23.9 \pm 0.1)\%$. All results are consistent with CP conservation.

Contents

List of Figures

List of Tables

1 Introduction

Our understanding of the world around us is founded on the search for patterns. This process is formalised in the practice of physics, where a disciplined search for objectively verifiable patterns is used as the basis for rational and predictive mathematical models. The strength of the scientific methodology lies in recognising that any model is only an approximation of reality; all models have limited realms of application and their predictions must always defer to experimental results. Once the limitations of a model are discovered, new models of wider scope can be developed which explain both the successes and the failures of the old model as well as making further testable predictions. These new models are then, in their turn, subject to experimental validation and refutation via a system of peer-review and informed consensus. Through this iterative process of modelling, prediction, experimentation and innovation, physics aims to unify superficially-disparate phenomena in a single mathematical framework.

It is always possible to create new physics models in an ad hoc manner, but this often leads to a proliferation of arbitrary free parameters without offering any new insights into the physical processes involved. In practice, the models which explain the most physics using the least number of parameters are not only the most intellectually satisfying but are often those which prove to be the most durable. The comprehensive success of such reductionist models strongly suggests that a wide variety of phenomena share the same underlying mechanisms in common. Indeed, all matter observed to date appears to be composed from a relatively small number of identical building blocks which interact in well-defined ways. The science of identifying the elementary constituents of matter and investigating their characteristics and interactions is known as particle physics.

The advent of modern particle physics was heralded by J.J. Thompson's discovery of the electron in 1897. Throughout the twentieth century experimental physicists continued

to identify a large number of previously unknown particles whilst theoretical physicists have tried to explain each particle's relevance and relationships. This work led to the development of our most successful current theory of matter - The Standard Model (SM).

Today, many aspects of the SM have been tested to an unprecedented level of accuracy, and no significant deviations from its predictions have yet been confirmed [1]. However, compelling theoretical arguments suggest that its description of physical processes operating on very small length scales is incomplete. Hence, consecutive generations of particle physics experiments attempt to probe ever-smaller distances by studying the interactions of particles accelerated to ever-higher energies. Contemporary particle accelerators operate at energies of the order 100 GeV, giving a corresponding sensitivity to length scales of approximately one hundredth of a proton radius in size.

One important aspect of the SM which has become accessible to experiment over the last decade is that of the self-interactions of the 'electroweak gauge bosons' - the photon (γ), the Z^0 boson, the W^+ boson and the W^- boson. These particles are responsible for mediating the electromagnetic and weak interactions in the SM, and are the main focus of this thesis. Specifically, this thesis makes use of data recorded by the OPAL detector at the LEP collider to study the formation of W pairs resulting from the collisions between electrons and positrons.

The Standard Model process of most interest in the analysis can be loosely described as one in which an electron and positron annihilate each other to form either a photon or Z^0 boson, which then rapidly decays to a W^+ and W^-. The Standard Model is a strictly quantum mechanical theory, but this classical picture is sufficient to show that simultaneous interactions between three gauge bosons ($W^+W^-Z^0$ or $W^+W^-\gamma$) are predicted. Such an interaction is known as a triple gauge coupling (TGC) and the form of this coupling is a strong test of the 'non-Abelian' nature of the weak force. Other 'anomalous couplings' may be present if physical mechanisms beyond those predicted by the SM are operating

in the electroweak sector, e.g. the supposedly point-like W bosons may actually contain sub-structure, or the coupling might involve exotic new particles whose effects have yet to be observed.

Every electroweak gauge boson has an associated spin vector whose alignment determines the boson's polarisation. The polarisations of the W bosons pair-produced at LEP depend upon the characteristics of the triple gauge couplings. Conversely, by measuring the bosons' polarisations we can probe the TGC physics. The longitudinal helicity component of polarisation is of particular interest as it arises in the SM through the electroweak symmetry-breaking mechanism which generates the masses of the W and Z^0 bosons. In addition, comparisons of the polarisation of the W^- and W^+ are sensitive to so-called CP-violating effects which can lead to differences between the observed reaction rates of matter compared to those of anti-matter.

Although W bosons have a very short natural lifetime of order 10^{-24}s [1], their existence can be unambiguously inferred from observations of their decay products. The latter are preferentially emitted along the direction of each W boson's spin vector, and it is this important characteristic which is exploited in this thesis to facilitate reconstruction of the spin state of the W bosons. Each W can decay either to a pair of quarks ($W \to q\bar{q}'$) or to a charged lepton and a neutrino ($W \to \ell\nu$). For practical reasons discussed later in this thesis, the polarisation measurements are made using W-pair events in which one W decays to leptons and one to quarks, denoted $e^+e^- \to W^+W^- \to q\bar{q}'\ell\nu_\ell$.

In summary, the challenges for this analysis are: to use the data recorded by the OPAL detector to identify likely $q\bar{q}'\ell\nu$ events, to determine which of those events involved pairs of W bosons, to reconstruct the W bosons' polarisations from measurements of the angular distributions of the decay products, and finally to relate the results to the predictions of the SM and consider any implications for possible anomalous TGC physics.

The SM and other background theory necessary to understand the analysis are de-

scribed in section 2. The relevant features of the LEP accelerator and the OPAL detector are summarised in sections 3 and 4 respectively, and a brief overview of the reconstruction of the data is given in section 5. The analysis itself is described in section 6 and the sources of systematic uncertainty studied are detailed in section 7. The measured fractions of longitudinally polarised W bosons and other related results are presented in section 8 and their implications discussed in section 9. Appendices A to F contain supporting results.

2 Theory

The Standard Model is unarguably the simplest self-consistent theory known to accurately describe all established results in particle physics, and it is therefore the starting point for any contemporary particle physics analysis. A brief overview of the SM particles and their interactions is given in section 2.1. The weak force is then described in section 2.2 with special emphasis on the role of the couplings between electroweak gauge bosons, and the reaction $e^+e^- \rightarrow W^+W^-$ is discussed in section 2.3. As the analysis presented in this thesis involves the measurement of the spin states of W bosons, section 2.4 discusses the application of the helicity formalism in representing the spin states, and section 2.5 describes how the information can be summarised by spin density matrices. Section 2.6 shows that the matrices can be obtained from experiment by applying a projection operator technique to the measured angular distributions of the W decay products. Sections 2.7 and 2.8 then show how the elements of the spin density matrices can be used to measure the polarised cross-sections of the W bosons and to test the CP invariance of the reaction. Finally, the limitations of the approximations made in the theoretical calculations with regard to the finite width of the W bosons and radiative corrections are discussed in sections 2.9 and 2.10 respectively.

2.1 The Standard Model of particle physics

The SM [2] consists of the electroweak theory of Glashow, Weinberg and Salam and quantum chromodynamics (QCD), both of which are renormalisable quantum field theories. Renormalisable theories are desirable because they give calculable predictions even at very small length scales (high energies), whilst the predictions of non-renormalisable theories generally diverge and become unphysical. The renormalisability of the SM is a consequence of the 'gauge invariance' of the Lagrangian used to describe the dynamics of the SM fields, i.e. even if the fields undergo certain unitary transformations, the physics characterised by the

Lagrangian remains unchanged. Imposing these symmetries on a Lagrangian which initially contains only matter fields, necessitates the introduction of gauge fields. Remarkably, the properties of the gauge fields appear to correspond exactly to the known forces in nature. This elegant result is the keystone of the SM.

The electromagnetic interaction is associated with a local $U(1)_{em}$ symmetry corresponding to a free choice of the phase convention for a wave-function, the weak interaction is associated with a (broken) local $SU(2)$ symmetry, and the strong interaction is associated with a local $SU(3)_c$ symmetry, where the designation 'c' refers to the 'colour' charge discussed later in the section.

The gauge-invariant Lagrangian describes both the dynamics of the fields and the interactions between them, where the strengths with which different fields couple to one another are characterised by 'coupling constants'. Although the parameters in the theory are indeed constant, the effective coupling strength between fields depends on the nature of the gauge fields and the centre-of-mass energy of the process being considered. This 'running' of the coupling constant occurs because charged particles tend to polarise the fields around them, so that the charge of the 'bare' particle is obscured. At low energies, the effective coupling strengths of the electromagnetic, weak and strong interactions are approximately $\alpha_{em} = \frac{1}{137}$, $\alpha_W = 10^{-6}$ and $\alpha_s = 1$ respectively. Provided that the strength of the coupling between fields is small, the Lagrangian representing their interactions can be expanded as a perturbation series in terms of the coupling constant. Each term in the series can be associated with a 'Feynman diagram' which is a time-ordered graph whose vertices represent the exchange of energy and momentum between different fields. The lowest-order terms in the perturbation expansion give the largest contribution to the series and are known as the 'tree-level' or Born-level terms.

In a quantum field theory, both the matter and gauge fields are quantised, and each of the field quanta represents a particle. All known particles obey either Fermi-Dirac or

Bose-Einstein statistics and are classified as fermions or bosons respectively. The spin-statistics theorem predicts that fermions have a half-integral spin and bosons have integral spin (measured in units of $\hbar$). The quanta of the gauge fields are bosons, known as 'gauge bosons', and those of the matter fields are fermions. The Lorentz-invariant formulation of the SM ensures that each particle has a corresponding anti-particle with the same mass but opposite quantum numbers.

The gauge boson for the electromagnetic interaction is the photon, γ, which couples to electric charge. The weak interaction's three gauge bosons are the W^+, W^- and Z^0 whose couplings depend on 'weak isospin' [1] in addition to electric charge. The strong interaction has eight gauge bosons, called gluons, which couple to the colour charge. In addition to the forces listed above, there is a putative gauge boson for gravity known as the graviton, but a self-consistent description of quantum gravity lies outside the scope of both the SM and this thesis.

Matter in the SM is composed from the twelve fundamental (i.e. without discernible sub-structure) fermions shown in table 1 which interact via the exchange of the gauge bosons described above. The momentum eigenstates of the fermions, u, are known as 'Dirac spinors' and are solutions of the Dirac equation,

$$(\gamma^\mu p_\mu - m)u \;=\; 0\,, \tag{1}$$

where p_μ [2] is the four-momentum of a particle with mass m, and γ^μ denotes the four Dirac gamma matrices (see for example reference [2]). For each matter solution, u, there is an anti-matter solution, v, e.g. the anti-matter partner of the electron, e^-, is the positron, e^+. The fundamental fermions are divided into three generations containing four fermions each,

[1] Weak isospin is discussed in section 2.2.

[2] Unless otherwise stated, formulas in this thesis use the standard convention that Greek indices $(\mu, \nu, ...)$ run from zero to three and Roman indices $(i, j, ...)$ run from one to three. The summation convention for contravariant and covariant tensor indices is assumed throughout such that $x^\mu y_\mu = \sum_{\mu=0}^{3} x_\mu g_{\mu\nu} y_\nu$ where $g_{\mu\nu}$ is the Minkowski metric.

Symbol	Name/ Flavour	Mass (GeV)	Charge (e)
e^-	Electron	5.11×10^{-4}	-1
ν_e	Electron neutrino	$< 3 \times 10^{-9}$	0
u	Up quark	$(1.5 - 4.5) \times 10^{-3}$	$\frac{2}{3}$
d	Down quark	$(5 - 8.5) \times 10^{-3}$	$-\frac{1}{3}$
μ^-	Muon	1.06×10^{-1}	-1
ν_μ	Muon neutrino	$< 1.9 \times 10^{-4}$	0
c	Charm quark	$(1.0 - 1.4)$	$\frac{2}{3}$
s	Strange quark	$(0.8 - 1.55) \times 10^{-1}$	$-\frac{1}{3}$
τ^-	Tau lepton	1.78	-1
ν_τ	Tau neutrino	$< 1.82 \times 10^{-2}$	0
t	Top quark	174	$\frac{2}{3}$
b	Bottom quark	$(4.0 - 4.5)$	$-\frac{1}{3}$

Table 1: The elementary fermions in the Standard Model. The theory does not predict the masses of the particles, and hence the experimentally determined values are shown [1]. The predicted values for the electric charges are shown in units of the positron charge.

where each generation differs from the other two only in the mass of the particles. Each generation comprises a pair of 'leptons' and a pair of 'quarks'. Leptons do not carry colour charge whereas quarks [3] do and therefore only the latter interact via the strong force. The strong force is unique amongst the forces, in that the attraction between coloured particles increases in strength as the distance between the particles is increased. This 'anti-screening' phenomenon ensures that coloured objects are always confined inside colour-neutral bound states called hadrons. Quarks and anti-quarks are assigned baryon numbers of $+\frac{1}{3}$ and $-\frac{1}{3}$ respectively. Hadrons with a total summed baryon number of 1 are known as baryons (e.g. protons), and those with a total summed baryon number of 0 are mesons (e.g. pions). The generic process by which unbound quarks and gluons rapidly form baryons and mesons is known as hadronisation. The consequences of hadronisation are used later in this thesis to

[3]The three possible colour states for a quark are conventionally referred to as red, green, and blue.

distinguish between the experimental signatures of quarks and leptons.

In each generation, one lepton and both quarks carry electric charge, the remaining lepton (the neutrino) is electrically neutral. This thesis retains the standard simplifying assumption that neutrinos are massless. In recent years, indirect experimental evidence has been found which strongly suggests that neutrinos in fact have a small non-zero rest mass [3]. Although this is a discovery of great importance to particle physics as a whole, its impact on this work is negligible.

In general, the mass terms of the fermions and weak gauge bosons violate the gauge invariance of the Lagrangian. This problem is solved through a symmetry-breaking mechanism, in which an additional complex scalar field is introduced into the theory - the Higgs field [4]. In the Higgs mechanism, three of the four degrees of freedom of the Higgs field are used to give rest mass to the three massive electroweak gauge bosons, W^+, W^- and Z^0. The masses acquired by the gauge bosons through their interaction with the Higgs field are not predicted by the theory. However, the mass of the W bosons, m_W, is measured to be 80.44 GeV and the mass of the Z^0 bosons, m_Z, is measured to be 91.19 GeV [1]. This is in striking contrast to photons and gluons which are apparently massless. The fourth degree of freedom of the Higgs field forms the physical Higgs boson, which, although yet to be observed, completes the list of elementary SM particles.

2.2 The weak force

The analysis presented in this thesis is primarily an investigation of the properties of the weak force and the gauge bosons which mediate it. Although the focus of the work is on the couplings between electroweak gauge bosons, any realizable experimental environment requires the bosons to be both produced and detected through their interactions with fermionic matter fields (i.e. electrons and positrons are collided to produce the bosons which subsequently decay to leptons and quarks). The analysis of the gauge boson self-couplings is therefore only possible because the form of the coupling between the electroweak gauge bosons and fermions is already well-measured and known to conform to the SM prediction [5]. Moreover, as is explained in the remainder of this section, the form of the couplings of gauge bosons to fermions in the SM leads naturally to the prediction that gauge bosons must also couple to one another.

The Lagrangian originally devised by Fermi to describe nuclear beta decays (mediated by the weak force) did not explicitly contain gauge bosons. It was a non-renormalisable low-energy approximation, in which it was assumed that the range of the weak interaction was small enough to be neglected. In this model, all four of the fermions which take part in a weak decay must meet at a single point, as shown in the Feynman diagram in figure 1, and hence neither the initial nor final states can have orbital angular momenta. Consequently, the calculated contribution of the lowest order partial wave to the probability that an electron, e^-, scatters from an electron neutrino, ν_e, diverges unphysically at high energies (violating unitarity). Attempts to remove the divergence led physicists to hypothesise the existence of the W boson [4] - a massive vector boson which mediates the interaction through the Feynman diagram shown in figure 2.

[4]The first direct experimental evidence for the existence of the W boson was reported by the experiments UA1 and UA2 in 1983.

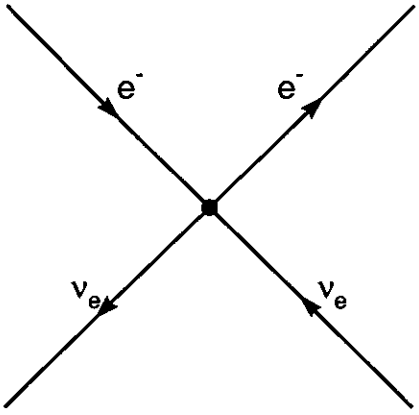

Figure 1: The Feynman diagram for the effective Fermi interaction between electrons and electron neutrinos.

Famously, in 1957 it was shown [6] that the weak force violates parity invariance [5]. This led to the later discovery that the W^- and W^+ bosons couple only to the 'left-handed' chiral states of fermions and to the 'right-handed' chiral states of anti-fermions. The chiral operators which project out the left-handed or right-handed chiral states of a Dirac spinor are defined as $\frac{1}{2}(1-\gamma^5)$ and $\frac{1}{2}(1+\gamma^5)$ respectively, where γ^5 is equal to $\gamma^0\gamma^1\gamma^2\gamma^3$.

As the left-handed states of both leptons in a generation couple to the W bosons whereas the right-handed states do not, a left-handed charged lepton and its associated left-handed neutrino can be thought of as a doublet, and the right-handed charged lepton as a singlet. There are no right-handed neutrinos in this model. Further weak isospin doublets can be formed from linear combinations of the quark mass eigenstates by a unitary transformation known as the Cabbibo-Kobayashi-Maskawa (CKM) matrix [2]. Therefore, in considering

[5]Under a parity operation, a right-handed Cartesian set of axes is transformed into a left-handed set via the mapping $x \to -x, y \to -y, z \to -z$.

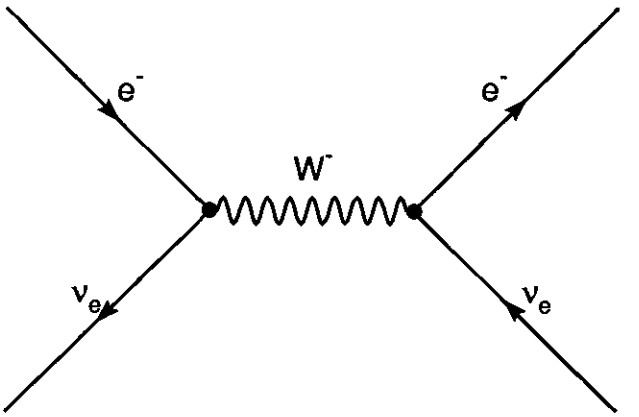

Figure 2: The tree-level Feynman diagram for a W boson mediating the interaction between electrons and electron neutrinos.

electroweak processes it is convenient to write the left-handed components of either a lepton or quark generation as a two-dimensional column vector, each component of which is a Dirac spinor. The SM weak isospin doublets can be written as,

$$\begin{pmatrix} \nu_e \\ e \end{pmatrix}_L, \quad \begin{pmatrix} \nu_\mu \\ \mu \end{pmatrix}_L, \quad \begin{pmatrix} \nu_\tau \\ \tau \end{pmatrix}_L, \quad \begin{pmatrix} u \\ d' \end{pmatrix}_L, \quad \begin{pmatrix} c \\ s' \end{pmatrix}_L, \quad \begin{pmatrix} t \\ b' \end{pmatrix}_L,$$

where d', s' and b' are the weak eigenstate equivalents of the down, strange and bottom quarks respectively. At tree-level, the W bosons couple with equal strength to each doublet.

Each vector is a representation of the left-handed part of a lepton or quark generation in a complex two-dimensional space known as 'weak isospin' space. Conventionally, the upper and lower components of the vector are assigned weak isospin values of $+\frac{1}{2}$ and $-\frac{1}{2}$ respectively. In this abstract space the W bosons are represented by rotation operators which transform an object with isospin $-\frac{1}{2}$ (e.g. an electron) into an object with isospin $+\frac{1}{2}$ (e.g. an electron neutrino) or vice versa. The process is mathematically similar to the

'flipping' of an electron's spin through its interaction with a single photon.

Since two operators are not sufficient to describe a general rotation in a two-dimensional complex space, a third gauge boson, W^0, is introduced by analogy with the three Pauli spin matrices [2] needed to generate the rotations of spin $\frac{1}{2}$ objects in physical space. The introduction of the third boson is a crucial step in preventing high-energy divergences in the process $e^+e^- \rightarrow W^+W^-$, which is described in section 2.3. Equation (2) shows the Lagrangian [7] for the three weak vector fields, $\vec{W}_\mu$.

$$\begin{aligned} \mathcal{L}_{\text{weak}} &= -\frac{1}{4}\left(\partial_\mu \vec{W}_\nu - \partial_\nu \vec{W}_\mu\right) \cdot \left(\partial^\mu \vec{W}^\nu - \partial^\nu \vec{W}^\mu\right) \\ &\quad + i\frac{g}{2}\bar{\Psi}_L \gamma^\mu \vec{W}_\mu \cdot \vec{\tau}\, \Psi_L \end{aligned} \tag{2}$$

The first term describes their dynamics in free-space and the second term describes their coupling to a weak isospin doublet of either quarks or leptons, Ψ, whose left-handed chiral state is denoted by Ψ_L. The components of $\vec{\tau}$ are the Pauli spin matrices, $\bar{\Psi}$ is defined as $\Psi^\dagger\gamma^0$, where $\dagger$ denotes the Hermitean conjugate, and g is the weak coupling constant.

Equations (3) to (5) show the relationship between the three massless $\vec{W}$ fields and the physical W^+, W^-, Z^0 and photon fields which are observed after symmetry-breaking. Equation (5) defines the weak mixing angle, θ_{wma}, where A_μ is the usual electromagnetic four-vector potential, and Z_μ is the equivalent potential for the Z^0. In addition, the weak coupling constant is predicted to be related to the positron charge as show in equation (6).

$$W^1_\mu = \frac{1}{\sqrt{2}}\left(W^+_\mu + W^-_\mu\right) \tag{3}$$

$$W^2_\mu = \frac{i}{\sqrt{2}}\left(W^+_\mu - W^-_\mu\right) \tag{4}$$

$$W^3_\mu = \cos(\theta_{\text{wma}})Z_\mu + \sin(\theta_{\text{wma}})A_\mu \tag{5}$$

$$g = e/\sin(\theta_{\text{wma}}) \tag{6}$$

If weak isospin is a conserved quantum number then the weak Lagrangian must be invariant under rotations in weak isospin space. This condition is equivalent to imposing

local $SU(2)_L$ gauge invariance, which, as was asserted at the beginning of section 2, ensures that the theory is renormalisable. As the generators of the gauge group do not commute (the group is non-Abelian), applying $SU(2)_L$ gauge invariance to the dynamical term in equation (2) produces the additional terms shown in equation (7) which represent self-interactions between the bosons.

$$\begin{aligned} \mathcal{L}_{GC} &= \frac{g}{2}\left(\partial_\mu \vec{W}_\nu - \partial_\nu \vec{W}_\mu\right).\left(\vec{W}^\mu \times \vec{W}^\nu\right) \\ &\quad -\frac{g^2}{4}\left(\vec{W}_\mu \times \vec{W}_\nu\right).\left(\vec{W}^\mu \times \vec{W}^\nu\right) \end{aligned} \tag{7}$$

The first term represents triple gauge couplings (TGC) between three gauge fields, and the second term represents quartic gauge couplings (QGC) between four gauge fields. The generic tree-level Feynman diagrams for these processes are shown in figure 3.

a b

Figure 3: Tree-level Feynman diagrams showing a) the generic TGC vertex, and b) the generic QGC vertex.

Table 2 shows the groupings of three or four electroweak gauge bosons which are predicted to couple together via the terms in equation (7). Electrically neutral couplings involving only the photon and Z^0 bosons are entirely absent at tree-level in the Standard Model [8]. The contributions from quartic gauge couplings to physics processes at the centre-of-mass energies used at LEP were negligible [9]. However, the triple gauge cou-

plings play a prominent role in the W pair production process discussed in more detail in the following section.

TGC	QGC
γWW ZWW	WWWW WWZZ WWZγ WW$\gamma\gamma$

Table 2: Table of Standard Model TGC and QGC vertices.

2.3 The process $e^+e^- \rightarrow W^+W^-$

W pairs can be produced through the annihilation of e^+e^- pairs provided that the collisions take place at centre-of-mass energies equal to or greater than twice the W boson rest mass. A schematic diagram for the process $e^+e^- \rightarrow W^+W^-$ is shown in figure 4, where an electron and positron with spinors u and v, and four-momenta k^μ and $\bar{k}^\mu$ respectively are shown colliding. The outgoing W^- and W^+ have polarisation four-vectors ϵ_-^μ and ϵ_+^μ, and four-momenta q^μ and $\bar{q}^\mu$ respectively.

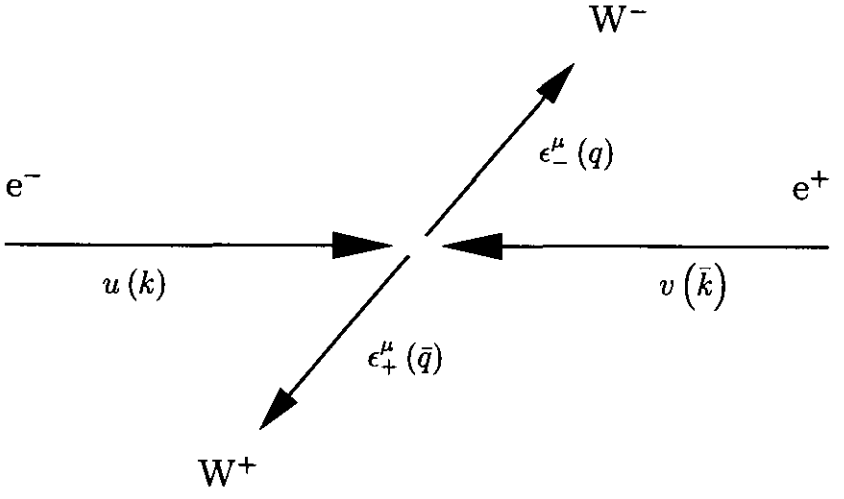

Figure 4: Generic schematic diagram of an $e^+e^- \rightarrow W^+W^-$ reaction.

The rate at which any reaction occurs is proportional to the modulus squared of its scattering amplitude, M, which is itself derived from the Lagrangian. The SM tree-level scattering amplitude for the process $e^+e^- \rightarrow W^+W^-$ can be conveniently divided into three parts,

$$M_{e^+e^- \rightarrow W^+W^-} = M_\gamma + M_Z + M_\nu \, . \tag{8}$$

The first term represents an s-channel processes in which the reaction is mediated by a virtual photon which couples to the W bosons through a TGC, as shown in the tree-level

Feynman diagram in figure 5b. It can be expressed in terms of the spinors and polarisation vectors by

$$M_\gamma = -e^2\{\bar{v}\gamma_\mu u\}\left[\frac{g^{\mu\nu}}{s}\right] \left\{\epsilon_+^{*\alpha}(g_{\alpha\beta}(\bar{q}-q)_\nu - g_{\alpha\nu}(q+2\bar{q})_\beta + g_{\beta\nu}(2q+\bar{q})_\alpha)\epsilon_-^{*\beta}\right\} , \quad (9)$$

where the centre-of-mass energy of the collision is denoted by $\sqrt{s}$ and the electric charge of the positron is denoted by e.

The second term represents a second s-channel process in which the reaction is mediated by a virtual Z^0 boson. The boson once again couples to the W bosons through a TGC, as shown in figure 5c. The term can be expressed as,

$$M_Z = -e^2\left\{\bar{v}\gamma_\mu(1-\frac{1-\gamma^5}{4\sin^2\theta_{\text{wma}}})u\right\}\left[\frac{g^{\mu\nu}-(\bar{k}+k)^\mu(\bar{k}+k)^\nu/m_Z^2}{s-m_Z^2}\right] \left\{\epsilon_+^{*\alpha}(g_{\alpha\beta}(\bar{q}-q)_\nu - g_{\alpha\nu}(q+2\bar{q})_\beta + g_{\beta\nu}(2q+\bar{q})_\alpha)\epsilon_-^{*\beta}\right\} . \quad (10)$$

The third term represents a t-channel process in which the electron and positron scatter by exchanging a virtual electron neutrino. The corresponding tree-level Feynman diagram is shown in figure 5a, and the term can be expressed as,

$$M_\nu = -\frac{e^2}{8\sin^2\theta_{\text{wma}}}\left\{\bar{v}\epsilon_+^{*\alpha}\gamma_\alpha(1-\gamma^5)\right\}\left[\frac{\gamma_\mu(\bar{k}-\bar{q})^\mu}{(\bar{k}-\bar{q})^2}\right]\left\{\epsilon_-^{*\beta}\gamma_\beta(1-\gamma_5)u\right\} . \quad (11)$$

These three dominant contributions to the scattering amplitude are collectively referred to as the CC03 (charged current) processes [10]. Figure 5 additionally shows a fourth W-pair production process which is mediated by the Higgs boson, but its contribution is only important in the limit of high energies, and can be ignored for this analysis.

The non-Abelian, $SU(2)_L$, group structure of the SM ensures that cancellations occur between the contributions to the scattering amplitude. Figure 6 shows how the total 'cross-section', σ, for $e^+e^- \to W^+W^-$ is predicted to change with centre-of-mass energy both with and without the contributions from M_γ and M_Z. The cross-section of a process is measured

in units of area [6] and is proportional to the reaction rate. Without the inclusion of both of the s-channel diagrams, the predicted cross-section rapidly diverges with increasing centre-of-mass energy, in contrast to the SM prediction and the measured data.

It is clear from the data that the SM prediction is at least approximately correct in the energy regime probed by the experiment. However, only the minimal set of couplings necessary to ensure gauge invariance is contained in the SM Lagrangian. In looking for physics beyond the SM additional tree-level couplings between gauge bosons can be introduced whilst preserving the gauge symmetry if the Lagrangian is allowed to be non-renormalisable [11]. Although this approach may seem to be in direct contradiction to the previous discussion, it is justified if we assume that any new terms are low-energy manifestations of new physics operating at a higher energy scale that is not yet directly accessible to experiment.

The most general Lorentz-invariant and $U(1)_{em}$ symmetric (electric charge conserving) WWγ coupling is described by seven coupling constants [12]. The number of parameters is consistent with the general observation that a particle with a spin of J can have no more than $6J + 1$ electromagnetic form factors [13]. An additional seven parameters are needed to describe the WWZ coupling. Although these parameters are not directly measured in this thesis, a brief discussion of them is included here because their values determine the polarisation of the W bosons.

A phenomenological Lagrangian [14] which can represent either the WWγ or WWZ coupling is shown in equation (12), where V_μ is the four-vector potential of either the Z^0 boson or the photon, γ, and $W_{\mu\nu}$ is the anti-symmetric field tensor $\partial_\mu W_\nu - \partial_\nu W_\mu$. The symbol $\epsilon_{\mu\nu\rho\sigma}$ denotes the 'totally anti-symmetric' or 'Bjorken-Drell' symbol, defined such that $\epsilon^{0123} = \epsilon_{0123} = 1$. The factor $g_{\mathrm{WW}\gamma}$ which appears in the WWγ Lagrangian is defined as the electric charge of the positron, e, and the factor g_{WWZ} which appears in the WWZ

[6] The unit of cross-section used in this thesis is the barn, b, which is equal to $10^{-28}\mathrm{m}^2$.

Lagrangian is defined as $e \cot \theta_{\text{wma}}$.

$$
\begin{aligned}
i\mathcal{L}_{\text{eff}}^{\text{WWV}}/g_{\text{WWV}} &= g_1^V V^\mu (W_{\mu\nu}^- W^{+\nu} - W_{\mu\nu}^+ W^{-\nu}) \\
&+ \kappa_V W_\mu^+ W_\nu^- V^{\mu\nu} \\
&+ \frac{\lambda_V}{m_W^2} V^{\mu\nu} W_\nu^{+\rho} W_{\rho\mu}^- \\
&+ i g_5^V \epsilon_{\mu\nu\rho\sigma} ((\partial^\rho W^{-\mu}) W^{+\nu} - W^{-\mu} (\partial^\rho W^{+\nu})) V^\sigma \\
&+ i g_4^V W_\mu^- W_\nu^+ (\partial^\mu V^\nu + \partial^\nu V^\mu) \\
&- \frac{\tilde{\kappa}_V}{2} W_\mu^- W_\nu^+ \epsilon^{\mu\nu\rho\sigma} V_{\rho\sigma} \\
&- \frac{\tilde{\lambda}_V}{2m_W^2} W_{\rho\mu}^- W_\nu^{+\mu} \epsilon^{\nu\rho\alpha\beta} V_{\alpha\beta}
\end{aligned}
\tag{12}
$$

In the phenomenological approach, the coupling constants (g_1, κ, λ, g_4, g_5, $\tilde{\kappa}$, $\tilde{\lambda}$) are free parameters to be fitted to the data, and the Standard Model Lagrangian is recovered by setting $\kappa_\gamma, \kappa_Z, g_1^\gamma$ and g_1^Z to one, and setting all the other parameters to zero (c.f. equation (7)). Any deviations from the SM values are known as anomalous couplings. Precision measurements from low-energy LEP data and other sources have previously been used to place model-dependent limits on some anomalous couplings [15]. In recent years these constraints have been supplemented by direct measurements of the gauge boson interactions made by the detector collaborations based at both the Tevatron [16] and LEP [17] colliders. Many of these measurements assume that there are constraints between the parameters in the phenomenological Lagrangian. Such constraints arise when assumptions are made about the energy scale of the new physics processes being probed, or when additional symmetry requirements are imposed.

An intuitive understanding of the implication of the anomalous couplings can be gained by considering the relationship between the WWγ coupling constants and the electromag-

netic multipole moments of the W boson given by:

$$q_W = e.g_1^\gamma \quad (13)$$

$$\mu_W = \frac{e}{2m_W}(g_1^\gamma + \kappa_\gamma + \lambda_\gamma) \quad (14)$$

$$Q_W = -\frac{e}{m_W^2}(\kappa_\gamma - \lambda_\gamma) \quad (15)$$

$$d_W = \frac{e}{2m_W}\left(\tilde{\kappa}_\gamma + \tilde{\lambda}_\gamma\right) \quad (16)$$

$$\tilde{Q}_W = -\frac{e}{m_W^2}\left(\tilde{\kappa}_\gamma - \tilde{\lambda}_\gamma\right) \quad , \quad (17)$$

where q_W is the electric charge of the W, μ_W is the magnetic dipole moment, Q_W is the electric quadrupole moment, d_W is the electric dipole moment and $\tilde{Q}_W$ is the magnetic quadrupole moment. These last two moments are CP-violating, as is the term in the Lagrangian associated with g_4^γ (see section 2.8). For each electromagnetic multipole moment there is an equivalent 'weak multipole' moment which can be obtained by substituting the $WW\gamma$ coupling constants in equations (13) to (17) by the corresponding WWZ coupling constants and multiplying each moment by a factor of $\cot(\theta_{wma})$ (the ratio of g_{WWZ} to $g_{WW\gamma}$).

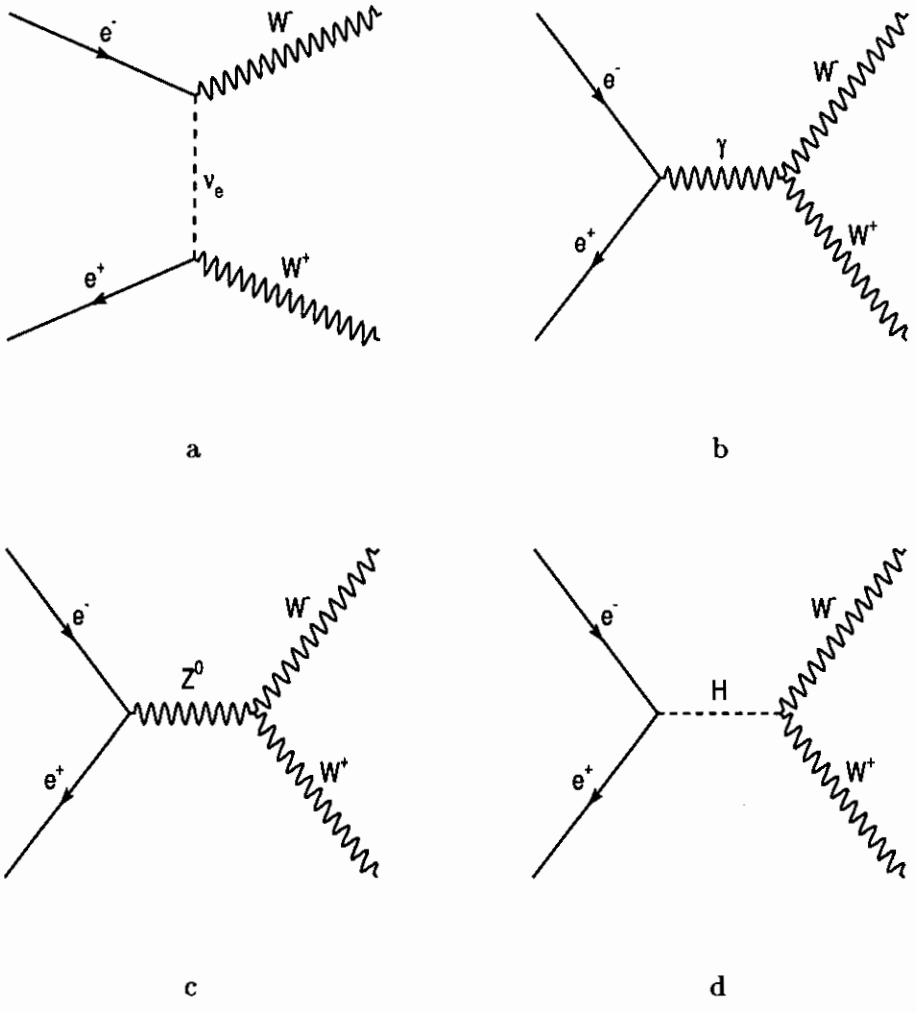

Figure 5: Tree-level Feynman diagrams for the process $e^+e^- \rightarrow W^+W^-$. Diagram a) shows the t-channel neutrino exchange diagram. Diagram b) shows the s-channel diagram with a photon propagator. Diagram c) shows the s-channel process with a Z^0 propagator. Diagram d) shows the Higgs s-channel diagram, which is not considered in this thesis as the coupling of the Higgs boson to the electron is vanishingly small.

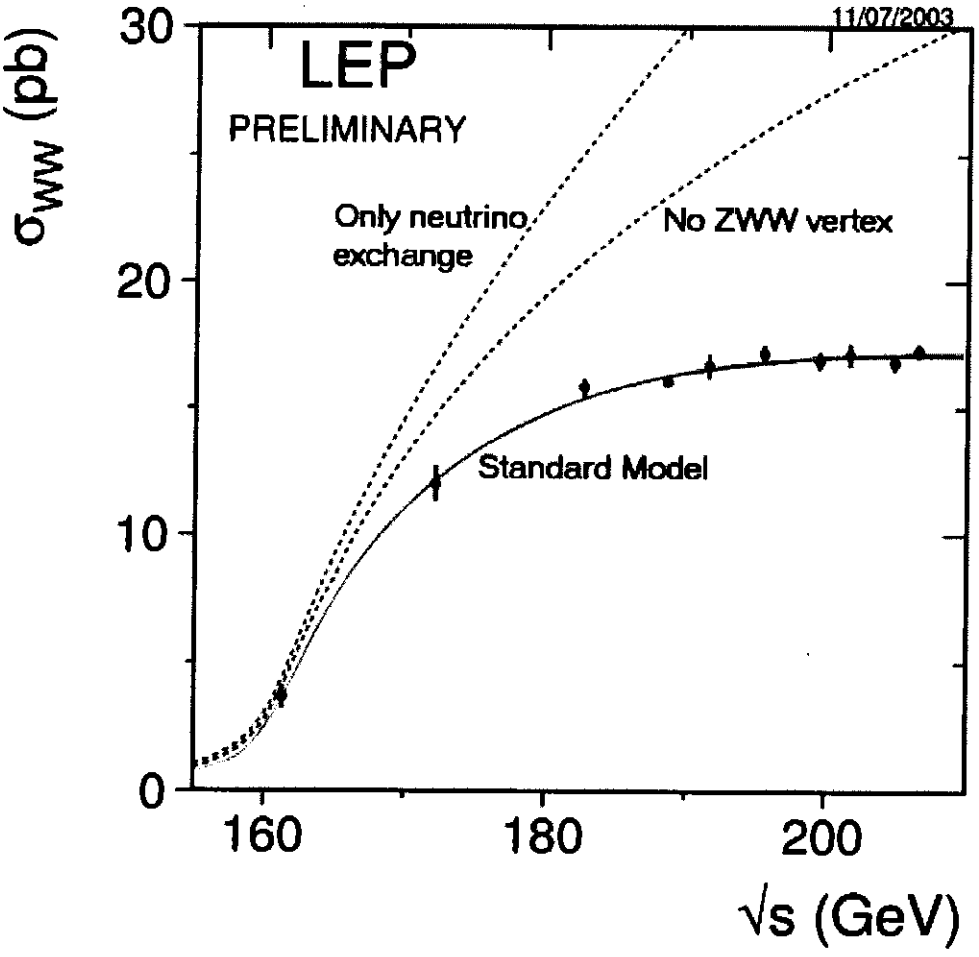

Figure 6: A preliminary measurement from the four LEP collaborations showing the total cross-section for the process $e^+e^- \rightarrow W^+W^-$ as a function of centre-of-mass energy. The lines show the predictions and the points show the measured results with error bars including both statistical and systematic uncertainties. This figure has been reproduced and adapted from that shown in reference [17].

2.4 Helicity amplitudes

As shown in the preceding section, introducing anomalous couplings into the TGC Lagrangian leads to changes in the multipole moments of the W bosons. Just as the angular distributions and polarisations of radio waves emitted from a transmitter depend on the multipole moments of the transmitter, so the multipole moments of the radiated W bosons determine their angular distributions and polarisations in the $e^+e^- \rightarrow W^+W^-$ reaction.

A particle is said to be polarised if its spin vector, $\vec{s}$, is preferentially aligned along a given direction in space. Alternatively, rather than expressing the spin vectors with respect to a fixed frame of reference, the spin can be represented in the helicity basis [18]. The helicity, h, is given by the projection of the particle's spin onto its direction of motion,

$$h = \frac{\vec{s} \cdot \vec{p}}{|\vec{p}|} . \tag{18}$$

The helicity formalism is used to express the spin states of particles throughout this thesis.

Photons can be polarised with their spin vector aligned either parallel or anti-parallel to their momentum vectors, where these two possibilities correspond to positive and negative helicity states respectively (the right-handed and left-handed circular polarisation modes of light). These states are also known as transverse polarisation modes, as the electric and magnetic components of the electromagnetic field are both aligned transverse to the photon's direction of motion. Massive vector bosons such as the W and Z^0 can additionally have their spin vectors oriented perpendicular to the direction of the particle's motion. This latter possibility corresponds to a zero or longitudinal helicity state.

A schematic diagram of the process $e^+e^- \rightarrow W^+W^-$ showing the electron, positron and W bosons in one possible configuration of helicity states is shown in figure 7. In general, the number of W bosons measured to be in a given helicity state will vary both with the centre-of-mass energy of the process and with the angle between the W^- and e^- momentum vectors in the centre-of-mass frame, θ_W. The helicities of the e^- and e^+ are denoted by λ

and $\bar{\lambda}$ respectively, and the helicities of the W^- and W^+ are denoted by τ and $\bar{\tau}$. As the W^- and W^+ are massive vector bosons, τ and $\bar{\tau}$ may take the values $\pm 1, 0$. The electron and positron are fermions with a spin of one half, and hence λ and $\bar{\lambda}$ can take the values $\pm\frac{1}{2}$.

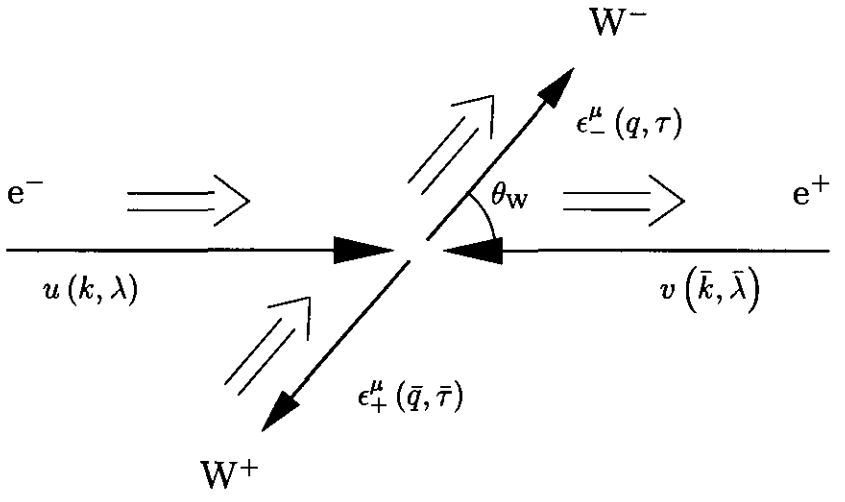

Figure 7: Schematic diagram of the $e^+e^- \rightarrow W^+W^-$ reaction with initial and final states of definite helicity. In this example, the electron is shown in a positive helicity state ($\lambda = \frac{1}{2}$), the positron is shown in a negative helicity state ($\bar{\lambda} = -\frac{1}{2}$) , the W^- is shown in a positive helicity state ($\tau = 1$) and the W^+ is shown in a negative helicity state ($\bar{\tau} = -1$).

The scattering amplitude for a final state of definite helicity is known as a helicity amplitude, F. As shown previously for the scattering amplitude, the helicity amplitude for the reaction $e^+e^- \rightarrow W^+W^-$ can be decomposed into the three CC03 contributions,

$$F^{(\tau,\bar{\tau};\lambda,\bar{\lambda})} = F_\gamma^{(\tau,\bar{\tau};\lambda,\bar{\lambda})} + F_Z^{(\tau,\bar{\tau};\lambda,\bar{\lambda})} + F_\nu^{(\tau,\bar{\tau};\lambda,\bar{\lambda})} .$$

Equations (21), (22) and (23) show the helicity amplitudes derived by the author of this thesis from the scattering amplitudes of equations (9), (10) and (11). The Lorentz factor of the W^- and W^+ is denoted γ_W, and the associated velocity measured in units of c is denoted β_W, where γ_W and β_W are related to the centre-of-mass energy of the collision and

the momentum and the mass of the W bosons by,

$$\gamma_W = \frac{\sqrt{s}}{2m_W} \tag{19}$$

$$\beta_W = \frac{2q}{\sqrt{s}} . \tag{20}$$

The symbol $\sin(\theta_{wma})$ denotes the sine of the weak mixing angle previously introduced in equation (5).

$$\begin{aligned} F_\gamma^{(\tau,\bar{\tau};\lambda,\bar{\lambda})} = & \frac{-e^2\beta_W}{2}\frac{1}{\sqrt{1+\tau^2}}\frac{1}{\sqrt{1+\bar{\tau}^2}} \\ & \Big\{ (1-4\lambda\bar{\lambda})\Big[(\tau\bar{\tau}(1+\tau\bar{\tau}) - (2\gamma_W^2+1)(\tau^2-1)(\bar{\tau}^2-1))\sin\theta_W \\ & +2\gamma_W(\tau(1-\bar{\tau}^2)+\bar{\tau}(1-\tau^2))\cos\theta_W \Big] \\ & +4\gamma_W(\lambda-\bar{\lambda})(\tau^2-\bar{\tau}^2) \Big\} \end{aligned} \tag{21}$$

$$\begin{aligned} F_Z^{(\tau,\bar{\tau};\lambda,\bar{\lambda})} = & \frac{e^2\beta_W}{2\sin(\theta_{wma})^2}\frac{m_W^2\gamma_W^2}{4m_W^2\gamma_W^2 - m_Z^2}\frac{1}{\sqrt{1+\tau^2}}\frac{1}{\sqrt{1+\bar{\tau}^2}} \\ & \Big\{ (1-4\lambda\bar{\lambda})\Big[(4\sin(\theta_{wma})^2-1) \\ & ((\tau\bar{\tau}(1+\tau\bar{\tau}) - (2\gamma_W^2+1)(\tau^2-1)(\bar{\tau}^2-1))\sin\theta_W \\ & +2\gamma_W(\tau(1-\bar{\tau}^2)+\bar{\tau}(1-\tau^2))\cos\theta_W) \\ & +2\gamma_W(\tau^2-\bar{\tau}^2)\Big] \\ & +2(\lambda-\bar{\lambda})\Big[(4\sin(\theta_{wma})^2-1)2\gamma_W(\tau^2-\bar{\tau}^2) \\ & +(\tau\bar{\tau}(1+\tau\bar{\tau}) - (2\gamma_W^2+1)(\tau^2-1)(\bar{\tau}^2-1))\sin\theta_W \\ & +2\gamma(\tau(1-\bar{\tau}^2)+\bar{\tau}(1-\tau^2))\cos\theta_W \Big] \Big\} \end{aligned} \tag{22}$$

$$
\begin{aligned}
F_{\nu}^{(\tau,\bar{\tau};\lambda,\bar{\lambda})} \;=\; & \frac{e^2(1+2\lambda)(1-2\bar{\lambda})}{4\beta_{\mathrm{W}}\sin(\theta_{\mathrm{wma}})^2}\frac{1}{\sqrt{1+\tau^2}}\frac{1}{\sqrt{1+\bar{\tau}^2}} \\
& \left\{ (\tau^2-1)(\bar{\tau}^2-1)\left(\frac{1}{\gamma_{\mathrm{W}}^2(1+\beta_{\mathrm{W}}^2-2\beta_{\mathrm{W}}\cos\theta_{\mathrm{W}})}-\gamma_{\mathrm{W}}^2\right)\sin\theta_{\mathrm{W}}\right. \\
& +\tau^2\bar{\tau}^2\left(\frac{\beta_{\mathrm{W}}^2+\beta_{\mathrm{W}}(\tau-\bar{\tau})-\tau\bar{\tau}}{1+\beta_{\mathrm{W}}^2-2\beta_{\mathrm{W}}\cos\theta_{\mathrm{W}}}+\tau\bar{\tau}\right)\sin\theta_{\mathrm{W}} \\
& +(\tau^2-1)\bar{\tau}\left(\frac{1-\bar{\tau}\beta_{\mathrm{W}}}{\gamma_{\mathrm{W}}(1+\beta_{\mathrm{W}}^2-2\beta_{\mathrm{W}}\cos\theta_{\mathrm{W}})}-\gamma_{\mathrm{W}}\right)(\cos\theta_{\mathrm{W}}+\bar{\tau}) \\
& \left. +(\bar{\tau}^2-1)\tau\left(\frac{1+\tau\beta_{\mathrm{W}}}{\gamma_{\mathrm{W}}(1+\beta_{\mathrm{W}}^2-2\beta_{\mathrm{W}}\cos\theta_{\mathrm{W}})}-\gamma_{\mathrm{W}}\right)(\cos\theta_{\mathrm{W}}-\tau)\right\} \qquad (23)
\end{aligned}
$$

The helicity amplitudes are identically zero unless $\mid \lambda - \bar{\lambda} \mid$ is equal to one, such that the spin vectors of the electron and positron are either both aligned parallel to the e^- beam direction, or else both aligned anti-parallel to it. This constraint is present in both the s-channel and t-channel but arises through two different mechanisms. The s-channel contributions, F_γ and F_{Z}, are constrained because they each couple to an intermediate vector gauge boson (a photon and Z^0 respectively) at a point. By contrast, in the t-channel contribution, F_ν, it is the form of the W boson coupling to fermions which selects specific helicity states of the electron and positron [7]. It is only the gauge structure of the theory which connects these, otherwise unrelated, phenomena.

The polarised differential cross-sections can be calculated from the helicity amplitudes by:

$$
\frac{\mathrm{d}\sigma(\tau,\bar{\tau})}{\mathrm{d}\cos\theta_{\mathrm{W}}} \;=\; \frac{\beta_{\mathrm{W}}}{64\pi^2 s}\sum_{\lambda,\bar{\lambda}}\left|F^{(\tau,\bar{\tau};\lambda,\bar{\lambda})}\right|^2 , \qquad (24)
$$

where the pre-factor takes into account the kinematics of the reaction. Note that the

[7] Equation (23) is only valid where the electron and positron are moving at relativistic velocities such that terms proportional to their rest mass divided by their respective total energies can be neglected.

unpolarised cross-section is simply given by the sum over all the polarised cross-sections,

$$\frac{\mathrm{d}\sigma}{\mathrm{d}\cos\theta_{\mathrm{W}}} = \sum_{\tau,\bar{\tau}} \frac{\mathrm{d}\sigma(\tau,\bar{\tau})}{\mathrm{d}\cos\theta_{\mathrm{W}}} \,. \tag{25}$$

The cross-sections shown in figures 8 and 9 were calculated by the author of this thesis at centre-of-mass energies corresponding to the lowest energy data (183 GeV) and highest energy data (209 GeV) studied in section 6. It can be seen that the dominant contribution to the total cross-section comes from the two helicity states with $|\tau - \bar{\tau}| = 2$ (denoted $+,-$ and $-,+$ on the figure). These states can only be generated through the t-channel neutrino exchange diagram and are therefore unaffected by TGC physics. The remaining seven helicity amplitudes can be generated through both the s-channel and t-channel processes. Each of these seven helicity amplitudes has a different dependence on the fourteen (seven $\mathrm{WW}\gamma$ and seven WWZ) parameters in the phenomenological Lagrangian of equation (12) (see reference [14] for details).

Figure 10 shows the predicted polarised cross-sections of the W^- averaged over the W^+ degrees of freedom at centre-of-mass energies of 183 GeV and 209 GeV. The large asymmetry of the distribution in the W^- production angle, θ_{W}, is a direct consequence of the prevalence of the t-channel which tends to favour scattering through small angles, as shown in the upper plot in figure 11. The s-channel contribution alone (summed over all helicity states) is symmetric about $\theta_{\mathrm{W}} = \frac{\pi}{2}$, as shown in the lower plot in figure 11. Sensitivity to anomalous couplings at LEP2 comes mainly from coherent interference between the t-channel and s-channel terms.

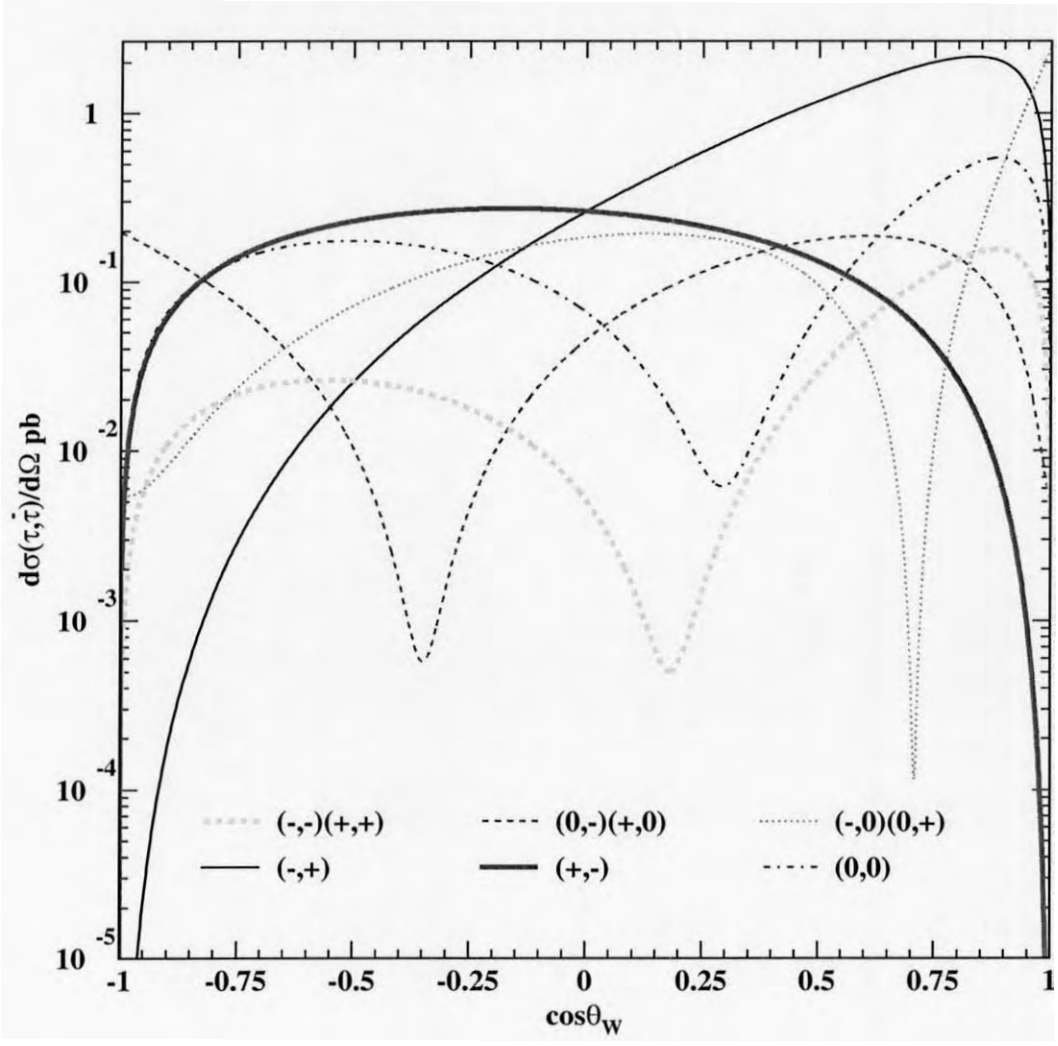

Figure 8: SM prediction of the differential cross-section for the process $e^+e^- \to W^+W^-$ for specific WW helicity states at 183 GeV. $\cos\theta_W$ is the cosine of the W^- production angle with respect to the e^- momentum in the centre-of-mass frame. The W^- and W^+ helicities are represented by τ and $\bar{\tau}$ respectively, and the y-axis is shown with a logarithmic scale.

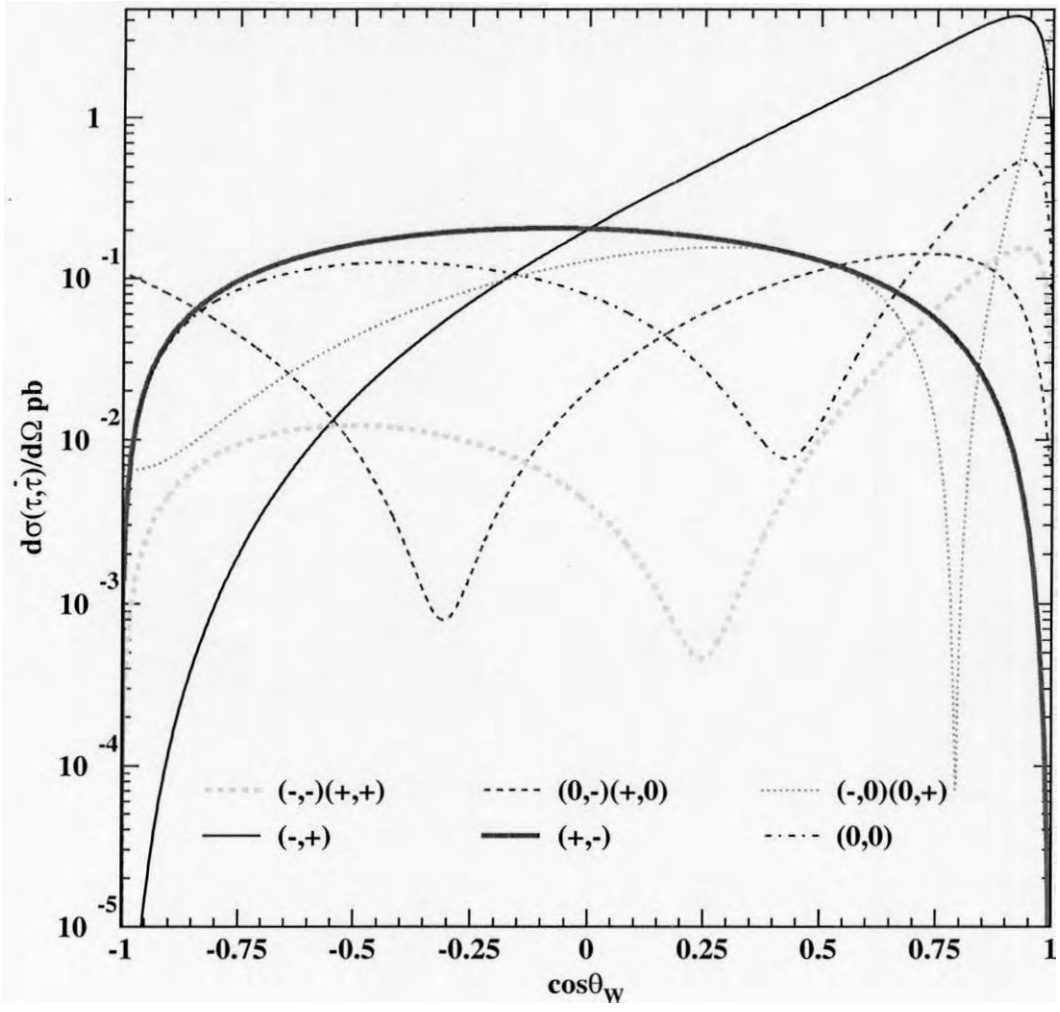

Figure 9: SM prediction of the differential cross-section for the process $e^+e^- \to W^+W^-$ for specific WW helicity states at 209 GeV. $\cos\theta_W$ is the cosine of the W^- production angle with respect to the e^- momentum in the centre-of-mass frame. The W^- and W^+ helicities are represented by τ and $\bar{\tau}$ respectively, and the y-axis is shown with a logarithmic scale.

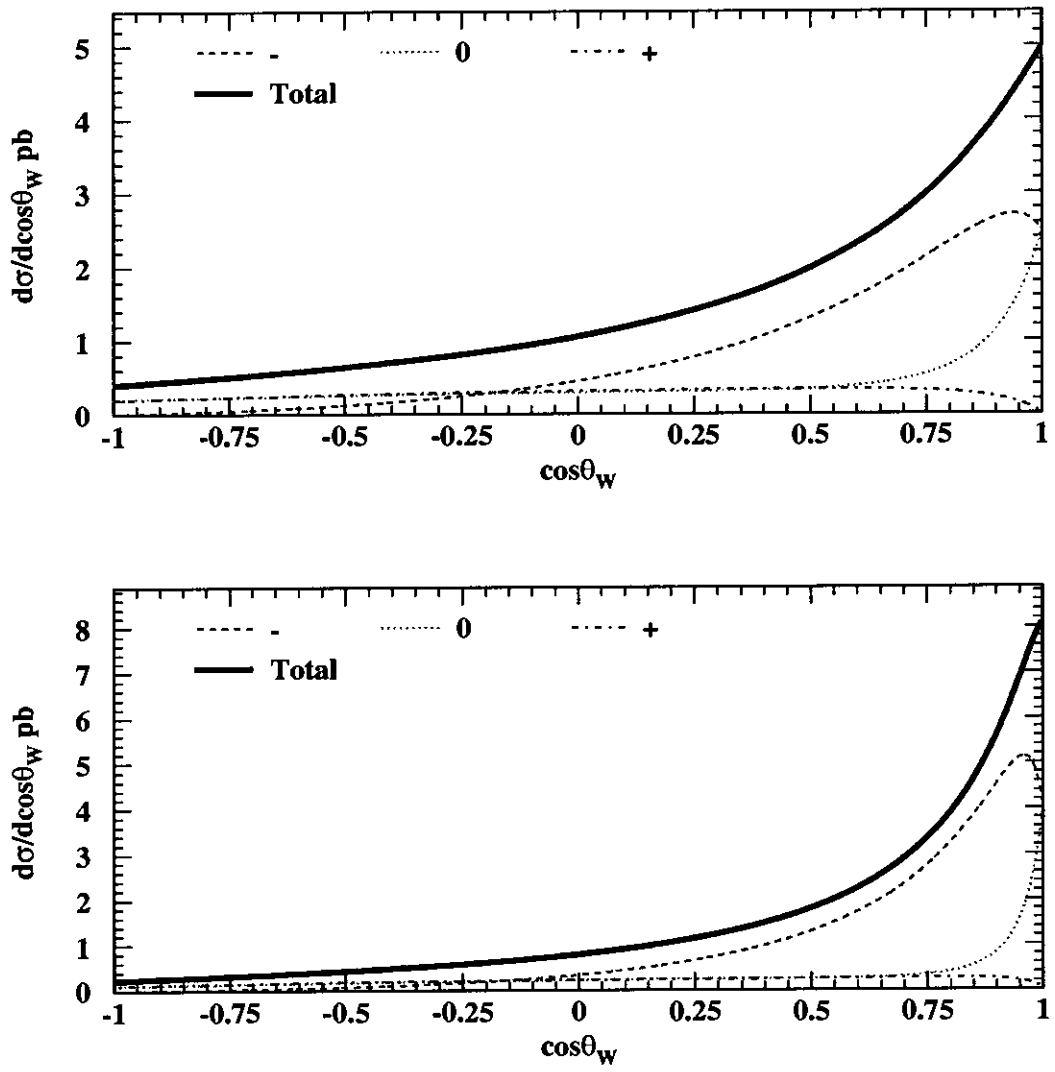

Figure 10: SM predictions of the differential cross-section for the process $e^+e^- \to W^+W^-$. The upper plot shows the cross-section calculated with a centre-of-mass energy of 183 GeV, and the lower plot shows the cross-section calculated with a centre-of-mass energy of 209 GeV. The dashed, dotted, and dash-dotted lines show the polarised cross-sections corresponding to the negative, longitudinal and positive helicity states of the W^-. The solid line shows the sum of the three polarised cross-sections (the unpolarised differential cross-section).

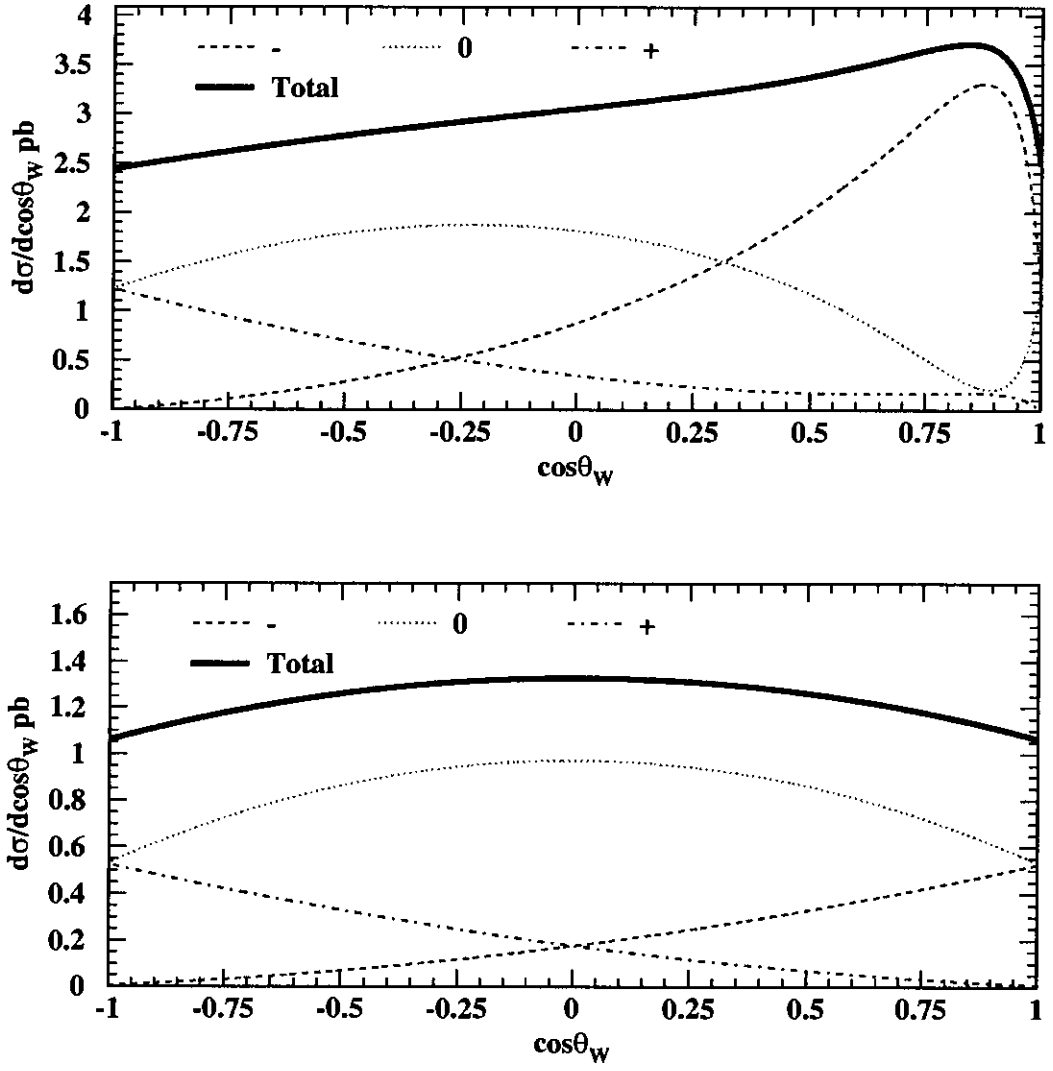

Figure 11: SM tree-level predictions of the differential cross-section for the process $e^+e^- \to W^+W^-$ at a centre-of-mass energy of 196 GeV. The upper plot shows the t-channel contribution and the lower plot shows the s-channel contribution. The dashed, dotted, and dash-dotted lines show the polarised cross-sections corresponding to the negative, longitudinal and positive helicity states of the W^-. The solid line shows the sum of the three polarised cross-sections (the unpolarised differential cross-section).

2.5 The spin density matrix

The composition of any spin state can be conveniently represented by the spin density matrix (SDM) as defined in appendix A. The SDM which describes the combined spin state of the W^+ and W^- in the reaction $e^+e^- \to W^+W^-$ is given by:

$$\rho^{WW}_{\tau,\tau',\bar{\tau},\bar{\tau}'}(s,\cos\theta_W) = \frac{\sum_{\lambda,\bar{\lambda}} F^{(\tau,\bar{\tau};\lambda,\bar{\lambda})}\left(F^{(\tau',\bar{\tau}';\lambda,\bar{\lambda})}\right)^*}{\sum_{\lambda,\bar{\lambda},\tau,\bar{\tau}}\left|F^{(\tau,\bar{\tau};\lambda,\bar{\lambda})}\right|^2} , \quad (26)$$

where $F^{(\tau,\bar{\tau};\lambda,\bar{\lambda})}$ is the helicity amplitude for producing a W^- with helicity τ and a W^+ with helicity $\bar{\tau}$ from an electron with helicity λ and positron with helicity $\bar{\lambda}$, following the convention of section 2.4. Possible additional terms associated with any transverse polarisation of the incoming electron or positron beams are ignored in equation (26), as the beam polarisation was negligible at all LEP centre-of-mass energies used for this analysis [19]. Moreover, the measurements presented in this thesis are expected to be inherently insensitive to transverse polarisation effects [20, 21].

The WW SDM can be reduced by summing over the degrees of freedom of the W^+ boson to give the W^- SDM [8],

$$\rho^{W^-}_{\tau,\tau'}(s,\cos\theta_W) = \frac{\sum_{\lambda,\bar{\lambda},\bar{\tau}} F^{(\tau,\bar{\tau};\lambda,\bar{\lambda})}\left(F^{(\tau',\bar{\tau};\lambda,\bar{\lambda})}\right)^*}{\sum_{\lambda,\bar{\lambda},\tau,\bar{\tau}}\left|F^{(\tau,\bar{\tau};\lambda,\bar{\lambda})}\right|^2} , \quad (27)$$

and the SDM for the W^+ is defined analogously by summing over the W^- degrees of freedom,

$$\rho^{W^+}_{\bar{\tau},\bar{\tau}'}(s,\cos\theta_W) = \frac{\sum_{\lambda,\bar{\lambda},\tau} F^{(\tau,\bar{\tau};\lambda,\bar{\lambda})}\left(F^{(\tau,\bar{\tau}';\lambda,\bar{\lambda})}\right)^*}{\sum_{\lambda,\bar{\lambda},\tau,\bar{\tau}}\left|F^{(\tau,\bar{\tau};\lambda,\bar{\lambda})}\right|^2} . \quad (28)$$

By construction, all spin density matrices are Hermitean matrices with unit trace. The W^- SDM and W^+ SDM are fully described by eight parameters each. The elements lying

[8] The sum over the unobserved degrees of freedom is incoherent such that $\bar{\tau} = \bar{\tau}'$.

on the major diagonal of the W^- matrix are the probabilities of observing a W^- in each of the three possible helicity states and are therefore positive as well as purely real. The diagonal elements of the W^+ SDM have the analogous interpretation for measurements of the W^+ helicity. The real and imaginary parts of the off-diagonal terms of the matrices measure the interference between the helicity amplitudes; i.e. if each W boson was produced in a definite helicity state rather than in a linear superposition of helicity states then the off-diagonal terms of the matrices would all be identically zero.

The SM tree-level predictions for the elements of the W^- and W^+ SDMs at a centre-of-mass energy of 196 GeV are shown in figures 12 and 13. Each SDM is displayed in two rows, where the first row shows the major diagonal elements from the matrix, and the second row shows the real parts of the off-diagonal elements of the matrix. The imaginary parts of the off-diagonal elements are not shown because they are identically zero at tree-level in the SM due to the presence of the symmetries discussed in section 2.8. The same symmetries additionally impose relationships between the real parts of the W^- and W^+ SDM, as can be seem by comparing figures 12 and 13 (for example $\rho^{W^-}_{++} = \rho^{W^+}_{--}$).

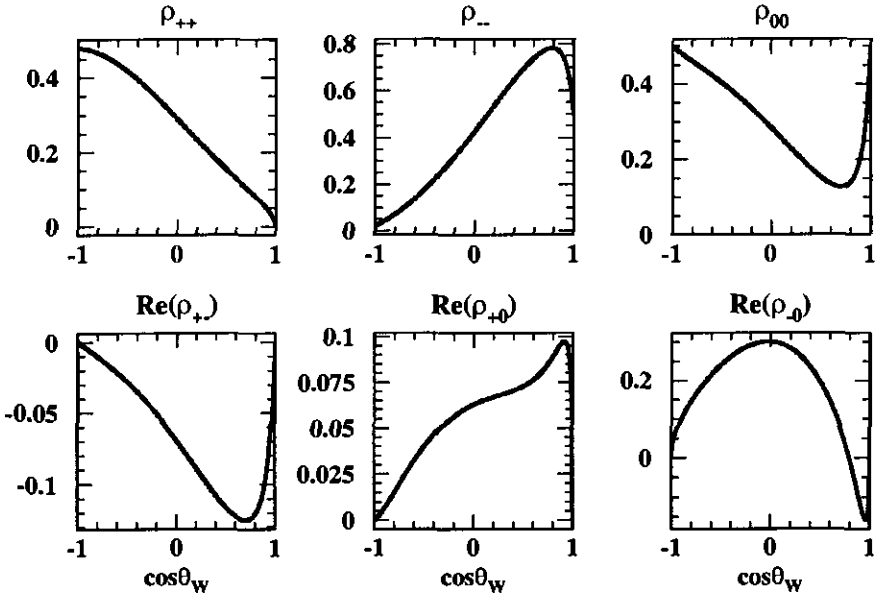

Figure 12: Tree-level SM predictions for the elements of the W^- spin density matrix in $e^+e^- \to W^+W^-$ collisions at a centre-of-mass energy of 196 GeV. Each element is shown as a function of $\cos\theta_W$.

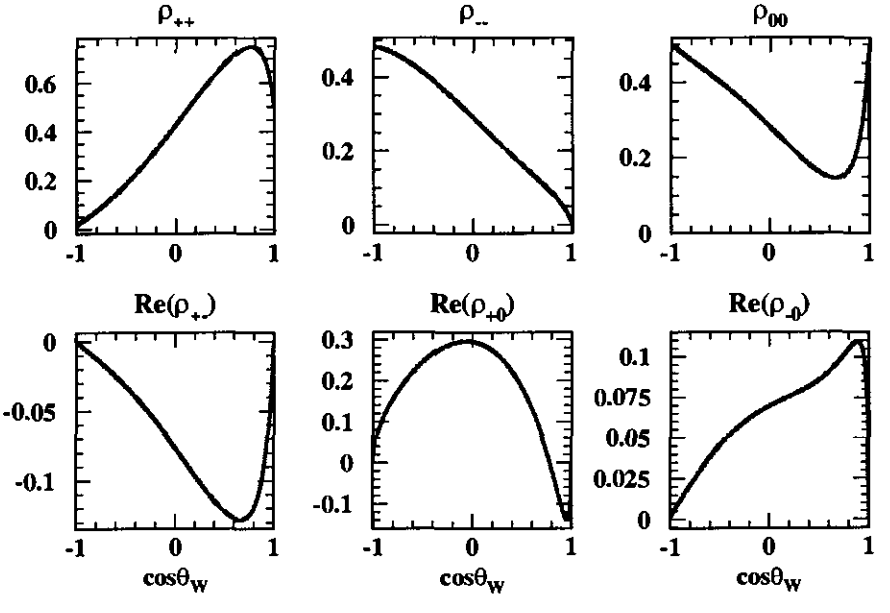

Figure 13: Tree-level SM predictions for the elements of the W^+ spin density matrix in $e^+e^- \to W^+W^-$ collisions at a centre-of-mass energy of 196 GeV. Each element is shown as a function of $\cos\theta_W$.

2.6 Decay distributions and projection operators

It was shown in the previous section that the W spin density matrices concisely summarise the contributions of the different helicity amplitudes in the reaction $e^+e^- \to W^+W^-$. This section details how, in principle, the spin density matrices can be reconstructed from experiment using the decay products of the W bosons as polarimeters.

Once produced, each W boson rapidly decays to a pair of fermions. The probability that a particle decays to a given final state is known as the 'branching fraction' or 'branching ratio' for that state. In the absence of radiated photons or gluons, the SM tree-level branching ratios for W decays to quarks and leptons are $\frac{2}{3}$ and $\frac{1}{3}$ respectively. As the decay mode of the W^- and W^+ in each WW event are independent of one another, approximately $\frac{4}{9}$ of WW events have a $q\bar{q}q\bar{q}$ final state, approximately $\frac{4}{9}$ have a $q\bar{q}'\ell\nu$ final state and $\frac{1}{9}$ have a $\ell\nu\ell\nu$ final state. The predicted branching ratio for the $q\bar{q}'\ell\nu$ and $q\bar{q}q\bar{q}$ final states are slightly enhanced when gluon radiation is included in the calculation, with $q\bar{q}q\bar{q}$ receiving the larger contribution.

A schematic diagram of the decay of the W bosons pair-produced in the lab frame is shown in figure 14. Due to the form of the W boson couplings, the angular distributions of the outgoing fermions depend on the polarisation of the W bosons. As previously, the polar angle of the W^- with respect to the electron beam direction is denoted by θ_W. The polar and azimuthal angles of the outgoing fermion in the rest frame of the parent W^- are denoted by $\theta^*_{f_1}$ and $\phi^*_{f_1}$ respectively [9]. The polar and azimuthal angles of the outgoing anti-fermion in the rest frame of the parent W^+ are denoted by $\theta^*_{\bar{f}_4}$ and $\phi^*_{\bar{f}_4}$ respectively. Collectively these five angles are denoted by Ω and fully describe the kinematics of a $e^+e^- \to W^+W^-$ reaction.

[9] The axes of the right-handed coordinate system in the parent W rest frame are defined using the helicity axes convention such that the z^*-axis is along the boost direction, $\hat{b}$, from the laboratory frame, and the y^*-axis is in the direction $\hat{k} \times \hat{b}$, where $\hat{k}$ is the direction of the incoming electron beam.

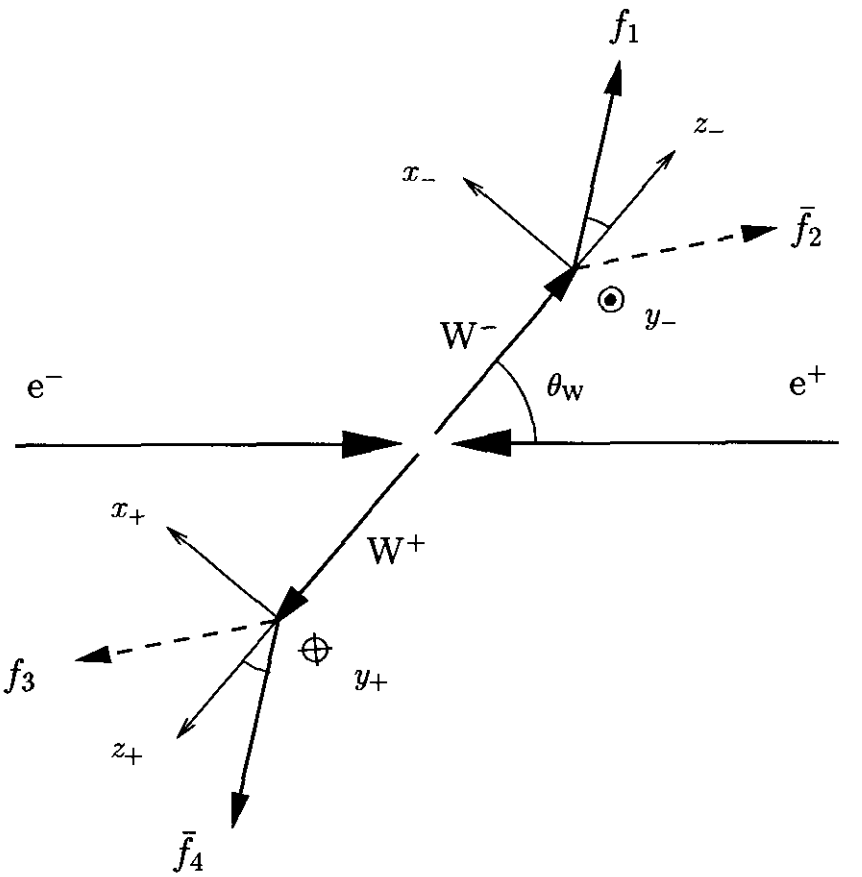

Figure 14: Schematic diagram showing the $e^+e^- \to W^+W^-$ scattering plane of an $e^+e^- \to W^+W^- \to f_1\bar{f}_2f_3\bar{f}_4$ event where the W^- decays to fermion f_1 and anti-fermion $\bar{f}_2$, and the W^+ decays to fermion f_3 and anti-fermion $\bar{f}_4$. The decay products (f_1, $\bar{f}_2$, f_3 and $\bar{f}_4$) are not confined to the $e^+e^- \to W^+W^-$ plane.

The differential cross-section for the process $e^+e^- \to W^+W^- \to f_1\bar{f}_2f_3\bar{f}_4$ is related to the spin density matrix by [14]

$$\frac{d^5\sigma}{d\Omega} = B\frac{\beta_W}{32\pi s}\left(\frac{3}{8\pi}\right)^2 \sum_{\tau,\bar{\tau},\tau',\bar{\tau}'} \tilde{\rho}^{WW}_{\tau,\tau',\bar{\tau},\bar{\tau}'} D_{\tau,\tau'}(\theta^*_{f_1},\phi^*_{f_1}) D_{\bar{\tau},\bar{\tau}'}(\pi-\theta^*_{\bar{f}_4},\pi+\phi^*_{\bar{f}_4}) \quad , \quad (29)$$

where $d\Omega$ is the differential element $d\cos\theta_W d\cos\theta^*_{f_1} d\phi^*_{f_1} d\cos\theta^*_{\bar{f}_4} d\phi^*_{\bar{f}_4}$, B is the fraction of WW events which decay to the state $f_1\bar{f}_2f_3\bar{f}_4$ and $\tilde{\rho}_{WW}$ is the un-normalised SDM (i.e. the numerator of equation (26)). The $D_{\tau,\tau'}$ are the angular decay distributions of the fermions. Critically, for fermions and anti-fermions moving with relativistic speeds, the left-handed

and right-handed chiral states produced by the weak interaction can be approximated by the left-handed and right-handed helicity states respectively. In practice, the ratios of the masses of the SM leptons and quarks to the mass of the W boson are sufficiently small that deviations from this approximation are negligible compared to the statistical uncertainties on the measurements being made[10]. The decay distributions of the W boson then follow from the Wigner-Eckart theorem,

$$D_{\tau,\tau'}(\theta^*_f,\phi^*_f) = l_\tau(\theta^*_f,\phi^*_f)l^*_{\tau'}(\theta^*_f,\phi^*_f) \tag{30}$$

$$l_{-1}(\theta^*_f,\phi^*_f) = \frac{1}{\sqrt{2}}(1+\cos\theta^*_f)e^{-i\phi^*_f} \tag{31}$$

$$l_0(\theta^*_f,\phi^*_f) = -\sin\theta^*_f \tag{32}$$

$$l_{+1}(\theta^*_f,\phi^*_f) = \frac{1}{\sqrt{2}}(1-\cos\theta^*_f)e^{i\phi^*_f}\ . \tag{33}$$

The polar angular decay distributions for fermions originating from polarised W^- bosons are shown in figure 15. By summing over the density matrix elements of one of the W bosons and integrating over the boson's decay angles, we can obtain the differential cross-section for the remaining W,

$$\frac{\mathrm{d}^3\sigma}{\mathrm{d}\cos\theta_{\mathrm{W}}\mathrm{d}\cos\theta^*_{f_1}\mathrm{d}\phi^*_{f_1}} = B\frac{\beta_{\mathrm{W}}}{32\pi s}\left(\frac{3}{8\pi}\right)\sum_{\tau,\tau'}\tilde{\rho}^{\mathrm{W}^-}_{\tau,\tau'}D_{\tau,\tau'}(\theta^*_{f_1},\phi^*_{f_1})\ , \tag{34}$$

$$\frac{\mathrm{d}^3\sigma}{\mathrm{d}\cos\theta_{\mathrm{W}}\mathrm{d}\cos\theta^*_{\bar{f}_4}\mathrm{d}\phi^*_{\bar{f}_4}} = B\frac{\beta_{\mathrm{W}}}{32\pi s}\left(\frac{3}{8\pi}\right)\sum_{\bar{\tau},\bar{\tau}'}\tilde{\rho}^{\mathrm{W}^+}_{\bar{\tau},\bar{\tau}'}D_{\bar{\tau},\bar{\tau}'}(\pi-\theta^*_{\bar{f}_4},\pi+\phi^*_{\bar{f}_4})\ . \tag{35}$$

In practice, the differential cross-sections can be measured from experiment and the SDM elements must then be derived from them. One possible method for achieving this is to extract the elements of the SDM by fitting the differential cross-sections to the angular distributions obtained from the data. Such an analysis has been published by the L3

[10]The top quark is too massive to be produced from on-shell W bosons and the production of bottom quarks is highly suppressed.

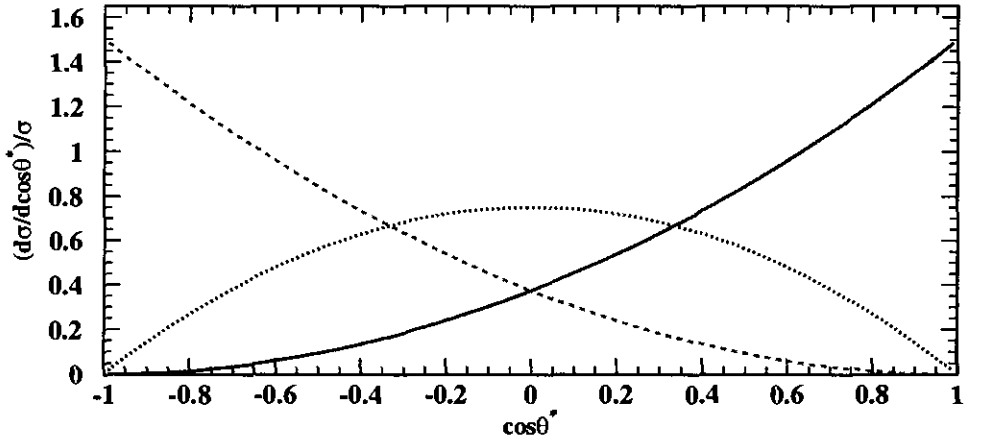

Figure 15: Distributions of the outgoing fermion in the rest-frame of its parent W^- boson resulting from each helicity state of the W^-. The solid line shows the distribution associated with the negative helicity state, the dashed line shows the distribution associated with the positive helicity state, and the dotted line shows the distribution associated with the longitudinal helicity state.

collaboration [22], in which they extracted the diagonal elements of the SDM from the $\cos\theta_f^*$ and $\cos\theta_{\bar{f}}^*$ distributions. As in previous OPAL analyses [23,24], this thesis employs the alternative method of constructing projection operators, $\Lambda_{\tau\tau'}$, which satisfy:

$$\rho^{W^-}_{\tau,\tau'}(s,\cos\theta_W) = \frac{\int \frac{d^3\sigma}{d\cos\theta_W d\cos\theta_f^* d\phi_f^*}\Lambda_{\tau\tau'} d\cos\theta_f^* d\phi_f^*}{\frac{d\sigma}{d\cos\theta_W}} . \quad (36)$$

Equations (37) to (39), listed below, give the projection operators used to extract the diagonal elements of the W^- SDM. They depend only on the polar production angle of the fermion, θ_f^*. The projection operators corresponding to the off-diagonal elements of the W^- SDM are given in equations (40) to (42) and have azimuthal angular dependence.

$$\Lambda_{--} = \tfrac{1}{2}(5\cos^2\theta_f^* + 2\cos\theta_f^* - 1) \quad (37)$$

$$\Lambda_{00} = 2 - 5\cos^2\theta_f^* \quad (38)$$

$$\Lambda_{++} = \tfrac{1}{2}(5\cos^2\theta_f^* - 2\cos\theta_f^* - 1) \quad (39)$$

$$\Lambda_{+-} = 2e^{2i\phi_f^*} \quad (40)$$

$$\Lambda_{+0} = \frac{-8}{3\pi\sqrt{2}}\left(1 - 4\cos\theta_f^*\right)e^{-i\phi_f^*} \quad (41)$$

$$\Lambda_{-0} = \frac{-8}{3\pi\sqrt{2}}\left(1 + 4\cos\theta_f^*\right)e^{i\phi_f^*} \quad (42)$$

The operators for the W^+ can be obtained by replacing $\cos\theta_f^*$ and ϕ_f^* by $\cos\theta_{\bar{f}}^*$ and $\phi_{\bar{f}}^*$.

2.7 Polarised cross-sections

Once the spin density matrices have been measured they can be used to obtain other quantities of interest. The most obvious of these are the polarised cross-sections shown previously in figure 10. The longitudinally and transversely polarised differential cross-sections for W production are given in terms of the SDM elements by [25]:

$$\frac{d\sigma_L}{d\cos\theta_W} = \rho_{00}\frac{d\sigma}{d\cos\theta_W} \quad (43)$$

$$\frac{d\sigma_T}{d\cos\theta_W} = (\rho_{++} + \rho_{--})\frac{d\sigma}{d\cos\theta_W} \quad . \quad (44)$$

The electric charge of the charged lepton in a $W \to \ell\nu$ decay can be reliably reconstructed so that there is no ambiguity in determining $\cos\theta_f^*$ or ϕ_f^* for use in the projection operators. The charge of a quark which undergoes hadronisation is not readily accessible, so the measured angular distributions for hadronically decaying W bosons ($W \to q\bar{q}'$) must be folded such that $\cos\theta_f^*$ lies between 0 and 1 and ϕ_f^* lies between 0 and π. Although neither ρ_{++} nor ρ_{--} can be measured individually after this folding, their sum is unchanged and the polarised differential cross-sections can still be evaluated.

The total polarised cross-sections are obtained by integrating the differential cross-sections in equations (43) and (44) with respect to $\cos\theta_W$:

$$\sigma_L = \int_{-1}^{1}\frac{d\sigma_L}{d\cos\theta_W}d\cos\theta_W \quad (45)$$

$$\sigma_T = \int_{-1}^{1}\frac{d\sigma_T}{d\cos\theta_W}d\cos\theta_W \quad . \quad (46)$$

It follows that the total fraction of longitudinally polarised W bosons is equal to,

$$f_L = \frac{\sigma_L}{\sigma_L + \sigma_T} . \quad (47)$$

2.8 CP and CP$\hat{\mathrm{T}}$ symmetries

In addition to the gauge symmetries, the SM physics also respects certain discrete symmetries. Systems related to one another under these symmetries should evolve in the same way and at the same rate. The parity operator (P) was introduced in section 2.2; two other important symmetry operations are charge conjugation (C) in which all particles are replaced with their corresponding anti-particles, and time-reversal (T) in which the initial and final states of a reaction are exchanged. Each of these symmetries are individually violated in the SM but the product of the three operations, CPT, is conserved in the SM and in all other local, Lorentz-invariant field theories of point-like particles [26]. Although violation of CP symmetry has only ever been observed in processes involving the weak eigenstates of the quarks, there are reasons to believe that there must be other CP-violating mechanisms in nature [27].

Much of the sensitivity of W pair production to CP-violating interactions is contained in the distributions of the azimuthal angles ϕ_f^* and $\phi_{\bar{f}}^*$. Both azimuthal angular distributions are symmetric about zero at tree-level in the SM. The presence of a CP-violating phase at the TGC vertex would, in general, shift the distributions to introduce an asymmetry. This effect can be measured from the off-diagonal elements of the SDM, as described below.

Under the assumption of CP invariance, the SDM for the W^- and the SDM for the W^+ are related by [28],

$$\rho^{W^-}_{\tau,\tau'} = \rho^{W^+}_{-\tau-\tau'} \ . \tag{48}$$

It is often difficult to produce two systems related to each other by the time-reversal operator, T, in a practical experimental environment, but the operator can be approximated by the pseudo time-reversal operator $\hat{\mathrm{T}}$ which transforms the helicity amplitudes into their complex conjugates rather than interchanging their initial and final states. At tree-level, the effect of the pseudo time-reversal operator is exactly equivalent to the effect of the true

time reversal operator [12,29]. Under the assumption of CP$\hat{\mathrm{T}}$ invariance, the SDM for the W^- and the SDM for the W^+ are related by,

$$\rho^{\mathrm{W}^-}_{\tau,\tau'} = \left(\rho^{\mathrm{W}^+}_{-\tau-\tau'}\right)^* \quad . \tag{49}$$

It follows from equations (48) and (49) that if both CPT and CP are conserved in W pair production then,

$$\rho^{\mathrm{W}^-}_{\tau,\tau'} = (\rho^{\mathrm{W}^-}_{\tau,\tau'})^* \tag{50}$$

$$\rho^{\mathrm{W}^+}_{\bar{\tau},\bar{\tau}'} = (\rho^{\mathrm{W}^+}_{\bar{\tau},\bar{\tau}'})^* \, , \tag{51}$$

and therefore the imaginary parts of both SDMs must be identically zero. Furthermore, any tree-level CP non-conserving effects will only violate the imaginary part of equation ((48)). Such effects could arise from non-zero values of the CP-violating terms in the phenomenological TGC Lagrangian of equation (12) (i.e. $\tilde{\kappa_\gamma}$, $\tilde{\lambda_\gamma}$, g_4^γ, $\tilde{\kappa_\mathrm{Z}}$, $\tilde{\lambda_\mathrm{Z}}$, or g_4^Z).

This observation motivates the construction of $\sigma^{\mathrm{W}^-}_{\tau\tau'}$ and $\sigma^{\mathrm{W}^+}_{\tau\tau'}$ which are defined below in terms of the imaginary parts of the off-diagonal SDM elements and are measured in units of cross-section:

$$\sigma^{\mathrm{W}^-}_{\tau\tau'} = \int_{-1}^{+1} Im\left\{\rho^{\mathrm{W}^-}_{\tau\tau'}\right\} \frac{\mathrm{d}\sigma}{\mathrm{d}\cos\theta_\mathrm{W}} \mathrm{d}\cos\theta_\mathrm{W} \tag{52}$$

$$\sigma^{\mathrm{W}^+}_{\bar{\tau}\bar{\tau}'} = \int_{-1}^{+1} Im\left\{\rho^{\mathrm{W}^+}_{\bar{\tau}\bar{\tau}'}\right\} \frac{\mathrm{d}\sigma}{\mathrm{d}\cos\theta_\mathrm{W}} \mathrm{d}\cos\theta_\mathrm{W} \quad . \tag{53}$$

From these quantities it is possible to form experimentally accessible CP-odd observables [11]:

$$\Delta^{\mathrm{CP}}_{+-} = \sigma^{\mathrm{W}^-}_{+-} - \sigma^{\mathrm{W}^+}_{-+} \tag{54}$$

$$\Delta^{\mathrm{CP}}_{+0} = \sigma^{\mathrm{W}^-}_{+0} - \sigma^{\mathrm{W}^+}_{-0} \tag{55}$$

$$\Delta^{\mathrm{CP}}_{-0} = \sigma^{\mathrm{W}^-}_{-0} - \sigma^{\mathrm{W}^+}_{+0} \, , \tag{56}$$

[11] A quantity is said to be CP-odd if it changes sign under a CP transformation.

and also construct CP$\hat{\text{T}}$-odd observables sensitive to the presence of loop effects:

$$\Delta_{+-}^{\text{CP}\hat{\text{T}}} = \sigma_{+-}^{\text{W}^-} + \sigma_{-+}^{\text{W}^+} \quad (57)$$

$$\Delta_{+0}^{\text{CP}\hat{\text{T}}} = \sigma_{+0}^{\text{W}^-} + \sigma_{-0}^{\text{W}^+} \quad (58)$$

$$\Delta_{-0}^{\text{CP}\hat{\text{T}}} = \sigma_{-0}^{\text{W}^-} + \sigma_{+0}^{\text{W}^+} \ . \quad (59)$$

Non-zero values of any of the CP-odd observables would indicate the presence of CP-violating mechanisms operating at the TGC vertex, whereas non-zero values of the CP$\hat{\text{T}}$-odd observables would show that the analysis is sensitive to terms beyond the tree-level approximation that has been considered in this derivation. No assumptions about the form of the TGC vertices are necessary to extract any of the observables from the data. Hence this study is complementary to the CP-violating TGC parameter measurements previously published by ALEPH and OPAL [23,30].

There are pre-existing tight limits on CP-violating electromagnetic interactions which arise from measurements of the electric dipole moment of the electron, neutron and atomic nuclei (see for example reference [31] and the references therein). However, the current direct constraints on CP-violating interactions at the WWZ vertex are less stringent, and the search for these possible interactions motivates the measurements of the Δ^{CP} and $\Delta^{\text{CP}\hat{\text{T}}}$ parameters in this analysis.

2.9 Four-fermion processes

The CC03 Feynman diagrams introduced in section 2.3 were shown to give a gauge-invariant description of the $e^+e^- \to W^+W^-$ process at tree-level. In that discussion it was implicitly assumed that the W bosons were not virtual, i.e. the bosons obey the relativistic energy equation, $E_W^2 = p_W^2 + m_W^2$, and can propagate in free space. However, in considering the decay of the W bosons to a four-fermion final state, it is necessary to take into account the finite width, Γ_W of the W boson resonance ($\Gamma_W = 2.12$ GeV [1]). In effect, promptly-decaying W bosons can be produced with a distribution of masses centred on the rest mass m_W with a spread characterised by Γ_W. The gauge invariance of the CC03 Feynman diagrams is broken by this behaviour, and it follows that further tree-level diagrams are required for a complete gauge invariant description of four-fermion production. These additional diagrams are not of direct interest in this analysis as they do not involve W-pair production, but coherent interference between the Feynman diagrams means that the CC03 contribution cannot be measured in isolation.

The number of additional Feynman diagrams which need to be considered depends on the type of fermions present in the four-fermion final state. For practical reasons, discussed in section 5.2, only the $q\bar{q}'\ell\nu$ final state was analysed for this thesis. There are ten tree-level Feynman diagrams, including the CC03 diagrams, associated with the $q\bar{q}'\ell\nu$ final state, where ℓ can be any charged lepton. Each diagram features at least one W boson; hence, they are collectively referred to as CC10. The CC10 diagrams for a $u\bar{d}\mu\bar{\nu}_\mu$ final state are shown in figure 16. As there is already an electron present in the initial state, the $q\bar{q}'e\nu$ final state is a special case and the extra ten Feynman diagrams shown in figure 17 must also be taken into account. Two of the diagrams involve TGC vertices and contribute to single-W production which has been analysed in reference [32]. Although there are no tree-level neutral current Feynman diagrams for the $q\bar{q}'\ell\nu$ final state, there are Feynman diagrams which lead to a $q\bar{q}\ell^+\ell^-$ final state, which can be mis-reconstructed as a $q\bar{q}'\ell\nu$ event due

to detector inefficiencies. Therefore, these diagrams must also be considered in a practical implementation of the analysis.

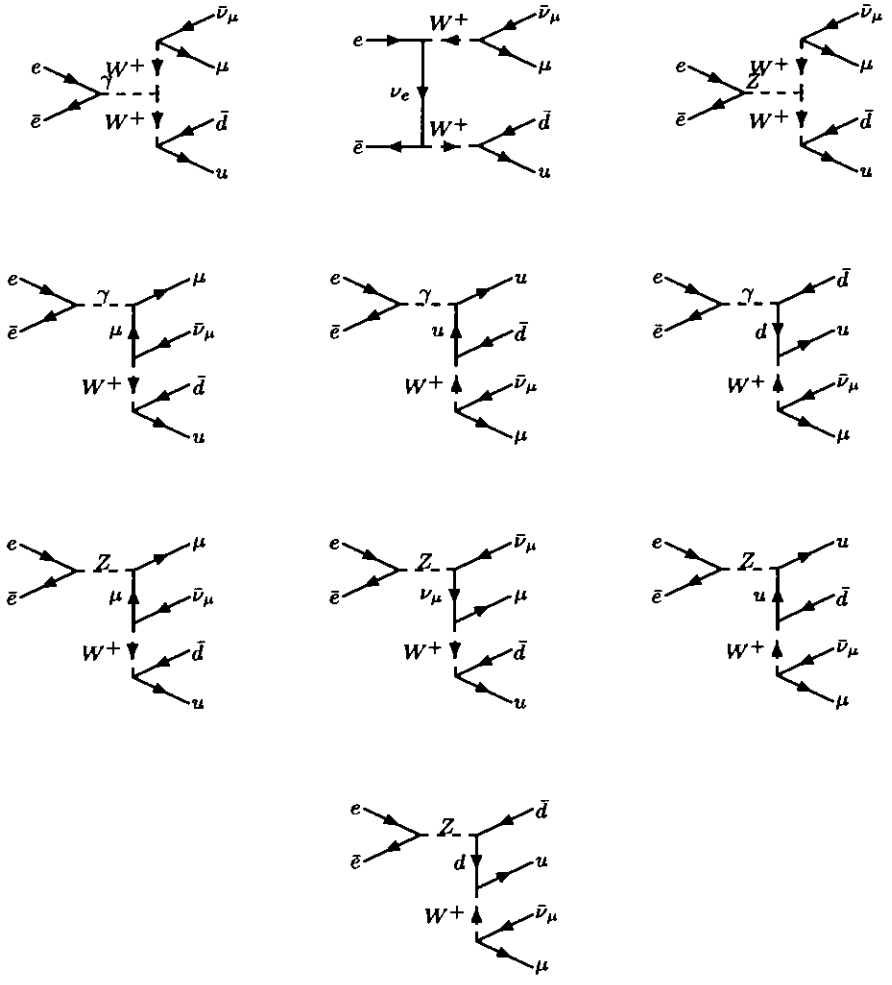

Figure 16: The CC10 tree-level Feynman diagrams for producing the $u\bar{d}\mu\bar{\nu}_\mu$ final state. The topmost row shows the CC03 Feynman diagrams. The diagrams were produced using the CalcHEP [33] software package.

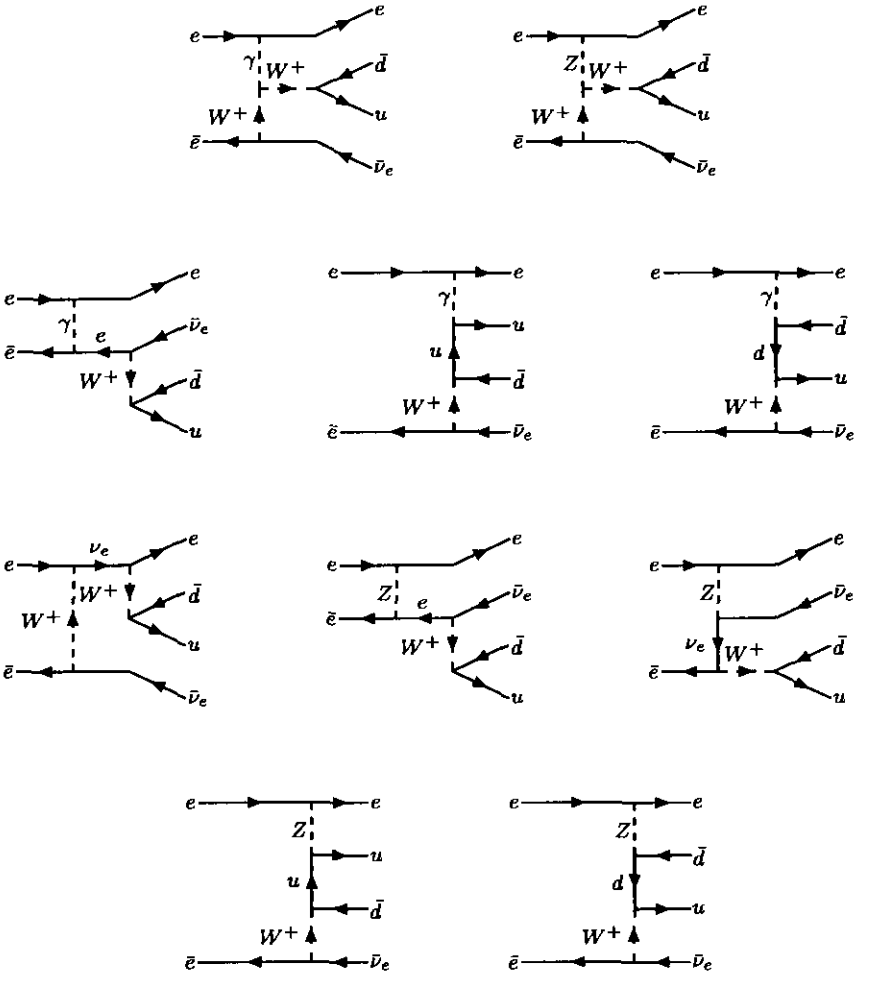

Figure 17: The additional tree-level Feynman diagrams needed to provide a gauge invariant description of the $u\bar{d}e\bar{\nu}_e$ final state. The topmost row contains the two diagrams which contribute to single-W production. The diagrams were produced using the CalcHEP [33] software package.

2.10 Radiative corrections

In addition to the tree-level processes of the preceding section it is also necessary to consider radiative processes in which gauge bosons are emitted from one or more of the particles appearing in the CC03 Feynman diagrams. Radiative processes involving W or Z bosons are highly suppressed because of the large mass of the bosons, but radiated gluons and photons give important contributions to the cross-sections.

Gluon radiation is limited to coloured objects, and is considered as part of the hadronisation process of the quarks produced from hadronically decaying W bosons. As this process is non-perturbative, it is not possible to implement algorithms which calculate the effects of hadronisation from first principles. In the simulations discussed in section 6.2, model-dependent approximations were used whose parameters were tuned such that their output agrees with previous experimental observations [34].

Radiative electromagnetic processes are shown in figure 18 and can be sub-divided into four categories: initial state radiation (ISR), final state radiation (FSR), intermediate state radiation [12], and virtual processes. The latter are further categorized as factorisable or non-factorisable. All such radiative processes are suppressed by at least a factor of $\mathcal{O}(\alpha)$ compared to the tree-level four-fermion diagrams considered previously. A full implementation of these $\mathcal{O}(\alpha)$ effects is currently impractical due to the large number of Feynman diagrams involved. The simulations of section 6.2 use approximations in which only the dominant contributions are considered.

[12] Denoted 'WSR' in the case of radiation from W bosons.

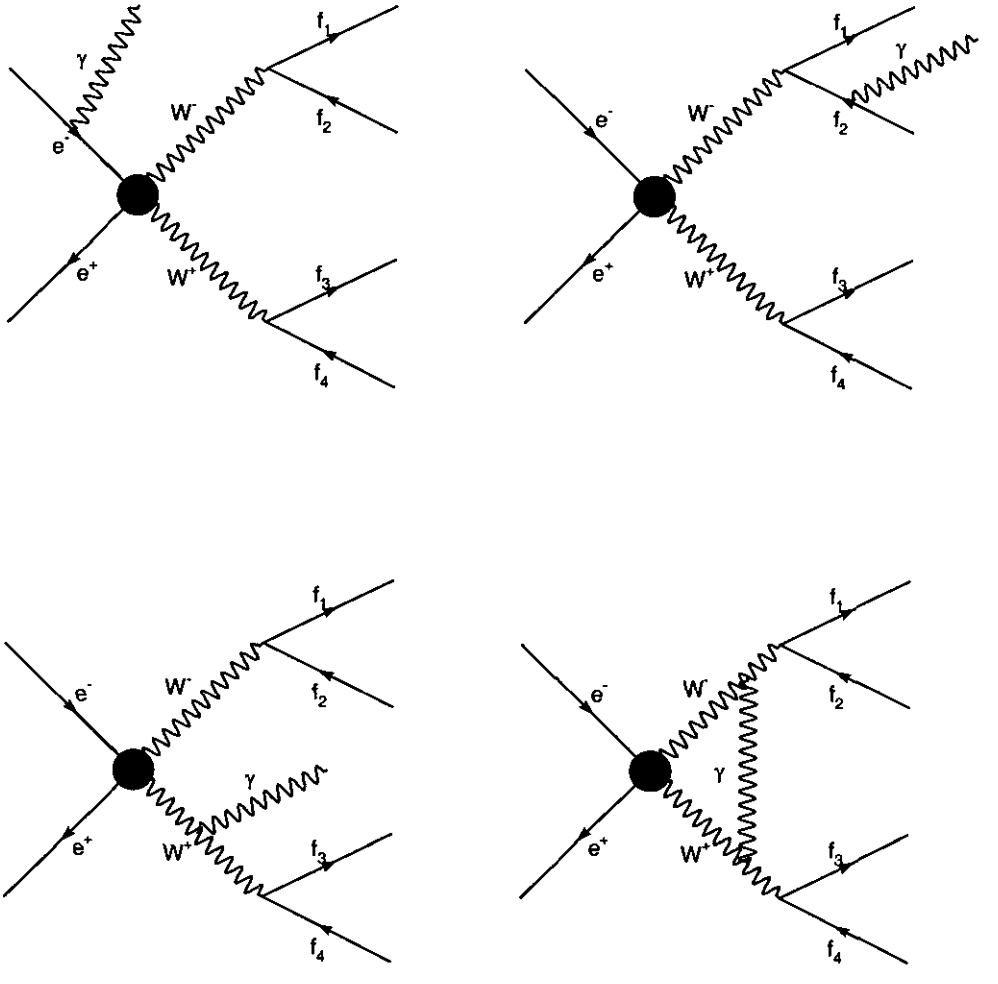

Figure 18: An illustration of the four categories of radiative corrections discussed in the text. The upper-left diagram shows the emission of an ISR photon, the upper-right diagram shows the emission of an FSR photon, the bottom-left diagram shows the emission of a WSR photon, and the bottom-right diagram shows the exchange of a virtual photon.

3 The Large Electron Positron Collider

The Large Electron Positron collider (LEP) was a circular particle accelerator with a circumference of approximately 27 km. It formed part of the accelerator complex built at CERN [13] - the international physics laboratory located on the Franco-Swiss border close to the city of Geneva. LEP was operational between the years 1989 and 2000, during which time it was used to accelerate counter-circulating beams of electrons and positrons and bring them into collision at the interaction points occupied by the four LEP experiments: ALEPH, DELPHI, L3 and OPAL. Figure 19 shows a schematic diagram of the accelerators at CERN prior to the decommissioning of LEP. A brief description of the LEP machine is given below; technical details can be found in reference [35] and the references therein.

The LEP Injector Linac (LIL) facility supplied LEP with both electrons and positrons. The electrons were generated by the familiar mechanism of thermionic emission, whilst the positrons were generated by accelerating electrons to 200 MeV in a linear accelerator (LINAC) and colliding them on to a fixed tungsten target. Once produced, both the positrons and electrons were accelerated to 600 MeV in the second LIL LINAC and stored in the electron-positron accumulator ring (EPA) in eight spatially-localised 'bunches'. The bunches were next accelerated to 3.5 GeV in the Proton Synchrotron (PS) and then to 22 GeV in the Super Proton Synchrotron (SPS) , before finally being injected into the LEP ring itself.

Once sufficient numbers of electrons and positrons had been accumulated within LEP, the eight bunches of each type from the SPS were formed into four bunches of each type and then accelerated to their required energy at a rate of 125 MeVs^{-1}. After the acceleration stage, electrostatic separators at the interaction points were turned off, bringing the beams into collision, and collimators were deployed to protect the LEP experiments from beam

[13] Originally the *Conseil Européen pour la Recherche Nucléarie* and now known officially as the *European Organisation for Nuclear Research* and commonly as the *European Laboratory for Particle Physics.*

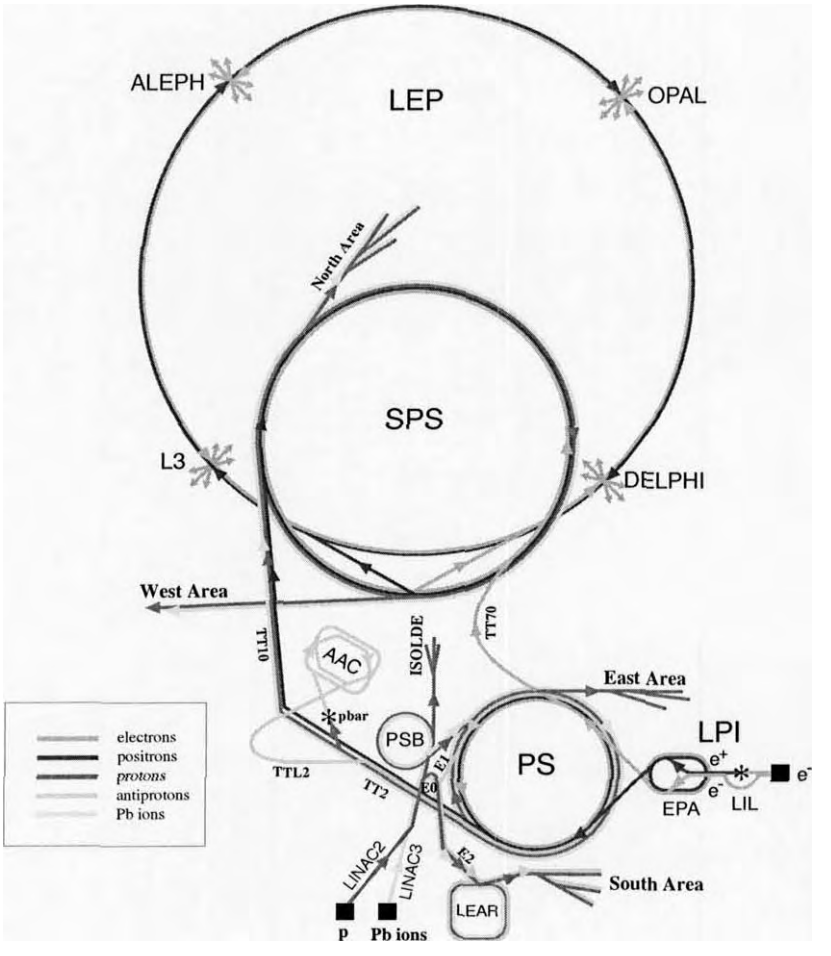

LEP: Large Electron Positron collider
SPS: Super Proton Synchrotron
AAC: Antiproton Accumulator Complex
ISOLDE: Isotope Separator OnLine DEvice
PSB: Proton Synchrotron Booster
PS: Proton Synchrotron

LPI: Lep Pre-Injector
EPA: Electron Positron Accumulator
LIL: Lep Injector Linac
LINAC: LINear ACcelerator
LEAR: Low Energy Antiproton Ring

Rudolf LEY, PS Division, CERN, 02.09.96

Figure 19: The accelerators at CERN prior to the decommissioning of LEP at the end of the year 2000. The figure is not to scale.

backgrounds. Near the collision points, each beam had a typical transverse r.m.s. spread of 150 μm by 5 μm (in x and y respectively - see section 4), and each bunch was of the order of 1 cm long [36] and contained approximately 250 billion electrons or positrons.

The entire collider was situated in a tunnel 3.8 m in diameter at a depth of roughly 100 m below ground-level. The LEP beam pipe itself had a diameter of approximately 10 cm, and consisted of eight straight sections of approximately 420 m in length, and eight arcs of 2.9 km in length. The interaction points were located at the middle of each straight section, which additionally housed the RF acceleration system. Bending and focussing of the beams was achieved using the dipole, quadrupole, sextupole and orbit correcting magnets surrounding the beam pipe. The beam pipe vacuum system had a total volume of 270,000 litres and was maintained at a pressure of 10^{-12} Torr by rotary, turbo-molecular and ion pumps, in addition to getter strips. The latter are metallic strips which adsorb gas molecules when heated.

For the first seven years of its lifetime, LEP operated with beam energies close to 45.6 GeV - a value chosen to enable detailed study of the Z^0 boson. During the second phase of it's operation (LEP2), the beam energies were gradually increased to a maximum of 104.5 GeV allowing a variety of other physics processes to be investigated including the production of pairs of W bosons. The data used in this thesis were recorded at LEP between 1997-2000 with beam energies in the range 91.5-104.5 GeV. As LEP was a circular accelerator, the maximum energy of the beams was limited by energy loss due to the emission of synchrotron radiation.

For centre-of-mass energies less than 100 GeV, the energy of the LEP beams was determined using the technique of 'resonant depolarisation', which relies on the electrons and positrons being slightly transversely polarised due to the Sokolov-Ternov effect [37]. However, at higher energies the polarisation of the beams was too small to measure and the beam energy had to be extrapolated using measurements from NMR probes which had previously been cross-calibrated with the resonant depolarisation technique at beam energies between 41 and 60 GeV. An independent energy measurement was made using a magnetic spectrometer.

The number of collisions that take place inside a particle collider depends on the luminosity of the beams. For a generic reaction $e^+e^- \rightarrow X$, the number of final state particles 'X' produced is related to the time-integrated beam luminosity of the experiment, $\mathcal{L}$, and the cross-section for the process, σ_X, by:

$$N_X = \mathcal{L}\sigma_X \ . \tag{60}$$

At LEP2, the peak luminosity of the beams was approximately 10^{-4} $pb^{-1}s^{-1}$ and the total time-integrated luminosity was approximately 700 pb^{-1} per LEP experiment. Additionally, the SM cross-section for W pair production was approximately 15 pb in the centre-of-mass energy range spanned by LEP2. This corresponds to roughly 10,000 W pairs being produced at each of the four LEP collision points, which is an order of magnitude less than the number of quark and lepton pairs expected to be produced at these energies through radiative return to the Z^0 mass pole. The cross-sections measured using the OPAL detector at LEP for a variety of important SM processes are shown in figure 20 as functions of the centre-of-mass energy of the e^+e^- collisions.

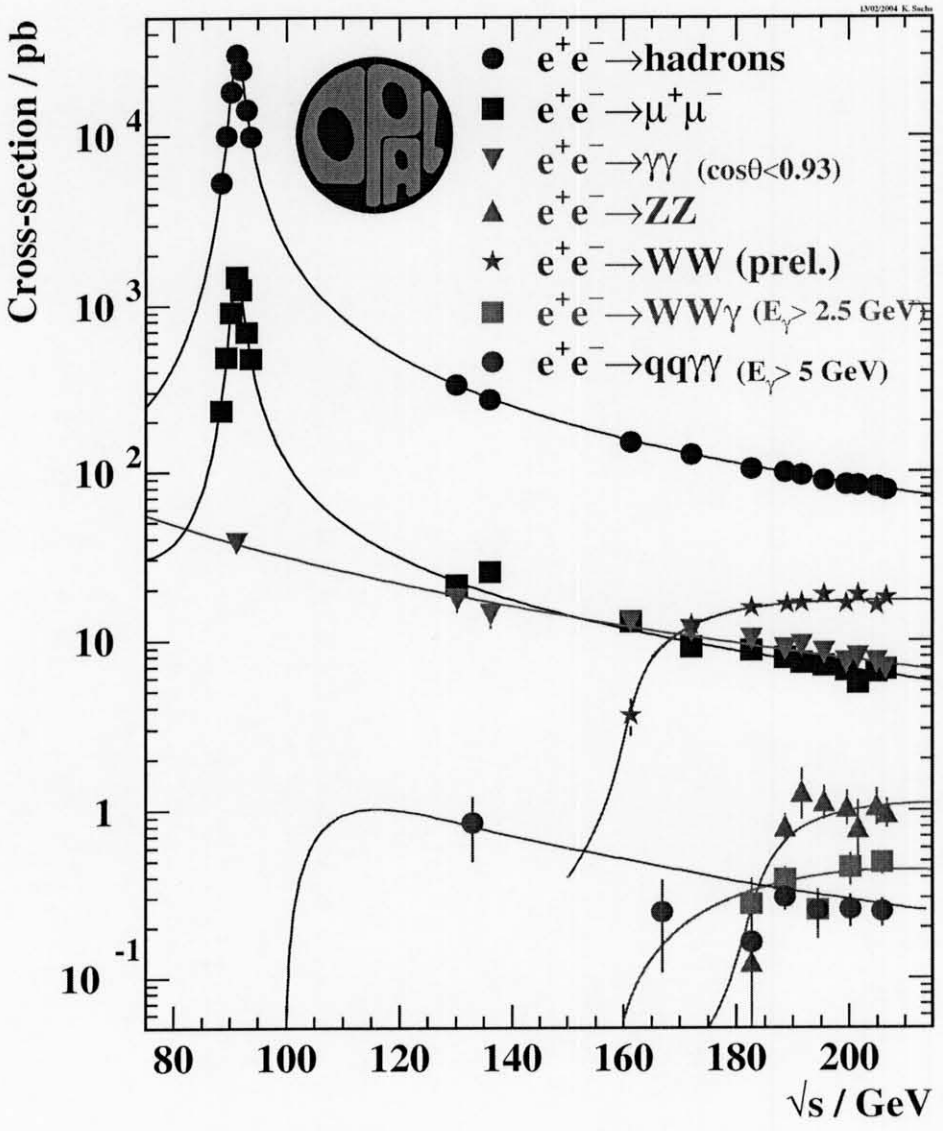

Figure 20: The SM cross-sections measured at LEP by the OPAL collaboration as a function of the centre-of-mass energy. The lines show the SM prediction and the points are obtained from the data. The data points for the reaction $e^+e^- \to W^+W^-$ are mostly preliminary [38] whereas the di-fermion, di-photon, Z-pair, WWγ and $qq\gamma\gamma$ data have been published in references [39], [40], [41], [42] and [43] respectively. The y-axis is logarithmic.

4 The OPAL detector

The OPAL detector was a general-purpose particle detector centred on and surrounding the nominal interaction point I6 at LEP. It operated from 1989 until being decommissioned at the end of the year 2000.

The superstructure of the detector measured approximately 12 m by 12 m by 12 m and consisted of an approximately cylindrical 'barrel' region sandwiched between two 'endcaps'. The barrel region contained concentric annular layers of sub-detectors and a solenoidal coil which generated a strong uniform magnetic field. The major axis of the barrel coincided with the major axis of the beam pipe containing the incident electron and positron beams [14].

Sub-detectors housed in the endcap regions gave complementary coverage to those in the barrel (with some overlap), enabling the detection of particles produced at small angles to the beam pipe. Only neutrinos and particles emitted at an angle less than 40 mrad to the incident beam directions were expected to be undetected. A cut-away view of the detector is shown in figure 21. A summary of the individual sub-detectors is given in the subsequent sections, and a more detailed account can be found in reference [44].

4.1 Central detector

The primary function of the central detector was to record the paths of the charged particles emanating from the interaction point as they passed though the detector under the influence of the axial magnetic field generated by the solenoid described in section 4.2. The detector consisted of a silicon micro-vertex detector and three-specialised drift chambers: the vertex chamber, the jet chamber and the z-chamber. The drift chambers were housed in an annular pressure vessel filled with a gas mixture of argon, methane and isobutane at a pressure of

[14]The OPAL Master Reference System is a right-handed Cartesian co-ordinate system defined such that its origin is at the nominal interaction point and the z-axis is aligned along the nominal electron beam direction. The x-axis is horizontal and pointed towards the centre of the quondam LEP ring. In addition, the azimuthal angle in the $x-y$ plane is denoted as ϕ and the polar angle from the positive z-axis is denoted as θ.

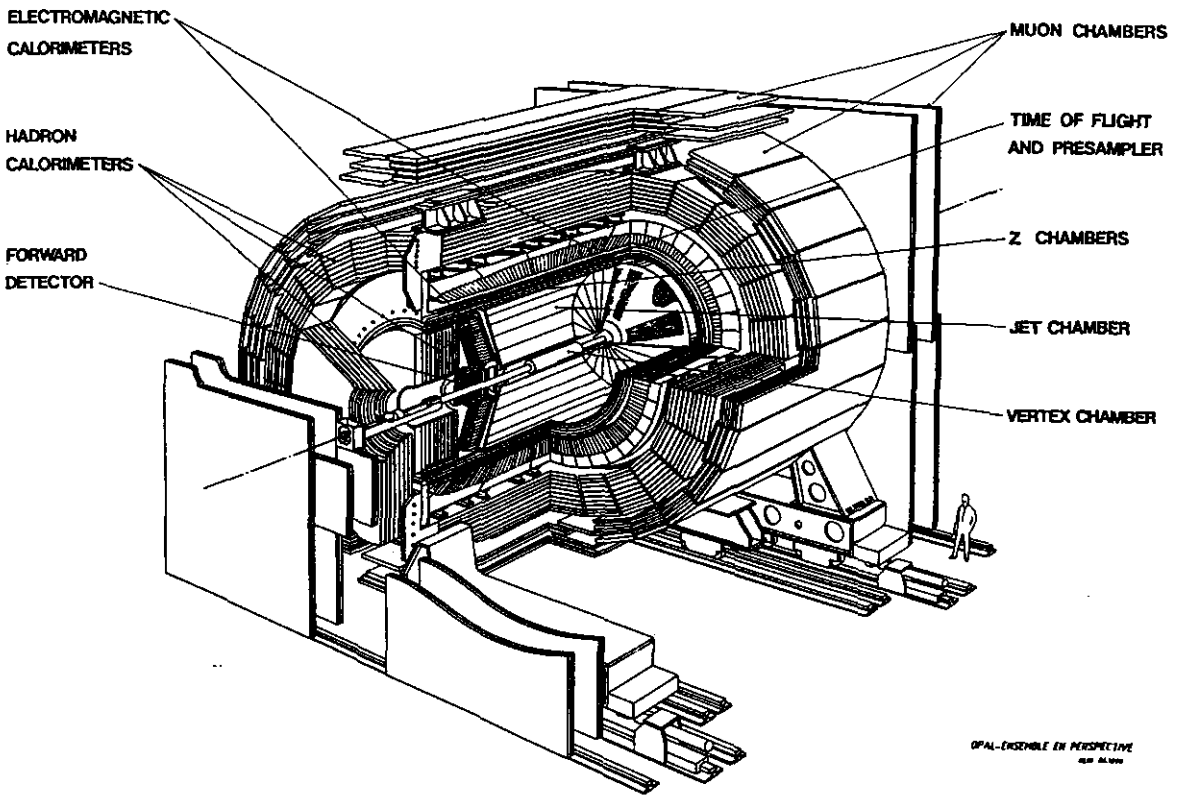

Figure 21: A cut-away view of the OPAL detector showing the main sub-detectors.

4 bar.

The typical momentum resolution of tracks associated with 45 GeV muons from di-muon events which were reconstructed using information combined from the four sub-detectors was measured to be approximately 1.5×10^{-3} GeV^{-1} multiplied by the square of the transverse momentum.

4.1.1 Microvertex detector

All the data used in this thesis were recorded after the 1995 installation of the phase III silicon microvertex detector [45]. The detector filled an annular volume between the beam

pipe's outer radius of 54 mm and the pressure vessel's inner radius of 78 mm, and consisted of two layers of silicon microstrip detectors with strips aligned both in the $r-\phi$ and $r-z$ planes.

4.1.2 Vertex detector

The vertex detector was a 1 m long jet drift chamber consisting of two layers of wire cells. The wires in the inner (axial) layer of cells were aligned parallel to the beam direction and the wires in the outer (stereo) layer were inclined at an angle of 4°. The detector extended out to a radius of 235 mm. Ionising particles passing through the chamber liberated electrons from the gas which then drifted to the sense (anode) wires. The time taken for the electrons to reach the wires (drift time) was used to reconstruct the position of the ionising particles. Information from both the axial and stereo wire cells was combined to provide measurements of the r, ϕ and z co-ordinates.

The vertex detector was used in conjunction with the microvertex detector to measure the position of secondary vertices resulting from the decay of short-lived particles (such as mesons containing b quarks).

4.1.3 Jet chamber

The jet chamber was a 4 m long drift chamber which surrounded the vertex chamber and had an outer radius of 185 cm. The chamber was divided into 24 sectors in ϕ where the sense wires in each sector were strung parallel to the z direction. The co-ordinates of charged particles in the $r-\phi$ plane were measured from the known positions of the sense wires and the drift time. A relatively crude measure of the z co-ordinates was obtained by measuring the charge division between the two ends of the wire. In addition, the total charge accumulated by each sense wire was used to measure the energy loss of each ionising particle ($\frac{\mathrm{d}E}{\mathrm{d}x}$), and hence to help identify the particle [46].

4.1.4 Z chambers

The z-chambers formed a layer 59 mm thick on the outside of the jet chamber with wires strung in the local ϕ direction. The role of the z-chambers was to improve the resolution of the z co-ordinate measured from the jet chamber. In addition, the ϕ co-ordinate was obtained using charge division.

4.2 Solenoid

A solenoidal coil was used to maintain a magnetic field of 0.435 T parallel to the z direction throughout the central detector. Non-uniformities in the magnetic field were measured to be less than 0.5%. The curvatures of the paths of the charged particles in the magnetic field were used to measure the particles' transverse momenta. The solenoid was designed such that the magnetic field between the coil and the iron return yoke was sufficiently small not to perturb the operation of the calorimeters which lay in this region.

4.3 Calorimeters

Surrounding the coil were several layers of calorimeters giving close to 4π acceptance. As different particles lose energy in matter at different rates and through different mechanisms, the distance which a particle travelled through the calorimeters before being fully absorbed was indicative of both the energy and nature of the particle.

4.3.1 Time-of-flight and pre-samplers

The time-of-flight sub-detectors were used primarily to generate trigger signals for the data acquisition system. Photons excited from trapezoidal scintillating counters in the barrel and planar scintillating tiles in the endcaps were directed along plexiglas light-guides and optical fibres to phototubes. The endcap time-of-flight detectors were originally installed in 1996 [47], and were supplemented by the Minimum Ionising Particle (MIP) plug from

1997 onwards. The MIP plug consisted of additional scintillating tiles which extended the coverage of the detectors down to an angle of 43 mrad from the beam axis.

The combined thickness of the central detector, pressure vessel and coil was approximately 2 radiation lengths, and consequently, the majority of electromagnetic showers began to develop before the photons and charged particles reached the main electromagnetic calorimeter. The electromagnetic presampler was used to detect these showers and hence improve both the discrimination between electrons and hadrons, and the overall energy resolution of the calorimeters. The barrel part of the presampler had an inner radius of 239 cm and a length of 662 cm and consisted of limited streamer tubes with anode wires aligned in the z-direction. The endcap presamplers were constructed from multiwire proportional counters.

4.3.2 Electromagnetic calorimeters

The electromagnetic calorimeter was designed to fully contain outgoing electrons, positrons and photons and their associated electromagnetic showers. The barrel calorimeter was constructed from lead glass blocks aligned in a quasi-pointing geometry forming a cylinder with an inner radius of 246 cm. Each block had a thickness of 37 cm (24.6 radiation lengths) and an approximate cross-section of 10 cm $\times$ 10 cm. The endcap calorimeters were dome-shaped arrays of lead glass blocks, in which each block was aligned in the z-direction. Čerenkov light generated by charged relativistic particles passing through the blocks was detected by phototubes and used to measure the energy deposited in the calorimeter. The photo-detectors used in the endcaps were vacuum photo-triodes which were tolerant of the high magnetic field in this region.

4.3.3 Hadron calorimeters

The iron return yoke of the magnet had a thickness of approximately 1 m (four interaction lengths) and was instrumented to detect hadronic showers and to assist in muon identi-

fication. The yoke was composed of layers of iron slabs interleaved with gas-filled PVC wire-chambers operating on the same principle as limited streamer tubes. The signals were not measured directly from charge accumulated on the wires in the chambers but from induced charge collected on aluminium pads and strips fixed to the chambers' surfaces.

Additional hadronic calorimeters known as the hadronic poletips were located in the regions close to the beam pipe on either side of the interaction point. These were constructed from multiwire proportional chambers operating in a similar fashion to the chambers in the barrel and endcaps.

4.4 Muon chambers

The majority of electromagnetically charged particles and hadrons were fully absorbed within the electromagnetic and hadronic calorimeters. However, muons are highly penetrating and typically passed through the hadron calorimeter with little interaction and then traversed the surrounding muon chambers. The muon chambers were used to identify these muons from a background of hadrons, and to provide position information.

The barrel part of the muon detector consisted of four layers of drift chambers varying between 6.0 m and 10.4 m in length. The endcap parts consisted of between two and four layers of limited streamer tubes divided amongst four quadrant chambers and two patch chambers which fitted around the detector support structure.

4.5 Forward detector

The forward detector consisted of drift chambers, lead-scintillator calorimeters (known as the forward calorimeter, far-forward monitor and gamma catcher) and silicon tungsten calorimeters [48] which were positioned close to the beam pipe on both ends of the detector, at distances of between 2 m and 3 m from the nominal collision point. One of their main functions was to detect e^+e^- pairs that had undergone Bhabha scattering, as the event rate of this process was used to calculate the instantaneous luminosity of the LEP beams.

5 Data reconstruction

Before the signals obtained from the OPAL sub-detectors could be used in the SDM analysis, the data had to undergo several stages of reconstruction. The preliminary stage of reconstruction, applied to all data recorded by OPAL, is described in section 5.1. The subsequent problem of distinguishing $e^+e^- \to W^+W^-$ reactions from other possible reactions, and the problem of reconstructing the momentum vectors of the W boson decay products are inter-dependent and cannot be cleanly separated from one another. For the purposes of this thesis, an overview of the reconstruction of $e^+e^- \to W^+W^-$ reactions is given in section 5.2 and further details and references are given in the discussion of the data selection procedures in section 6.3.

5.1 Preliminary reconstruction

The bunches of electrons and positrons circulating through the LEP beam pipe were coincident with the OPAL interaction point approximately 45000 times a second. Individual electrons and positrons could interact with one another during each of these 'bunch crossings', but, in practice, interesting reactions occurred at a far lower rate of order 10 Hz. During each bunch crossing, the OPAL trigger system [49] analysed the activity in the sub-detectors to identify interesting 'physics events' from a background of electrical noise and other parasitic physics. Any inefficiencies in the trigger's acceptance of the events relevant to this thesis were negligible compared to the statistical uncertainties obtained at LEP2. Once the trigger had identified an event, the signals from the sub-detectors were read-out over a period of 5 ms before being collated and passed to the data acquisition system, which processed and stored the data for later analysis. The reconstruction of each event from the raw data was automated by a computer software package known as ROPE (Reconstruction of OPAL Physics Events).

Among other tasks, ROPE was used to interpolate the trajectories of outgoing charged

particles from the measured co-ordinates of ionised charges produced in the central detector. Each measurement was known as a 'hit', and the reconstructed trajectories were known as 'tracks', where the momentum of the particle hypothesised to have produced a track was inferred from the track curvature. Signals associated with the deposition of energy in the calorimeters were grouped together to form 'clusters', where the summed energy in each cluster was likely to have originated from a single particle or group of closely collimated particles. If the extrapolated trajectory of a track coincided with the position and orientation of a cluster then the track and cluster were considered 'associated' with one another. Conversely, clusters without an associated track were referred to as 'unassociated', and were typical signatures of photons or neutral hadrons. Figure 22 shows a graphical representation of an OPAL event following reconstruction by ROPE.

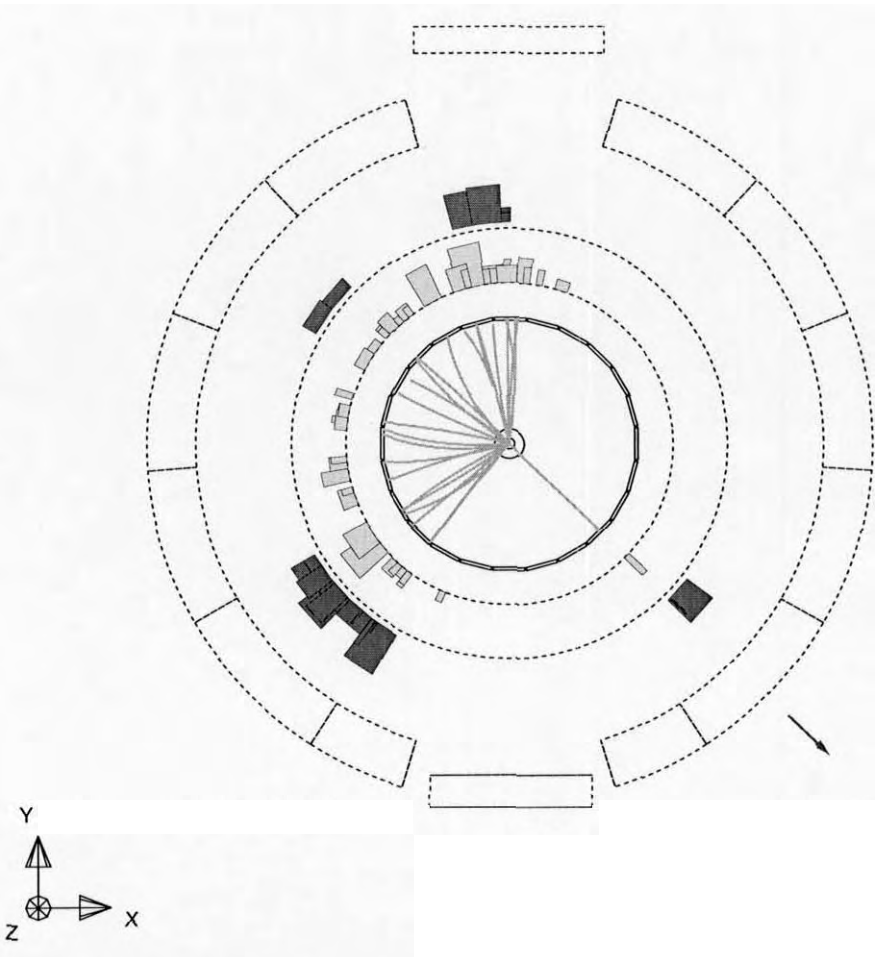

Figure 22: Graphical representation of an OPAL event with a centre-of-mass energy of 202 GeV reconstructed by the ROPE software package. The tracks and clusters in the figure have been projected onto the plane perpendicular to the electron beam direction. Each concentric ring in the figure denotes an interface between adjacent sub-detectors in the OPAL barrel region, with the smallest ring showing the beam pipe and the largest showing the inner radius of the hadronic barrel calorimeter. The segmented arcs outside the hadronic calorimeters represent the chambers of the muon barrel calorimeter. The thick lines running from the centre of the beam pipe to the edge of the pressure vessel are the reconstructed tracks of charged particles. The shaded rectangles in the electromagnetic and hadronic calorimeters represent energy clusters, where the area of each rectangle is directly proportional to the amount of energy contained in the cluster. For clarity, clusters in the forward calorimeters have not been shown. The small arrow drawn outside of the detector indicates the path of a muon candidate reconstructed from hits in the muon chambers.

5.2 W-pair reconstruction

As was mentioned in section 2.6, the $e^+e^- \rightarrow W^+W^-$ reaction results in one of three final states: $q\bar{q}q\bar{q}$, $q\bar{q}'\ell\nu$ or $\ell\nu\ell\nu$. In all three cases, each of the four fermions in the final state carries roughly one quarter of the total centre-of-mass energy of the e^+e^- collision, i.e. around 50 GeV at LEP2. However, as charged leptons, neutrinos, and quarks all behaved very differently within the OPAL detector, each final state presented different reconstruction challenges.

Each quark produced in a $W \rightarrow q\bar{q}'$ decay rapidly hadronised to form a collimated group of hadrons in the lab frame known as a 'jet'. Each jet produced 10 ± 4 tracks in the central detector as well as numerous associated and unassociated clusters in the calorimeters. The jets often overlapped with one another spatially as the typical angular spread of the tracks belonging to each jet was $60° \pm 30°$. In reconstructing the event, tracks and clusters were assigned to each jet by a jet algorithm [50].

In a $W \rightarrow \ell\nu$ decay, the neutrino left no trace in the OPAL detector, whilst the interaction between the detector and the charged lepton depended on the lepton's flavour. Electrons typically resulted in a single high-momentum track in the central detector with an associated cluster in the electromagnetic calorimeter, and little or no activity in the hadronic calorimeter. Muons also typically left a single track in the central detector, but, in contrast to electrons, little of their energy was deposited in the calorimeters. Instead, muons were identified from hits registered in the muon chambers [15]. The τ-lepton is far more massive than either of the other two charged leptons and has a short lifetime of order 10^{-13}s. Consequently, it decayed weakly within a distance of approximately 2 mm of the beam interaction point producing either an electron ($\tau \rightarrow e\nu_e\nu_\tau$), a muon ($\tau \rightarrow \mu\nu_\mu\nu_\tau$), or

[15] Small amounts of energy were also deposited in the hadronic calorimeter. As most hadrons were absorbed within the inner layers of the hadronic calorimeter, activity in the outer layers of the calorimeter provided an additional indication of the passage of a muon.

a mixture of charged and neutral pions (or kaons), $\tau \to \pi\nu_\tau(\pi^0)(\pi^-\pi^+)$. In the latter case, the τ-lepton decays are classified by the number of tracks produced in the central detector (*i.e.* typically the number of charged pions produced in the decay), where the majority of decays produced either one track or three tracks.

Although the $q\bar{q}q\bar{q}$ final state has a large branching fraction, there is an ambiguity in assigning the hadronic jets to their parent W bosons which means that neither the charges of the W bosons nor the charges of the quarks could be measured with any certainty. In addition, there were large systematic uncertainties associated with possible interactions between jets originating from the W^- boson and jets originating from the W^+ boson [51].

By contrast, it was comparatively simple to identify which of the two charged leptons in a $\ell\nu\ell\nu$ final state originated from which parent W boson. However, the loss of information associated with the two undetected neutrinos made the kinematic properties of such events difficult to reconstruct unambiguously. For these reasons, neither the $q\bar{q}q\bar{q}$ nor $\ell\nu\ell\nu$ channels were used in this SDM analysis - although, in principle, it is possible to construct CP-odd and CP$\hat{\text{T}}$-odd observables for these events [29].

The $q\bar{q}'\ell\nu$ final state was relatively simple to reconstruct. The main challenge was to correctly identify which tracks and clusters were produced by the charged lepton and which by the hadronic jets. This identification process was part of the event selection procedure discussed in section 6.3 which also details how the energy and momentum of the quarks (E_q, p_q, $E_{\bar{q}}$, $p_{\bar{q}}$) and the charged lepton (E_ℓ, p_ℓ) were obtained from the tracks and clusters.

In order to reconstruct the neutrino energy and momentum (E_ν, p_ν) it was necessary to make use of kinematic constraints arising from energy and momentum conservation. As the OPAL detector was nearly hermetic, the sums of the energy (E_i) and momenta ($\vec{p}_i$) of all the particles in the final state were expected to equal the energy and momentum of the

incoming electron and positron,

$$\sum_i E_i = \sqrt{s} \quad (61)$$

$$= E_q + E_{\bar{q}} + E_\ell + E_\nu \quad (62)$$

$$= E_{\rm vis} + E_{\rm mis} \quad (63)$$

$$\sum_i \vec{p}_i = \vec{0} \quad (64)$$

$$= \vec{p}_q + \vec{p}_{\bar{q}} + \vec{p}_\ell + \vec{p}_\nu \quad (65)$$

$$= \vec{p}_{\rm vis} + \vec{p}_{\rm mis} \quad (66)$$

where the label 'vis' denotes the visible (detectable) energy and momentum in the detector and the label 'mis' denotes the missing energy and momentum. The missing energy and momentum in the detector can be attributed solely to the neutrino in the $q\bar{q}'\ell\nu$ event, provided that all other particles in the event were detected. Additional undetected particles could include ISR photons emitted close to the beam pipe direction, or additional neutrinos coming from weak decays. The average energy loss due to ISR photons in $q\bar{q}'\ell\nu$ events was estimated from simulations to be approximately 5 GeV. Figure 23 shows a momentum-space representation of a $q\bar{q}'\ell\nu$ event where the final state is assumed to have evolved through a W-pair without the emission of ISR photons. The diagram can be compared to the schematic WW decay shown previously in figure 14 which defines the angles of interest in an SDM analysis.

The reconstructed physics event previously depicted in figure 22 was selected as a $q\bar{q}'\mu\nu$ candidate by the selection procedure described later in section 6.3. During the selection, the tracks and clusters most likely to be associated with the muon were identified, and the remaining tracks and clusters were divided into two hadronic jets as described above. This is illustrated in figure 24, in which an arrow originating at the centre of the beam pipe represents the neutrino momentum direction as calculated from the kinematic constraints.

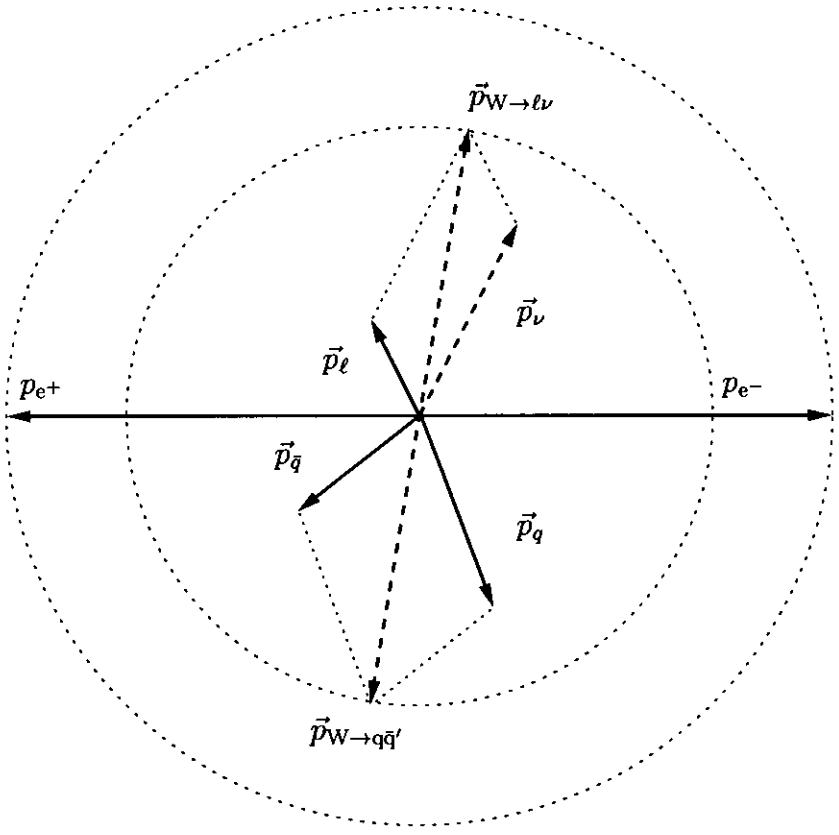

Figure 23: Generic momentum-space diagram of a $e^+e^- \to W^+W^- \to q\bar{q}'\ell\nu_\ell$ event projected onto a plane which contains the incoming beam direction. The solid lines depict the momenta that can in principle be measured using the OPAL detector, the dashed lines depict the momenta that cannot be measured directly, and the dotted lines show kinematic constraints. The radius of the outer dotted ring represents the maximum momentum available to any particle in the initial or final states, and depends on the centre-of-mass energy. The radius of the inner dotted ring shows the momenta of the outgoing W bosons, which will vary depending on the mass of the bosons (which can be virtual).

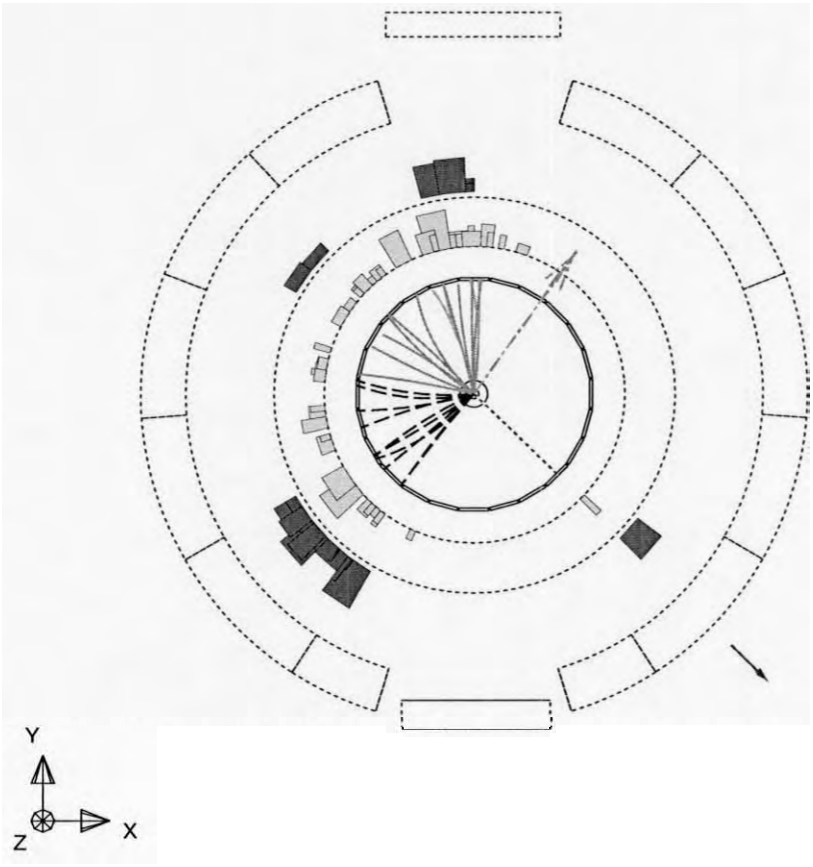

Figure 24: Reconstruction of an event recorded by the OPAL detector and selected as a $q\bar{q}'\mu\nu$ candidate. The tracks have been divided into three groups: the tracks associated with one of the quarks are shown by solid lines, the tracks associated with the second quark are shown with dashed lines, and the track associated with the muon is shown by a dotted line. The dash-dot arrow indicates the direction of the neutrino obtained from the kinematic constraints.

6 SDM analysis

The following sections describe the procedure used to measure the W^- SDM and W^+ SDM of section 2.5 from the OPAL data. Particular emphasis was placed on providing a robust measurement of the fraction of longitudinally polarised W bosons. The composition of the analysed data samples, and the definitions of useful 'signal' physics events and contaminating 'background' physics events are discussed in section 6.1. The computer-generated 'pseudo-data' samples (Monte Carlo simulations) used to study the response of the detector to different types of physics events are discussed in section 6.2. The algorithms used to identify signal events are detailed in section 6.3, and the subsequent measurements of SDM elements using these events are explained in section 6.4. Finally, the problem of obtaining unbiased results and the methods for combining these results are discussed in sections 6.5 and 6.6 respectively.

Unless otherwise specified, all the algorithms described in the following sections were implemented in the FORTRAN 77 programming language and were compiled and executed on a variety of computer platforms at CERN and the University of Victoria.

6.1 Data sample

This analysis used data collected by the OPAL detector during the years 1997 to 2000. The data were collected with centre-of-mass energies clustered around eight nominal energy values: 183 GeV, 189 GeV, 192 GeV, 196 GeV, 200 GeV, 202 GeV, 205 GeV and 207 GeV. The luminosity-weighted mean centre-of-mass energies of the data samples [52] and their integrated luminosities [39], as obtained from measurements of small angle Bhabha events in the silicon tungsten forward calorimeter, are listed in table 3. Each mean centre-of-mass energy measurement had an estimated uncertainty of approximately 0.05 GeV, and each integrated luminosity measurement had a fractional uncertainty of approximately 0.3%. The luminosity-weighted mean energy of the eight samples combined was 196.5 GeV, and

the total integrated luminosity was 678.5 pb^{-1}.

Nominal Energy (GeV)	$\sqrt{s}$ (GeV)	$\mathcal{L}(pb^{-1})$
183	182.7	57.4
189	188.6	183.0
192	191.6	29.3
196	195.5	76.4
200	199.5	76.6
202	201.6	37.7
205	204.9	81.6
207	206.6	136.5
		678.5

Table 3: The mean centre-of-mass energies and the integrated luminosity values for the data samples at each of the eight nominal energies. The bottommost row shows the sum of the luminosities.

During the year 2000, the procedure used by LEP to accelerate the e^+e^- beams was altered such that the energy of the beams continued to be increased (ramped) to higher energies after the electrostatic separators at the interaction points had been turned off and whilst OPAL was recording data. The data recorded during these 'mini-ramps' has been excluded from this analysis and does not appear in table 3, as the centre-of-mass energies of the collisions were not well-measured. The integrated luminosity of the excluded data was approximately 2 pb^{-1}.

Approximately one hundred million events were recorded by OPAL in total, of which only ten thousand were expected to involve the creation of a W pair, and approximately 5000 were expected to have $q\bar{q}'\ell\nu$ final states. The eight data samples were analysed separately and the results from each of these analyses were then combined using the method described in section 6.6.1. Events with $q\bar{q}'\ell\nu$ final states originating from a pair of W bosons (i.e. processes involving the CC03 Feynman diagrams plus any radiative corrections), where the charged lepton can be either an electron, muon or τ-lepton, are referred to as 'signal' in the remainder of this thesis. Events of all other types are referred to as 'background'. Only those

data events compatible with having a $q\bar{q}'\ell\nu$ final state (see section 6.3 for details) were used to form the SDM. As was explained in section 2.9, the $q\bar{q}'\ell\nu$ final state receives coherently interfering contributions from a variety of tree-level Feynman diagrams, not all of which contain the W pairs required by the signal definition. This difference between the signal definition and the observable final states was taken into account in the purity correction of section 6.4.2 formed from the Monte Carlo samples described below in section 6.2.

6.2 Monte Carlo simulations

Monte Carlo (MC) computer simulations were used to predict the particle composition and kinematic properties for large numbers of simulated physics events belonging to some subset of the possible SM processes. The software packages used were commonly referred to as MC generators, and a set of physics events simulated with a common centre-of-mass energy and with common input parameters was known as a generator-level MC sample. For each event in each generator-level sample, the expected response of the OPAL detector was calculated using the full OPAL detector simulation program, GOPAL [53]. These 'pseudo-data' were then stored in the same format as that of the real data recorded by the OPAL trigger and data acquisition system. The generator-level information was used in evaluating the SM predictions for the measured spin density matrices, whilst the relationship between the pseudo-data and generator-level information was used to form the detector correction described in section 6.4.2.

MC samples containing only those four-fermion final states consistent with the possibility of having been produced via a pair of W bosons were generated using the KandY Monte Carlo generator formed from the YFSWW3 [54] and KORALW 1.51 [55] software packages. To provide pseudo-data samples conforming to the W-pair signal definition, each $q\bar{q}'\ell\nu$ event was weighted by a positive factor, $\mathrm{Pr}_{\mathrm{WW}}/\mathrm{Pr}_{4f}$, calculated on an event-by-event basis using KandY. The factor was defined as the probability of producing the generator-

level MC event when only W-pair processes were considered, divided by the probability of producing the event when the full set of four-fermion Feynman diagrams included in KandY were considered. Each $q\bar{q}'\ell\nu$ event also contributed to the background pseudo-data samples with a weight $1 - \mathrm{Pr_{WW}}/\mathrm{Pr}_{4f}$. Events with four-fermion final states other than $q\bar{q}'\ell\nu$ were considered background and were not weighted by $\mathrm{Pr_{WW}}/\mathrm{Pr}_{4f}$.

Background four-fermion final states inconsistent with having been produced via a pair of W bosons (e.g. $q\bar{q}\ell^+\ell^-$) were generated using KORALW 1.42 [56]. Additional samples of four-fermion and W-pair events used in studies of systematic effects were also generated using KORALW 1.42. The EXCALIBUR [57] MC generator was used to re-weight four-fermion events for parts of the systematic error analysis (see section 7). The hadronisation of quarks in the KandY and KORALW samples used in the main analysis was simulated by JETSET [58]. To estimate the fragmentation and hadronisation systematic uncertainties, HERWIG 6.2 [59] and ARIADNE 4.11 [60] were used as alternatives to JETSET for simulating hadronisation in some KORALW samples (see section 7).

In addition to four-fermion events, only quark-pair or two-photon events were found to be significant sources of background for the event selection described in section 6.3. Samples of $Z^0/\gamma \to q\bar{q}$ events were generated by KK2F [61] and hadronised by JETSET. In these events, one or more ISR photons are typically emitted such that the effective centre-of-mass energy of the colliding e^+e^- pair ($\sqrt{s'}$) is close to m_Z. The event then evolves through a Z^0 boson which decays to a quark anti-quark pair, whilst the ISR photons are typically emitted at a small angle to the beam pipe and may not pass through the instrumented volume of the detector. The event topology therefore appears qualitatively similar to that of a $q\bar{q}'\ell\nu$ event, where the missing energy due to the undetected ISR photon mimics the missing energy expected from a neutrino. Multi-peripheral two-photon processes with hadronic final states ($e^+e^- \to e^+e^-\gamma\gamma \to e^+e^-q\bar{q}'$) were simulated by HERWIG. In these $e^+e^- \to e^+e^-\gamma\gamma \to e^+e^-q\bar{q}'$ processes the electron and positron emit photons which then

interact to form a quark pair. If the electron and/or positron are not scattered into the instrumented volume of the detector by the interaction, then this event topology is again qualitatively similar to that of a $q\bar{q}'\ell\nu$ event.

Table 4 shows a complete list of the MC samples used to simulate SM physics for the purposes of this analysis. Samples were generated at each of the eight mean centre-of-mass energies shown in table 3. Samples used in systematic studies are listed separately in section 7. The table shows the 'run number' of each sample (a unique identification number by which the sample is known within the OPAL collaboration) and the integrated luminosity represented by the sample. Each KandY run contained one million simulated physics events.

At each nominal centre-of-mass energy, a complete SM pseudo-data sample containing both signal and background events normalised to the luminosity of the data sample was obtained by weighting and combining all of the MC runs in the corresponding column of table 4. Each event in each MC run was scaled by a weight, $w_{\mathcal{L}}$, equal to the integrated luminosity of the data sample, $\mathcal{L}_{\text{data}}$, divided by the integrated luminosity of the MC run itself, $\mathcal{L}_{\text{run}}$:

$$w_{\mathcal{L}} = \frac{\mathcal{L}_{\text{data}}}{\mathcal{L}_{\text{run}}}. \tag{67}$$

6.3 Event selection

In broad terms, the experimental signature of a $q\bar{q}'\ell\nu$ event in the OPAL detector was the presence of two hadronic jets, missing energy associated with the neutrino, and one or more high momentum tracks associated with the charged lepton. The selection algorithm used to identify $q\bar{q}'\ell\nu$ candidate events in the data had four parts: the pre-selection, the likelihood selection, the kinematic fit and the final selection. The first three parts of the algorithm were developed collectively by the OPAL collaboration for use in a wide variety of W-pair physics analyses. The final part of the selection algorithm was developed collectively by the

Generator & Process	Nominal Energy (GeV)					
	183		189		192	
	Run	$\mathcal{L}$	Run	$\mathcal{L}$	Run	$\mathcal{L}$
KandY 4f	11801	29.72	11802	28.01	11803	27.45
KoralW 4f	10304	11.66	9323	10.95	9920	10.72
KK2F $Z^0/\gamma \to q\bar{q}$	5184	2.29	5188/5189	2.52/2.50	5195	2.64
HERWIG $e^+e^-\gamma\gamma$	1048	0.51	1062/1066	0.50/0.52	1495	1.13

Generator & Process	Nominal Energy (GeV)					
	196		200		202	
	Run	$\mathcal{L}$	Run	$\mathcal{L}$	Run	$\mathcal{L}$
KandY 4f	11804	26.91	11805	26.56	11806	26.43
KoralW 4f	9921	10.51	99224	10.37	9923	10.32
KK2F $Z^0/\gamma \to q\bar{q}$	5196	2.78	5119	3.51	5199	3.00
HERWIG $e^+e^-\gamma\gamma$	1085/1087	0.48/0.52	1086/1088	0.48/0.52	1496	1.09

Generator & Process	Nominal Energy (GeV)			
	205		207	
	Run	$\mathcal{L}$	Run	$\mathcal{L}$
KandY 4f	11807	26.34	11808	26.22
KoralW 4f	11404	10.28	11414	10.22
KK2F $Z^0/\gamma \to q\bar{q}$	5183	3.07	5190	6.30
HERWIG $e^+e^-\gamma\gamma$	1498	1.08	1499	1.07

Table 4: The identifying run numbers and integrated luminosities measured in units of inverse femtobarns of the Monte Carlo samples used to calculate the central values in this analysis. Samples with four-fermion final states are denoted '4f'.

OPAL TGC working group (to which the author of this thesis contributed as a member) to identify those W-pair events in which the momentum vectors of the four primary fermions were accurately measured. Sections 6.3.1 to 6.3.7 give an overview of each part of the selection [16]. Further details of the pre-selection and likelihood selection can be found in [24, 62–64], and were based on the previously devised 172 GeV $q\bar{q}'\ell\nu$ selection described in appendix A of [65]. Details of the kinematic fits and final selection can be found in [66]. Where there are differences between the selection described in the thesis and those in the

[16] This selection was produced collectively within the OPAL collaboration and is not presented here as original work by the author of this thesis.

references, the thesis should be considered to be authoritative. The numbers of events passing the full selection are shown in table 5 and are consistent between data and pseudo-data within the Poisson statistical uncertainties.

Nominal	Selected events	
Energy (GeV)	Data	Pseudo-data
183	329	331.0
189	1090	1124.7
192	170	182.7
196	511	483.2
200	457	479.4
202	242	237.4
205	482	516.0
207	895	862.7
Total	4176	4214.5

Table 5: The number of data events passing the event selection detailed in section 6.3 for each data sample and the expected number of events as calculated using the Monte Carlo samples listed in table 4.

6.3.1 Sub-detector requirements

Not all of the sub-detectors described in section 4 are of equal importance to every analysis, and hence data were recorded even at times when the performances of some of the sub-detectors were degraded. The data used in this SDM analysis were recorded whilst at least the following detectors were operating normally: either the central vertex or silicon microvertex detectors, the central jet chamber, the electromagnetic calorimeters in both the barrel and endcap regions, the silicon tungsten detector, the forward detector and the muon endcap detectors.

6.3.2 Track and cluster quality cuts

Tracks and clusters reconstructed by ROPE varied in quality according to the amount and nature of detector information available for the reconstruction. In general, those tracks

which appeared to originate from a particle with anomalously high momentum, or did not fit the hits in the central detector well, or whose distance of closest approach to the nominal interaction point was large, or which had few associated hits in the central jet chamber were considered to be poorly reconstructed. In addition, those tracks which crossed the anode planes in the jet chamber or which were later considered as originating from lepton candidates were subject to more rigorous checks. The requirements for a reconstructed track to be included in the analysis are summarised below:

- If the nominal centre-of-mass energy was less than 196 GeV then
  - $p_{\text{track}} < 100$ GeV - where p_{track} is the reconstructed momentum associated with the track.
- If the nominal centre-of-mass energy was equal to or greater than 196 GeV then
  - $p_{\text{track}} < 120$ GeV - where p_{track} is the reconstructed momentum associated with the track.
- $p^T_{\text{track}} > 0.150$ GeV - where p^T_{track} is the reconstructed transverse momentum associated with the track, and 'transverse' refers to the plane orthogonal to the incident beam direction.
- $d_0 < 2$ cm - where d_0 is the impact parameter of the track with respect to the origin of the OPAL co-ordinate system.
- $z_0 < 25$ cm - where z_0 is the z co-ordinate of the track at its point of closest approach to the origin in the OPAL co-ordinate system.
- $\chi^2_{r-\phi}/\text{d.o.f.} < 100$ - where $\chi^2_{r-\phi}/\text{d.o.f.}$ is the Chi-squared per degree of freedom between the track and its hits projected on to the $r-\phi$ plane.

- $\chi^2_{s-z}/\text{d.o.f.} < 100$ - where $\chi^2_{s-z}/\text{d.o.f.}$ is the Chi-squared per degree of freedom between the track and its hits projected on to the $s-z$ plane (where, in this context, s denotes the $r-\phi$ path integral along the track from the point of closest approach of the track to the origin in the OPAL co-ordinate system).

- If $7.0° < q \times \phi_{\text{CJ}} < 10.5°$ - where q is the reconstructed charge associated with the track and ϕ_{CJ} is the local azimuthal angle of a track inside one of the 24 sectors of the central jet chamber defined such that the anode plane is at 7.5°, then

  - $\sigma_p/p_{\text{track}} < 0.5$ - where σ_p is the uncertainty on the track momentum.

- If $N_{\text{hits}}^{\text{max}} \geq 80$ where $N_{\text{hits}}^{\text{max}}$ is the maximum number of possible hits that could be associated with the track in principle (given the geometry of the detector and the direction of the track) then

  - $N_{\text{hits}} \geq 40$, where N_{hits} is the number of hits associated with the track.

- If $40 < N_{\text{hits}}^{\text{max}} < 80$ then

  - $N_{\text{hits}} \geq \frac{1}{2} N_{\text{hits}}^{\text{max}}$

- If $N_{\text{hits}}^{\text{max}} \leq 40$ then

  - $N_{\text{hits}} \geq 20$

For a cluster in the electromagnetic, hadronic or forward calorimeters to be considered in the analysis, the energy of the cluster had to be in excess of thresholds determined by the level of electrical noise in the sub-detectors. Clusters in the electromagnetic calorimeter had to contain more than 0.25 GeV, and also still contain more than 0.001 GeV after corrections which take into account the effect of the material lying in front of the calorimeter had been applied. Clusters in the hadronic calorimeter had to contain more than 0.60 GeV. In addition, clusters in the hadronic poletip calorimeter (in which unexpectedly high levels

of electrical noise were observed) were required to have a minimum energy of 1.5 GeV, and, in addition, a cone of half-angle 30° around the cluster was required to contain a charged track or electromagnetic cluster with a minimum energy of 1.5 GeV. Clusters in the gamma catcher were required to have energies greater than 5 GeV, and clusters in the forward calorimeter or silicon-tungsten forward calorimeter were required to have energies greater than 2 GeV.

6.3.3 $q\bar{q}'\ell\nu$ pre-selection

The $q\bar{q}'\ell\nu$ pre-selection consisted of a series of loose cuts to veto those events which contained fewer than six reconstructed tracks or fewer than six energy clusters or whose summed reconstructed energy was less than 20% of the centre-of-mass energy of the e^+e^- beams.

6.3.4 Identification of lepton candidates

Following the $q\bar{q}'\ell\nu$ pre-selection, an attempt was made to identify the nature of the conjectured charged lepton in each remaining event. Six different hypotheses for the lepton were considered: e, μ, $\tau \to e\nu_e\nu_\tau$, $\tau \to \mu\nu_\mu\nu_\tau$, $\tau \to h\nu_\tau$ and $\tau \to 3h\nu_\tau$(where $\tau \to h\nu_\tau$ denotes a τ-lepton decaying to a final state containing one charged hadron, and $\tau \to 3h\nu_\tau$ denotes a τ-lepton decaying to a final state containing three charged hadrons.). The sorting of each event into one of these six categories (or the rejection of the event if it matched none of the categories well) is described in section 6.3.5. However, before an event could be categorized in this way, it was first necessary to consider each hypothesis in turn and to identify which of the tracks in the event were most likely to be associated with the charged lepton in each case. The properties of these identified tracks were subsequently used in the categorization and selection of the events.

The identification of the candidate lepton tracks was itself accomplished using a likelihood selection technique based on reference probability distributions of kinematic observables obtained from SM MC samples corresponding to each hypothesis. In each case, the

track (or set of tracks for $\tau \rightarrow 3h\nu_\tau$) which had the highest likelihood (product of probabilities) was identified as the best lepton candidate. Only those tracks which passed both the quality cuts of section 6.3.2 and additionally had associated momentum greater than 1 GeV with a fractional uncertainty less than 50% were considered. Different sets of kinematic variables were used for each of the six hypotheses. The reference distributions were generated at nominal centre-of-mass energies of 183 GeV, 189 GeV, 200 GeV, and 206 GeV, where only those distributions whose nominal centre-of-mass energy was closest to that of the event being processed were employed to determine the likelihood. A list of all the variables calculated for each track is given below and table 6 shows which variables were used for determining the best lepton candidate for each hypothesis.

- p_ℓ - The reconstructed momentum associated with the candidate track (or the sum of the momenta associated with the three tracks in the $\tau \rightarrow 3h\nu_\tau$ case).
- E_ℓ - The energy of the electromagnetic calorimeter cluster associated with the candidate track.
- E_ℓ/p_ℓ - The ratio of E_ℓ to p_ℓ.
- $\Delta\phi_{\mathrm{EC/CT}}$ - The difference between the reconstructed azimuthal angle measured from the candidate track information and from the associated cluster information.
- E_τ - The sum of p_ℓ and the energy contained in the electromagnetic calorimeter clusters within a cone of 200 mrad half-angle centred on the candidate track (excluding clusters associated with the track).
- M_τ - The invariant mass calculated from E_τ and p_ℓ.
- I_{200} - The sum of p_ℓ and the momenta associated with all tracks and the energy associated with all electromagnetic calorimeter clusters within an isolation cone of

200 mrad half-angle centred on the candidate track (excluding clusters associated with the track).

- I_{200}^{CT} - The sum of the momenta associated with all tracks within an isolation cone of 200 mrad half-angle centred on the candidate track.

- $I_{200-500}$ - The sum of the momenta associated with all tracks and the energy associated with all clusters in the electromagnetic calorimeter which lay within a conical annulus of 200 mrad to 500 mrad half-angle centred on the candidate track.

- $\frac{\mathrm{d}E}{\mathrm{d}x}|_{\mathrm{track}}$ - The rate of energy loss associated with the candidate track.

- $X_{\mathrm{e^+e^-}}$ - The estimated probability that the track was caused by an electron or positron originating from the pair-conversion of a photon ($\gamma \rightarrow \mathrm{e^+e^-}$), as defined by the ROPE algorithm 'IDGCON' described in reference [67].

- N_{blk}^{90} - The number of lead-glass blocks in the electromagnetic calorimeter which must be included in a sum of deposited energy to obtain 90% of the total energy in the electromagnetic calorimeter cluster.

- N_{HC} - The number of layers in the hadronic calorimeter containing hits associated with the track candidate.

- N_{HC2} - The number of layers of the hadronic calorimeter containing hits associated with the track candidate (considering the first two layers of the hadronic calorimeter only).

- N_{MU} - The number of hits in the muon chambers associated with the candidate track.

- $X_{\mathrm{hits/layer}}$ - The number of hits in the associated hadron calorimeter cluster divided by the number of layers containing hits.

- $\cos(\theta_{\ell\vec{p}})$ - The cosine of the angle between the momentum associated with the candidate track and the missing momentum calculated from equation (64).

- $N_{\rm CT}^{\ell,\rm jet}$ The total number of tracks in the jet containing the candidate track, after the event was forced into three jets. (See section 6.3.6).

	Lepton hypothesis					
Variable	e	μ	$\tau \to {\rm e}\nu_{\rm e}\nu_\tau$	$\tau \to \mu\nu_\mu\nu_\tau$	$\tau \to {\rm h}\nu_\tau$	$\tau \to 3{\rm h}\nu_\tau$
p_ℓ		-		-		-
E_ℓ	-	-	-	-		
E_ℓ/p_ℓ	-		-			
$\Delta\phi_{\rm EC/CT}$	-		-			
E_τ					-	
M_τ					-	-
I_{200}	-	-	-	-		
$I_{200}^{\rm CT}$					-	-
$I_{200-500}$					-	-
$\frac{{\rm d}E}{{\rm d}x}\vert_{\rm track}$	-		-			
$X_{\rm e^+e^-}$	-		-			
$N_{\rm blk}^{90}$	-		-			
$N_{\rm HC}$		-		-		
$N_{\rm HC2}$	-		-			
$N_{\rm MU}$		-		-		
$X_{\rm hits/layer}$		-		-		
$\cos(\theta_{\ell\vec{p}})$					-	
$N_{\rm CT}^{\ell,\rm jet}$					-	-

Table 6: The table of variables used in identifying the best lepton candidate track for each of the six lepton hypotheses. A dash indicates that the variable in that row was used in selecting tracks for the hypothesis in that column.

6.3.5 Likelihood selection

Following the $q\bar{q}'\ell\nu$ pre-selection and the identification of lepton candidates, each event was tentatively considered to be a $q\bar{q}'\ell\nu$ candidate and was partially reconstructed under each of the six lepton hypotheses introduced in section 6.3.3. All tracks and unassociated clusters not selected as being related to the charged lepton were forced into two jets by the Durham $k_\perp$ jet algorithm [68]. The energies of the tracks and clusters in the jets were then adjusted using the 'Globally Corrected Energy' (GCE) algorithm [69] to prevent the double-counting of energy measurements for particles that were detected by more than one sub-detector. The GCE algorithm scaled the total energy measured in each of the calorimeter sub-detectors by an amount which depended on the total number of tracks reconstructed in the central detector. The algorithm distinguished between activity due to pions, electrons and muons. The tracks and adjusted clusters were then used to obtain the momenta of the two jets in each event as defined in equation (68), where $\vec{p}_{\rm track}$ is the reconstructed momentum associated with a track, $\vec{p}_{\rm EC}$ is the reconstructed momentum associated with a cluster in the electromagnetic calorimeter, $\vec{p}_{\rm HC}$ is the reconstructed momentum associated with a cluster in the hadronic calorimeter, and the summations run over all tracks and clusters in a jet.

$$\vec{p}_{\rm jet} = \sum \vec{p}_{\rm track} + \sum \vec{p}_{\rm EC} + \sum \vec{p}_{\rm HC} \qquad (68)$$

The direction of the momentum vector associated with a cluster in one of the calorimeters was extrapolated from the position of the nominal interaction point and the position of the hits in the calorimeter. The momentum of the primary quark or anti-quark hypothesised to originate a jet was then assumed to be approximately equal to the measured jet momentum.

The energy and momentum of electron candidates were estimated from the cluster associated with the electron candidate track, and the energy and momentum of muon candidates were estimated from the muon candidate track. The energy and momentum of

τ-lepton candidates were estimated by the sum of the energy of the tau candidate tracks plus the energy contained in those unassociated clusters in the electromagnetic calorimeter which lay within a cone of half-angle 200 mrad about the summed track momentum.

The reconstructed properties of each event were used to identify which, if any, of the six lepton hypotheses it was likely to originate from. Six separate selections were used, where each selection corresponded to one of the six lepton hypotheses and consisted of a further pre-selection and a likelihood selection. Only events which passed a given pre-selection were subsequently analysed by its associated likelihood selection. In the case of the $q\bar{q}'e\nu$ selection, candidate events which passed the pre-selection were vetoed if the charged lepton candidate was kinematically consistent with being either an electron or positron produced in the pair-conversion of an ISR photon (see reference [63] for details). Additionally, to save computer processing time, only those events which failed the $q\bar{q}'e\nu$ and $q\bar{q}'\mu\nu$ likelihood selections were considered as possible $q\bar{q}'\tau\nu$ candidates.

Each likelihood selection used MC reference distributions to calculate the likelihood that an event belonged to a given signal hypothesis relative to the likelihood of it being a $Z^0/\gamma \rightarrow q\bar{q}$ event (which was the dominant background at this point in the selection procedure). The reference distributions were generated at nominal centre-of-mass energies of 183 GeV, 189 GeV, 200 GeV, and 206 GeV, where only those distributions whose nominal centre-of-mass energy was closest to that of the event being processed were employed to determine the likelihood. Events were considered to pass a selection if they satisfied the criteria,

$$\frac{L(q\bar{q}'\ell\nu;\ \ell = X)}{L(q\bar{q}'\ell\nu;\ \ell = X) + L(Z^0/\gamma \rightarrow q\bar{q})} \ > \ 0.5 \ \ ,(X = e, \mu, ...) \qquad (69)$$

where $L(q\bar{q}'\ell\nu;\ \ell = X)$ represents the likelihood that the event belonged to the signal hypothesis with a charged lepton of type 'X', and $L(Z^0/\gamma \rightarrow q\bar{q})$ represents the likelihood that the event originated from a $Z^0/\gamma \rightarrow q\bar{q}$ process.

An event could pass none, one or more than one of the six selections (e.g. an event could be selected as being consistent with both the $q\bar{q}'e\nu$ and $q\bar{q}'\mu\nu$ hypotheses). Events which passed none of the six selections were rejected from the event sample. Events which passed only one of the six likelihood selections were categorized as belonging to that hypothesis. Events which passed more than one of the likelihood selections were categorized as belonging to the hypothesis which resulted in the greatest likelihood (more details of the categorization can be found in reference [63]). Events failing all of the selections, as well as those events selected as being $q\bar{q}\ell^+\ell^-$, $q\bar{q}\nu\nu$ or $We\bar{\nu}_e$ were removed from the sample. Finally, the $q\bar{q}'e\nu$ and $q\bar{q}'\mu\nu$ candidate events were subject to a further likelihood selection which was designed to find and recategorize mis-identified $q\bar{q}'\tau\nu$ events in which the τ-lepton had decayed leptonically. The whole procedure was optimised to reduce the background contamination by $Z^0/\gamma \to q\bar{q}$ events in the data sample.

The variables used in the pre-selections and likelihood selections were:

- E_ℓ - The reconstructed energy of the lepton.
- $\log_{10} \Pr(\ell)$ - The logarithm of the lepton identification probability from the track selection described previously in section 6.3.4.
- I_{200} - The sum of p_ℓ and the momenta associated with all tracks and the energy associated with all electromagnetic calorimeter clusters within an isolation cone of 200 mrad half-angle centred on the candidate track (excluding clusters associated with the candidate track or tracks).
- I_{200}^{CT} - The sum of the momenta associated with all tracks within an isolation cone of 200 mrad half-angle centred on the candidate track.
- $I_{200-500}$ - The sum of the momenta associated with all tracks and the energy associated with all electromagnetic clusters within a conical annulus of 200 mrad to 500 mrad

half-angle centred on the candidate track.

- N_{CT} - The number of charged tracks passing the quality cuts of section 6.3.2.
- N_{EC} The number of clusters in the electromagnetic calorimeter passing the quality cuts of section 6.3.2.
- y_{23} - The value of y_{cut} for the transition between a 2-jet and 3-jet event, as defined by the Durham jet algorithm.
- $\cos(\theta_{\mathrm{mis}})$ - The cosine of the polar angle of the missing momentum calculated from equation (64).
- R_{vis} - The visible energy (the GCE-corrected sum of the energy measurements made by the detector) in the event divided by the centre-of-mass energy of the collision.
- R_{shw} - The total energy reconstructed in the electromagnetic calorimeters divided by the centre-of-mass energy of the collision.
- R_{mis} - The ratio of the missing energy in the event (the centre-of-mass energy of the collision minus the visible energy) divided by the centre-of-mass energy of the collision.
- p_T^{mis} - The missing transverse momentum.
- $\cos(\theta_\ell)$ - The cosine of the polar angle of the lepton candidate momentum.
- $\cos(\theta_{\ell,\mathrm{pmis}})$ - The cosine of the angle between the lepton candidate momentum and the missing momentum.
- $\cos(\theta_{\ell,\mathrm{jet}})$ - The cosine of the angle between the lepton candidate momentum and the nearest of the two jet momenta.

- $Pr(s')$ - The probability that the event was consistent with being a $Z^0/\gamma \rightarrow q\bar{q}$ event with an effective centre-of-mass energy of $\sqrt{s'}$ following the emission of an ISR photon. The probability was calculated from a kinematic fit (see section 6.3.6).
- $\sqrt{s'}$ - The value of the effective centre-of-mass energy of the event.
- N_{CT}^{min} - The minimum number of tracks in a jet when all tracks in the event were forced into 3 jets by the Durham jet algorithm.
- N_{CT}^{ℓ} - The number of tracks in the jet which contained the charged lepton candidate track when all tracks in the event are forced into 3 jets by the Durham jet algorithm.
- E_{qq} - The summed energy of the two jets (assuming the jet mass is zero).
- $m_{\ell\nu}$ - The invariant mass of the lepton candidate momentum and missing momentum.
- E_{FD} - The total energy in the forward detectors.
- E_{γ} - The energy of the highest-energy isolated cluster in the electromagnetic calorimeter.

Tables showing which of the variables listed were used in the six different pre-selections and likelihood selections can be found in reference [63]. Examples of the distributions obtained from data and pseudo-data for those variables used in the 189 GeV $q\bar{q}'e\nu$ likelihood selections are shown in figure 25. The data and pseudo-data show reasonable agreement within the statistical uncertainties, validating the use of the MC generators employed to form the likelihood distributions. At this stage in the selection procedure, the efficiency and purity for selecting signal events were approximately 86% and 90% respectively with small variations (of the order of 1%) between selections carried out at each of the eight nominal centre-of-mass energies. The efficiencies for selecting signal $q\bar{q}'e\nu$, $q\bar{q}'\mu\nu$, or $q\bar{q}'\tau\nu$ events and correctly categorizing them were approximately 85% , 89%, and 68% respectively.

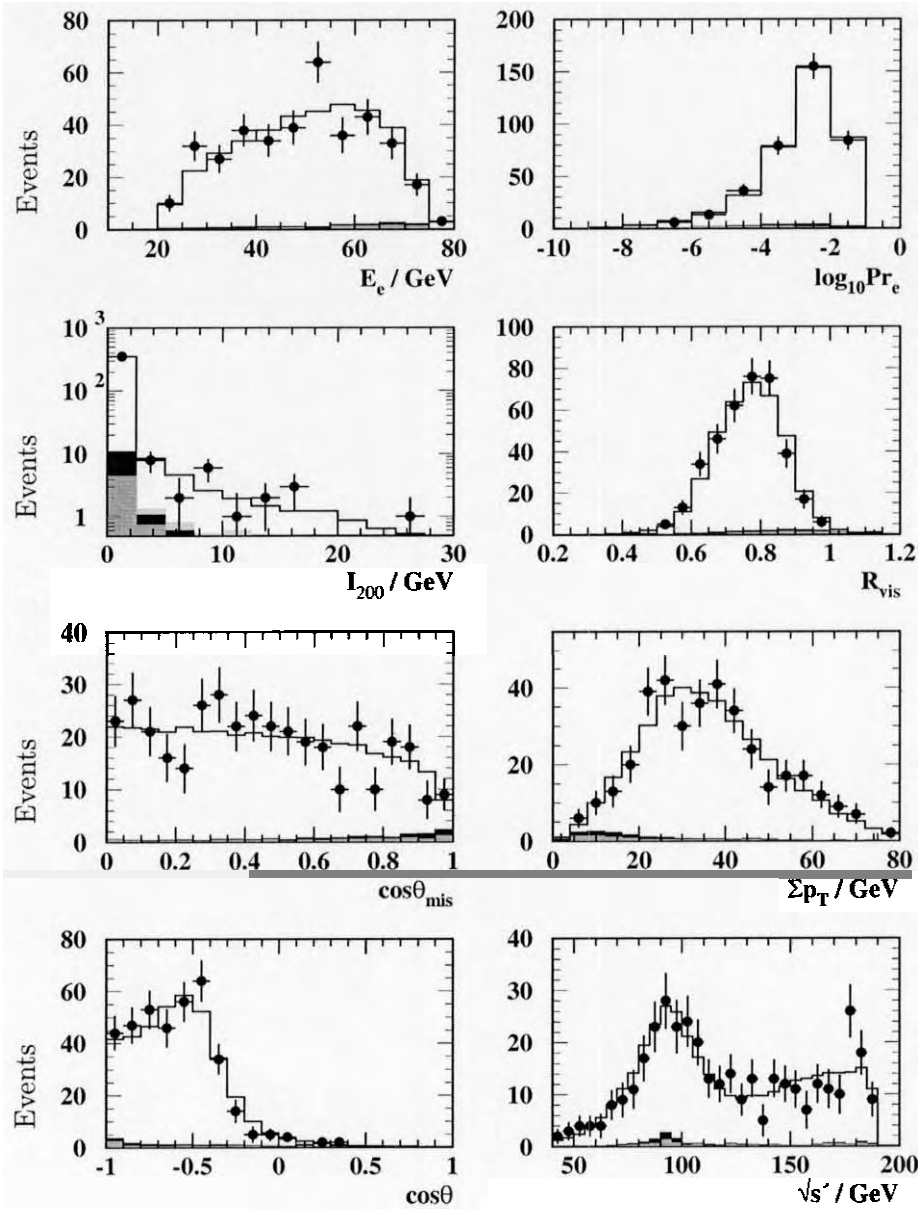

Figure 25: The 189 GeV $q\bar{q}'e\nu$ likelihood variable distributions for those events which passed the $q\bar{q}'e\nu$ selection. The points show data and the histogram shows the pseudo-data, with the unshaded region showing signal and shaded region showing background. The vertical error bars show the statistical uncertainty on the data. This plot has been reproduced from reference [63]. The notation used in this plot and the notation used in the main text of this thesis are identical except that the labels $\cos(\theta)$ and Σp_T refer to $\cos(\theta_\ell)$ and $p_T^{\rm mis}$ respectively.

6.3.6 Kinematic fit

The events surviving the likelihood selection were subject to a second reconstruction procedure which placed particular emphasis on the need to accurately reconstruct the angles required for the SDM analysis. As before, all tracks and clusters not previously selected as being related to the charged lepton were forced into two jets by the Durham $k_\perp$ jet algorithm. For each jet, the 'MaTching track and cluster' (MT) algorithm described in [70] was applied to prevent the double-counting of energy measurements made by the OPAL sub-detectors. The energy of the clusters in the calorimeters was reduced on a cluster-by-cluster basis such that if a track and cluster were associated with one another then the momentum of the track was subtracted from the energy of the cluster. Like the GCE algorithm used previously, the MT algorithm distinguished between hadrons, electrons and muons and adjusted the energy of electromagnetic and hadronic clusters accordingly.

The momentum of each primary quark was approximated by the jet momentum. As mentioned previously, it was not possible to reliably determine which jet was produced by the quark and which by the anti-quark, and so an arbitrary assignment was made. The uncertainty on the measured value of a jet momentum was given by the square root of the sum in quadrature of the uncertainties on each individual track and cluster in the jet.

For events categorized as $q\bar{q}'e\nu$ or $q\bar{q}'\mu\nu$, reconstructed photon candidates (characterised by isolated clusters in the electromagnetic calorimeter) were recombined with the charged lepton if they were closer to the lepton than to the jets and the angle between the photon and the charged lepton track was less than 0.15 radians. Clusters recombined in this way were not included among the tracks and clusters processed by the jet algorithm. The momentum vector of an electron in a $q\bar{q}'e\nu$ event was then given by the reconstructed momentum of its cluster(s) in the electromagnetic calorimeter. The momentum vector of a muon in a $q\bar{q}'\mu\nu$ event was given by the reconstructed momentum of its charged track.

In the case of events categorized as $q\bar{q}'\tau\nu$ with the τ-lepton decaying to one or more

visible decay products, the direction of the summed momenta of the decay products was used as an estimate of the direction of the parent τ-lepton momentum in the lab frame. Reference [71] contains an analysis of this approximation by the author of this thesis. The validity of the approximation cannot be established by considering kinematic constraints alone, as the angle between the visible decay products of the τ-lepton and the τ-lepton itself in the lab frame can be large if the invariant mass of the decay products is small (e.g. the angle can be as large as 16° if the visible decay product is a single charged pion). However, Monte Carlo simulations showed that the average angle between the decay products and the true τ-lepton direction in the lab frame was expected to be approximately 2° in the SM. The magnitude of the τ-lepton momentum in the lab frame could not be directly measured, and was estimated by the procedure described in [72].

The measured four-momentum vectors of the jets and of the charged lepton in the lab frame were next adjusted to compensate for differences between the MC modelling and the properties of di-jet and di-lepton events observed in $Z^0/\gamma \to q\bar{q}$ and $Z^0/\gamma \to \ell^-\ell^+$ reactions at OPAL with centre-of-mass energies close to the Z^0 mass pole [73], as discussed in section 7. The adjusted momentum vectors were next processed by a series of 'kinematic fits' [74] which varied the measured momenta within their estimated uncertainties subject to kinematic constraints arising from the hypothesis that the event originated from a $WW \to q\bar{q}'\ell\nu$ process. The fits improved the angular and energy resolutions of the measured momenta, and produced an estimate for the unmeasured momentum vector of the neutrino associated with the production of the charged lepton. Additionally, the fitting procedure provided the probability (Pr) that the event was consistent with the fit hypothesis.

The kinematic constraints used in each of the three fits (labelled A, B and C) are summarised below. None of the fit hypotheses included the presence of initial-state radiation (ISR).

Fit A

- Conserve four-momentum using known beam momenta (as shown previously in equations (61) and (64)).

Fit B

- Conserve four-momentum using known beam momenta.
- Constrain W masses to be equal.

Fit C

- Conserve four-momentum using known beam momenta.
- Constrain W masses to be equal.
- Constrain W masses to be 80.44 GeV.

If a kinematic fit is to have a unique solution which minimises the measurement uncertainties then the system of equations which govern the fit must be over-constrained. A kinematic fit for which the number of constraint equations minus the number of unmeasured quantities equals 'n' is known as an n-C fit. For a $q\bar{q}'e\nu$ or $q\bar{q}'\mu\nu$ event, it follows that fit A is a 1-C fit, fit B is a 2-C fit and fit C is a 3-C fit. In the case of $q\bar{q}'\tau\nu$ events, the neutrino associated with the τ-lepton decay removes a further three constraints compared to $q\bar{q}'e\nu$ and $q\bar{q}'\mu\nu$ events. As explained above, this problem was partially resolved by approximating the direction of the τ-lepton by the direction of its decay products in the lab frame. The error on the magnitude of the τ-lepton momentum was assumed to be arbitrarily large when used in the fits.

6.3.7 Final selection

Following the kinematic fits, a final selection was made by rejecting the events for which the kinematic fits either failed to converge or else converged with low fit probabilities. For $q\bar{q}'\tau\nu$ candidate events, the cuts were chosen to suppress those events in which the tracks associated with the τ-lepton had been wrongly identified. The number of such events in the event sample following the final selection was approximately 12%. The cuts are summarised below:

- WW decay modes: $q\bar{q}'e\nu$ or $q\bar{q}'\mu\nu$
  - $Pr_C \geq 0.001$ - Use result from fit C.
  - $Pr_C < 0.001$ and $Pr_A \geq 0.001$ - Use result from fit A.
  - $Pr_C < 0.001$ and $Pr_A < 0.001$ - Reject.
- WW decay modes: $q\bar{q}'\tau\nu$
  - $Pr_B \geq 0.025$ - Use result from fit B.
  - $Pr_B < 0.025$ - Reject.

Additionally, in order to identify which fermions belonged to which W boson, it was necessary to measure the charge of the charged lepton, Q_ℓ, defined as the sum of the reconstructed charges of the tracks previously selected as belonging to the lepton. As a consequence, any events for which Q_ℓ was zero were rejected at this stage of the analysis, which automatically excluded any events for which no tracks had been selected as belonging to the lepton.

The composition of the pseudo-data events passing the full event selection at 196 GeV are detailed in table 7. Equivalent tables for all eight centre-of-mass energies can be found in appendix B. Each table shows the admixture of pseudo-data events from the individual signal and background sources which were categorized as $q\bar{q}'e\nu$, $q\bar{q}'\mu\nu$ or $q\bar{q}'\tau\nu$ during the

event selection, where the $q\bar{q}'\tau\nu$ category includes all four of the τ-lepton decay modes considered in the likelihood selection described previously.

It can be calculated from the tables that the estimated purities of the $q\bar{q}'e\nu$, $q\bar{q}'\mu\nu$ or $q\bar{q}'\tau\nu$ event samples following the full selection were approximately 90%, 94% and 78% respectively at 196 GeV, and the variation in the purities between different centre-of-mass energies was less than 5% in all cases. The comparatively low purity of the $q\bar{q}'\tau\nu$ selection reflects the difficulty of identifying a τ-lepton from its visible decay products in the presence of hadronic jets produced from the hadronically-decaying W boson.

Even in the $q\bar{q}'\tau\nu$ case, the contamination of the event sample by background events was low and was mainly due to mis-classified W-pair $q\bar{q}'\ell\nu$ events (e.g. events generated as $q\bar{q}'e\nu$ in the MC samples but reconstructed as being $q\bar{q}'\tau\nu$ during the event selection). In practice, the following analysis made no distinction between $q\bar{q}'e\nu$, $q\bar{q}'\mu\nu$ and $q\bar{q}'\tau\nu$ events when calculating the SDMs and so all such mis-classified WW events were treated as signal, giving an overall purity for the $q\bar{q}'\ell\nu$ selection of approximately 93% at 196 GeV. The remaining 7% of background contamination was predominantly due to non-WW $q\bar{q}'\ell\nu$ events and residual $Z^0/\gamma \to q\bar{q}$ events. The total efficiency for selecting signal events at 196 GeV was approximately 79%. Further figures of merit for the selection are discussed in section 6.4.2.

	Generated event type								
Reconstructed event type	$e^+e^-\gamma\gamma$	$q\bar{q}'$	$q\bar{q}'\ell\nu$ (not CC03)	$\ell\nu\ell\nu$	$q\bar{q}q\bar{q}$	$q\bar{q}'e\nu$ (CC03)	$q\bar{q}'\mu\nu$ (CC03)	$q\bar{q}'\tau\nu$ (CC03)	
$q\bar{q}'e\nu$	0.11	0.52	1.45	0.01	0.02	31.75	0.04	1.36	35.26
$q\bar{q}'\mu\nu$	0.00	0.26	0.39	0.01	0.14	0.07	32.66	1.35	34.89
$q\bar{q}'\tau\nu$	0.03	1.26	2.39	0.00	0.21	1.18	1.42	23.35	29.85
	0.14	2.05	4.23	0.01	0.37	33.01	34.11	26.07	

Table 7: The composition of events passing the total event selection at 196 GeV as calculated from the MC samples listed in section 6.2. Each number shows the percentage of selected events that have a given generated event type and a given reconstructed event type, normalised to the total number of events passing the selection. The far right-hand column and bottommost row show summed totals.

6.4 Angular and SDM distributions

The following sections describe how the SDM matrices of section 2.5 and other quantities of interest were measured from the reconstructed properties of the events which passed the full $q\bar{q}'\ell\nu$ selection described in section 6.3.

Section 6.4.1 describes how the momenta of the four reconstructed fermions in each event were related to the production and decay angles of the two hypothesised parent W bosons. Section 6.4.2 describes how the measured angular distributions were adjusted to compensate for inefficiencies, impurities and resolution effects inherent in the event selection and reconstruction procedure. Finally, section 6.4.3 describes the measurement of the SDM matrix elements, the polarised differential cross-sections, the total fraction of longitudinally polarised W bosons and the CP-odd and CP$\hat{\text{T}}$-odd observables of section 2.8.

6.4.1 Measuring angular distributions

For each selected $q\bar{q}'\ell\nu$ candidate event, the fitted momentum vectors of the four fermions ($\vec{p}_\ell$, $\vec{p}_\nu$, $\vec{p}_q$, $\vec{p}_{\bar{q}}$) and the reconstructed lepton charge, Q_ℓ, were used to calculate the production and decay angles of the W bosons, Ω, as defined in section 2.6.

The momentum vector of the hadronically decaying W boson was simply given by the sum of the momentum vectors of the two jets. As θ_{W} was defined as the polar production angle of the W^- [17], its value depended on Q_ℓ. If Q_ℓ was positive then

$$\cos\theta_{\text{W}} = \frac{(\vec{p}_q + \vec{p}_{\bar{q}}).\vec{z}}{|\vec{p}_q + \vec{p}_{\bar{q}}|.|z|}\,, \tag{70}$$

whereas if Q_ℓ was negative then

$$\cos\theta_{\text{W}} = \frac{(\vec{p}_\ell + \vec{p}_\nu).\vec{z}}{|\vec{p}_\ell + \vec{p}_\nu|.|z|}\,, \tag{71}$$

[17] Note that the kinematic constraints in the kinematic fit ensured that the centre-of-mass frame of the four reconstructed fermions was coincident with the lab-frame. Because of ISR, these frames were not generally coincident when considering generator-level momentum vectors. In this latter case the momentum vectors of the four fermions were Lorentz-transformed to the centre-of-mass frame before the W production angle was calculated.

where z refers to the central axis of the detector in the OPAL master reference system. The values of $\theta^*_{f_1}$ and $\phi^*_{f_1}$ (needed to reconstruct the W^- SDM) and the values of $\theta^*_{\bar{f}_4}$ and $\phi^*_{\bar{f}_4}$ (needed to reconstruct the W^+ SDM) were likewise dependent on the value of Q_ℓ. If Q_ℓ was negative then the fermion from the W^- decay, f_1, was identified with the charged lepton in the $W \to \ell\nu$ decay, and the anti-fermion from the W^+ decay, $\bar{f}_4$, was identified with the anti-quark in the $W \to q\bar{q}'$ decay. Similarly, if Q_ℓ was positive then f_1 was identified with the quark in the $W \to q\bar{q}'$ decay, and $\bar{f}_4$ was identified with the neutrino in the $W \to \ell\nu$ decay. Following the convention of section 2.6, the polar and azimuthal production angles of the charged lepton in the rest-frame of its parent W boson are denoted θ^*_ℓ and ϕ^*_ℓ, and those of the quark (or anti-quark, as they were not distinguished between) in its parent rest-frame are denoted by θ^*_q and ϕ^*_q. The angles of the neutrino in its parent W rest-frame are trivially related to those of the charged lepton by $\theta^*_\nu = \pi - \theta^*_\ell$ and $\phi^*_\nu = \pi + \phi^*_\ell$. The procedure for extracting $\cos\theta^*_\ell$, ϕ^*_ℓ, $\cos\theta^*_q$ and ϕ^*_q from the reconstructed momentum vectors is described in appendix C. The procedure ensured that the extracted angles always lay in the physically-allowed region. The $\cos\theta^*_q$ and ϕ^*_q distributions were folded as described in section 2.7, and the folded variables are denoted hereafter by $|\cos\theta^*_q|$ and $[\phi^*_q]$ respectively.

Figure 26 shows the measured angular distributions, and table 26 shows the Chi-squared statistics describing the goodness of the fit between the data and pseudo-data. It can be seen that there is good overall agreement between data and pseudo-data for all five distributions, but closer inspection reveals that the pseudo-data systematically over-estimate the steepness of the slope in the $\cos\theta_W$ distribution. This effect is taken into account in the systematic uncertainties of section 7.

	$\cos\theta_W$	$\cos\theta^*_\ell$	ϕ^*_ℓ	$\lvert\cos\theta^*_q\rvert$	$[\phi^*_q]$
χ^2/d.o.f.	1.69	1.22	1.51	0.57	0.80

Table 8: The Chi-squared per degree of freedom for the angular distributions shown in figure 26.

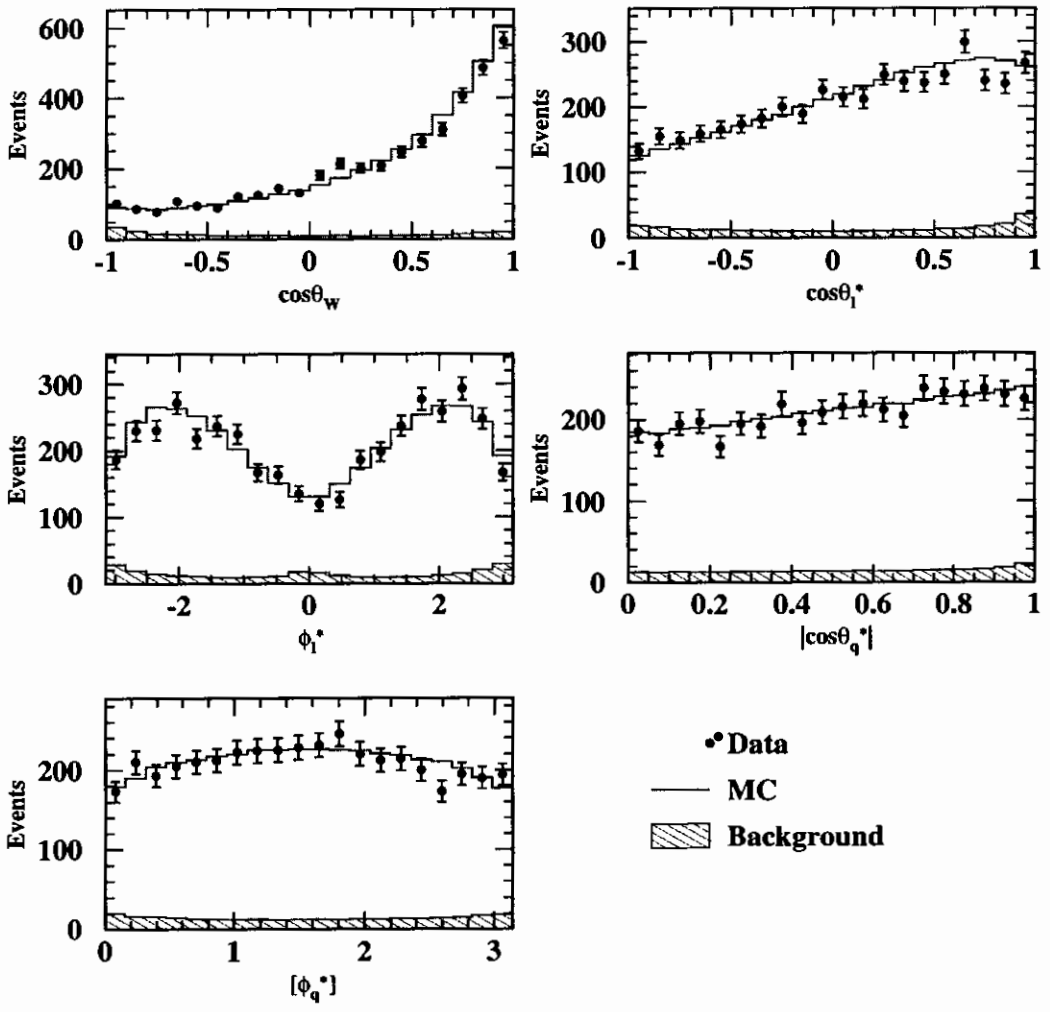

Figure 26: The WW production angle and decay angle distributions showing the number of events reconstructed in each angular bin as obtained from the full data set summed over all eight nominal centre-of-mass energies. The points show the data and the un-filled histogram shows the pseudo-data from both signal and background MC samples combined. The hatched histogram shows the pseudo-data from background MC samples only. The error bars on the points show the statistical uncertainties on the data.

There are a large number of possible techniques for realising the equations of section 2 from the discrete distributions measured experimentally. In this analysis, the events were first divided into eight $\cos\theta_W$ bins of equal width. The true number of signal events produced in each $\cos\theta_W$ bin was estimated by,

$$N_k = \sum_{i=1}^{n_k} \frac{p(\Omega_i)}{\epsilon(\Omega_i)} , \tag{72}$$

where the sum is over all n_k data events reconstructed in the angular bin and $p(\Omega)/\epsilon(\Omega)$ is the detector correction factor (defined in section 6.4.2) which allowed for variations with the polar and azimuthal angles of the efficiency, purity and angular resolutions. The uncertainties on the N_k were estimated from Poisson statistics by,

$$s_k^{(N)} = \sqrt{\sum_{i=1}^{n_k} \left(\frac{p(\Omega_i)}{\epsilon(\Omega_i)}\right)^2} . \tag{73}$$

The unpolarised differential cross-section integrated over each $\cos\theta_W$ bin, $\partial\sigma_k$, was needed to evaluate equations (43), (44), (52) and (53), and was estimated by dividing the number of events, N_k, by the luminosities given in table 3:

$$\partial\sigma_k = \frac{N_k}{\mathcal{L}} . \tag{74}$$

The uncertainties on the $\partial\sigma_k$ follow from equations (73) and (74) using the standard quadratic error-propagation formula, in which both the uncertainty on N_k and the uncertainty on the luminosity (see section 6.1) were included.

The generalisation of the equations defined in this section to apply to the number of events produced in any other angular region in the five-dimensional Ω space is trivially obtained by changing the region of the summation in equations (72) and (73) appropriately. The resulting angular distributions for $\cos\theta_W$, $\cos\theta_\ell^*$, ϕ_ℓ^* and $|\cos\theta_q^*|$ are shown later in section 6.4.2 following a description of the details of the detector correction. The $[\phi_q^*]$ distribution is not shown as it was not used in the SDM analysis.

6.4.2 Detector correction

The MC samples listed in section 6.2 were used to estimate the efficiency and purity of the event selection and the angular resolution with which the directions of the W bosons and their decay products were reconstructed in the detector. The efficiency for selecting a signal event with generator-level angular co-ordinates Ω^G was estimated by,

$$e(\Omega^G) \;=\; \frac{n_{\rm sig}(\Omega^G)}{N_{\rm sig}(\Omega^G)}\,, \tag{75}$$

where $N_{\rm sig}(\Omega^G)$ denotes the number of MC signal events which were generated in an angular bin containing the point Ω^G, and $n_{\rm sig}(\Omega^G)$ denotes the number of MC signal events which were generated in the angular bin and subsequently passed the selection. Similarly, the purity of an event with reconstructed angular co-ordinates Ω^R was estimated by,

$$p(\Omega^R) \;=\; \frac{n_{\rm sig}(\Omega^R)}{n_{\rm sig}(\Omega^R) + n_{\rm bgd}(\Omega^R)}\,, \tag{76}$$

where $n_{\rm sig}(\Omega^R)$ and $n_{\rm bgd}(\Omega^R)$ denote the number of pseudo-data signal and background events which passed the selection and were reconstructed in an angular bin containing the point Ω^R. Therefore, the estimates of the efficiency and purity depended on the size of the angular bins used to determine $n_{\rm sig}$, $n_{\rm bgd}$ and $N_{\rm sig}$. Wider bins reduced the statistical uncertainties on the estimates (determined by Poisson statistics), whilst narrower bins reduced the sensitivity of the estimates to the shape of the MC generator-level distributions. The size of the bins also determined the size and types of biases in the final results (see section 6.5).

An estimate of the global efficiency was given by considering a single angular bin which spans the whole angular space of Ω^G, and the global purity was given by considering a single angular bin which spans the whole angular space of Ω^R. The global efficiency of the selection used in this analysis varied between 78% and 81%, and the global purity varied between 93% and 95% depending on the centre-of-mass energy as shown in figure 27. In addition,

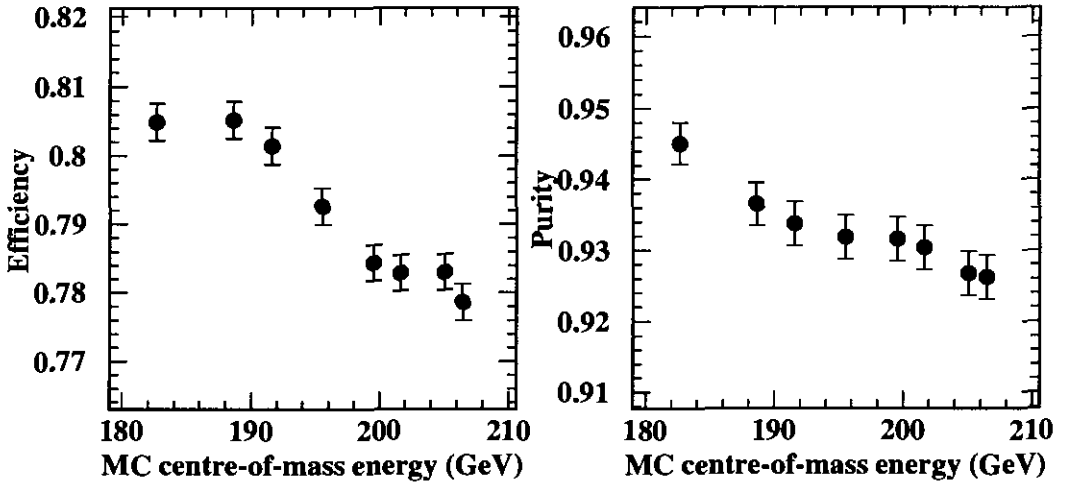

Figure 27: The global efficiency and purity of the event selection plotted as functions of centre-of-mass energy as obtained from the MC samples listed in table 4. The error bars show the statistical uncertainties on the data.

the efficiency varied between 44% and 92%, and the purity varied between 15% and 100% in the $\cos\theta_W - \cos\theta_l^*$ plane. Variations of the efficiency and purity with $\cos\theta_q^*$ and ϕ_l^* were smaller but significant. Figures showing these variations can be found in appendix D.2 and appendix D.3.

The large variations in purity in the $\cos\theta_W - \cos\theta_l^*$ plane can be mainly attributed to the variations with angle in the number of signal events selected (and generated) whilst the number of background events selected remains approximately constant (see figure 26). The efficiency was high in most angular bins but dropped sharply if the charged lepton was emitted close to the beam-pipe (i.e. $\cos\theta_l^* \approx 1$ and either $\cos\theta_W \approx 1$ or $\cos\theta_W \approx -1$). In addition, the efficiency for selecting an event decreased if it was emitted in the opposite direction to its parent W boson (i.e. $\cos\theta_l^* \approx -1$), as this reduced its energy in the lab

frame.

The difference between the generated and reconstructed angles of a MC signal event is governed by the angular resolution of the reconstruction. The angular resolution was dominated by the measurement uncertainties in the four-momenta of the hadronically decaying W bosons, but additionally included a small contribution from the 3% of charged leptons which were assigned an incorrect charge (9% in the $q\bar{q}'\tau\nu$ decay mode and less than 1% in the $q\bar{q}'e\nu$ and $q\bar{q}'\mu\nu$ decay modes). As the generator-level MC values of θ_W were obtained after boosting to the centre-of-mass frame of the four fermions, whereas the reconstructed values were measured in the lab frame, the angular resolution was sensitive to ISR effects. Example plots of the angular resolution obtained at 196 GeV are shown in figure 28. As can be seen in appendix D.2, there were considerable variations between the detector corrections calculated for the three reconstruction categories $q\bar{q}'e\nu$, $q\bar{q}'\mu\nu$ and $q\bar{q}'\tau\nu$. In particular the $q\bar{q}'\tau\nu$ decay mode had lower efficiencies and purities and a larger angular resolution than measured for the $q\bar{q}'e\nu$ and $q\bar{q}'\mu\nu$ modes. In this analysis, no distinction was made between the three modes and all charged leptons were treated alike. This approximation is valid provided that the branching fractions for the three modes as predicted by the SM are consistent with the branching fractions measured from the data. This has been shown to be the case in the analysis of the OPAL data contained in reference [39].

As shown in section 6.4, each selected data event was weighted by a detector correction factor ($p(\Omega)/\epsilon(\Omega)$ in equation (72)) given by the purity divided by an efficiency-like scaling factor defined as,

$$\epsilon(\Omega^G) \;=\; \frac{n_{\rm sig}(\Omega^R)|_{\Omega^R=\Omega^G}}{N_{\rm sig}(\Omega^G)} \,. \tag{77}$$

The scaling factor differed subtley from the true efficiency defined in equation (75) as it was defined in terms of both the reconstructed and generated angular spaces (where the values of the co-ordinates in the space of reconstructed angles are set equal to the values

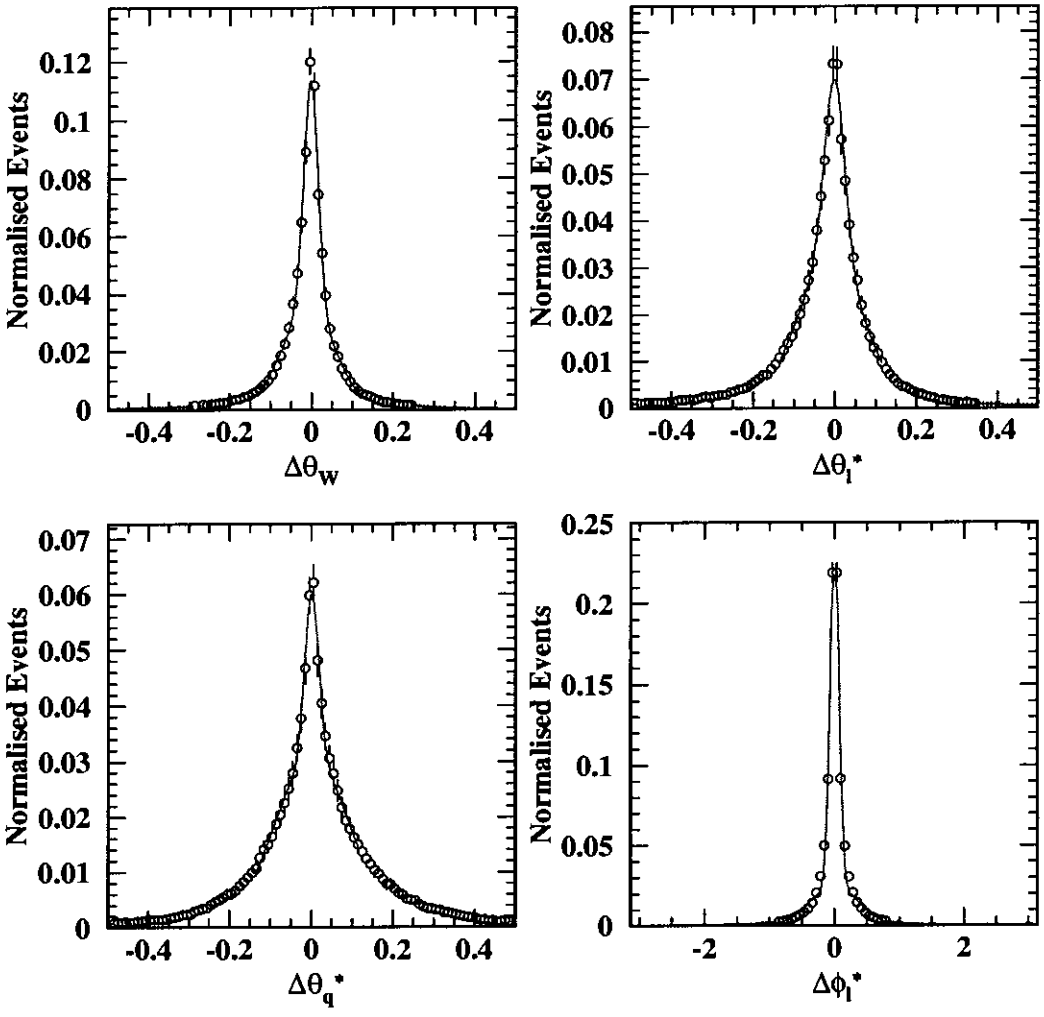

Figure 28: The angular resolution in θ_W, θ_ℓ^*, θ_q^* and ϕ_ℓ^* (in radians) as obtained from SM MC samples with a centre-of-mass energy of 196 GeV. The open circles show the values calculated from the MC samples and the error bars show the statistical uncertainties on the data. The histograms have been normalised to have unit area. For illustrative purposes a solid line is superimposed on each plot to show the function composed of the sum of two Gaussians which best fits the data, where the best fit was determined by minimising a Chi-squared difference between the function values and the points.

of the co-ordinates in the space of generated angles). It therefore included the effects of both the efficiency and angular resolution under the assumption that the shapes of the MC angular distributions closely approximated those of the data. Approximately 16% of the MC events which passed the selection were reconstructed outside of the $\cos\theta_W$ bin in which they were generated, where the exact fraction depended on the centre-of-mass energy. In studies using the full unfolding procedures described in [75,76], the bin-to-bin migration led to correlations as high as 40% between the statistical uncertainties in neighbouring $\cos\theta_W$ bins. As the SDM estimators in each $\cos\theta_W$ bin are statistically uncorrelated with one another by construction, special care should be exercised if using the results of this analysis in fitting procedures. More details can be found in appendix E.

It can be seen from the figures in appendix D that ϵ differed substantially from the efficiency, e, in some angular bins. Where ϵ is less than e there was a net outward migration of the events generated in that angular bin (i.e. the number of selected events reconstructed in the bin was less than the number of selected events generated in that bin). Conversely, where ϵ is greater than e there was a net inward migration of events generated in the surrounding angular bins. One consequence of this is that ϵ could take values greater than 1 in some angular bins. Large values of ϵ were seen in the region $\cos\theta_W \approx -1$ and $\cos\theta_\ell^* \approx 1$ where the number of generated signal events was low. The events migrating into this region were mostly $q\bar{q}'\tau\nu$ signal events with mis-reconstructed τ-leptons. Such events were approximately uniformally distributed over the whole angular space.

The numbers of angular bins used to parameterise the detector correction for leptonically and hadronically decaying W bosons and for diagonal and off-diagonal elements of the SDM are summarised in table 9.

These were chosen to make best use of the MC statistics whilst reducing possible bias effects (see section 6.5). The detector corrections for positively and negatively charged W bosons were combined by making use of the approximate CP invariance of both the SM

SDM elements	Decay mode	$\cos\theta_W$	$\cos\theta^*_\ell$	ϕ^*_ℓ	$\lvert\cos\theta^*_q\rvert$
ρ_{--}, ρ_{++}, ρ_{00}	$W \to \ell\nu$	8	20	-	-
	$W \to q\bar{q}'$	8	-	-	10
ρ_{+-}, ρ_{+0}, ρ_{-0}	$W \to \ell\nu$	8	5	5	-
	$W \to q\bar{q}'$	-	-	-	-

Table 9: The numbers of equal-width bins into which each angular distribution was subdivided to parameterise the detector correction. The hadronically decaying W bosons were not used to measure the off-diagonal SDM elements, and hence there were no bins in $[\phi^*_q]$.

MC and the response of the OPAL detector [77].

The measured angular distributions of $\cos\theta_W$ following the detector correction are shown in figure 29 and the lepton and quark distributions are shown in figure 30. It can be seen that the detector correction maintains the overall good agreement between the data and pseudo-data seen in figure 26. The top row of figure 30 shows the angular distributions related to calculating the diagonal elements of the SDM for leptonically and hadronically decaying W bosons, and the remaining two rows show the distributions related to the off-diagonal elements of the SDM for W^- and W^+ bosons.

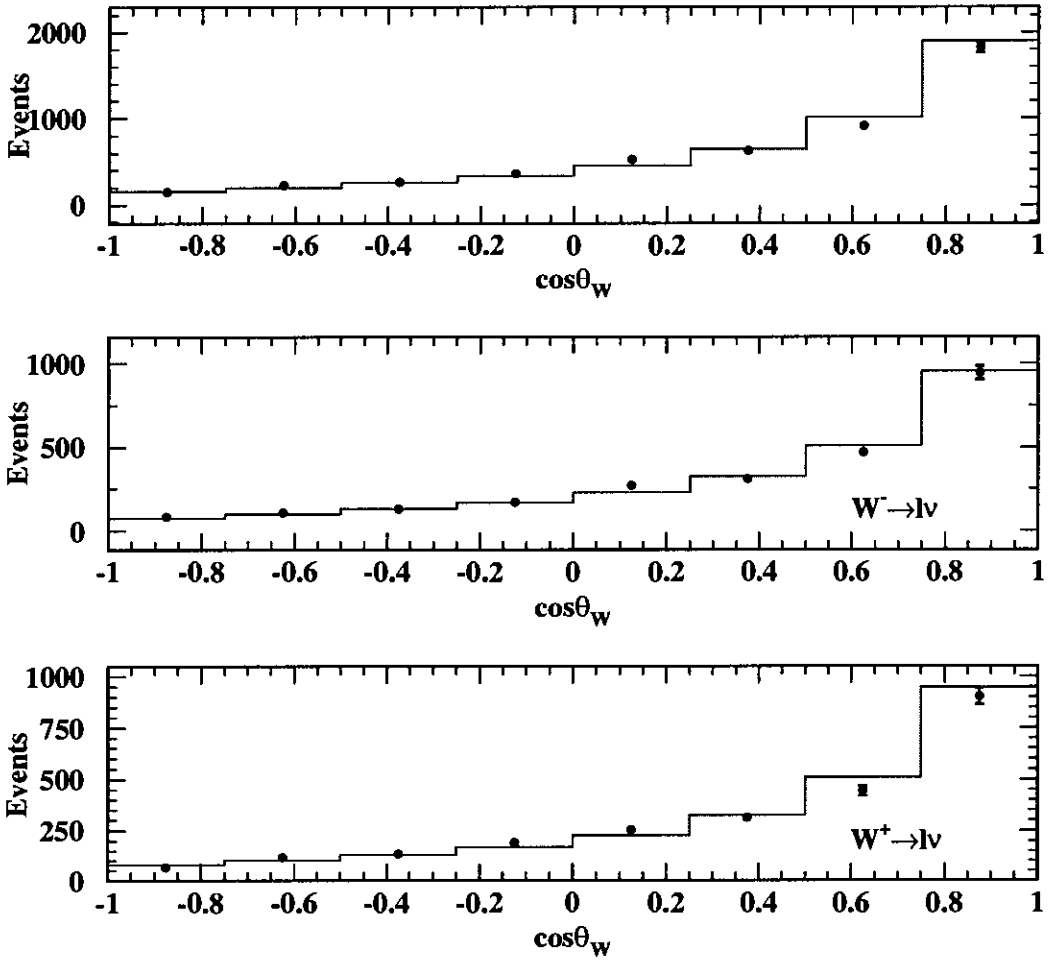

Figure 29: The measured $\cos\theta_W$ distributions obtained from the full data set summed over all centre-of-mass energies following the detector correction. The points show the measured values from the data and the histogram shows the prediction from SM generator-level MC samples. The topmost plot shows the distribution obtained using the full data set and the lower plots show the distributions obtained using only those events in which the W^- decayed leptonically or in which the W^+ decayed leptonically.

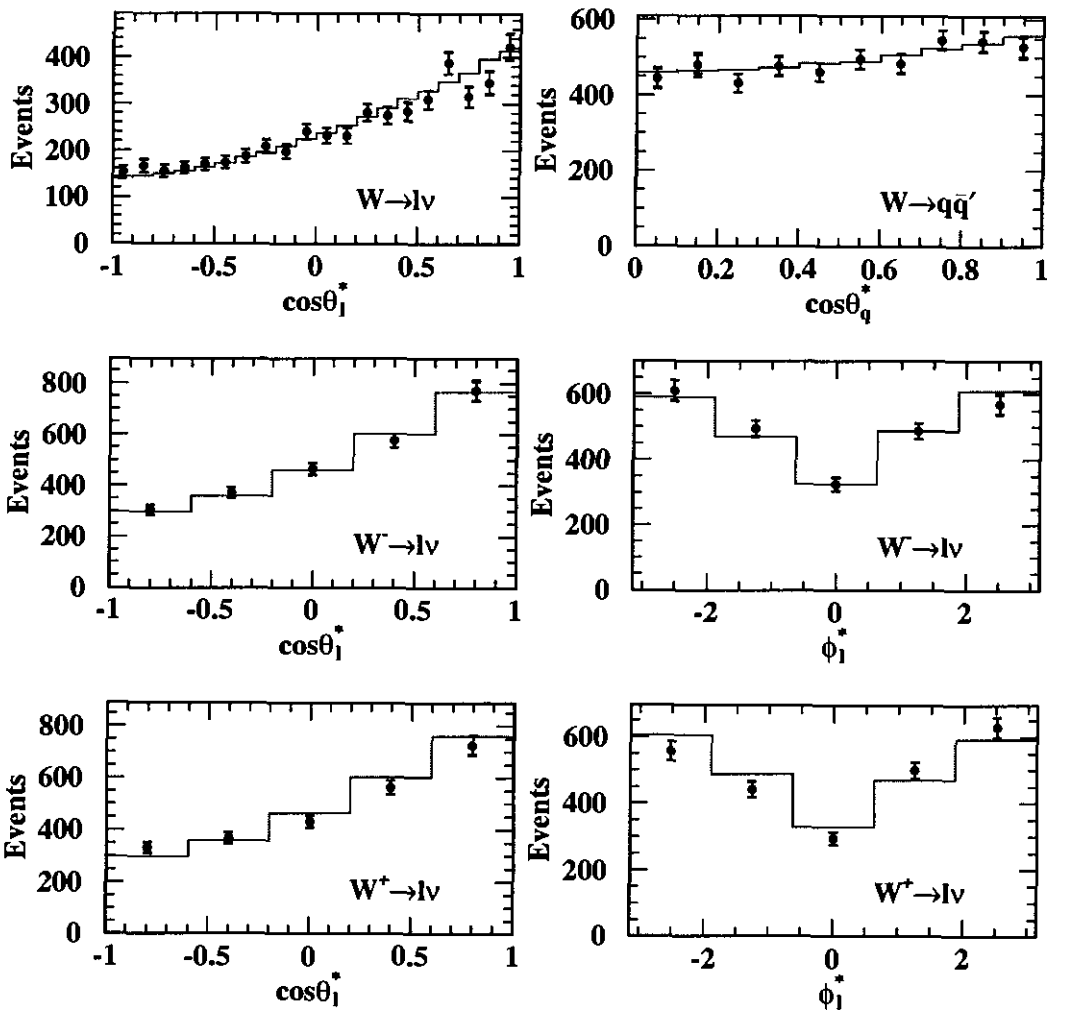

Figure 30: The angular distributions of the W decay products obtained from the full data set summed over all centre-of-mass energies following the detector correction. The points show the measured values from the data and the histogram shows the prediction from SM generator-level MC samples. The inner error bars show the statistical uncertainty on the data and the outer error bars show the total error including the systematic uncertainty (see section 7). The ϕ_ℓ^* distribution for the W^+ bosons has been offset by π radians so that it can be readily compared with the ϕ_ℓ^* distribution for the W^- bosons.

6.4.3 Measuring SDM distributions

The analyses of the diagonal and off-diagonal elements of the SDM were carried out separately. By construction, the diagonal elements of the single W SDM are invariant under CP transformations, and so the projection operator distributions from the W^- and W^+ bosons were combined prior to calculating the SDM without loss of any important information. However, as the distributions from the quarks were folded, the ρ_{++} and ρ_{--} elements could only be measured from leptonically decaying W bosons. For this reason the diagonal elements of the SDM were calculated separately for $W \to \ell\nu$ and $W \to q\bar{q}'$, and the two results for the ρ_{00} element were combined later in the analysis. The combination procedures are described in section 6.6.

As discussed in section 2.8, the off-diagonal elements of the SDM were sensitive to CP-violating effects, and so the off-diagonal elements of the W^- SDM and W^+ SDM were calculated separately. Moreover, because the folding of the quark distributions in the $W \to q\bar{q}'$ events forced the distributions to be CP-even, only the $W \to \ell\nu$ decay angles were used in this part of the analysis.

Using the same notation as in section 6.4.1, the statistical estimators for the SDM elements of equations (27) and (28) were given by,

$$\rho^k_{\tau\tau'} = \frac{1}{N_k} \sum_{i=1}^{n_k} \frac{p(\Omega_i)}{\epsilon(\Omega_i)} \Lambda_{\tau\tau'}(\Omega_i) \quad , \tag{78}$$

and hence were simply the mean value of the projection operators defined in section 2.6. An example of the Λ_{00} (see equation (38)) distributions obtained from the data without the detector correction (i.e. with $p(\Omega)/\epsilon(\Omega)$ replaced by 1 in equation (78)) is shown in figure 31. The figure shows histograms of the number of events reconstructed in each of 14 bins of Λ_{00}, where each histogram corresponds to events reconstructed in one of the eight bins in $\cos\theta_W$. The figure also contains a summary plot showing the mean values of each of the eight histograms (i.e. the estimators for ρ_{00}). The data and pseudo-data can be seen

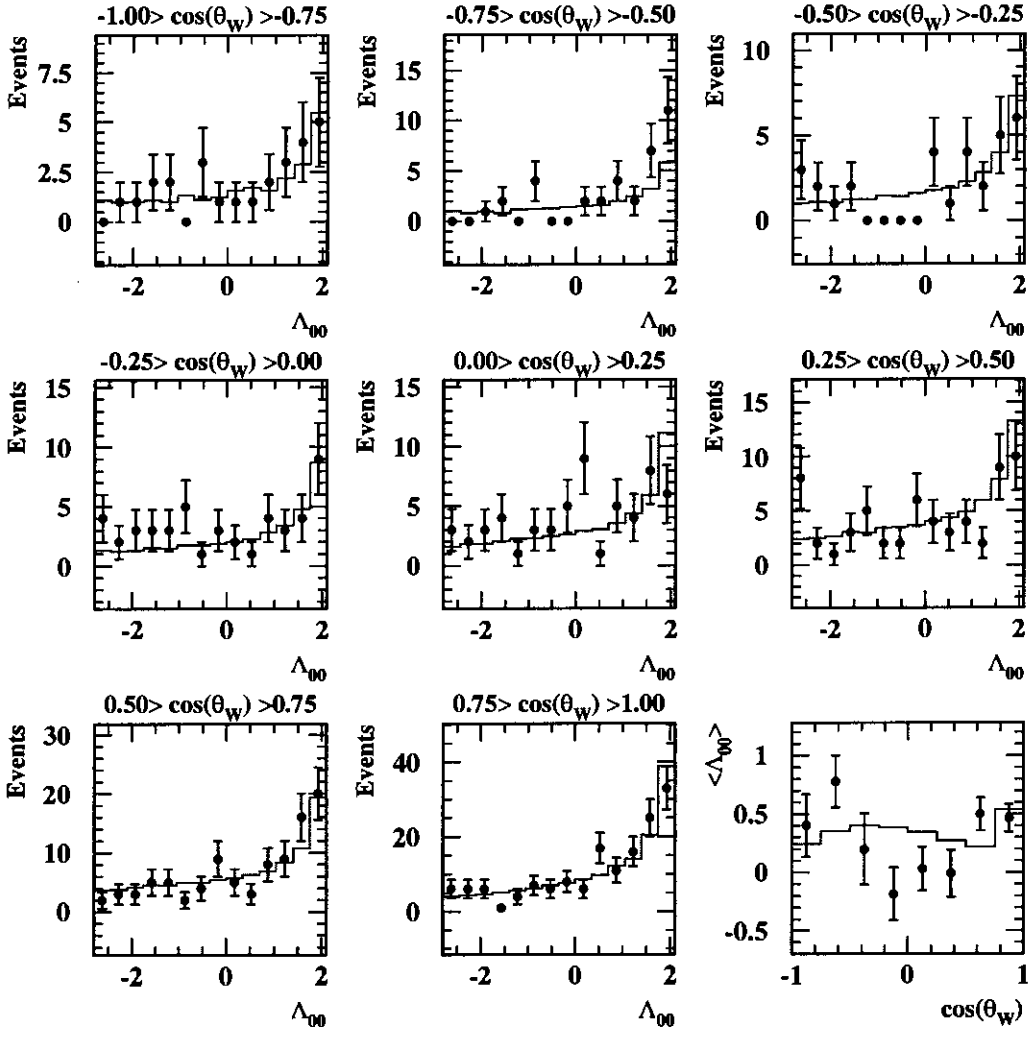

Figure 31: The distribution of the projection operator Λ_{00} obtained from the data and pseudo-data at a centre-of-mass energy of 196 GeV for leptonically decaying W bosons. The dots represent the data, the bars show the statistical uncertainty, and the histogram shows the pseudo-data prediction from SM MC samples. The first eight histograms show the distributions of Λ_{00} in each of the eight $\cos\theta_W$ bins. The last (bottom right-hand) histogram shows the mean values of Λ_{00} (i.e. ρ_{00}) in each $\cos\theta_W$ bin.

to agree within the statistical uncertainties on the data. An equivalent set of histograms in which the detector correction was applied is shown in figure 32, and the corrected data and generator-level MC can once again be seen to be in agreement.

The widths of the projection operator distributions were defined as,

$$s^{(\Lambda)}_{k\tau\tau'} = \sqrt{\frac{1}{N_k}\sum_{i=1}^{n_k}\frac{p(\Omega_i)}{\epsilon(\Omega_i)}\left(\Lambda_{\tau\tau'}(\Omega_i)\right)^2 - \left[\frac{1}{N_k}\sum_{i=1}^{n_k}\frac{p(\Omega_i)}{\epsilon(\Omega_i)}\left(\Lambda_{\tau\tau'}(\Omega_i)\right)\right]^2}, \quad (79)$$

and the errors on the estimators of the SDM elements were then derived from the central limit theorem:

$$s^{(\rho)}_{k\tau\tau'} = \frac{s^{(\Lambda)}_{k\tau\tau'}}{\sqrt{N_k^{(\mathrm{eff})}}}, \quad (80)$$

where the number of effective events in each bin, $N_k^{(\mathrm{eff})}$, was defined as,

$$N_k^{(\mathrm{eff})} = \frac{\left(\sum_{i=1}^{n_k}\frac{p(\Omega_i)}{\epsilon(\Omega_i)}\right)^2}{\sum_{i=1}^{n_k}\left(\frac{p(\Omega_i)}{\epsilon(\Omega_i)}\right)^2}. \quad (81)$$

In the results shown in section 8, the denominator of equation (80) was calculated from the data but the numerator was calculated from large MC samples. This avoided the difficulty of having to estimate the standard deviation from sparsely occupied data bins which would otherwise lead to the bias discussed in section 6.5.1.

The estimators for the diagonal elements of the SDM were not explicitly constrained to lie between 0 and 1, and hence could have unphysical values due to statistical fluctuations in the data. For example, the projection operator Λ_{00} can take any value in the range -3 to 2, and it is therefore possible for the estimator of ρ^k_{00} calculated using equation (78) to also take any value in this range, even though the true value of ρ^k_{00} as calculated from equation (36) is constrained to lie in the range 0 to 1.

By definition, the fraction of longitudinally polarised W bosons in each $\cos\theta_W$ bin was equal to the value of ρ^k_{00} in that bin, and the fraction of transversely polarised W bosons in

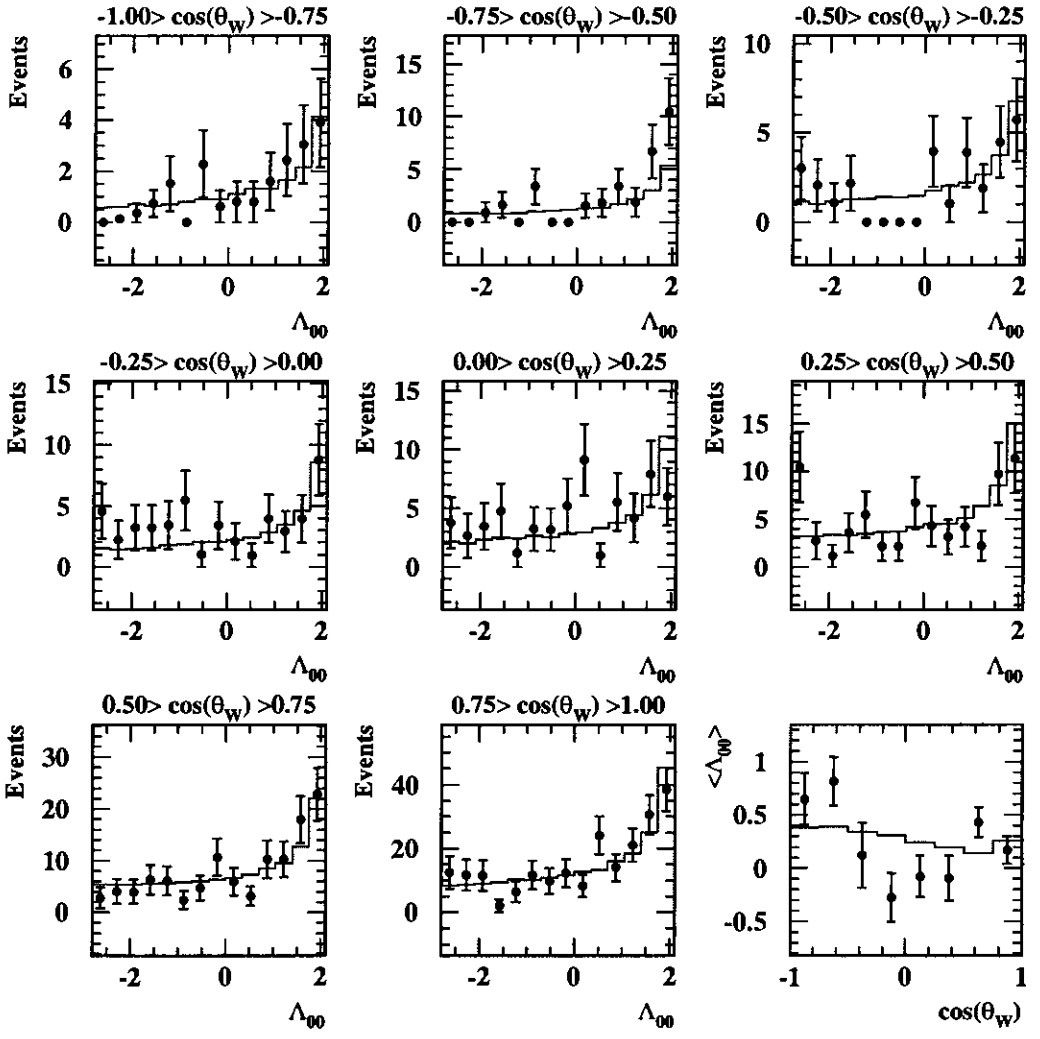

Figure 32: The distribution of the projection operator Λ_{00} obtained from the detector-corrected data and generator-level MC samples at a centre-of-mass energy of 196 GeV for leptonically decaying W bosons. The dots represent the data, the bars show the statistical uncertainty, and the histogram shows the prediction from generator-level SM MC samples. The first eight histograms show the distributions of Λ_{00} in each of the eight $\cos\theta_W$ bins. The last (bottom right-hand) histogram shows the mean values of Λ_{00} (i.e. ρ_{00}) in each $\cos\theta_W$ bin.

each $\cos\theta_W$ bin was equal to the sum of ρ^k_{++} and ρ^k_{--} in that bin. The estimator for the total fraction of longitudinal polarisation of the W bosons was therefore given by,

$$f_L = \frac{\sum_k \partial\sigma_k \rho^k_{00}}{\sum_k \partial\sigma_k}, \tag{82}$$

and the estimator for the fraction of transverse polarisation of the W bosons was given similarly by,

$$f_T = \frac{\sum_k \partial\sigma_k (\rho^k_{++} + \rho^k_{--})}{\sum_k \partial\sigma_k}. \tag{83}$$

In addition, the quantity $\partial\sigma_k \rho^k_{00}$ which appears in the numerator of equation (82) divided by the width of the $\cos\theta_W$ bin was used as an estimate of the average value of the longitudinally polarised differential cross-section of equation (43) in that $\cos\theta_W$ bin. Similarly, the quantity $\partial\sigma_k(\rho^k_{++} + \rho^k_{--})$ which appears in the numerator of equation (83) divided by the width of the $\cos\theta_W$ bin was used as an estimate of the average value of the transversely polarised differential cross-section of equation (44) in that $\cos\theta_W$ bin. The total unpolarised cross-section σ was simply estimated by the sum of the $\partial\sigma_k$ over all $\cos\theta_W$ bins. The uncertainties on f_L, f_T, the polarised cross-sections and unpolarised cross-sections were derived from the uncertainties on $\partial\sigma_k$ and the uncertainties on the SDM elements using the standard quadratic error-propagation formula.

The CP-odd observables defined in equations (54), (55) and (56) were estimated by,

$$\Delta^{\mathrm{CP}}_{\tau\tau'} = \sum_k \left(\partial\sigma^{\mathrm{W}^-}_k Im(\rho^{\mathrm{W}^-}_{\tau\tau'}) - \partial\sigma^{\mathrm{W}^+}_k Im(\rho^{\mathrm{W}^+}_{\tau\tau'}) \right) , \tag{84}$$

where $\partial\sigma^{\mathrm{W}^-}_k$ and $\partial\sigma^{\mathrm{W}^+}_k$ were the total unpolarised differential cross-sections measured in each bin of $\cos\theta_W$ for the leptonically decaying W^- and W^+ bosons respectively. Finally, the CP$\hat{\mathrm{T}}$-odd observables defined in equations (57), (58) and (59) were estimated analogously by,

$$\Delta^{\mathrm{CP}\hat{\mathrm{T}}}_{\tau\tau'} = \sum_k \left(\partial\sigma^{\mathrm{W}^-}_k Im(\rho^{\mathrm{W}^-}_{\tau\tau'}) + \partial\sigma^{\mathrm{W}^+}_k Im(\rho^{\mathrm{W}^+}_{\tau\tau'}) \right) . \tag{85}$$

6.5 Biases and bias correction

Section 6.4 defined estimators for the values of the SDM elements ($\rho_{TT'}$) and for their statistical uncertainties. This section describes the procedures used to ensure that any biases in the estimators were removed or shown to be negligible compared to the size of the statistical uncertainties. The expected statistical uncertainty on each SDM element when data from all eight nominal centre-of-mass energies and all eight $\cos\theta_W$ bins were combined was approximately 0.02.

Three sources of significant bias in the estimators were identified:

I Low data statistics in specific angular bins.

II The size of the angular bins into which the detector correction was divided.

III The diagonalised form of the detector correction.

6.5.1 Type I biases

Type I biases occurred when there were too few events in a given $\cos\theta_W$ bin for the central limit theorem to be applied to the projection operator distributions. Although the estimators of the SDM elements were not themselves affected, the estimators of their statistical uncertainties (see equations (79) and (80)) were systematically biased by an amount which depended on the values of the SDM elements. Toy-model simulations in Mathematica [78] were used to study this effect and found that the estimated value of the SDM element had an average pull of approximately 20% when only ten events were reconstructed in a bin which was reduced to an average pull of approximately 3% when one hundred events were reconstructed in a bin. Examples of the pull distributions for 1000 simulated data samples are shown in figure 33.

As mentioned in section 6.4, this bias was removed by using large MC samples to estimate the widths of the projection operator distributions. It is valid to use these SM

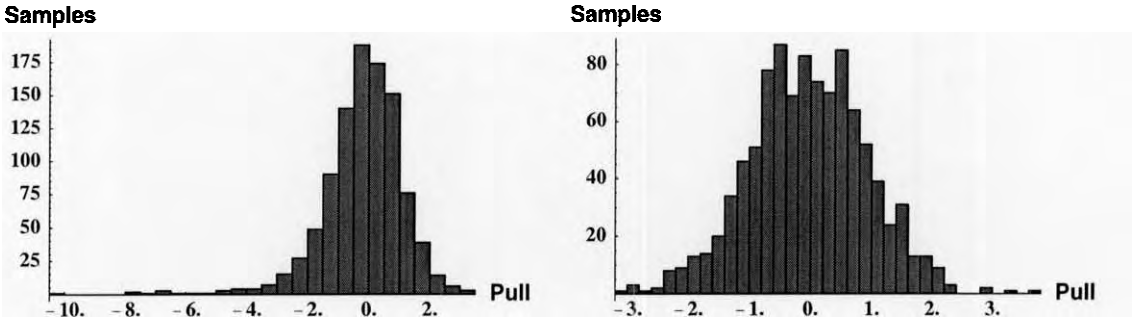

Figure 33: The pull distributions for the estimated value of ρ_{--} (the mean of the projection operator Λ_{--}). The distributions were generated from a Mathematica MC toy-model in which the mean and variance of the projection operator distribution was estimated from one thousand small samples of pseudo-data. The pseudo-data samples consisted of random instances of the angular distributions expected from the SM CC03 prediction for $e^+e^- \to W^+W^-$ events with a centre-of-mass energy of 196 GeV. In the figure on the left, each sample contained ten events. In the figure on the right, each sample contained one hundred events.

MC estimates only if the widths of the projection operator distributions do not sensitively depend on the values of the SDM elements themselves. The dependencies were calculated analytically and the widths were shown to vary by less than 5% when the SDM elements were varied by ± 0.1 of their SM values.

6.5.2 Type II biases

Type II biases occurred when the sizes of the angular bins used in forming the detector correction were comparable to the size of the features to which one or more of the projection operator functions was sensitive. In these cases, the detector correction distorted the projection operator distributions and hence biased the measured values of the SDM elements. This effect was examined by reconstructing large pseudo-data samples and applying the detector correction to them. The MC samples used in these tests were the same signal MC samples as were previously used to define the detector correction, and hence any differences between the resulting angular distributions and their associated generator-level distributions were attributed entirely to the binning bias. No background MC samples were used in the tests, and the purity correction was therefore set to unity.

Figures 34, 35 and 36 show the distributions obtained for the diagonal SDM elements and the real and imaginary parts of the off-diagonal SDM elements respectively. It can be seen that any bias in the diagonal elements of the SDM due to detector binning was negligible compared to the expected statistical uncertainty on the data. This was also true of any bias in the unpolarised differential cross-section. However, the deviations between the generator-level and reconstructed MC distributions for the off-diagonal elements of the SDM in some $\cos\theta_W$ bins were too large to be neglected. Particularly significant biases were present in the real part of ρ_{+-} in most $\cos\theta_W$ bins, and in the real parts of ρ_{+0} and ρ_{-0} for the rightmost $\cos\theta_W$ bin in the figures. Smaller biases were also found in the imaginary parts of ρ_{+0} and ρ_{-0} for some $\cos\theta_W$ bins.

A Mathematica toy model was used to study how the biases in the off-diagonal SDM elements changed as a function of the number of angular bins used to parameterise the detector correction in $\cos\theta_\ell^*$ and ϕ_ℓ^*. For example, figure 37 shows how the bias in ρ_{+-} was expected to vary with the number of angular bins in ϕ_ℓ^*.

Two methods were used to remove the type II bias from the off-diagonal elements

of the SDM. In the first method the default parameterisation of the detector correction was used with eight bins in $\cos\theta_W$, five bins in $\cos\theta^*_\ell$ and five bins in ϕ^*_ℓ. The bias was removed by simply subtracting the difference between the reconstructed detector-corrected pseudo-data and generator-level MC distributions from the reconstructed detector-corrected data distributions. The uncertainty on this bias correction was estimated by the statistical uncertainty on the MC values and was included in the systematic uncertainties discussed in section 7.

In the second method, an alternative parameterisation of the detector correction was used with eight bins in $\cos\theta_W$, twenty bins in ϕ^*_ℓ and no binning in $\cos\theta^*_\ell$. This method was only appropriate for the element ρ_{+-} as it is the only SDM element with no dependence on the polar angle θ^*_ℓ. As can be seen from figure 37, the expected bias in both the real and imaginary parts of ρ_{+-} are negligibly small for this parameterisation. The first method was used to correct the central values of the off-diagonal elements of the SDM presented in section 8, and the second method was used as a cross-check.

In addition to the bias, figure 34 shows a difference in the shape of the MC distributions of ρ_{00} for leptonically and hadronically decaying W bosons. These differences are due to the treatment of radiative effects within the KandY MC generator. Throughout this thesis, photons apparently radiated from the leptonically-decaying W bosons in the generator-level MC samples have not been recombined with their parent boson as there is no clear distinction between WSR and other radiative corrections. Within the MC generator, there are no equivalent photons radiated from hadronically decaying W bosons and therefore the quark and lepton angular distributions differ from one another slightly. However, the total fraction of longitudinally polarised W bosons calculated from leptonically decaying W bosons using the MC generator-level information is in good agreement with the total fraction calculated from hadronically decaying W bosons.

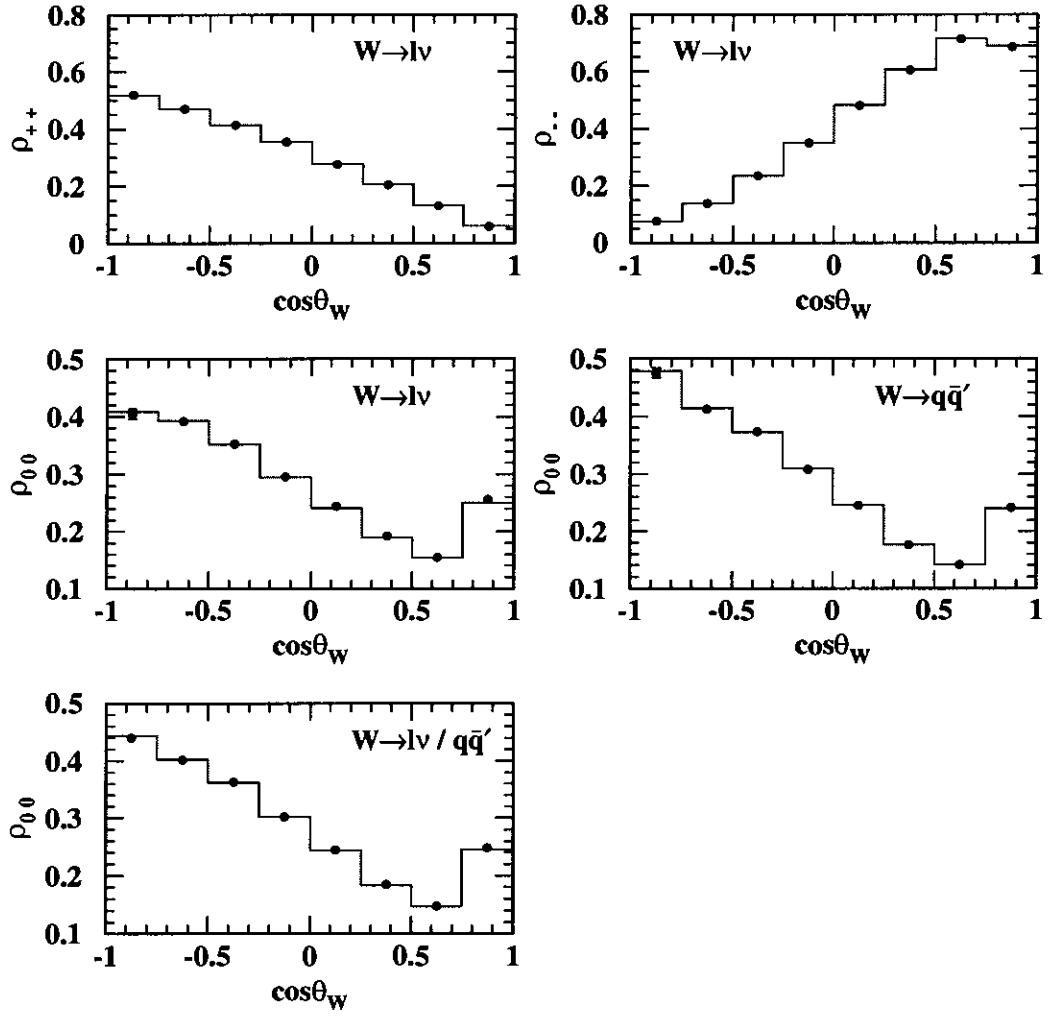

Figure 34: The diagonal elements of the SDM as functions of $\cos\theta_W$ as obtained from the KandY signal MC samples combined in a luminosity-weighted average (defined in section 6.6). The points show the pseudo-data after detector correction, and the (very small) error bars show the statistical uncertainties. The histogram shows the generator-level KandY MC prediction. The figures in the top row show ρ_{++} and ρ_{--} for leptonically decaying W bosons. The figures in the middle row show ρ_{00} for leptonically decaying W bosons and hadronically decaying W bosons separately. The figure in the bottom row shows ρ_{00} with the leptonic and hadronic decay modes combined. By construction, the diagonal elements of the SDM are related to each other by the normalisation condition $\rho_{++} + \rho_{--} + \rho_{00} = 1$, but have not been individually constrained to the physically-allowed region between zero and one.

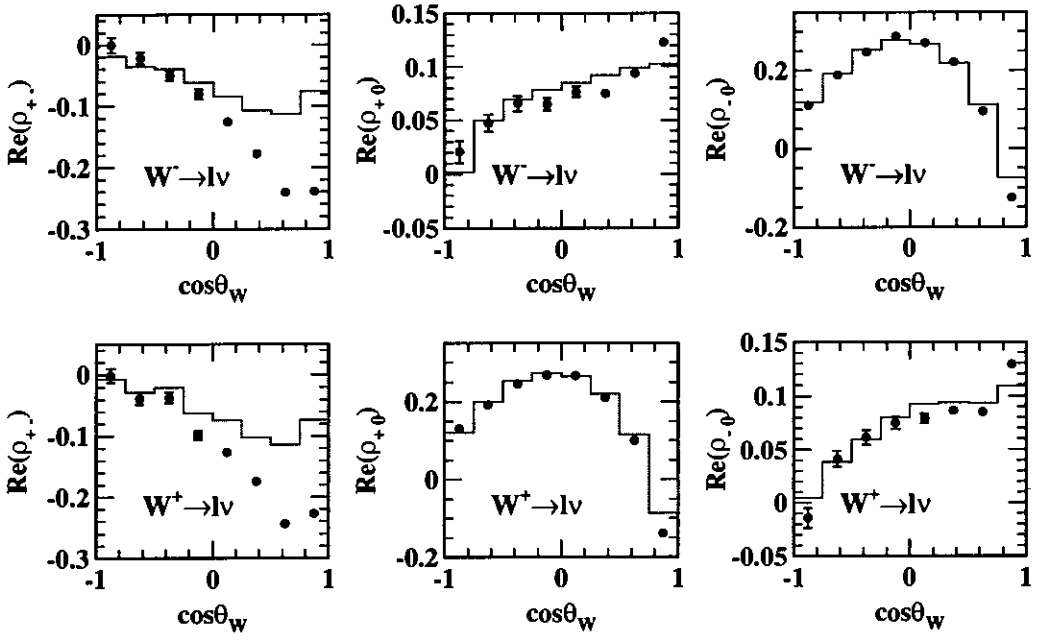

Figure 35: The real parts of the off-diagonal elements of the SDM as functions of $\cos\theta_W$ as obtained from the KandY signal MC samples combined in a luminosity-weighted average (defined in section 6.6). The points show the pseudo-data after detector correction, and the error bars show the statistical uncertainties. The histogram shows the generator-level KandY MC prediction. The top row shows the elements measured from W^- leptonic decays, and the bottom row shows the elements measured from W^+ leptonic decays.

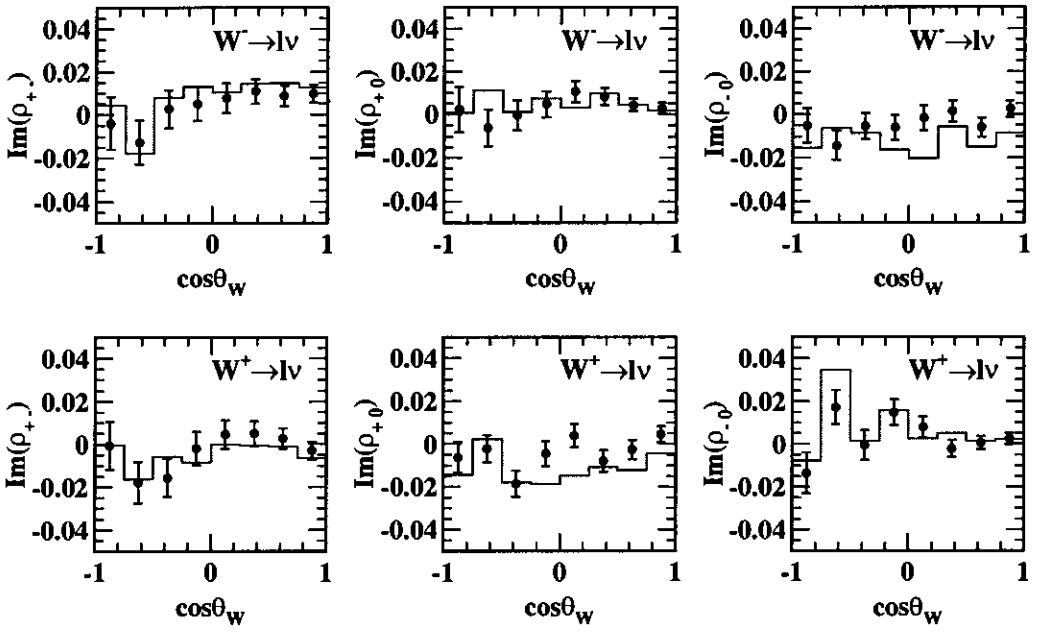

Figure 36: The imaginary parts of the off-diagonal elements of the SDM as functions of $\cos\theta_W$ as obtained from the KandY signal MC samples combined in a luminosity-weighted average (as defined in section 6.6). The points show the pseudo-data after detector correction, and the error bars show the statistical uncertainties. The histogram shows the generator-level KandY MC prediction. The top row shows the elements measured from W^- leptonic decays, and the bottom row shows the elements measured from W^+ leptonic decays.

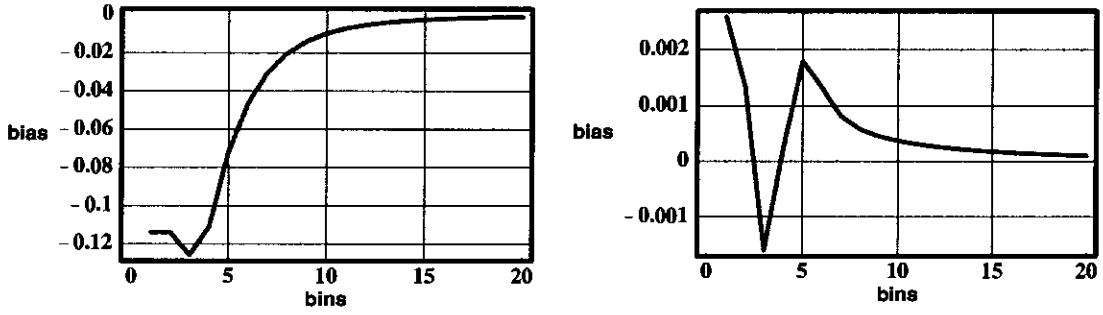

Figure 37: Dependence of the expected binning bias in ρ_{+-} on the number of ϕ_ℓ^* bins into which the detector correction was divided, as calculated from a toy-model in Mathematica based on the predictions of the SM MC samples. The left-hand plot shows the bias in the real part of the SDM element, and the right-hand plot shows the (typically much smaller) bias in the imaginary part.

6.5.3 Type III biases

By far the largest bias for the diagonal elements of the SDM were of type III. The bias was a natural consequence of the angular resolution of the reconstruction being greater than the width of the angular bins. This meant that the detector correction tended to bias the final result towards the Standard Model prediction (see appendix E). In order to correct for this effect in the W polarisation measurement, a bias correction was applied to each diagonal element of the SDM and to the $\cos\theta_W$ distribution.

For each $\cos\theta_W$ bin, the biases in the measured values of a quantity 'y' were calculated using the KandY MC samples of table 4 where 'y' was one of ρ_{00}, ρ_{--} or the number of reconstructed events in the bin, N. As for the type II bias described previously, the bias in 'y', b_y, was defined as the value of 'y' measured from the MC pseudo-data following application of the detector correction minus the value obtained from the generator-level distributions. The MC sample at each centre-of-mass energy was consecutively re-weighted so that the values of its generator-level SDM elements in a given $\cos\theta_W$ bin took each value on a grid of 40 equally-spaced values of ρ_{00} and 40 equally-spaced values of ρ_{--} distributed between 0 and 1. The value of ρ_{++} was calculated from the normalisation constraint $\rho_{++} + \rho_{--} + \rho_{00} = 1$, and the bias was only calculated for those points on the grid for which all three of the diagonal SDM elements lay in the physically-allowed region between 0 and 1.

The expected bias on the value of 'y' measured from the data was estimated by a weighted average of the biases calculated from the re-weighted MC samples. Equation (86) shows the estimated average bias on 'y' (denoted $\bar{b}^y$), where the sum is over all the re-weighted MC samples at a given centre-of-mass energy. The vector $\vec{\rho}_i$ represents the values of ρ_{00} and ρ_{--} for the i'th re-weighted MC sample. The vector $\vec{r}$ represents the values measured from the data sample with error matrix R. The bias in 'y' for the i'th re-weighted

MC sample is denoted by b_i^y.

$$\begin{aligned}\bar{b}^y(\vec{r},R) &= \sum_i \Pr(\vec{\rho}_i|\,\vec{r})\; b_i^y \\ &= \sum_i \frac{\Pr(\vec{r}|\,\vec{\rho}_i)\Pr(\vec{\rho}_i)}{\Pr(\vec{r})}\; b_i^y \\ &= \frac{1}{G}\sum_i \exp\left[\frac{1}{2}(\vec{r}-\vec{\rho}_i)\cdot R^{-1}\cdot(\vec{r}-\vec{\rho}_i)\right]\; b_i^y \end{aligned} \tag{86}$$

Equation 86 was derived from Bayes' theorem. In the last line of the derivation a uniform prior probability distribution for $\vec{\rho}_i$ was assumed and the conditional probability $\Pr(\vec{r}|\,\vec{\rho}_i)$ was approximated by a Gaussian distribution. The normalisation constant, G was defined by,

$$G = \sum_i \exp\left[\frac{1}{2}(\vec{r}-\vec{\rho}_i)\cdot R^{-1}\cdot(\vec{r}-\vec{\rho}_i)\right]. \tag{87}$$

The values of $\bar{b}^y$ for elements of the SDM typically had a magnitude less than 0.1.

The bias in the data [18] was corrected for by subtracting the values of $\bar{b}^y$ from the measured values of 'y'. The uncertainty on this bias correction was estimated by the standard deviation of the biases, s_b, where,

$$s_b^2 = \sum_i \Pr(\vec{\rho}_i|\,\vec{r})\,(b_i^y)^2 - (\bar{b}^y)^2\,. \tag{88}$$

The error estimates for the SDM elements were typically smaller than 0.2. As the statistical uncertainties on the bias corrections and on the values of 'y' were fully correlated they were added to one another linearly to give the total statistical uncertainties quoted in the results in section 8.

Because the biases, b_i^y, varied significantly over the range of measured values of $\vec{r}$ spanned by the statistical errors on the data, the uncertainty on the correction was often larger than the correction itself. As an example, the dependence of the bias in the measured

[18] The bias on the value of ρ_{++} measured from the data was calculated from the estimated biases on the measured values of ρ_{00} and ρ_{--} and the normalisation constraint.

value of ρ_{00} with $1.0 < \cos\theta_W < 0.8$ at 196 GeV on the generator-level value of ρ_{00} is shown in figure 38. For example, it can be seen from the lefthand plot that if the true value of ρ_{00} in the $\cos\theta_W$ bin is actually 0.6, and a measurement is made with a detector correction formed from SM MC, then the result is expected to be biased such that it is approximately 0.1 too low (i.e. the result will tend to 0.5 in the limit of high statistics).

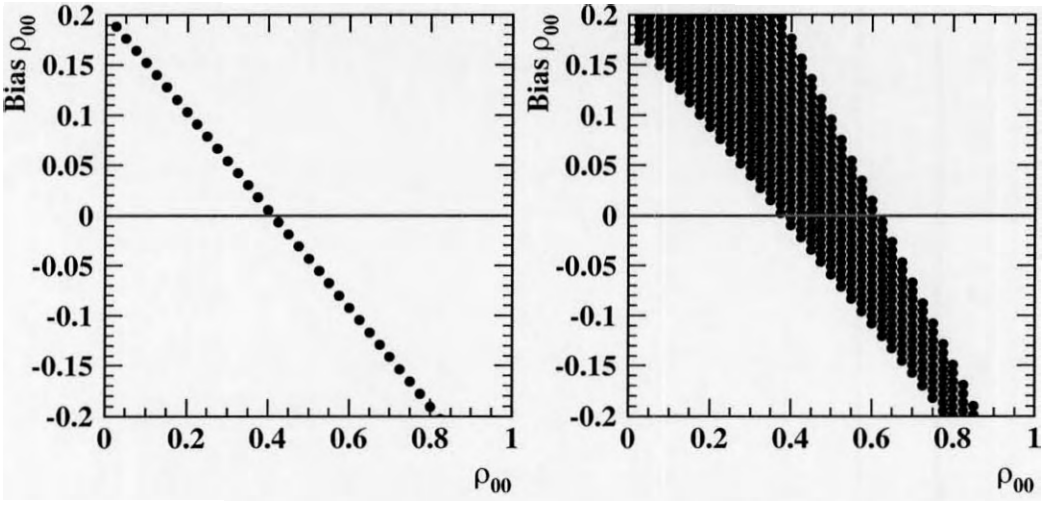

Figure 38: Dependence of the type III bias in the measured value of ρ_{00} on the true value of ρ_{00}. The values were evaluated using MC events with a nominal centre-of-mass energy of 196 GeV and with the generated value of $\cos\theta_W$ in the range $1.0 < \cos\theta_W < 0.8$. In the figure on the left, the true value of ρ_{--} was fixed at its SM value. In the figure on the right, ρ_{--} was allowed to vary within the range 0 to 1. It can be seen that the bias is zero when the true values of ρ_{00} and ρ_{--} coincide with the SM prediction.

The shifts in the measured fraction of longitudinally polarised W bosons, f_L, (see equation (82)) which result from applying the calculated bias corrections to the SDM elements and to the differential cross-section are shown in table 10. The uncertainty in each shift was evaluated by smearing all the individual bias corrections by their uncertainties. Specifically, a pseudo-random number was added to each bias correction, where the number was drawn from a Gaussian distribution with a mean of zero and a width set equal to the uncertainty

on the bias correction. The smearing was repeated six times in total and the standard deviation of the resulting six values of f_L was assigned as the uncertainty on the shift in f_L. At each centre-of-mass energy and for both decay modes, the shift in f_L due to the bias corrections is smaller than the statistical uncertainty on f_L (c.f. table 18). Tests with MC samples were used to show that this bias correction procedure results in unbiased estimators which give Gaussian pull distributions as illustrated in figure 39. The magnitudes of the

	Bias Correction (%)	
$\sqrt{s}$ (GeV)	$W \to \ell\nu$	$W \to q\bar{q}'$
183	-0.8 ± 1.7	3.0 ± 1.9
189	-1.1 ± 1.1	-0.8 ± 1.2
192	3.7 ± 2.4	2.0 ± 1.9
196	-0.6 ± 1.3	-0.5 ± 1.4
200	1.9 ± 1.0	2.7 ± 2.2
202	-0.1 ± 1.6	2.5 ± 2.4
205	0.6 ± 1.5	2.6 ± 2.2
207	-1.0 ± 1.1	-0.3 ± 1.6

Table 10: Absolute shifts in the percentage of longitudinally polarised W bosons due to the bias corrections applied at each centre-of-mass energy.

biases in the measured values of the off-diagonal elements of the SDM were also investigated and shown to be typically of the order 0.01.

This bias correction technique was designed to be widely applicable to any bias regardless of the form of the bias' dependence on the values being measured. A variety of different detector corrections were investigated in the course of the development of the analysis, but none were seen to substantially reduce the size of the biases on the SDM elements.

The type III bias correction was not extended to include the off-diagonal elements of the SDM as the computer processing time required was prohibitive. To compensate, the systematic uncertainties on these elements were increased as described in section 7.

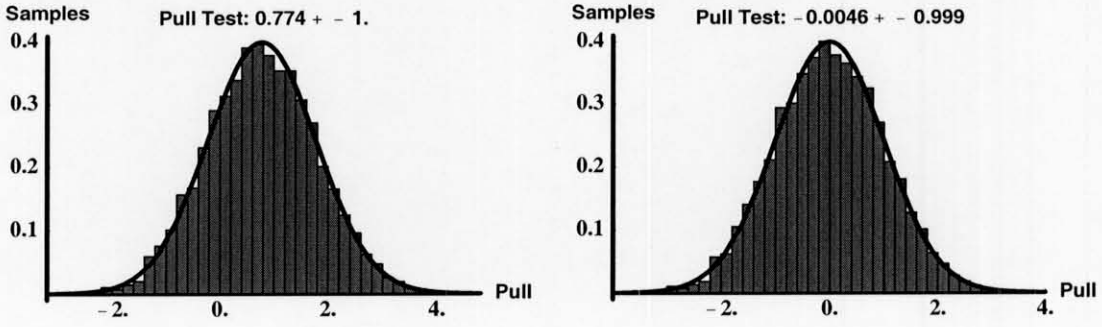

Figure 39: The figure on the left shows a Mathematica toy-model prediction of the pull distribution expected for the measurement of a generic SDM element. The figure on the right shows the pull distribution for the same SDM element after the bias correction shown in equation (86) was applied. The legend above the histogram shows the mean and standard deviation of the pull distribution. The solid lines show the Gaussian distributions which best fit the pseudo-data in each case.

6.6 Combining results

6.6.1 Decay modes

Where appropriate, the measurements of a quantity (generically denoted y in the equation below) calculated from the $W \to q\bar{q}'$ and $W \to \ell\nu$ decay modes were combined using the Best Linear Unbiased Estimator (BLUE) method [79]. This method is suited to combining measurements of the same quantity from different decay modes or different experiments were there may be correlations between the individual measurements. The estimator is simply the weighted-average of the individual results:

$$\hat{y} = \vec{y}^T.\vec{w} , \tag{89}$$

where $\vec{y}$ is the vector of measurements and $\vec{w}$ is the vector of weights. Each component of the weight vector is defined as,

$$w_i = \frac{\sum_j Y_{ij}^{-1}}{\sum_{i,j} Y_{ij}^{-1}} , \tag{90}$$

where Y is the full covariance matrix for the measurements of $\vec{y}$ including both the statistical and systematic uncertainties. The correlations between the statistical uncertainties for the two decay modes were measured from the data at each centre-of-mass energy and found to have a magnitude of less than 10% in each case. Correlations between the systematic uncertainties on different measured quantities are discussed in section 7.

The uncertainty on $\hat{y}$ due to any given error source is given by,

$$s_{\hat{y}} = \vec{w}^T.Y'.\vec{w} , \tag{91}$$

where Y' is the covariance matrix corresponding to the error source under consideration. If Y' is set equal to the full covariance matrix, Y, then $s_{\hat{y}}$ is an estimator of the total uncertainty on $\hat{y}$.

6.6.2 Centre of mass energies

As the values of the elements of the SDM depended on the centre-of-mass energy of the $e^+e^- \rightarrow W^+W^-$ collisions, the measurements made at each of the eight nominal centre-of-mass energies were combined with one another in a luminosity-weighted average rather than with the BLUE technique [19]. The form of the average and the uncertainty on the average is the same as shown previously in equations (89) and (91), where the weights are replaced by,

$$w_i = \frac{\mathcal{L}_i}{\sum_i \mathcal{L}_i} , \tag{92}$$

and the luminosities, $\mathcal{L}$, can be found in table 3.

[19] In practice, the differences between the values obtained using the BLUE technique and the values obtained using the luminosity-weighted average were negligibly small.

7 Sources of systematic uncertainty

There were uncertainties in the shape of the MC angular distributions due to the measurement errors on the parameters in the SM (such as the mass of the W boson), to the incomplete description of non-perturbative physics effects in MC generators, and to the simplifying assumptions made in modelling the detector response. This leads to uncertainties in the detector corrections applied to the data and gives systematic errors on the final results. For each source of systematic uncertainty, the full analysis of the data was repeated using a range of different MC samples (or a single MC sample re-weighted appropriately) to form the detector correction. Unless otherwise stated, the full difference between the results obtained using each of the detector corrections in turn was assigned as the error estimate for the error source being considered. The error estimates were considered to be symmetric with respect to the central values such that a measurement of a quantity y with an error estimate δ corresponded to the range of values $y \pm \delta$.

The total systematic error on each measured quantity was calculated by summing the errors associated with each source of uncertainty in quadrature. The error sources are listed on pages 126 to 131 and details of the additional MC runs used in evaluating the systematic uncertainties are shown in table 11. As representative examples, the contributions of each systematic error source to the total uncertainty on the values of ρ_{00} and on the values of the real and imaginary parts of ρ_{+-} in each $\cos\theta_{\mathrm{W}}$ bin are shown in tables 12 to 15. Additionally, the systematic uncertainties in the fraction of longitudinally polarised W bosons, f_L, at each centre-of-mass energy are shown in table 16, and the contributions to the total systematic error on the luminosity-weighted average fraction of longitudinally polarised W bosons is shown in table 17. The systematic uncertainty tended to be largest for low values of $\cos\theta_{\mathrm{W}}$ where the MC statistics were lowest and the amount of background contamination comparatively high.

There are in principle four sets of correlations that have to be known before the systematic (or statistical) uncertainties on the measured SDM elements can be combined with one another: the correlation between decay modes ($W \to \ell\nu$ and $W \to q\bar{q}'$), the correlation between centre-of-mass energies, the correlation between values in different $\cos\theta_W$ bins, and the correlations among the SDM elements. There are apriori assumed to be no correlations among the different systematic uncertainty sources themselves or between any systematic source and the statistical uncertainty on the data. Nevertheless, the complete correlation matrix for any given error source is prohibitively large (1280 by 1280) in the most general case. Fortunately, the total errors on the results presented in this thesis are dominated by their statistical uncertainties, and even the fluctuation in the total error caused by varying all the correlations of all the systematic uncertainties between 0% and 100% simultaneously was typically small, e.g. fluctuations in the systematic uncertainty on f_L were less than 15% of the total uncertainty on f_L.

In the results shown in the next section, each source of systematic uncertainty was assumed to be 100% correlated between centre-of-mass energies and between decay modes unless the source was obviously dependent on statistical fluctuations in the MC samples, in which case the systematic uncertainties were assumed to be 0% correlated. Tables 12 to 17 indicate which sources were considered correlated and which were not. Each source of systematic uncertainty was additionally assumed to be 100% correlated between the W^- and W^+ SDMs, as identical detector corrections were used to evaluate the two matrices in all cases. As none of the results in this thesis required different elements of the same SDM to be combined, the correlations between the elements need not be considered here. To avoid having to consider the effects of correlations between the values of ρ_{00} in different $\cos\theta_W$ bins, the total fraction of longitudinally polarised W bosons was calculated each time the analysis code was run so that no explicit error-propagation was required to evaluate its uncertainties. In all other cases in which results from different $\cos\theta_W$ bins were combined,

the systematic uncertainties were conservatively assumed to be 100% correlated.

1. The effects of the uncertainties in the modelling of the background MC samples were evaluated by re-weighting the contribution of the two-photon and four-fermion backgrounds one at a time. The two-photon samples were weighted by a factor of two and subsequently by a factor of a half, and the contribution from the four-fermion background samples were weighted by a factor of 1.2. These factors were obtained by the OPAL TGC group for use in the CP-conserving TGC parameter measurements [66] using comparisons of the data and pseudo-data cross-sections described in [64]. In addition, the effect of the uncertainty in the modelling of $Z^0/\gamma \to q\bar{q}$ events was evaluated by comparing MC samples hadronised by JETSET to samples hadronised by HERWIG. The hadronisation of both the $Z^0/\gamma \to q\bar{q}$ background and the $q\bar{q}'\ell\nu$ signal events (see item 3) gave large contributions to the total systematic uncertainties of all the SDM elements and the $\cos\theta_W$ distribution.

2. Unlike the MC generators used in the previous SDM analyses published by the OPAL collaboration [23, 24], the KandY MC generator contains a full treatment of electroweak radiative corrections up to $\mathcal{O}(\alpha)$ in the double-pole approximation. The double-pole approximation considers only radiation from those Feynman diagrams which contain two W bosons (and are therefore 'doubly-resonant'). The contribution of the radiation originating from other diagrams is suppressed by at least a factor $\mathcal{O}(\frac{\Gamma_W}{m_W})$. The WW cross-section predicted by KandY is approximately 2% less than that predicted by less-complete semi-analytical calculations such as those of the GENTLE software package [80], and the shapes of the $\cos\theta_W$ distributions from the different generators vary by approximately 0.5%. The effects of the missing higher-order corrections above $\mathcal{O}(\alpha)$ were estimated conservatively by re-weighting the KandY MC samples to remove the $\mathcal{O}(\alpha)$ next-to-leading electroweak corrections and the screened

Coulomb correction completely. The uncertainty in the implementation of initial state radiation effects within KandY is discussed separately in item 5 of this list.

3. The error due to uncertainty in the modelling of the jet hadronisation was estimated by contrasting the results obtained when forming the detector correction from WW MC samples generated by KORALW and hadronised using one of JETSET, HERWIG and ARIADNE which implement the 'string', 'cluster' and 'colour dipole' models of hadronisation respectively. The KORALW WW MC samples were produced at 189 GeV, 200 GeV and 206 GeV only. The systematic errors at all eight nominal centre-of-mass energies were then interpolated from these three energy points: i.e. the uncertainty evaluated at 189 GeV was applied to the data results obtained at 183 GeV, 189 GeV and 192 GeV, the uncertainty evaluated at 200 GeV was applied to the results obtained at 196 GeV, 200 GeV and 202 GeV, and the uncertainty obtained at 206 GeV was applied to the results obtained at 205 GeV and 207 GeV. In addition to the WW signal MC samples, KORALW was also used to generate four-fermion MC samples (see table 11 for details). The four-fermion background was then approximated by combining the WW and four-fermion samples but giving all events in the WW samples a weight of minus one. Interference terms between the CC03 and other Feynman diagrams were therefore treated as background. As this treatment differs from that applied to the KandY samples used in the main analysis, the results from the KORALW samples were compared only to one another. This source of systematic uncertainty gave the predominant contribution to the total systematic uncertainty on most of the measured quantities in most bins of $\cos\theta_W$.

4. The W mass obtained from Tevatron and UA2 data is 80.452 ± 0.062 GeV [1]. The systematic error due to the difference between this mass and the W mass used in generating the KandY MC samples (80.33 GeV) was estimated by re-weighting the

KandY samples using the EXCALIBUR MC generator. EXCALIBUR contains a convenient interface for calculating the differential cross-section ($\frac{d^5\sigma}{d\Omega}$) for four-fermion production as a function of the generator-level four-momenta and flavours of the fermions. The weight applied to each KandY event was given by the ratio of the EXCALIBUR differential cross-section calculated for the event assuming a W mass of 80.454 GeV, divided by the differential cross-section calculated assuming a W mass of 80.33 GeV. The procedure was then repeated with the mass of the W boson set to 80.391 GeV and 80.514 GeV sequentially when calculating the numerator of the ratio. The LEP measurements of the W mass were not themselves used in evaluating the systematic uncertainty, as the published analyses implicitly assumed that the W pairs were produced via the Standard Model mechanism.

5. The KandY MC generator includes an $\mathcal{O}(\alpha^3)$ treatment of initial state radiation (ISR). A conservative estimate of the effect of missing higher order diagrams was obtained by re-weighting the KandY signal MC samples to use a less-complete $\mathcal{O}(\alpha)$ treatment. The weights required were provided by the KandY MC generator package.

6. As explained in section 6.3.6, the modelling of the OPAL detector's response to hadrons and leptons in GOPAL was compared to the response seen in $Z^0/\gamma \to q\bar{q}$, $Z^0/\gamma \to e^+e^-$ and $Z^0/\gamma \to \mu^+\mu^-$ calibration data collected at intervals during the period 1996 to 2000 with centre-of-mass energies close to the Z^0 mass. As the energies of the jet and leptons produced in the calibration data were close to those of the jets and leptons produced in the WW data (approximately 45 GeV), any differences between the GOPAL simulation of the OPAL detector and the detector response as measured from the calibration data were assumed to be also present in the WW data. The three aspects of the detector modelling considered in this analysis were:

   - The absolute energy of the reconstructed jets or leptons as a function of their

polar angle in the detector.

- The width of the resolution of the reconstructed energy of the jet or lepton as functions of their polar angle in the detector.
- The widths of the angular resolution of the reconstructed polar and azimuthal angles of the jet or lepton as functions of the angles.

No separate analyses of τ-leptons were carried out, as these were treated as low-multiplicity jets.

The angles and energies of the reconstructed jets and charged leptons from the pseudo-data samples used in the SDM analysis were subsequently 'smeared' to compensate for the small differences observed between the calibration data and corresponding Z^0 pseudo-data. The smearing was achieved by scaling the central values and errors of the reconstructed momentum vectors prior to processing them with the kinematic fit procedure described in section 6.3.6. The error associated with the uncertainty on this smearing was evaluated by varying the smearing within its assigned statistical errors. A fuller account of this procedure can be found in [73, 81, 82].

7. Some areas of the W boson production and decay phase-space were sparsely populated by MC events. The effect of the limited MC statistics was evaluated by smearing the efficiency-like scaling factor in each angular bin by its statistical error in that bin (by adding a pseudo-random number from a Gaussian distribution with a mean of zero and a width set equal to the Poisson statistical error for that bin). This process was repeated five times using different random number 'seeds' to ensure a different smearing in each bin each time. The error due to the statistical uncertainties was then estimated by the standard deviation of the values obtained from the five smeared samples and the central un-smeared sample. The whole procedure was repeated for the purity correction.

8. As described in section 6.5, biases of type II were negligible for the diagonal elements of the SDM but were large in some $\cos\theta_W$ bins for the off-diagonal elements of the SDM. The biases were estimated by carrying out the full analysis using KandY pseudo-data samples in place of real data and then comparing the reconstructed values of the SDM elements to their MC generator-level values. These expected biases were subtracted from the values of the SDM elements measured from the data, and the systematic uncertainty on each bias correction was estimated by the statistical error on the corresponding MC generator-level values.

   Variations were observed in the bias estimates calculated from differently re-weighted MC samples. Specifically, the MC samples were re-weighted such that any asymmetry in the pseudo-data ϕ_ℓ^* distribution (about the point $\phi_\ell^* = 0$) was varied within a factor of two of the value found from the unweighted MC samples. However, the magnitude of the shifts in the biases was negligible compared to the size of the statistical error on the MC generator-level values, and this effect was therefore not included in the systematic uncertainty.

9. Section 6.5 explains how biases of type III were removed from the diagonal elements of the SDM and the $\cos\theta_W$ distribution using a probabilistic correction, where the uncertainty of the correction was included in the statistical errors on the measured quantities. However, such biases in the off-diagonal elements of the SDM were not explicitly removed. Instead the KandY MC samples used to calculate the detector correction were re-weighted using a simple tree-level CC03 calculation to simulate anomalous values of the CP-violating TGC parameters ($\tilde{\kappa}_Z$, $\tilde{\lambda}_Z$ and g_Z^4) which alter the shape of the ϕ_f^* and $\phi_{\bar{f}}^*$ angular distributions. The weight of a given event was defined as the ratio of the differential cross-section ($\frac{d^5\sigma}{d\Omega}$) for producing an equivalent W-pair event (one which gave the same values of the angles Ω as the four-fermion

KandY event being weighted) assuming anomalous values of the TGC parameters, divided by the differential cross-section assuming SM values of the TGC couplings. These weights were only applied to the signal events. Each of the TGC parameters was varied sequentially by plus and minus one standard deviation of its value as measured in the OPAL 189 GeV analysis [23].

Systematic Uncertainty	Generator & Process	Nominal Energy (GeV)					
		183		189		192	
		Run	$\mathcal{L}$	Run	$\mathcal{L}$	Run	$\mathcal{L}$
1	HERWIG $Z^0/\gamma \to q\bar{q}$	5168	2.29	5169/5170	2.52/2.50	5171	2.64
3	KORALW (JETSET) WW	-	-	11101	60.34	-	-
3	KORALW (HERWIG) WW	-	-	12422	60.34	-	-
3	KORALW (ARIADNE)WW	-	-	12513	60.34	-	-
3	KORALW $q\bar{q}q\bar{q}$	-	-	8636	20.00	-	-
3	KORALW $q\bar{q}\ell^+\ell^-$	-	-	8637	20.00	-	-
3	KORALW qqe^+e^-	-	-	7849	5.00	-	-

Systematic Uncertainty	Generator & Process	Nominal Energy (GeV)					
		196		200		202	
		Run	$\mathcal{L}$	Run	$\mathcal{L}$	Run	$\mathcal{L}$
1	HERWIG $Z^0/\gamma \to q\bar{q}$	5172	2.78	5173	3.51	5174	3.00
3	KORALW (JETSET) WW	-	-	11111	57.51	-	-
3	KORALW (HERWIG) WW	-	-	12014	57.51	-	-
3	KORALW (ARIADNE)WW	-	-	11999	57.51	-	-
3	KORALW $q\bar{q}q\bar{q}$	-	-	9207	20.00	-	-
3	KORALW $q\bar{q}\ell^+\ell^-$	-	-	9208	20.00	-	-
3	KORALW qqe^+e^-	-	-	9318	5.00	-	-

Systematic Uncertainty	Generator & Process	Nominal Energy (GeV)					
		205		206		207	
		Run	$\mathcal{L}$	Run	$\mathcal{L}$	Run	$\mathcal{L}$
1	HERWIG $Z^0/\gamma \to q\bar{q}$	5176	3.07	-	-	5179	6.30
3	KORALW (JETSET) WW	-	-	11121	57.08	-	-
3	KORALW (HERWIG) WW	-	-	12428	57.08	-	-
3	KORALW (ARIADNE)WW	-	-	12514	57.08	-	-
3	KORALW $q\bar{q}q\bar{q}$	-	-	10107	20.00	-	-
3	KORALW $q\bar{q}\ell^+\ell^-$	-	-	10106	20.00	-	-
3	KORALW qqe^+e^-	-	-	10075	5.00	-	-

Table 11: The identifying run numbers and integrated luminosities measured in units of inverse femtobarns of the Monte Carlo samples used to measure the systematic uncertainties in this analysis. The number in the left-hand column refers to the list of systematic error sources in the main text.

	$\cos\theta_W$ bin								
	1	2	3	4	5	6	7	8	Total
Two-photon MC†	0.012	0.005	0.002	0.005	0.001	0.001	0.001	0.003	0.031
$Z^0/\gamma \to q\bar{q}$ MC†	0.013	0.012	0.011	0.009	0.005	0.006	0.003	0.004	0.063
Four-fermion MC†	0.003	0.003	0.006	0.003	0.002	0.002	0.002	0.002	0.023
$\mathcal{O}(\alpha)$ radiation†	0.003	0.003	0.005	0.005	0.005	0.006	0.003	0.005	0.034
Hadronisation†	0.017	0.019	0.008	0.012	0.015	0.010	0.006	0.012	0.100
$m_W{}^\dagger$	0.004	0.003	0.003	0.003	0.002	0.003	0.003	0.002	0.023
ISR†	0.000	0.000	0.000	0.000	0.000	0.000	0.000	0.000	0.000
Jet/ℓ angular res.	0.000	0.000	0.000	0.000	0.001	0.001	0.001	0.004	0.008
Jet/ℓ energy res.	0.001	0.001	0.001	0.001	0.001	0.001	0.001	0.001	0.008
Jet/ℓ energy scale	0.001	0.001	0.002	0.002	0.001	0.003	0.002	0.001	0.013
Efficiency statistics	0.017	0.011	0.010	0.013	0.006	0.009	0.003	0.003	0.073
Purity statistics	0.014	0.007	0.006	0.008	0.004	0.004	0.001	0.002	0.047
Total	0.034	0.027	0.020	0.023	0.019	0.017	0.009	0.015	0.164

Table 12: The systematic uncertainties for the luminosity-weighted average of ρ_{00} for the $W \to \ell\nu$ decay mode. Error sources marked by a † were considered to be 100% correlated between the $W \to \ell\nu$ and $W \to q\bar{q}'$ decay modes and also among the centre-of-mass energies. All other sources were assumed to be completely uncorrelated. The bottommost row shows the sum in quadrature of the uncertainties associated with each individual error source, and the rightmost column shows the linear sum of the uncertainties in each individual $\cos\theta_W$ bin.

	$\cos\theta_W$ bin								
	1	2	3	4	5	6	7	8	Total
Two-photon MC†	0.012	0.003	0.003	0.002	0.001	0.001	0.001	0.002	0.025
$Z^0/\gamma \to q\bar{q}$ MC†	0.016	0.012	0.009	0.006	0.006	0.002	0.002	0.004	0.058
Four-fermion MC†	0.001	0.001	0.001	0.001	0.000	0.000	0.000	0.000	0.004
$\mathcal{O}(\alpha)$ radiation†	0.010	0.003	0.003	0.002	0.004	0.002	0.002	0.004	0.030
Hadronisation†	0.010	0.017	0.010	0.014	0.021	0.010	0.019	0.013	0.114
m_W†	0.006	0.008	0.005	0.011	0.012	0.010	0.012	0.011	0.076
ISR†	0.000	0.000	0.000	0.000	0.000	0.000	0.000	0.000	0.001
Jet/ℓ angular res.	0.000	0.000	0.000	0.000	0.000	0.000	0.000	0.000	0.002
Jet/ℓ energy res.	0.001	0.002	0.001	0.001	0.001	0.000	0.001	0.001	0.007
Jet/ℓ energy scale	0.001	0.001	0.001	0.001	0.001	0.001	0.001	0.001	0.008
Efficiency statistics	0.007	0.015	0.006	0.006	0.005	0.004	0.004	0.005	0.052
Purity statistics	0.010	0.010	0.003	0.004	0.003	0.001	0.001	0.002	0.034
Total	0.028	0.029	0.017	0.020	0.026	0.015	0.023	0.019	0.177

Table 13: The systematic uncertainties for the luminosity-weighted average of ρ_{00} for the $W \to q\bar{q}'$ decay mode. Error sources marked by a † were considered to be 100% correlated between the $W \to \ell\nu$ and $W \to q\bar{q}'$ decay modes and also among the centre-of-mass energies. All other sources were assumed to be completely uncorrelated. The bottommost row shows the sum in quadrature of the uncertainties associated with each individual error source, and the rightmost column shows the linear sum of the uncertainties in each individual $\cos\theta_W$ bin.

	$\cos\theta_W$ bin								
	1	2	3	4	5	6	7	8	Total
Two-photon MC†	0.011	0.001	0.004	0.002	0.002	0.001	0.001	0.001	0.022
$Z^0/\gamma \to q\bar{q}$ MC†	0.019	0.004	0.007	0.009	0.008	0.004	0.002	0.003	0.055
Four-fermion MC†	0.010	0.004	0.002	0.001	0.001	0.001	0.001	0.001	0.021
$\mathcal{O}(\alpha)$ radiation†	0.013	0.001	0.003	0.004	0.003	0.003	0.001	0.006	0.034
Hadronisation†	0.012	0.025	0.011	0.008	0.014	0.011	0.007	0.004	0.093
$m_W{}^\dagger$	0.005	0.003	0.003	0.002	0.002	0.001	0.001	0.001	0.017
ISR†	0.007	0.000	0.001	0.001	0.000	0.000	0.000	0.000	0.010
Jet/ℓ angular res.	0.000	0.002	0.000	0.001	0.000	0.000	0.001	0.001	0.006
Jet/ℓ energy res.	0.001	0.001	0.001	0.001	0.001	0.001	0.000	0.001	0.006
Jet/ℓ energy scale	0.001	0.001	0.001	0.001	0.001	0.001	0.000	0.000	0.006
Efficiency statistics	0.013	0.016	0.016	0.009	0.006	0.005	0.004	0.002	0.072
Purity statistics	0.011	0.009	0.008	0.006	0.004	0.003	0.002	0.001	0.044
Bias type II	0.016	0.013	0.012	0.010	0.009	0.007	0.006	0.005	0.079
Bias type III $(\tilde{\kappa}_Z)^\dagger$	0.023	0.015	0.010	0.006	0.006	0.004	0.002	0.001	0.066
Bias type III $(\tilde{\lambda}_Z)^\dagger$	0.025	0.023	0.012	0.012	0.009	0.005	0.002	0.002	0.091
Bias type III $(g_Z^4)^\dagger$	0.012	0.013	0.008	0.004	0.003	0.003	0.001	0.001	0.046
Total	0.053	0.046	0.032	0.024	0.023	0.017	0.011	0.010	0.217

Table 14: The systematic uncertainties for the luminosity-weighted average of $Re\{\rho_{+-}\}$ for the $W^- \to \ell^-\bar{\nu}_\ell$ decay mode. Error sources marked by a † were considered to be 100% correlated between the $W \to \ell\nu$ and $W \to q\bar{q}'$ decay modes and also among the centre-of-mass energies. All other sources were assumed to be completely uncorrelated. The bottommost row shows the sum in quadrature of the uncertainties associated with each individual error source, and the rightmost column shows the linear sum of the uncertainties in each individual $\cos\theta_W$ bin.

	$\cos\theta_W$ bin								
	1	2	3	4	5	6	7	8	Total
Two-photon MC†	0.010	0.004	0.003	0.002	0.002	0.002	0.001	0.001	0.023
$Z^0/\gamma \to q\bar{q}$ MC†	0.026	0.007	0.009	0.008	0.004	0.002	0.002	0.002	0.061
Four-fermion MC†	0.007	0.002	0.003	0.001	0.001	0.001	0.000	0.000	0.015
$\mathcal{O}(\alpha)$ radiation†	0.014	0.005	0.003	0.000	0.004	0.002	0.002	0.002	0.033
Hadronisation†	0.018	0.013	0.012	0.020	0.012	0.010	0.009	0.005	0.100
m_W†	0.004	0.003	0.002	0.002	0.002	0.002	0.001	0.001	0.018
ISR†	0.002	0.001	0.001	0.000	0.000	0.000	0.000	0.000	0.006
Jet/ℓ angular res.	0.001	0.001	0.000	0.000	0.000	0.000	0.000	0.002	0.005
Jet/ℓ energy res.	0.002	0.002	0.002	0.001	0.001	0.001	0.001	0.001	0.010
Jet/ℓ energy scale	0.002	0.002	0.002	0.001	0.001	0.001	0.001	0.001	0.010
Efficiency statistics	0.016	0.016	0.010	0.007	0.009	0.007	0.007	0.006	0.078
Purity statistics	0.017	0.009	0.005	0.003	0.004	0.003	0.002	0.004	0.048
Bias type II	0.016	0.014	0.012	0.011	0.009	0.008	0.006	0.005	0.080
Bias type III $(\tilde{\kappa}_Z)$†	0.017	0.010	0.009	0.005	0.004	0.002	0.002	0.001	0.050
Bias type III $(\tilde{\lambda}_Z)$†	0.029	0.014	0.015	0.011	0.007	0.006	0.003	0.003	0.089
Bias type III (g_Z^4)†	0.013	0.010	0.008	0.005	0.005	0.004	0.004	0.002	0.051
Total	0.059	0.035	0.030	0.029	0.021	0.017	0.015	0.012	0.218

Table 15: The systematic uncertainties for the luminosity-weighted average $Im\{\rho_{+-}\}$ for the $W^- \to \ell^-\bar{\nu}_\ell$ decay mode. Error sources marked by a † were considered to be 100% correlated between the $W \to \ell\nu$ and $W \to q\bar{q}'$ decay modes and also among the centre-of-mass energies. All other sources were assumed to be completely uncorrelated. The bottommost row shows the sum in quadrature of the uncertainties associated with each individual error source, and the rightmost column shows the linear sum of the uncertainties in each individual $\cos\theta_W$ bin.

	183 GeV		189 GeV		192 GeV		196 GeV	
	$\ell\nu$	$q\bar{q}'$	$\ell\nu$	$q\bar{q}'$	$\ell\nu$	$q\bar{q}'$	$\ell\nu$	$q\bar{q}'$
Two-photon MC†	0.00	0.00	0.03	0.04	0.26	0.02	0.08	0.05
$Z^0/\gamma \to q\bar{q}$ MC†	0.63	0.65	0.43	0.30	0.05	0.29	0.29	0.43
Four-fermion MC†	0.19	0.02	0.19	0.02	0.09	0.04	0.21	0.03
$\mathcal{O}(\alpha)$ radiation†	0.05	0.79	0.27	0.02	0.07	0.13	0.19	0.10
Hadronisation†	0.32	1.41	0.32	1.11	0.32	1.11	0.17	1.22
m_W†	0.27	1.11	0.10	1.11	0.22	1.13	0.02	1.11
ISR†	0.00	0.01	0.00	0.01	0.00	0.01	0.01	0.01
Detector Response	0.25	0.19	0.44	0.07	0.21	0.07	0.32	0.27
MC statistics	0.69	0.48	0.58	0.37	0.70	0.50	0.73	0.36
Total	1.08	2.13	0.97	1.64	0.88	1.70	0.92	1.77

	200 GeV		202 GeV		205 GeV		207 GeV	
	$\ell\nu$	$q\bar{q}'$	$\ell\nu$	$q\bar{q}'$	$\ell\nu$	$q\bar{q}'$	$\ell\nu$	$q\bar{q}'$
Two-photon MC†	0.12	0.19	0.01	0.18	0.11	0.14	0.23	0.08
$Z^0/\gamma \to q\bar{q}$ MC†	0.36	0.26	0.26	0.12	0.07	0.49	0.17	0.14
Four-fermion MC†	0.11	0.01	0.21	0.05	0.23	0.01	0.21	0.04
$\mathcal{O}(\alpha)$ radiation†	0.18	0.07	0.39	0.10	0.68	0.34	0.01	0.17
Hadronisation†	0.17	1.22	0.17	1.22	0.63	1.38	0.63	1.38
m_W†	0.18	0.86	0.07	1.07	0.08	0.98	0.19	1.03
ISR†	0.00	0.01	0.00	0.01	0.00	0.01	0.01	0.01
Detector Response	0.28	0.26	0.20	0.22	0.64	0.04	0.52	0.16
MC statistics	0.99	0.41	1.46	0.70	0.73	0.43	0.73	0.56
Total	1.15	1.61	1.57	1.80	1.37	1.85	1.17	1.83

Table 16: The systematic uncertainties for the percentage of longitudinally polarised W bosons at each centre-of-mass energy. Error sources marked by a † were considered to be 100% correlated between the $W \to \ell\nu$ and $W \to q\bar{q}'$ decay modes and also among the centre-of-mass energies. All other sources were assumed to be completely uncorrelated. The systematic uncertainties associated with the modelling of the detector response to jets and leptons (source 6 in the main text) have been combined under the heading 'Detector Response', and the effect of the limited MC statistics on the efficiency and purity (source 7 in the main text) have been combined under the heading 'MC statistics'.

	$W \to \ell\nu$	$W \to q\bar{q}'$
Two-photon MC†	0.10	0.08
$Z^0/\gamma \to q\bar{q}$ MC†	0.30	0.32
Four-fermion MC†	0.19	0.03
$\mathcal{O}(\alpha)$ radiation†	0.23	0.18
Hadronisation†	0.38	1.23
m_W†	0.13	1.07
ISR†	0.01	0.01
Detector Response	0.19	0.06
MC statistics	0.29	0.18
Total	0.68	1.68

Table 17: The systematic uncertainties for the luminosity-weighted average percentage of longitudinally polarised W bosons. The error sources appear in the same order as in the list in section 7. For the combination procedures described in section 8, the error sources marked by a † were considered to be 100% correlated between the $W \to \ell\nu$ and $W \to q\bar{q}'$ decay modes and also among the centre-of-mass energies. All other sources were assumed to be completely uncorrelated. The systematic uncertainties associated with the modelling of the detector response to jets and leptons (source 6 in the main text) have been combined under the heading 'Detector Response', and the effect of the limited MC statistics on the efficiency and purity (source 7 in the main text) have been combined under the heading 'MC statistics'.

8 Results

At each nominal centre-of-mass energy the following quantities were measured from the data: the diagonal elements of the W SDM (ρ_{++}, ρ_{--} and ρ_{00}) for leptonically and hadronically decaying W bosons (with the W^- and W^+ contributions combined); the fraction of longitudinally polarised W bosons (f_L) for leptonically and hadronically decaying W bosons; the real and imaginary parts of the off-diagonal elements of the W^- and W^+ SDMs (ρ_{+-}, ρ_{+0} and ρ_{+-}) for leptonically decaying W bosons; and the CP-odd (Δ^{CP}) and CP$\hat{T}$-odd ($\Delta^{CP\hat{T}}$) observables for leptonically decaying W bosons. Of these results, the quantity of most obvious interest is arguably the fraction of longitudinally polarised W bosons. This fraction along with other results related to the diagonal elements of the SDM are presented in section 8.1. The off-diagonal elements of the SDM and the associated symmetry tests are presented in section 8.2. All the results presented have been corrected for the detector effects described in section 6.4.2 and the biases described in section 6.5. Those figures which are marked 'OPAL' have previously been published by the author of this thesis on behalf of the OPAL collaboration in reference [83].

8.1 W polarisation

Figures 41 and 44 show the values of the ρ_{00} and ρ_{--} elements of the SDM in each $\cos\theta_W$ bin as measured from leptonically decaying W bosons at each nominal centre-of-mass energy. The values of the ρ_{++} element are not shown as they are trivially related to the ρ_{00} and ρ_{--} distributions through the SDM normalisation constraint. Figure 42 shows ρ_{00} for the hadronically decaying W bosons, whereas the ρ_{--} and ρ_{++} elements are not shown as these could not be measured individually from the folded angular distributions of the quarks.

It can be seen from figures 41 and 42 that the measured values of ρ_{00} obtained from the leptonic and hadronic decays were consistent both with the SM prediction and with one another. The measured distributions were therefore combined together using the BLUE

method as described in section 6.6.1. Each source of systematic error was assumed to be uncorrelated with all other sources of systematic error and either 100% or 0% correlated between the two decay modes (see section 7 for details). Figure 43 shows the values of ρ_{00} in each bin of $\cos\theta_W$ at each nominal centre-of-mass energy following combination of the decay channels. The longitudinally and transversely polarised differential cross-sections were then formed from the SDM distributions and from the unpolarised cross-section (defined by equation (74)) measured in each bin of $\cos\theta_W$. The polarised cross-sections in each bin of $\cos\theta_W$ at each nominal centre-of-mass energy are shown in figures 45 and 46.

The measurements of the SDM elements at the eight nominal centre-of-mass energies were themselves combined to make a luminosity-weighted average as described in section 6.6.2. The correlations between the values of the systematic uncertainties at different centre-of-mass energies were again approximated as being either 100% or 0%. The luminosity-weighted averages of ρ_{++}, ρ_{--} and ρ_{00} are shown in figure 47. The corresponding polarised differential cross-sections are shown in figure 48. The numerical values associated with these figures can be found in tables 19 to 25 and have been submitted to the Durham HEPDATA database [84].

The fractions of longitudinally polarised W bosons measured (see equation (82)) from the data at each nominal centre-of-mass energy are shown in table 18. For comparison with the data, table 18 also gives the fraction of longitudinally polarised W bosons predicted by the KandY [54,55] MC samples. The table shows the values calculated from the leptonically and hadronically decaying W bosons separately and the values obtained from the two decay modes combined using the BLUE technique.

The combined values obtained from the data at each centre-of-mass energy are summarised in figure 40 and compared with the Born-level CC03 prediction. The figure also shows the values obtained from the KandY generator-level MC samples. It can be seen that both the data and the MC values are in reasonable agreement with the Born-level

	Longitudinal polarisation (%)			
Nominal energy (GeV)	OPAL Data $W \to \ell\nu$	$W \to q\bar{q}'$	Combined	MC Combined
183	$18.8 \pm 10.3 \pm 1.1$	$31.1 \pm 10.4 \pm 2.1$	$24.8 \pm 7.4 \pm 1.4$	26.4 ± 0.2
189	$17.6 \pm 5.8 \pm 1.0$	$21.0 \pm 5.8 \pm 1.5$	$19.2 \pm 4.3 \pm 1.1$	25.6 ± 0.2
192	$56.7 \pm 14.3 \pm 0.9$	$21.7 \pm 13.8 \pm 1.7$	$38.6 \pm 9.7 \pm 1.1$	25.2 ± 0.2
196	$16.8 \pm 8.3 \pm 0.9$	$7.8 \pm 8.3 \pm 1.8$	$12.4 \pm 5.9 \pm 1.1$	23.9 ± 0.2
200	$32.5 \pm 8.4 \pm 1.1$	$35.5 \pm 9.4 \pm 1.6$	$33.9 \pm 6.2 \pm 1.1$	23.2 ± 0.2
202	$30.4 \pm 11.8 \pm 1.6$	$33.7 \pm 12.5 \pm 1.8$	$31.9 \pm 8.9 \pm 1.3$	23.2 ± 0.2
205	$33.1 \pm 8.7 \pm 1.4$	$35.3 \pm 9.3 \pm 1.9$	$34.1 \pm 6.4 \pm 1.4$	22.2 ± 0.2
207	$17.5 \pm 6.4 \pm 1.2$	$21.3 \pm 6.8 \pm 1.8$	$19.2 \pm 4.8 \pm 1.3$	21.7 ± 0.2
Average	$23.6 \pm 2.9 \pm 0.7$	$24.5 \pm 3.0 \pm 1.7$	$23.9 \pm 2.1 \pm 1.1$	23.9 ± 0.1

Table 18: The fraction of longitudinal polarisation for the leptonically and hadronically decaying W bosons at each nominal centre-of-mass energy after detector and bias corrections. Also shown is the combined result obtained from the BLUE technique [79]. The values extracted from the data are shown with both statistical and systematic errors. The values extracted from the generator-level KandY MC samples are shown with statistical errors only. The last row of the table shows the luminosity-weighted averages.

prediction. The Chi-squared statistic for the agreement between the data and MC values is 15.7 for 8 degrees of freedom, corresponding to an upper-tail probability of approximately 5%.

The luminosity-weighted averages of the values of f_L at each nominal centre-of-mass energy were obtained in the same way as for the SDM elements described above. The average longitudinal polarisation was found to be $(23.9 \pm 2.1 \pm 1.1)\%$, which is in good agreement with the KandY MC prediction of $(23.9 \pm 0.1)\%$. The values obtained at 183 GeV and 189 GeV differ slightly from those previously published by OPAL [23, 24] due to the use of improved MC generators (see item 2 in section 7), to the inclusion of the bias correction, and to minor changes to the event reconstruction procedure.

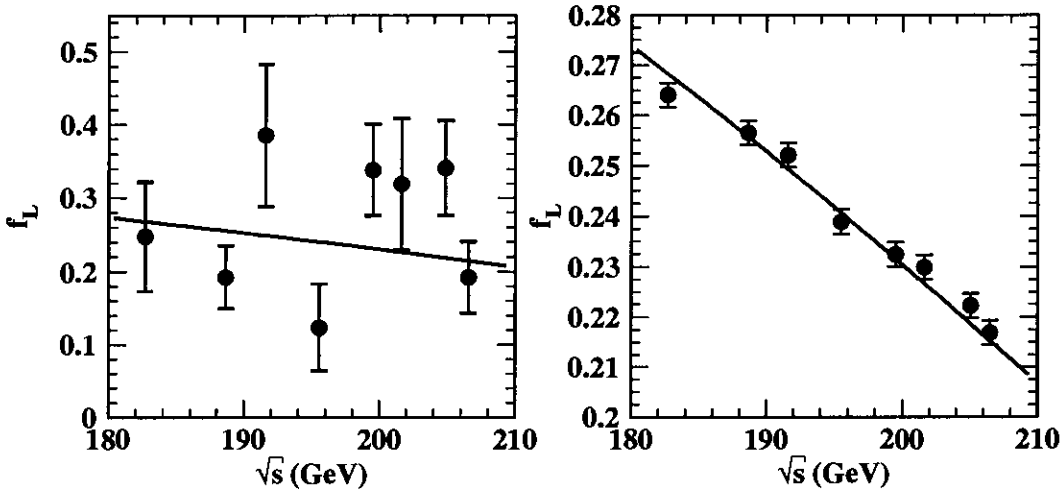

Figure 40: The total fraction of longitudinally polarised W bosons as a function of centre-of-mass energy. In the left-hand figure, the points show the values of f_L measured from the data after detector and bias corrections. The inner error bars show the statistical uncertainty on the data values and the outer error bars show the total error including the systematic uncertainty. In the right-hand figure, the points show the generator-level values of f_L from the KandY signal MC samples and the error bars shows their statistical uncertainties. In both figures, the line shows the Born-level CC03 prediction, and the results from the leptonically-decaying and hadronically W bosons have been combined.

$\cos\theta_W$			ρ_{++}	s^{ρ}_{stat}	s^{ρ}_{sys}
-1.00	-	-0.75	0.332	0.074	0.024
-0.75	-	-0.50	0.481	0.066	0.014
-0.50	-	-0.25	0.461	0.064	0.010
-0.25	-	0.00	0.468	0.053	0.014
0.00	-	0.25	0.274	0.041	0.011
0.25	-	0.50	0.231	0.035	0.010
0.50	-	0.75	0.094	0.027	0.003
0.75	-	1.00	0.076	0.019	0.004

Table 19: Luminosity-weighted averages of ρ_{++} as functions of $\cos\theta_W$ for the $W \to \ell\nu$ decay mode. s^{ρ}_{stat} denotes the statistical uncertainty and s^{ρ}_{sys} denotes the systematic uncertainty.

$\cos\theta_W$	ρ_{--}	s^{ρ}_{stat}	s^{ρ}_{sys}
-1.00 - -0.75	0.102	0.048	0.019
-0.75 - -0.50	0.099	0.049	0.018
-0.50 - -0.25	0.293	0.055	0.015
-0.25 - 0.00	0.466	0.052	0.018
0.00 - 0.25	0.451	0.046	0.011
0.25 - 0.50	0.630	0.046	0.011
0.50 - 0.75	0.635	0.040	0.007
0.75 - 1.00	0.712	0.032	0.011

Table 20: Luminosity-weighted averages of ρ_{--} as functions of $\cos\theta_W$ for the $W \to \ell\nu$ decay mode. s^{ρ}_{stat} denotes the statistical uncertainty and s^{ρ}_{sys} denotes the systematic uncertainty.

$\cos\theta_W$	ρ_{00}	s^{ρ}_{stat}	s^{ρ}_{sys}
-1.00 - -0.75	0.566	0.102	0.034
-0.75 - -0.50	0.421	0.093	0.027
-0.50 - -0.25	0.246	0.095	0.020
-0.25 - 0.00	0.065	0.083	0.023
0.00 - 0.25	0.275	0.069	0.019
0.25 - 0.50	0.139	0.066	0.017
0.50 - 0.75	0.271	0.056	0.009
0.75 - 1.00	0.212	0.044	0.015

Table 21: Luminosity-weighted averages of ρ_{00} as functions of $\cos\theta_W$ for the $W \to \ell\nu$ decay mode. s^{ρ}_{stat} denotes the statistical uncertainty and s^{ρ}_{sys} denotes the systematic uncertainty.

$\cos\theta_W$	ρ_{00}	s^{ρ}_{stat}	s^{ρ}_{sys}
-1.00 - -0.75	0.259	0.100	0.028
-0.75 - -0.50	0.288	0.093	0.029
-0.50 - -0.25	0.457	0.094	0.017
-0.25 - 0.00	0.303	0.082	0.020
0.00 - 0.25	0.368	0.069	0.026
0.25 - 0.50	0.240	0.066	0.015
0.50 - 0.75	0.147	0.056	0.023
0.75 - 1.00	0.224	0.043	0.019

Table 22: Luminosity-weighted averages of ρ_{00} as functions of $\cos\theta_W$ for the $W \to q\bar{q}'$ decay mode. s^{ρ}_{stat} denotes the statistical uncertainty and s^{ρ}_{sys} denotes the systematic uncertainty.

$\cos\theta_W$	ρ_{00}	s^{ρ}_{stat}	s^{ρ}_{sys}
-1.00 - -0.75	0.407	0.073	0.060
-0.75 - -0.50	0.356	0.067	0.052
-0.50 - -0.25	0.353	0.068	0.033
-0.25 - 0.00	0.187	0.060	0.035
0.00 - 0.25	0.322	0.049	0.037
0.25 - 0.50	0.191	0.047	0.025
0.50 - 0.75	0.210	0.040	0.027
0.75 - 1.00	0.219	0.031	0.029

Table 23: Luminosity-weighted averages of ρ_{00} as functions of $\cos\theta_W$ for the $W \to \ell\nu$ and $W \to q\bar{q}'$ decay modes combined. s^{ρ}_{stat} denotes the statistical uncertainty and s^{ρ}_{sys} denotes the systematic uncertainty.

$\cos\theta_W$	$d\sigma_L/d\cos\theta_W$	s^{L}_{stat}	s^{L}_{sys}
-1.00 - -0.75	0.343	0.068	0.059
-0.75 - -0.50	0.467	0.094	0.073
-0.50 - -0.25	0.517	0.105	0.049
-0.25 - 0.00	0.351	0.126	0.075
0.00 - 0.25	0.959	0.158	0.118
0.25 - 0.50	0.673	0.175	0.097
0.50 - 0.75	1.091	0.220	0.160
0.75 - 1.00	2.371	0.338	0.301

Table 24: The luminosity-weighted average longitudinally polarised differential cross-section (in units of picobarns / 0.25) for the $W \to \ell\nu$ and $W \to q\bar{q}'$ decay modes combined. s^{L}_{stat} denotes the statistical uncertainty and s^{L}_{sys} denotes the systematic uncertainty.

$\cos\theta_W$	$d\sigma_T/d\cos\theta_W$	s^T_{stat}	s^T_{sys}
-1.00 - -0.75	0.515	0.071	0.069
-0.75 - -0.50	0.833	0.099	0.086
-0.50 - -0.25	0.949	0.111	0.066
-0.25 - 0.00	1.686	0.142	0.091
0.00 - 0.25	2.115	0.170	0.129
0.25 - 0.50	2.941	0.196	0.102
0.50 - 0.75	4.230	0.244	0.139
0.75 - 1.00	8.315	0.375	0.436

Table 25: The luminosity-weighted average transversely polarised differential cross-section (in units of picobarns / 0.25) for the $W \to \ell\nu$ and $W \to q\bar{q}'$ decay modes combined. s^T_{stat} denotes the statistical uncertainty and s^T_{sys} denotes the systematic uncertainty.

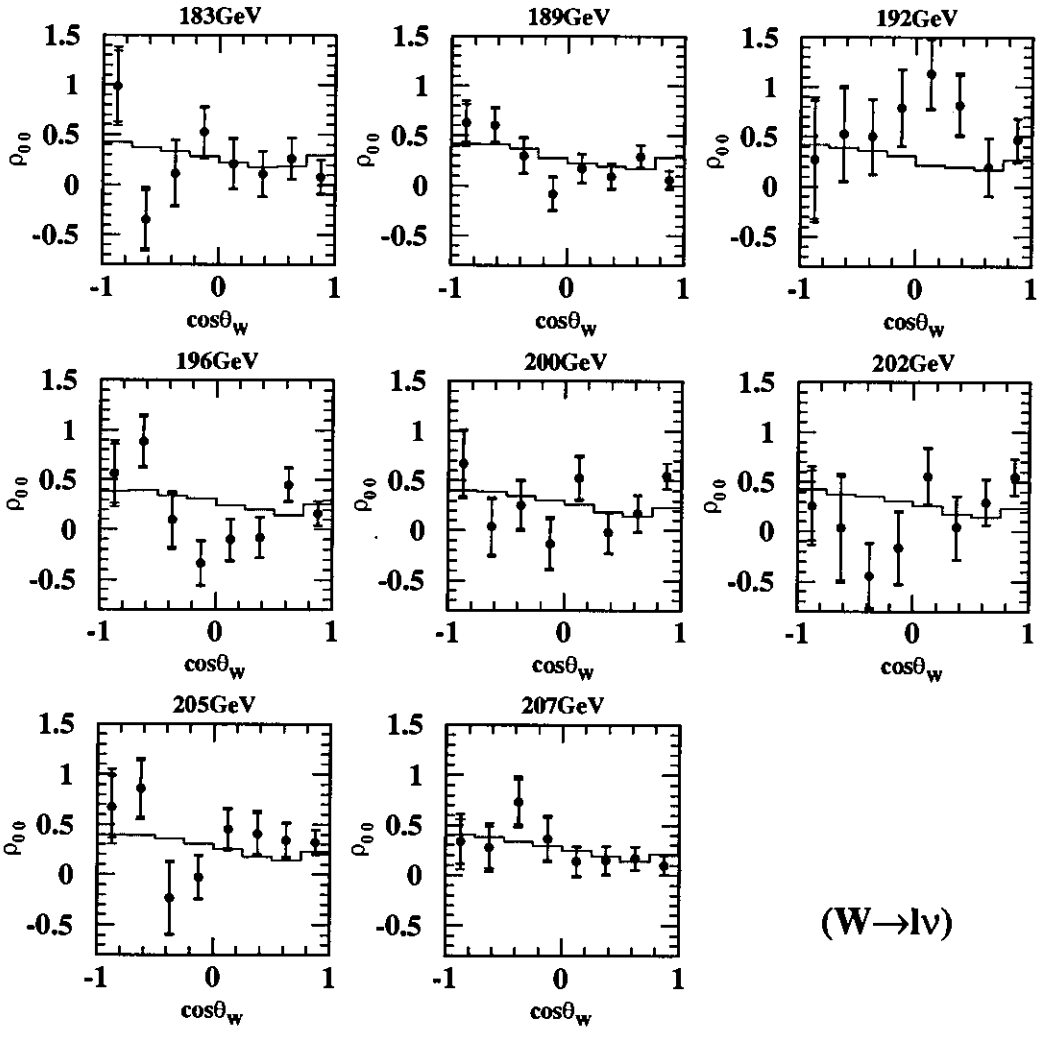

Figure 41: The value of ρ_{00} measured from leptonically decaying W bosons as a function of $\cos\theta_W$ for each centre-of-mass energy. The points show the data after detector and bias corrections. The inner error bars show the statistical uncertainties on the data and the outer error bars show the total errors including systematic uncertainties. The histograms show the generator-level MC prediction. The values of ρ_{00} are not constrained to lie in the physically-allowed region and so can have negative values.

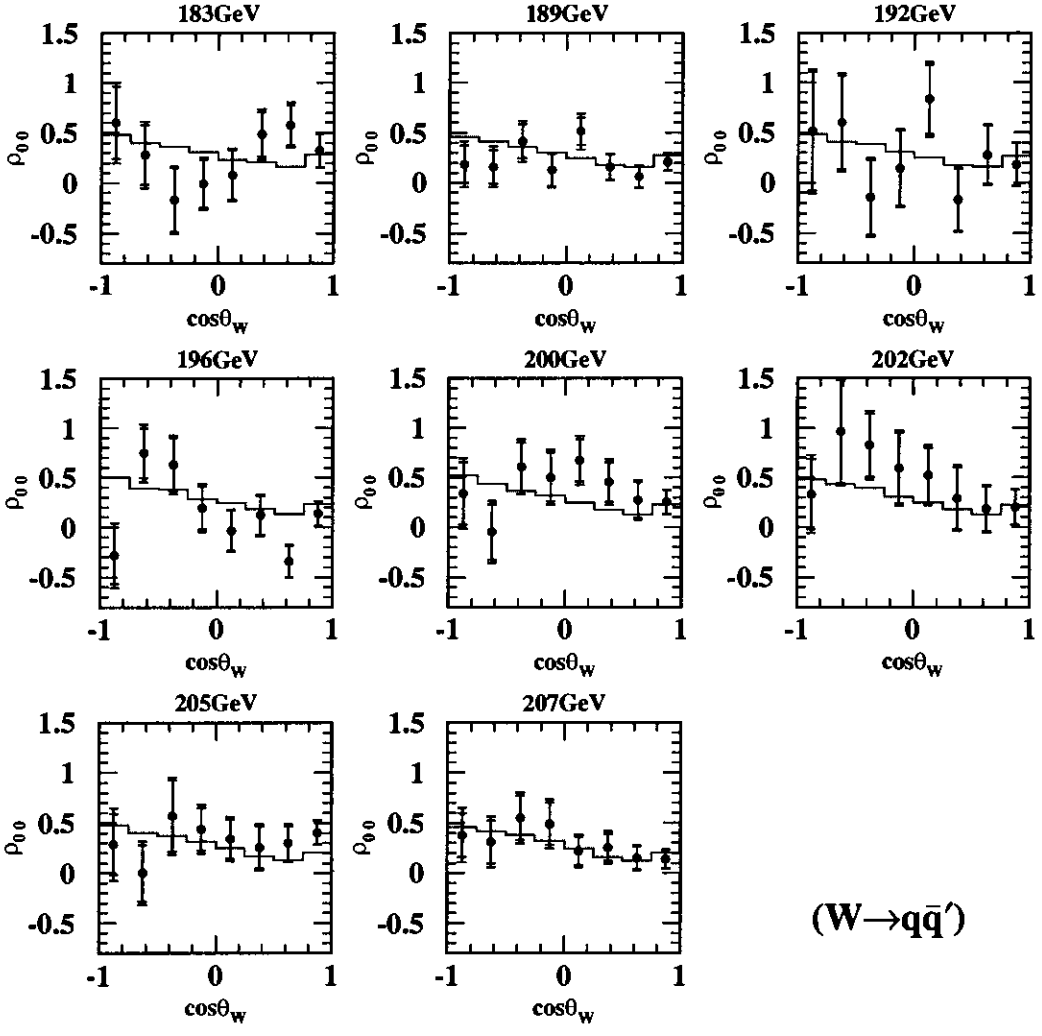

Figure 42: The value of ρ_{00} measured from hadronically decaying W bosons as a function of $\cos\theta_W$ for each centre-of-mass energy. The points show the data after detector and bias corrections. The inner error bars show the statistical uncertainties on the data and the outer error bars show the total errors including systematic uncertainties. The histograms show the generator-level MC prediction. The values of ρ_{00} are not constrained to lie in the physically-allowed region and so can have negative values.

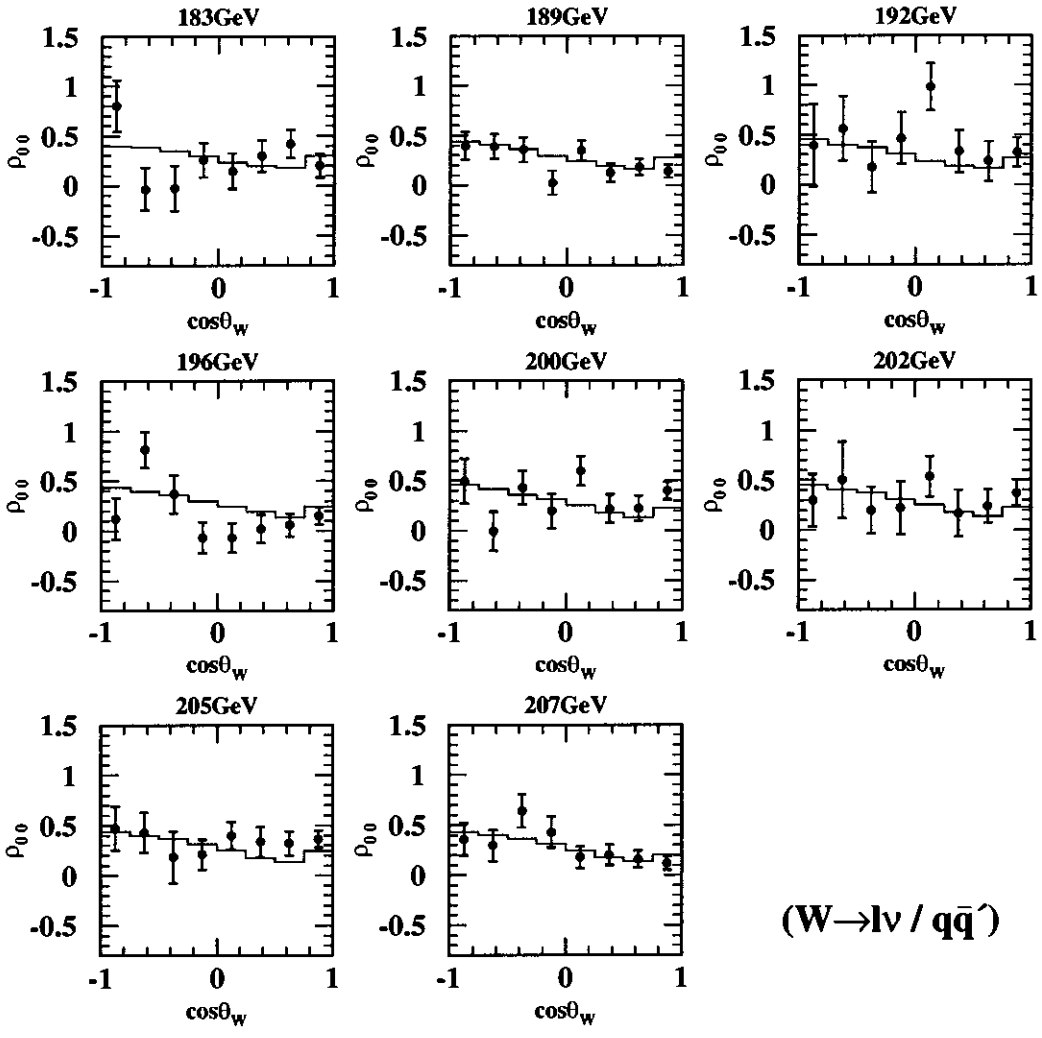

Figure 43: The value of ρ_{00} measured from the data as a function of $\cos\theta_W$ for each centre-of-mass energy. The leptonic and hadronic decay modes have been combined with one another. The points show the data after detector and bias corrections. The inner error bars show the statistical uncertainties on the data and the outer error bars show the total errors including systematic uncertainties. The histograms show the generator-level MC prediction. The values of ρ_{00} are not constrained to lie in the physically-allowed region and so can have negative values.

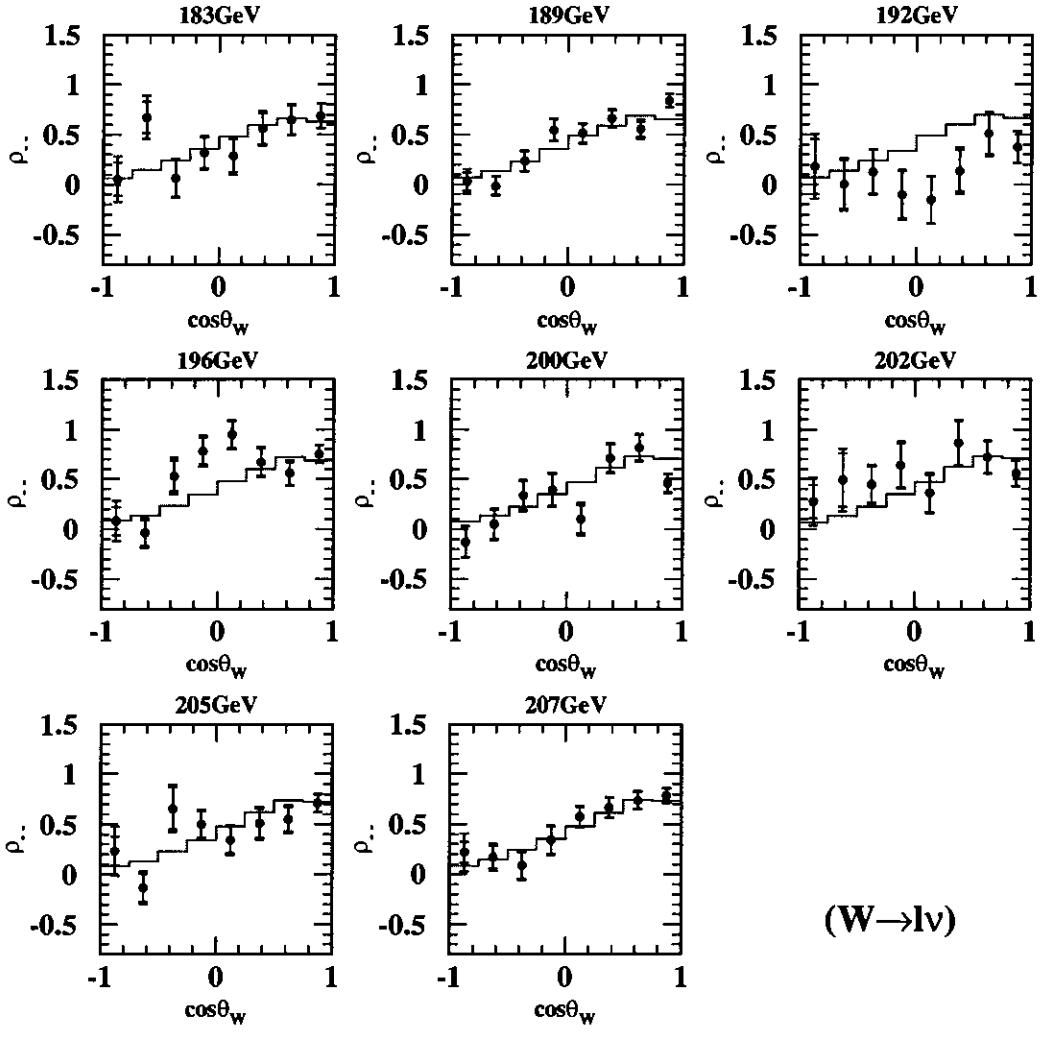

Figure 44: The value of ρ_{--} measured from leptonically decaying W bosons as a function of $\cos\theta_W$ for each centre-of-mass energy. The points show the data after detector and bias corrections. The inner error bars show the statistical uncertainties on the data and the outer error bars show the total errors including systematic uncertainties. The histograms show the generator-level MC prediction. The values of ρ_{--} are not constrained to lie in the physically-allowed region and so can have negative values.

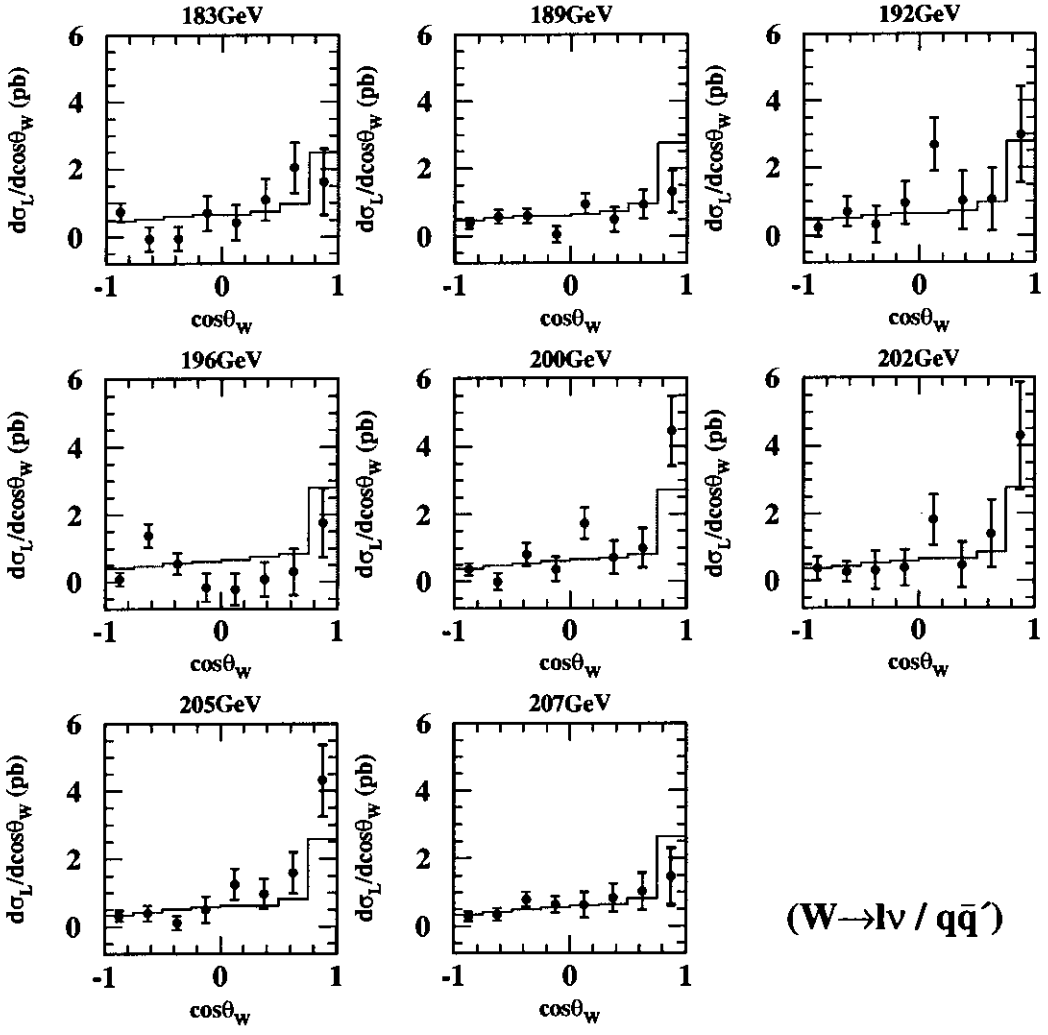

Figure 45: Longitudinally polarised differential cross-sections in picobarns as a function of $\cos\theta_W$ for each centre-of-mass energy. The leptonic and hadronic decay modes have been combined. The points show the data after detector and bias corrections. The inner error bars show the statistical uncertainties on the data and the outer error bars show the total errors including systematic uncertainties. The histograms show the generator-level MC prediction. The values have been averaged over the $\cos\theta_W$ bin width. The cross-sections are not constrained lie in the physically-allowed region and so can have negative values.

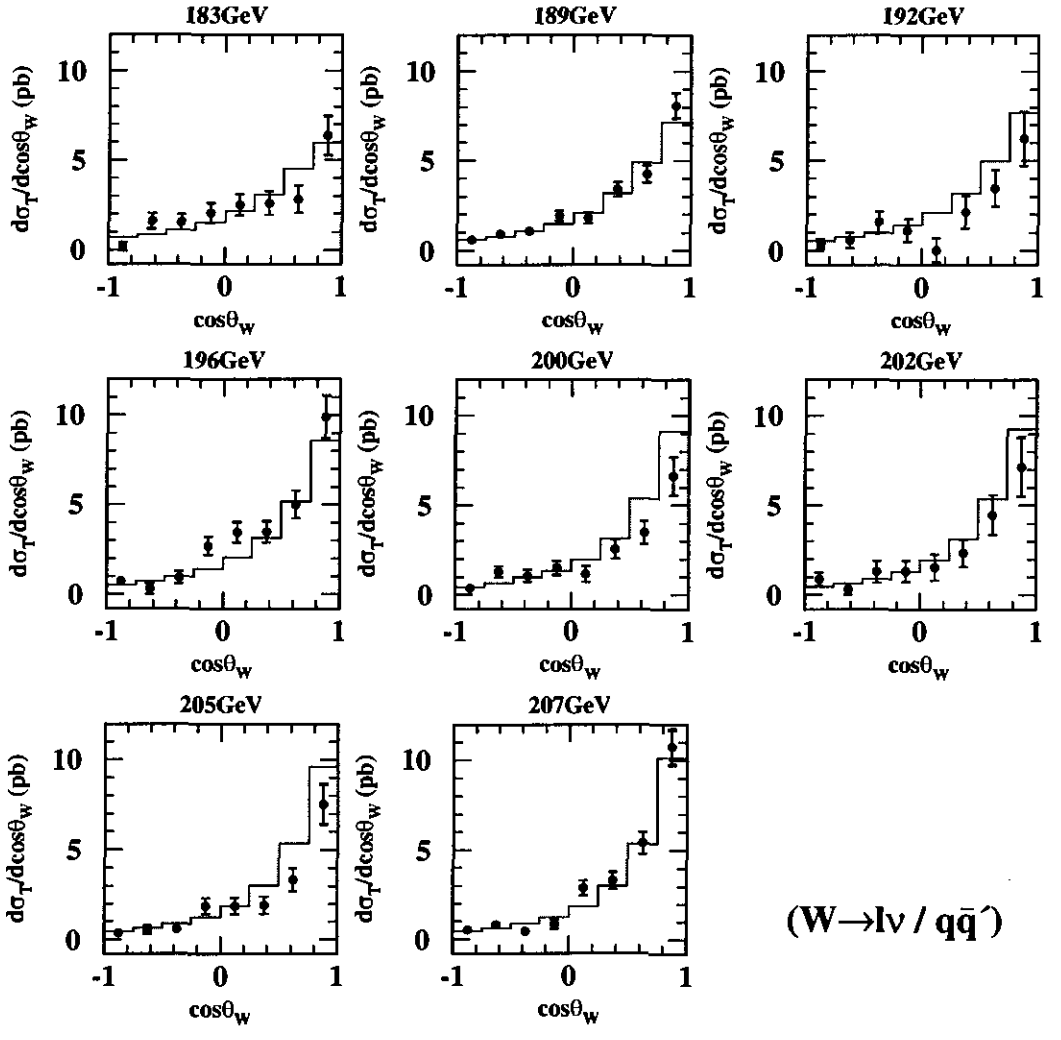

Figure 46: Transversely polarised differential cross-sections in picobarns as a function of $\cos\theta_W$ for each centre-of-mass energy. The leptonic and hadronic decay modes have been combined. The points show the data after detector and bias corrections. The inner error bars show the statistical uncertainties on the data and the outer error bars show the total errors including systematic uncertainties. The histograms show the generator-level MC prediction. The values have been averaged over the $\cos\theta_W$ bin width. The cross-sections are not constrained lie in the physically-allowed region and so can have negative values.

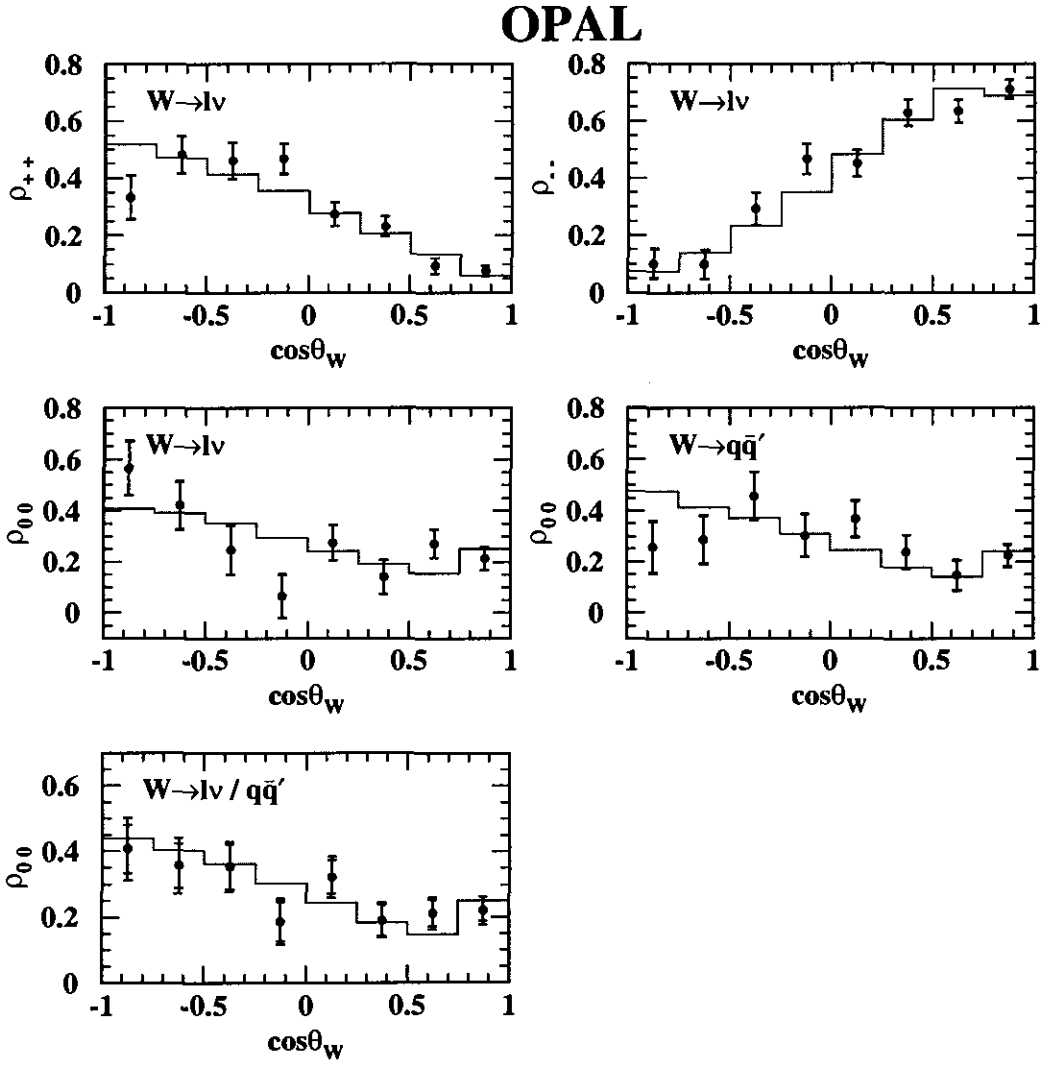

Figure 47: Luminosity-weighted averages of the diagonal elements of the SDM as functions of $\cos\theta_W$. The points show the data after detector and bias corrections. The inner error bars show the statistical uncertainties and the outer error bars show the total uncertainties including both the statistical and systematic contributions. The histograms show the generator-level KandY MC prediction. The figures in the top row show ρ_{++} and ρ_{--} for leptonically decaying W bosons. The figures in the middle row show ρ_{00} for leptonically decaying W bosons and hadronically decaying W bosons separately. The figure in the bottom row shows ρ_{00} with the leptonic and hadronic decay modes combined.

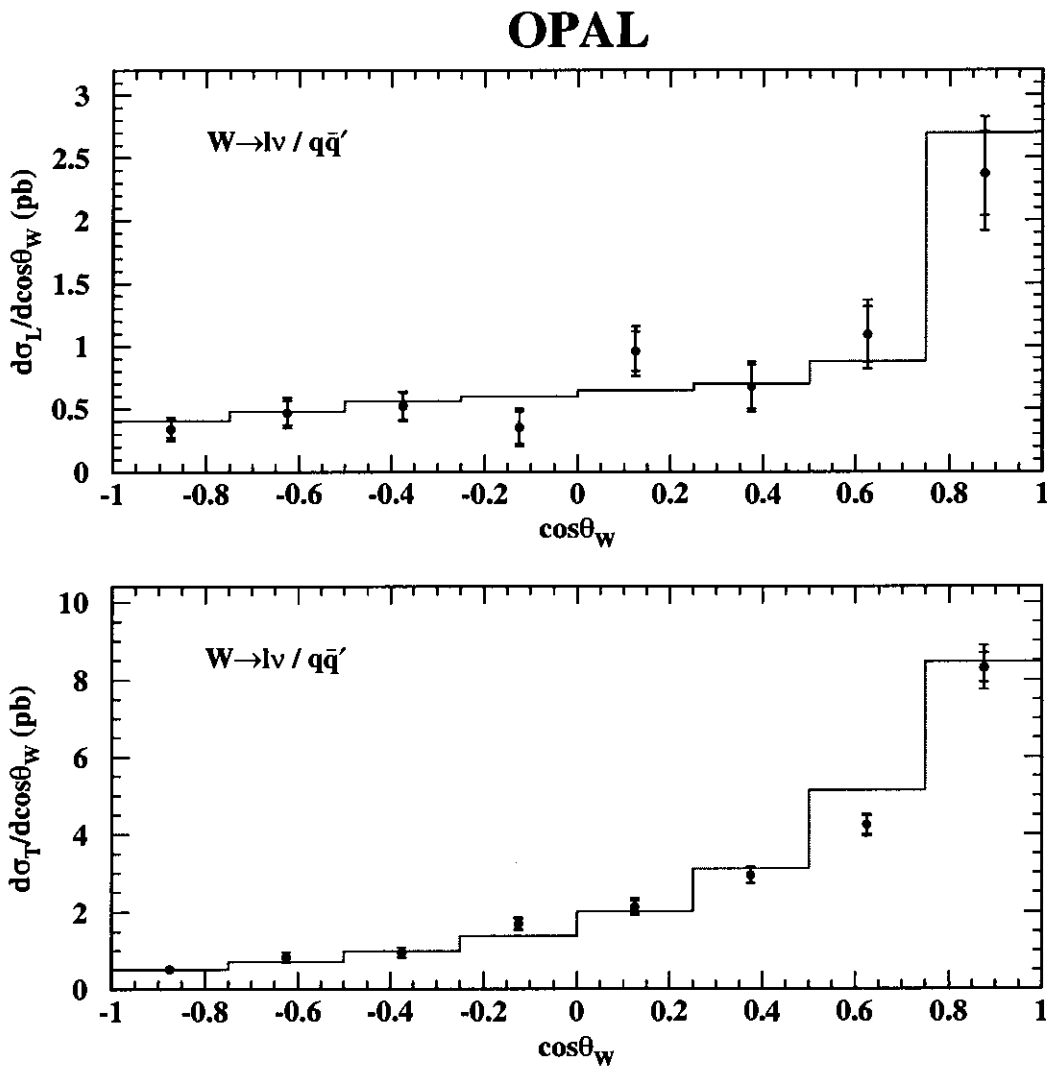

Figure 48: The luminosity-weighted average polarised differential cross-sections where the average is over the eight nominal centre-of-mass energies and over the $\cos\theta_W$ bin width. The points show the data after detector and bias corrections. The inner error bars show the statistical uncertainties and the outer error bars show the total uncertainties including both the statistical and systematic contributions. The histograms show the generator-level KandY MC prediction.

8.2 CP/CPT̂ tests

The measured values of the off-diagonal elements of the W^- and W^+ SDM in each $\cos\theta_W$ bin as obtained from leptonically decaying W bosons are presented in appendix F. All data distributions show reasonable agreement with the MC generator-level predictions. The values of the CP-odd (CPT̂-even) and CPT̂-odd (CP-even) observables of section 2.8 were calculated at each centre-of-mass energy from the W^- and W^+ SDM elements (see equations (84) and (85)). Each source of systematic uncertainty in the off-diagonal elements of the SDM was assumed to be 100% correlated between the W^- and W^+ results. The measured values of the CP-odd observables are summarised in table 26, and the measured values of the CPT̂-odd observables are summarised in section 27. The luminosity-weighted average values of the CP-odd and CPT̂-odd observables as obtained using the technique of section 6.6.2 are also included in the table.

$\sqrt{s}$/GeV	Δ^{CP}_{+-} (pb)	Δ^{CP}_{+0} (pb)	Δ^{CP}_{-0} (pb)
183	$0.74 \pm 0.55 \pm 0.11$	$-0.10 \pm 0.39 \pm 0.07$	$-0.38 \pm 0.48 \pm 0.09$
189	$0.64 \pm 0.32 \pm 0.09$	$-0.08 \pm 0.22 \pm 0.06$	$-0.13 \pm 0.27 \pm 0.09$
192	$0.11 \pm 0.75 \pm 0.10$	$0.21 \pm 0.53 \pm 0.09$	$0.50 \pm 0.64 \pm 0.08$
196	$-0.19 \pm 0.52 \pm 0.09$	$0.68 \pm 0.35 \pm 0.08$	$0.80 \pm 0.46 \pm 0.10$
200	$0.23 \pm 0.50 \pm 0.09$	$0.26 \pm 0.34 \pm 0.08$	$-0.08 \pm 0.45 \pm 0.10$
202	$-0.54 \pm 0.72 \pm 0.11$	$-0.62 \pm 0.49 \pm 0.10$	$-0.29 \pm 0.63 \pm 0.11$
205	$0.12 \pm 0.47 \pm 0.09$	$-0.01 \pm 0.31 \pm 0.06$	$0.01 \pm 0.41 \pm 0.08$
207	$0.50 \pm 0.40 \pm 0.11$	$0.21 \pm 0.26 \pm 0.08$	$-0.02 \pm 0.36 \pm 0.13$
Average	$0.33 \pm 0.17 \pm 0.06$	$0.09 \pm 0.11 \pm 0.04$	$0.02 \pm 0.15 \pm 0.06$
MC	0.03 ± 0.01	0.00 ± 0.01	-0.01 ± 0.01

Table 26: The CP-odd observables described in section 2.8 measured in picobarns for each centre-of-mass energy. The values extracted from the data are shown with both statistical and systematic errors. The last two rows show the luminosity-weighted average for the data and Monte Carlo. The Monte Carlo predictions come from the KandY generator-level four-vectors and have statistical errors only.

Any significant deviations from zero in any element of table 26 would constitute an unambiguous signature of CP violation. Any significant deviations from zero in any element

$\sqrt{s}$/ GeV	$\Delta_{+-}^{\mathrm{CP\hat{T}}}$ (pb)	$\Delta_{+0}^{\mathrm{CP\hat{T}}}$ (pb)	$\Delta_{-0}^{\mathrm{CP\hat{T}}}$ (pb)
183	$0.57 \pm 0.55 \pm 0.11$	$-0.00 \pm 0.39 \pm 0.07$	$-0.21 \pm 0.48 \pm 0.09$
189	$0.17 \pm 0.32 \pm 0.09$	$-0.44 \pm 0.22 \pm 0.06$	$-0.71 \pm 0.27 \pm 0.09$
192	$0.02 \pm 0.75 \pm 0.10$	$0.19 \pm 0.53 \pm 0.09$	$-0.24 \pm 0.64 \pm 0.08$
196	$0.10 \pm 0.52 \pm 0.09$	$-0.01 \pm 0.35 \pm 0.08$	$0.23 \pm 0.46 \pm 0.10$
200	$-0.35 \pm 0.50 \pm 0.09$	$0.12 \pm 0.34 \pm 0.08$	$0.71 \pm 0.45 \pm 0.10$
202	$0.48 \pm 0.72 \pm 0.11$	$0.73 \pm 0.49 \pm 0.10$	$0.73 \pm 0.63 \pm 0.11$
205	$-1.02 \pm 0.47 \pm 0.09$	$-0.25 \pm 0.31 \pm 0.06$	$-0.11 \pm 0.41 \pm 0.08$
207	$-0.37 \pm 0.40 \pm 0.11$	$-0.08 \pm 0.26 \pm 0.08$	$0.78 \pm 0.36 \pm 0.13$
Average	$-0.10 \pm 0.17 \pm 0.06$	$-0.10 \pm 0.11 \pm 0.04$	$0.07 \pm 0.15 \pm 0.06$
MC	0.06 ± 0.01	0.03 ± 0.01	-0.08 ± 0.01

Table 27: The CP$\hat{\mathrm{T}}$-odd observables described in section 2.8 measured in picobarns for each centre-of-mass energy. The values extracted from the data are shown with both statistical and systematic errors. The last two rows show the luminosity-weighted average for the data and Monte Carlo. The Monte Carlo predictions come from the KandY generator-level four-vectors and have statistical errors only.

of table 27 would show the presence of loop effects. Here, all data results are consistent with the SM tree-level prediction of zero within the quoted errors. It is interesting to note that the KandY generator-level predictions for the CP$\hat{\mathrm{T}}$-odd observables do deviate from zero. This is expected, as KandY contains $\mathcal{O}(\alpha)$ radiative corrections including loop effects. Additional checks showed similar deviations from zero in the CP$\hat{\mathrm{T}}$-odd observables constructed from each of the $\mathrm{W} \to \mathrm{e}\nu_{\mathrm{e}}$, $\mathrm{W} \to \mu\nu_{\mu}$ and $\mathrm{W} \to \tau\nu_{\tau}$ decay modes individually as well as from hadronically decaying W bosons.

In addition to the results presented above, the luminosity-weighted averages of the observables are shown as functions of $\cos\theta_{\mathrm{W}}$ in figure 49, and the numerical values associated with the figure are presented in tables 28 to 33.

$\cos\theta_W$	Δ_{+-}^{CP}	s_{stat}^{Δ}	s_{sys}^{Δ}
-1.00 - -0.75	0.222	0.093	0.073
-0.75 - -0.50	0.209	0.124	0.062
-0.50 - -0.25	-0.011	0.140	0.054
-0.25 - 0.00	0.067	0.166	0.060
0.00 - 0.25	0.272	0.200	0.075
0.25 - 0.50	-0.081	0.225	0.065
0.50 - 0.75	0.404	0.280	0.081
0.75 - 1.00	0.226	0.461	0.137

Table 28: The luminosity-weighted average of the CP-odd observable Δ_{+-}^{CP} (in units of picobarns / 0.25) measured from the $W \to \ell\nu$ decay channel. s_{stat}^{Δ} denotes the statistical uncertainty and s_{sys}^{Δ} denotes the systematic uncertainty.

$\cos\theta_W$	$\Delta_{+-}^{CP\hat{T}}$	s_{stat}^{Δ}	s_{sys}^{Δ}
-1.00 - -0.75	0.189	0.093	0.073
-0.75 - -0.50	-0.157	0.124	0.062
-0.50 - -0.25	-0.231	0.140	0.054
-0.25 - 0.00	-0.054	0.166	0.060
0.00 - 0.25	0.275	0.200	0.075
0.25 - 0.50	-0.371	0.225	0.065
0.50 - 0.75	-0.199	0.280	0.081
0.75 - 1.00	0.135	0.461	0.137

Table 29: The luminosity-weighted average of the CP$\hat{T}$-odd observable $\Delta_{+-}^{CP\hat{T}}$ (in units of picobarns / 0.25) measured from the $W \to \ell\nu$ decay channel. s_{stat}^{Δ} denotes the statistical uncertainty and s_{sys}^{Δ} denotes the systematic uncertainty.

$\cos\theta_W$	Δ_{+0}^{CP}	s_{stat}^{Δ}	s_{sys}^{Δ}
-1.00 - -0.75	-0.004	0.078	0.043
-0.75 - -0.50	-0.056	0.102	0.065
-0.50 - -0.25	0.036	0.113	0.048
-0.25 - 0.00	-0.001	0.130	0.056
0.00 - 0.25	0.313	0.148	0.067
0.25 - 0.50	-0.276	0.156	0.052
0.50 - 0.75	0.020	0.185	0.046
0.75 - 1.00	0.333	0.285	0.102

Table 30: The luminosity-weighted average of the CP-odd observable Δ_{+0}^{CP} (in units of picobarns / 0.25) measured from the $W \to \ell\nu$ decay channel. s_{stat}^{Δ} denotes the statistical uncertainty and s_{sys}^{Δ} denotes the systematic uncertainty.

$\cos\theta_W$	$\Delta_{+0}^{CP\hat{T}}$	s_{stat}^{Δ}	s_{sys}^{Δ}
-1.00 - -0.75	-0.068	0.078	0.043
-0.75 - -0.50	0.119	0.102	0.065
-0.50 - -0.25	0.079	0.113	0.048
-0.25 - 0.00	-0.077	0.130	0.056
0.00 - 0.25	-0.136	0.148	0.067
0.25 - 0.50	-0.090	0.156	0.052
0.50 - 0.75	-0.146	0.185	0.046
0.75 - 1.00	-0.086	0.285	0.102

Table 31: The luminosity-weighted average of the $CP\hat{T}$-odd observable $\Delta_{+0}^{CP\hat{T}}$ (in units of picobarns / 0.25) measured from the $W \to \ell\nu$ decay channel. s_{stat}^{Δ} denotes the statistical uncertainty and s_{sys}^{Δ} denotes the systematic uncertainty.

$\cos\theta_W$	Δ_{-0}^{CP}	s_{stat}^{Δ}	s_{sys}^{Δ}
-1.00 - -0.75	-0.072	0.057	0.056
-0.75 - -0.50	0.005	0.082	0.045
-0.50 - -0.25	0.081	0.101	0.052
-0.25 - 0.00	-0.019	0.129	0.044
0.00 - 0.25	0.147	0.166	0.056
0.25 - 0.50	-0.368	0.197	0.060
0.50 - 0.75	-0.181	0.259	0.072
0.75 - 1.00	0.479	0.424	0.180

Table 32: The luminosity-weighted average of the CP-odd observable Δ_{-0}^{CP} (in units of picobarns / 0.25) measured from the $W \to \ell\nu$ decay channel. s_{stat}^{Δ} denotes the statistical uncertainty and s_{sys}^{Δ} denotes the systematic uncertainty.

$\cos\theta_W$	$\Delta_{-0}^{CP\hat{T}}$	s_{stat}^{Δ}	s_{sys}^{Δ}
-1.00 - -0.75	-0.018	0.057	0.056
-0.75 - -0.50	0.030	0.082	0.045
-0.50 - -0.25	0.196	0.101	0.052
-0.25 - 0.00	-0.082	0.129	0.044
0.00 - 0.25	-0.130	0.166	0.056
0.25 - 0.50	0.038	0.197	0.060
0.50 - 0.75	0.060	0.259	0.072
0.75 - 1.00	0.188	0.424	0.180

Table 33: The luminosity-weighted average of the $CP\hat{T}$-odd observable $\Delta_{-0}^{CP\hat{T}}$ (in units of picobarns / 0.25) measured from the $W \to \ell\nu$ decay channel. s_{stat}^{Δ} denotes the statistical uncertainty and s_{sys}^{Δ} denotes the systematic uncertainty.

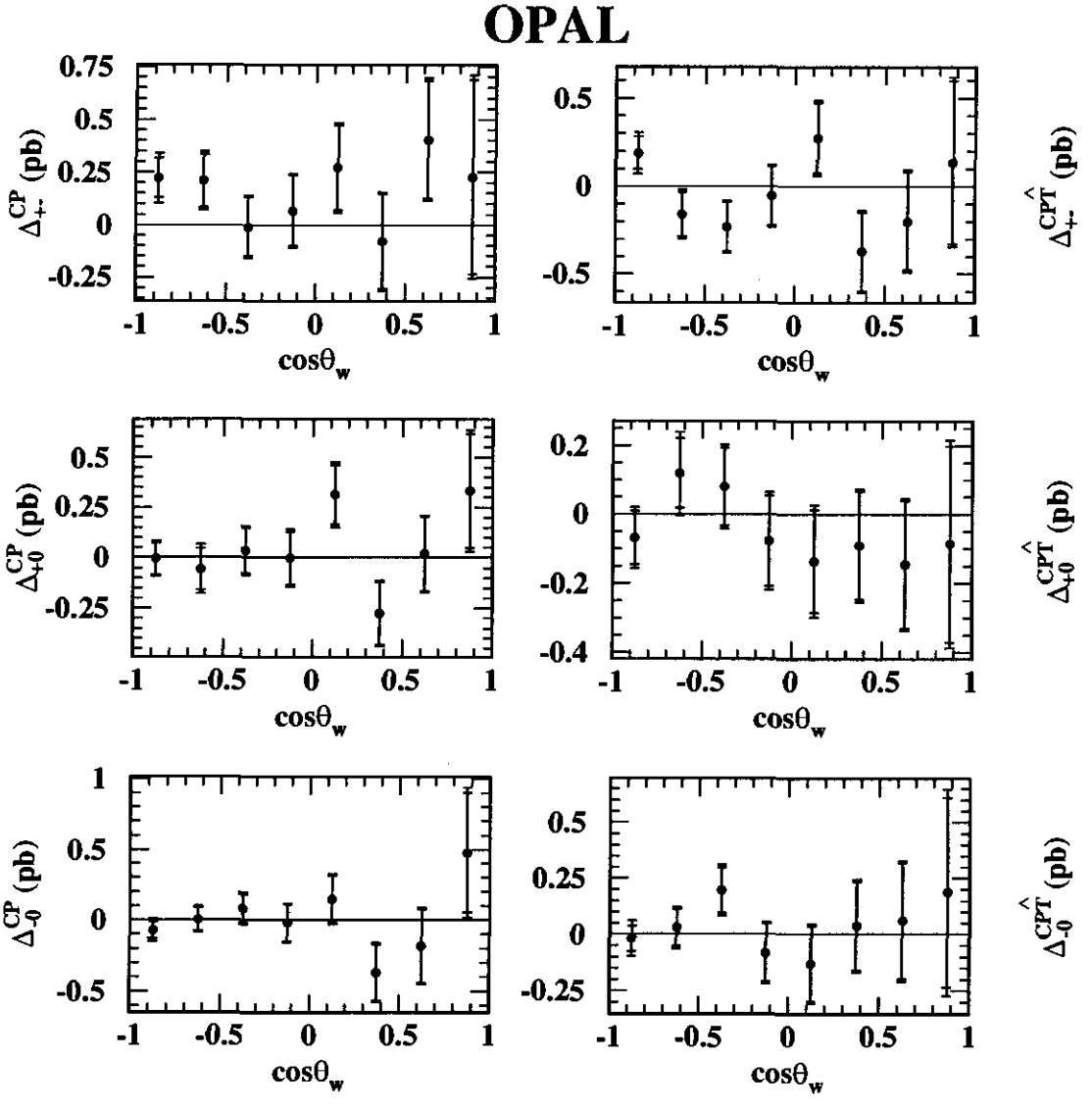

Figure 49: The luminosity-weighted average of the CP-odd and CP$\hat{\text{T}}$-odd observables of section 2.8, where the average is over the eight nominal centre-of-mass energies and over the $\cos\theta_W$ bin width. The observables are measured in units of picobarns and shown as functions of $\cos\theta_W$. The points show the data after detector correction. The inner error bars show the statistical uncertainties and the outer error bars show the total uncertainties including both the statistical and systematic contributions. The solid lines show the SM tree-level prediction.

9 Discussion and conclusions

A spin density matrix analysis of W bosons pair-produced at LEP has been presented. The diagonal elements of the SDM, the differential polarised cross-sections and the fractions of longitudinal polarisation all show good agreement with the SM prediction for each of the analysed data samples and for their luminosity-weighted average. The results are also consistent with the fraction of longitudinal polarisation recently measured by the L3 collaboration at LEP using pairs of W bosons decaying to the $q\bar{q}'e\nu$ and $q\bar{q}'\mu\nu$ final states [22], $f_L = (21.8 \pm 2.7 \pm 1.6)\%$, and preliminary results from Delphi [85], $f_L = (24.9 \pm 3.2)\%$. It is hoped that there will be a future combined measurement of the W polarisation results from the three contributing LEP experiments [20]. A naive combination of the three results using the BLUE technique yields a value of $f_L = (23.6 \pm 1.5 \pm 1.3)\%$, where the systematic uncertainty on the Delphi result was estimated by the arithmetic mean of the L3 and OPAL systematic uncertainties, and the systematic uncertainties of all three experiments were assumed to be 100% correlated to each other. If the systematic uncertainties are assumed to be completely uncorrelated between the experiments then the BLUE combined average becomes $f_L = (23.5 \pm 1.5 \pm 0.8)\%$.

LEP is not the only collider facility at which the polarisation of W bosons can be measured. The CDF collaboration at the Tevatron proton anti-proton collider based at Fermilab have published a measurement of the helicity states of W bosons produced in decays of the top quark [87], and a similar study is being pursued by the D0 collaboration [88]. However, the production of W bosons from top quark decay does not involve the TGC vertex at tree-level and these measurements are therefore complementary to those made at LEP. A more direct comparison of the LEP and Tevatron results can be made by studying their respective measurements of the anomalous TGC couplings [16,17].

[20] A preliminary study of the W polarisation using data from the other LEP experiment, Aleph, can he found at [86].

In the future, more precise measurements of many of the TGC parameters are expected be made at the Large Hadron Collider (LHC) through analysis of $W\gamma$ and WZ production [89]. The speculative future Linear Collider (LC) will be the next experimental environment in which the pair-production of W bosons and their polarisations can be easily investigated [90]. It is hoped that some of the techniques developed in this thesis may have application in a future LC SDM analysis.

One interesting aspect of the $e^+e^- \to W^+W^-$ physics which has not been specifically explored in this thesis is that of the coupling between two longitudinally polarised W bosons. At high energies the Higgs boson Feynman diagram shown in figure 5 is required in the SM to prevent the production rate of longitudinally polarised W bosons diverging unphysically. However, if the Higgs boson is absent or has a mass above a few hundred GeV then additional new physics is required. In one approach, the divergence can be prevented if the strength of the coupling between longitudinal modes of the W bosons becomes stronger than the strength predicted by the SM [91]. The relevant measurement of the element ρ_{0000} of the full WW SDM of equation (26) is difficult to make because the biases introduced by the detector correction are expected to be comparatively large. However, a preliminary analysis by the author of this thesis using the OPAL data yields a luminosity-weighted average measurement of $f_{LL} = (13.9 \pm 3.8)\%$, where only the *statistical uncertainty* has been evaluated. This result was obtained using a detector correction with 8 bins in $\cos\theta_W$, 7 bins in $\cos\theta^*_\ell$, and 7 bins in $\cos\theta^*_q$. No bias correction has been evaluated or applied. This result is in reasonable agreement with the SM prediction from the KandY generator-level MC samples of $f_{LL} = (8.8 \pm 0.2)\%$. Further investigation of this measurement at future machines with higher luminosity could prove fruitful.

In addition to the diagonal elements of the $W^- \to \ell^-\bar{\nu}_\ell$ and $W^+ \to \ell^+\bar{\nu}_\ell$ SDMs, the off-diagonal elements of these matrices have been calculated and show good agreement with the SM MC predictions. No evidence was found for CP violation in WW production,

although the statistical precision of the analysis was not high enough to measure loop-level effects. The absence of CP-violating effects in this model-independent study places loose limits on the possible values of the CP-violating TGC parameters ($\tilde{\kappa}_V$, $\tilde{\lambda}_V$, g_Z^4) [14], which are constrained to be of the order $\Delta_{\tau\tau'}^{\mathrm{CP}}/\sigma$, where σ is the total unpolarised cross-section for the $\mathrm{e^+e^-} \to \mathrm{W^+W^-} \to \mathrm{q\bar{q}'}\ell\nu_\ell$ reaction [28]. The CP-odd observable $\Delta_{+-}^{\mathrm{CP}}$ showed the largest deviation from zero with a luminosity-weighted average value of $0.33 \pm 0.17 \pm 0.06$ picobarns. It follows from this result that the CP-violating TGC parameters are expected to be of order $\mathcal{O}(10^{-1})$ or less on average in the centre-of-mass energy range covered by this analysis. Future determinations of these parameters are expected to be published by all four LEP collaborations.

Studies of the interactions between the electroweak gauge bosons have formed a major sub-discipline of particle physics for the past two decades. The results from the analysis presented in this thesis form part of the large framework of electroweak measurements which confirm that the SM provides an accurate description of the nature of matter at currently accessible energies. However, there is a widespread expectation in the particle physics community that over the next two decades the SM will be shown to be insufficient to describe physics at energies much above the electroweak symmetry-breaking scale. Analyses of the polarisation of W bosons may prove to be an important probe of this new physics and are likely to play a pertinent role in particle physics for the foreseeable future.

Bibliography

[1] Particle Data Group, K. Hagiwara *et al.*, Phys. Rev. **D66** (2002) 1.

[2] P. Renton, "Electroweak Interactions", Cambridge University Press (1999).

[3] SNO Collaboration, Q.R. Ahmad *et al.*, Phys. Rev. Lett. **89** (2002) 011301.

[4] P.W. Higgs, Phys. Rev. **145** (1966) 1156.

[5] OPAL Collaboration, G. Abbiendi *et al.*, Phys. Lett. **B447** (1999) 134;
OPAL Collaboration, G. Abbiendi *et al.*, Phys. Lett. **B551** (2003) 35.

[6] C.S. Wu *et al.*, Phys. Rev. **105** (1957) 1413.

[7] I.J.R. Aitchison, A.J.G. Hey, "Gauge Theories in Particle Physics", Institute of Physics Publishing (1993).

[8] G.J. Gounaris, J. Laysaac and F.M. Renard, Phys. Rev. **D61** (2000) 073013;
G.J. Gounaris, J. Laysaac and F.M. Renard, Phys. Rev. **D62** (2000) 073012;
G.J. Gounaris, J. Laysaac and F.M. Renard, Phys. Rev. **D62** (2000) 073013.

[9] G. Belanger *et al.*, Eur. Phys. J. **C13** (2000) 283;
W.J. Stirling, A. Werthenbach, Eur. Phys. J. **C14** (2000) 103.

[10] Physics at LEP2, edited by G. Altarelli, T. Sjöstrand and F. Zwirner, CERN 96-01 Vol. 2, 11.

[11] G.J. Gounaris and F.M. Renard, Z. Phys. **C59** (1993) 133.

[12] K. Hagiwara, R.D. Peccei, D. Zeppenfeld and K. Hikasa, Nucl. Phys. **B282** (1987) 253.

[13] F. Boudjema and C. Hamzaoui, Phys. Rev. **D43** (1991) 3748.

[14] Physics at LEP2, edited by G. Altarelli, T. Sjöstrand and F. Zwirner, CERN 96-01 Vol. 1, 525.

[15] M. Beccaria, F.M. Renard, S. Spagnolo and C. Verzegnassi, Phys. Lett. **B448** (1999) 129;
S. Alam, S. Dawson and R. Szalapski, Phys. Rev. **D57** (1998) 1577.

[16] CDF Collaboration, F. Abe, *et al.*, Phys. Rev. Lett. **78** (1997) 4536;
D0 Collaboration, B. Abbott, *et al.*, Phys. Rev. **D62** (2000) 052005.

[17] J. Alcaraz, *et al.*, "A combination of the preliminary results on gauge boson couplings measured by the LEP experiments", LEP-EWWG/2003-02, pre-print **hep-ex/0312023**.

[18] Martin L. Perl, "High Energy Hadron Physics", John Wiley and Sons (1974).

[19] D. Brandt *et al.*, Rep. Prog. Phys. **63** (2000) 939.

[20] K. Hikasa, Phys. Rev. **D33** (1986) 3203.

[21] M. Diehl, O. Nachtmann, F. Nagel, Eur. Phys. J. **C32** (2003) 17.

[22] L3 Collaboration, P. Achard *et al.*, Phys. Lett. **B557** (2003) 147.

[23] OPAL Collaboration, G. Abbiendi *et al.*, Eur. Phys. J. **C19** (2001) 229.

[24] OPAL Collaboration, G. Abbiendi *et al.*, Eur. Phys. J. **C8** (1999) 191.

[25] G. Gounaris, J. Layssac, G. Moultaka and F.M. Renard, Int. J. Mod. Phys. **A8** (1993) 3285.

[26] R.G. Sachs, "The Physics of Time Reversal", University of Chicago Press (1987).

[27] M.S. Baek, S.Y. Choi and K. Hagiwara, "CP violation at electron-positron colliders", Proceedings of the *KEK meetings on* CP *violation and its origins* (1997), pre-print **hep-ph/9708333**.

[28] G. Gounaris, D. Schildknecht and F.M. Renard, Phys. Lett. **B263** (1991) 291.

[29] D. Chang, W. Keung and I. Phillips, Phys. Rev. **D48** (1993) 4045.

[30] ALEPH Collaboration, A. Heister *et al.*, Eur. Phys. J. **C21** (2001) 423.

[31] M.V. Romalis, W.C. Griffiths, J.P. Jacobs and E.N. Forston, Phys. Rev. Lett. **86** (2001) 2505.

[32] OPAL Collaboration, OPAL physics note **PN427** (2000).

[33] A. Pukhov *et al.*, pre-print **hep-ph/9908288**.

[34] R. Hemingway, OPAL technical note **TN707** (2001).

[35] D. Brandt *et al.*, Rep. Prog. Phys. **63** (2000) 939.

[36] R. Hawkings, OPAL technical note **TN676** (2001).

[37] R.W. Assmann, "The regimes of polarization in a high energy e^+e^- storage ring", *Proceedings of the 1999 particle accelerator conference* (1999).

[38] OPAL Collaboration, K. Ackerstaff *et al.*, Phys. Lett. **B389** (1996) 416;
OPAL Collaboration, K. Ackerstaff *et al.*, Eur. Phys. J. **C1** (1998) 395;
OPAL Collaboration, G. Abbiendi *et al.*, Eur. Phys. J. **C8** (1999) 191;
OPAL Collaboration, G. Abbiendi *et al.*, Phys. Lett. **B493** (2000) 249;
OPAL Collaboration, OPAL physics note **PN420** (1999);
OPAL Collaboration, OPAL physics note **PN469** (2001).

[39] OPAL Collaboration, G. Abbiendi *et al.*, Eur. Phys. J. **C19** (2001) 587;
OPAL Collaboration, K. Ackerstaff *et al.*, Phys. Lett. **B412** (1997) 225;
OPAL Collaboration, K. Ackerstaff *et al.*, Eur. Phys. J. **C6** (1999) 1;
OPAL Collaboration, G. Abbiendi *et al.*, Eur. Phys. J. **C33** (2004) 173.

[40] OPAL Collaboration, M.Z. Akrawy *et al.*, Phys. Lett. **B257** (1991) 531;
OPAL Collaboration, K. Ackerstaff *et al.*, Eur. Phys. J. **C1** (1998) 21;
OPAL Collaboration, G. Abbiendi *et al.*, Eur. Phys. J. **C26** (2003) 331.

[41] OPAL Collaboration, G. Abbiendi *et al.*, Phys. Lett. **B476** (2000) 256 ;
OPAL Collaboration, G. Abbiendi *et al.*, Eur. Phys. J. **C32** (2004) 303.

[42] OPAL Collaboration, G. Abbiendi *et al.*, Phys. Lett. **B580** (2004) 17.

[43] OPAL Collaboration, G. Abbiendi *et al.*, OPAL paper **395** (2004) submitted to Phys. Rev. D, preprint CERN-PH-EP-2004-003.

[44] OPAL Collaboration, K. Ahmet *et al.*, Nucl. Instr. Meth. **A305** (1991) 275.

[45] S. de Jong on behalf of the OPAL Collaboration, Nucl. Instr. Meth. **A386** (1997) 23.

[46] M. Hauschild *et al.* on behalf of the OPAL Collaboration, Nucl. Instr. Meth. **A314** (1992) 74;
O. Biebel *et al.* on behalf of OPAL Collaboration, Nucl. Instr. Meth. **A323** (1992) 169.

[47] G. Aguillion *et al.* on behalf of the OPAL Collaboration, Nucl. Instr. Meth. **A417** (1998) 266.

[48] B.E. Anderson *et al.*, IEEE Trans. Nucl. Sci. **41** (1994) 845.

[49] M. Arignon *et al.* on behalf of the OPAL Collaboration, Nucl. Instr. Meth. **A313** (1992) 103.

[50] S. Bethke, Z. Kunszt, D.E. Soper, W.J. Stirling, Nucl. Phys. **B370** (1992) 310.

[51] OPAL Collaboration, OPAL paper **PR398** (2004) submitted to Eur. Phys. J. C, preprint CERN-EP-2004-008;
OPAL Collaboration, OPAL paper **PR379** (2003) submitted to Eur. Phys. J. C, preprint CERN-EP-2003-031.

[52] LEP Energy Working Group, A. Blondel *et al.*, Eur. Phys. J. **C11** (1999) 573;
LEP Energy Working Group Notes 99-01, 00-01, 01-01;
OPAL Collaboration, G. Abbiendi *et al.*, OPAL Dispatch DP1860 (in OPAL editorial process).

[53] J. Allison *et al.*, Nucl. Instr. Meth. **A317** (1992) 47.

[54] S. Jadach *et al.*, Phys. Rev. **D61** (2000) 113010;
S. Jadach *et al.*, Comput. Phys. Commun. **140** (2001) 432.

[55] S. Jadach *et al.*, Comput. Phys. Commun. **140** (2001) 475.

[56] M. Skrzypek *et al.*, Comput. Phys. Commun. **94** (1996) 216;
M. Skrzypek *et al.*, Phys. Lett. **B372** (1996) 289;
S. Jadach *et al.*, Comput. Phys. Commun. **119** (1999) 272.

[57] F.A. Berends, R. Pittau and R. Kleiss, Comput. Phys. Commun. **85** (1995) 437;
F.A. Berends and A.I. van Sighem, Nucl. Phys. **B454** (1995) 467.

[58] T. Sjöstrand, Comput. Phys. Commun. **82** (1994) 74.

[59] G. Marchesini *et al.*, Comput. Phys. Commun. **67** (1992) 465.

[60] L. Lönnblad, Comput. Phys. Commun. **71** (1992) 15.

[61] S. Jadach, B.F.L. Ward and Z. Wąs, Phys. Lett. **B449** (1999) 97;
S. Jadach, B.F.L. Ward and Z. Wąs, Comput. Phys. Commun. **130** (2000) 260.

[62] E. Torrence *et al.*, WW115 manual, internal OPAL publication (2002).

[63] M. Thomson, OPAL technical note **TN635** (2000).

[64] OPAL Collaboration, G. Abbiendi *et al.*, Phys. Lett. **B493** (2000) 249.

[65] OPAL Collaboration, K. Ackerstaff *et al.*, Eur. Phys. J. **C1** (1998) 395.

[66] OPAL Collaboration, G. Abbiendi *et al.*, Eur. Phys. J. **C19** (2001) 1;
OPAL Collaboration, G. Abbiendi *et al.*, Eur. Phys. J. **C33** (2004) 463.

[67] M. Morii, OPAL technical note **TN190** (1993).

[68] N. Brown and W.J. Stirling, Phys. Lett. **B252** (1990) 657;
S. Catani *et al.*, Phys. Lett. **B269** (1991) 432;
S. Bethke, Z. Kunszt, D. Soper and W.J. Stirling, Nucl. Phys. **B370** (1992) 310;
N. Brown and W.J. Stirling, Z. Phys. **C53** (1992) 629.

[69] E. Duchovni *et al.*, OPAL technical note **TN306** (1995).

[70] T. Omori *et al.*, OPAL technical note **TN381** (1996);
S. Mihara and S. Yamashita, OPAL technical note **TN575** (1998).

[71] I. Bailey, OPAL technical note **TN660** (2000).

[72] R. Rylko, OPAL technical note **TN332** (1995);
R.L. Coxe and D.A. Glenzinski, OPAL technical note **TN534** (1998).

[73] D.R. Ward and C.P. Ward, OPAL technical note **TN715** (2002).

[74] L. Lyons, "Statistics for nuclear and particle physicists", Cambridge University Press (1986).

[75] A. Höcker and V. Kartvelishvili, Nucl. Instr. Meth. **A372** (1995) 469.

[76] G. D. Agostini, Nucl. Instr. Meth. **A362** (1995) 487.

[77] OPAL Collaboration, K. Ackerstaff *et al.*, Z. Phys. **C74** (1997) 413.

[78] S. Wolfram, "The Mathematica book", 3rd edition, Cambridge University Press (1996).

[79] L. Lyons, D.Gibaut and P. Clifford, Nucl. Instr. Meth. **A270** (1988) 110.

[80] D. Bardin *et al.*, Comput. Phys. Commun. **104** (1997) 161.

[81] OPAL Collaboration, G. Abbiendi *et al.*, Phys. Lett. **B507** (2001) 29.

[82] OPAL Collaboration, G. Abbiendi *et al.*, OPAL Dispatch DP1859 (in OPAL editorial process).

[83] OPAL Collaboration, G. Abbiendi *et al.*, Phys. Lett. **B585** (2004) 223.

[84] HEPDATA: The Durham RAL Databases, Durham Database Group, Durham University (UK), http://www-spires.dur.ac.uk/HEPDATA.

[85] C. De Clercq on behalf of Delphi Collaboration, "Study of W boson polarisations in the reaction $e^+e^- \rightarrow W^+W^-$ at energies between 189 and 208 GeV", presented at *International Europhysics Conference on High Energy Physics* (2003).

[86] D. Fayolle, "Production de paires de Z et polarisation des W à LEP2 avec le détecteur ALEPH", PhD thesis, Université Blaise Pascal (2002).

[87] CDF Collaboration, T. Affolder *et al.*, Phys. Rev. Lett. **84** (2000) 216.

[88] Y. Kulik on behalf of the D0 Collaboration, "Recent Top Quark Results at the D0", to appear in the proceedings of *39th Rencontres De Moriond On Electroweak Interactions And Unified Theories* (2004).

[89] M. Dobbs, "Probing the Three Gauge-boson Couplings in 14 TeV Proton-Proton Collisions", PhD thesis, University of Victoria (2002).

[90] F. Boudjema, "Aspects of W Physics at the Linear Collider.", proceedings of *Physics and Experiments with Linear Colliders*, Vol 1 (1996), preprint **hep-ph/9701409**;
W. Beenakker, Acta. Phys. Polon. **B28** (1997) 1461, preprint **hep-ph/9704401**;
K. Mönig, "Physics of Electroweak Gauge Bosons", to appear in *Linear Collider Physics in the New Millenium*, World Scientific, preprint **hep-ph/0303023**.

[91] R.S. Chivukula, M.J. Dugan, M. Golden and E.H. Simmons, Ann. Rev. Nucl. Part. Sci. **45** (1995) 255.

[92] J.W. Gary, PX v1.08 manual, internal OPAL publication (1993).

[93] G. Cowan, "A survey of unfolding methods for particle physics", Proceedings of *Advanced Statistical Techniques in Particle Physics* (2002), IPPP/02/39.

A The density matrix

The density matrix describes physical states which are both statistical and quantum mechanical in nature. The wave-function of a pure quantum mechanical system, Ψ, can be expressed as a coherent sum over a complete set of accessible eigenstates, ϕ_i, as in equation (93).

$$\Psi = \sum_{i=1}^{n} a_i \phi_i \tag{93}$$

The expectation value of some observable, O, is given by,

$$< O > = \sum_{i=1}^{n} \sum_{j=1}^{n} a_i a_j^* < \phi_i | O | \phi_j > \quad . \tag{94}$$

A more general system may be in one of N different quantum mechanical states, Ψ_k, with some statistical probability, p_k. The expectation value of O in such a system is then given by,

$$< O > = \sum_{k=1}^{N} \sum_{i=1}^{n} \sum_{j=1}^{n} a_{i,k} a_{j,k}^* p_k < \phi_i | O | \phi_j > \quad . \tag{95}$$

This situation can arise where we do not have complete knowledge of a system's history. In the case of WW production at LEP2 the initial e^+e^- polarisations for a particular event are unknown. The resulting W-pair system is therefore in one of two possible pure quantum mechanical states [21], i.e. $N = 2$.

Equation (95) can be rewritten as,

$$< O > = \sum_{i=1}^{n} \sum_{j=1}^{n} \rho_{i,j} < \phi_i | O | \phi_j > \quad , \tag{96}$$

where the entity, ρ, is the density matrix for the basis ϕ, given explicitly by,

$$\rho_{i,j} = \sum_{k=1}^{N} a_{i,k} a_{j,k}^* p_k \quad . \tag{97}$$

[21] Although there are four possible polarisations for e^+e^- only two of these can result in a W pair at tree level in the SM if the electron and positron are travelling at relativistic velocities in the centre-of-mass frame.

Calculations carried out in this paper use the density matrix with a basis of helicity eigenstates. The WW density matrix is found using equation (98) which relates it to the e^+e^- density matrix through the helicity amplitudes, F, of section 2.4.

$$\rho^{WW}_{\tau,\tau',\bar{\tau},\bar{\tau}'} = \frac{\sum_{\lambda,\bar{\lambda},\lambda',\bar{\lambda}'} F^{(\tau,\bar{\tau};\lambda,\bar{\lambda})} \left(F^{(\tau',\bar{\tau}';\lambda',\bar{\lambda}')}\right)^* \rho^{e^+e^-}_{\lambda,\lambda',\bar{\lambda},\bar{\lambda}'}}{\sum_{\tau,\bar{\tau},\lambda,\bar{\lambda},\lambda',\bar{\lambda}'} F^{(\tau,\bar{\tau};\lambda,\bar{\lambda})} \left(F^{(\tau,\bar{\tau};\lambda',\bar{\lambda}')}\right)^* \rho^{e^+e^-}_{\lambda,\lambda',\bar{\lambda},\bar{\lambda}'}} \tag{98}$$

Assuming that the electrons and positrons are unpolarised, their density matrix, $\rho^{e^+e^-}_{\lambda,\lambda',\bar{\lambda},\bar{\lambda}'}$, is just the 4×4 identity matrix and equation (98) reduces to,

$$\rho^{WW}_{\tau,\tau',\bar{\tau},\bar{\tau}'} = \frac{\sum_{\lambda,\bar{\lambda}} F^{(\tau,\bar{\tau};\lambda,\bar{\lambda})} \left(F^{(\tau',\bar{\tau}';\lambda,\bar{\lambda})}\right)^*}{\sum_{\tau,\bar{\tau},\lambda,\bar{\lambda}} \left|F^{(\tau,\bar{\tau};\lambda,\bar{\lambda})}\right|^2} \; . \tag{99}$$

B Composition of event samples

This appendix contains the tables detailing the composition of the data samples at each nominal centre-of-mass energy after the full selection of section 6.3, as estimated from the MC samples of table 4. Tables 34 to 41 show the admixture of pseudo-data events from the individual signal and background sources which were categorized as $q\bar{q}'e\nu$, $q\bar{q}'\mu\nu$ or $q\bar{q}'\tau\nu$ during the event selection, where the $q\bar{q}'\tau\nu$ category includes all four of the τ-lepton decay modes considered in the likelihood selection of section 6.3.5. The numbers in the tables are normalised to the total number of events passing the selection.

	Generated event type								
Reconstructed event type	$e^+e^-\gamma\gamma$	$q\bar{q}'$	$q\bar{q}'\ell\nu$ (not CC03)	$\ell\nu\ell\nu$	$q\bar{q}q\bar{q}$	$q\bar{q}'e\nu$ (CC03)	$q\bar{q}'\mu\nu$ (CC03)	$q\bar{q}'\tau\nu$ (CC03)	
$q\bar{q}'e\nu$	0.00	0.43	0.99	0.01	0.02	32.79	0.03	1.26	35.52
$q\bar{q}'\mu\nu$	0.00	0.17	0.34	0.00	0.09	0.05	33.29	1.34	35.30
$q\bar{q}'\tau\nu$	0.03	1.44	1.82	0.00	0.14	1.02	1.43	23.29	29.18
	0.03	2.04	3.15	0.01	0.25	33.86	34.76	25.89	

Table 34: The composition of events passing the total event selection at 183 GeV as calculated from the MC samples listed in section 6.2. Each number shows the percentage of selected events that have a given generated event type and a given reconstructed event type, normalised to the total number of events passing the selection. The far right-hand column and bottommost row show summed totals.

	Generated event type								
Reconstructed event type	$e^+e^-\gamma\gamma$	$q\bar{q}'$	$q\bar{q}'\ell\nu$ (not CC03)	$\ell\nu\ell\nu$	$q\bar{q}q\bar{q}$	$q\bar{q}'e\nu$ (CC03)	$q\bar{q}'\mu\nu$ (CC03)	$q\bar{q}'\tau\nu$ (CC03)	
$q\bar{q}'e\nu$	0.08	0.42	1.15	0.01	0.01	32.14	0.03	1.30	35.14
$q\bar{q}'\mu\nu$	0.00	0.23	0.38	0.00	0.08	0.05	32.89	1.33	34.98
$q\bar{q}'\tau\nu$	0.03	1.55	2.08	0.00	0.20	1.17	1.41	23.43	29.89
	0.11	2.20	3.61	0.01	0.29	33.37	34.33	26.07	

Table 35: The composition of events passing the total event selection at 189 GeV as calculated from the MC samples listed in section 6.2. Each number shows the percentage of selected events that have a given generated event type and a given reconstructed event type, normalised to the total number of events passing the selection. The far right-hand column and bottommost row show summed totals.

	Generated event type								
Reconstructed event type	$e^+e^-\gamma\gamma$	$q\bar{q}'$	$q\bar{q}'\ell\nu$ (not CC03)	$\ell\nu\ell\nu$	$q\bar{q}q\bar{q}$	$q\bar{q}'e\nu$ (CC03)	$q\bar{q}'\mu\nu$ (CC03)	$q\bar{q}'\tau\nu$ (CC03)	
$q\bar{q}'e\nu$	0.06	0.38	1.30	0.01	0.02	32.05	0.03	1.32	35.17
$q\bar{q}'\mu\nu$	0.00	0.27	0.31	0.01	0.10	0.06	32.56	1.37	34.69
$q\bar{q}'\tau\nu$	0.10	1.44	2.39	0.00	0.23	1.17	1.42	23.38	30.14
	0.16	2.09	4.01	0.02	0.35	33.28	34.01	26.08	

Table 36: The composition of events passing the total event selection at 192 GeV as calculated from the MC samples listed in section 6.2. Each number shows the percentage of selected events that have a given generated event type and a given reconstructed event type, normalised to the total number of events passing the selection. The far right-hand column and bottommost row show summed totals.

	Generated event type								
Reconstructed event type	$e^+e^-\gamma\gamma$	$q\bar{q}'$	$q\bar{q}'\ell\nu$ (not CC03)	$\ell\nu\ell\nu$	$q\bar{q}q\bar{q}$	$q\bar{q}'e\nu$ (CC03)	$q\bar{q}'\mu\nu$ (CC03)	$q\bar{q}'\tau\nu$ (CC03)	
$q\bar{q}'e\nu$	0.11	0.52	1.45	0.01	0.02	31.75	0.04	1.36	35.26
$q\bar{q}'\mu\nu$	0.00	0.26	0.39	0.01	0.14	0.07	32.66	1.35	34.89
$q\bar{q}'\tau\nu$	0.03	1.26	2.39	0.00	0.21	1.18	1.42	23.35	29.85
	0.14	2.05	4.23	0.01	0.37	33.01	34.11	26.07	

Table 37: The composition of events passing the total event selection at 196 GeV as calculated from the MC samples listed in section 6.2. Each number shows the percentage of selected events that have a given generated event type and a given reconstructed event type, normalised to the total number of events passing the selection. The far right-hand column and bottommost row show summed totals.

	Generated event type								
Reconstructed event type	$e^+e^-\gamma\gamma$	$q\bar{q}'$	$q\bar{q}'\ell\nu$ (not CC03)	$\ell\nu\ell\nu$	$q\bar{q}q\bar{q}$	$q\bar{q}'e\nu$ (CC03)	$q\bar{q}'\mu\nu$ (CC03)	$q\bar{q}'\tau\nu$ (CC03)	
$q\bar{q}'e\nu$	0.06	0.41	1.51	0.01	0.03	31.96	0.05	1.42	35.45
$q\bar{q}'\mu\nu$	0.02	0.29	0.38	0.01	0.15	0.07	32.63	1.46	35.00
$q\bar{q}'\tau\nu$	0.08	1.10	2.54	0.00	0.25	1.17	1.49	22.92	29.55
	0.16	1.80	4.43	0.02	0.43	33.20	34.17	25.79	

Table 38: The composition of events passing the total event selection at 200 GeV as calculated from the MC samples listed in section 6.2. Each number shows the percentage of selected events that have a given generated event type and a given reconstructed event type, normalised to the total number of events passing the selection. The far right-hand column and bottommost row show summed totals.

	Generated event type								
Reconstructed event type	$e^+e^-\gamma\gamma$	$q\bar{q}'$	$q\bar{q}'\ell\nu$ (not CC03)	$\ell\nu\ell\nu$	$q\bar{q}q\bar{q}$	$q\bar{q}'e\nu$ (CC03)	$q\bar{q}'\mu\nu$ (CC03)	$q\bar{q}'\tau\nu$ (CC03)	
$q\bar{q}'e\nu$	0.10	0.53	1.64	0.01	0.02	31.84	0.06	1.51	35.71
$q\bar{q}'\mu\nu$	0.00	0.21	0.37	0.01	0.13	0.08	32.40	1.49	34.69
$q\bar{q}'\tau\nu$	0.03	1.03	2.62	0.00	0.26	1.25	1.47	22.94	29.60
	0.13	1.77	4.63	0.02	0.41	33.17	33.93	25.93	

Table 39: The composition of events passing the total event selection at 202 GeV as calculated from the MC samples listed in section 6.2. Each number shows the percentage of selected events that have a given generated event type and a given reconstructed event type, normalised to the total number of events passing the selection. The far right-hand column and bottommost row show summed totals.

	Generated event type								
Reconstructed event type	$e^+e^-\gamma\gamma$	$q\bar{q}'$	$q\bar{q}'\ell\nu$ (not CC03)	$\ell\nu\ell\nu$	$q\bar{q}q\bar{q}$	$q\bar{q}'e\nu$ (CC03)	$q\bar{q}'\mu\nu$ (CC03)	$q\bar{q}'\tau\nu$ (CC03)	
$q\bar{q}'e\nu$	0.09	0.35	1.76	0.01	0.02	31.65	0.05	1.46	35.40
$q\bar{q}'\mu\nu$	0.00	0.26	0.38	0.01	0.18	0.08	32.40	1.52	34.82
$q\bar{q}'\tau\nu$	0.03	1.07	2.87	0.00	0.28	1.37	1.47	22.67	29.78
	0.13	1.69	5.01	0.02	0.48	33.10	33.91	25.66	

Table 40: The composition of events passing the total event selection at 205 GeV as calculated from the MC samples listed in section 6.2. Each number shows the percentage of selected events that have a given generated event type and a given reconstructed event type, normalised to the total number of events passing the selection. The far right-hand column and bottommost row show summed totals.

	Generated event type								
Reconstructed event type	$e^+e^-\gamma\gamma$	$q\bar{q}'$	$q\bar{q}'\ell\nu$ (not CC03)	$\ell\nu\ell\nu$	$q\bar{q}q\bar{q}$	$q\bar{q}'e\nu$ (CC03)	$q\bar{q}'\mu\nu$ (CC03)	$q\bar{q}'\tau\nu$ (CC03)	
$q\bar{q}'e\nu$	0.12	0.45	1.74	0.01	0.03	31.75	0.05	1.46	35.62
$q\bar{q}'\mu\nu$	0.00	0.23	0.40	0.01	0.17	0.09	32.39	1.45	34.73
$q\bar{q}'\tau\nu$	0.09	1.10	2.75	0.00	0.27	1.34	1.53	22.56	29.65
	0.21	1.78	4.90	0.02	0.47	33.18	33.97	25.47	

Table 41: The composition of events passing the total event selection at 207 GeV as calculated from the MC samples listed in section 6.2. Each number shows the percentage of selected events that have a given generated event type and a given reconstructed event type, normalised to the total number of events passing the selection. The far right-hand column and bottommost row show summed totals.

C W rest-frame angles

This appendix briefly describes the method used to extract the angles θ^*_ℓ, ϕ^*_ℓ, θ^*_q and ϕ^*_q from the momentum vectors of the four fermions in a WW $\rightarrow$ $q\bar{q}'\ell\nu$ event. The kinematic fitting procedure of section 6.3.6, processed the measured momentum vectors of the two jets (quark and anti-quark) and the charged lepton (previously identified as an electron, muon or τ-lepton) to calculate estimated momentum vectors for all four fermions. The energy component of the four-momentum for each fermion was obtained trivially by the relativistic energy formula, where the rest-mass of the charged lepton was assumed to be equal to its experimentally-determined value given in table 1, and both the neutrino and the jets were treated as being massless.

The four-momentum of the leptonically decaying W boson was given by the sum of the four-momenta of the charged lepton and neutrino, and the four-momentum of the hadronically decaying W boson was given by the sum of the four-momenta of the two jets. The rest-mass of the W boson in each case was naively given by the relatvistic energy formula. The four-momenta of the charged lepton and neutrino were next Lorentz-transformed to the rest-frame of the leptonically decaying W boson, and the four-momenta of the jets were Lorentz-transformed to the rest-frame of the hadronically decaying W boson. The general form of the transformation of a four-momentum vector p ($p = (E, \vec{p})$) to the rest-frame of a W boson with four-momentum p_{W} ($p_{\mathrm{W}} = (E_{\mathrm{W}}, \vec{p}_{\mathrm{W}})$) and rest-mass m_{W}, was [92],

$$E^* = \frac{p^\mu_{\mathrm{W}} p_\mu}{m_{\mathrm{W}}} \tag{100}$$

$$\vec{p}^* = \vec{p} - f \cdot \vec{p}_{\mathrm{W}} \tag{101}$$

where the momentum vector in the rest-frame is denoted p^*, and the factor 'f' was given by,

$$f = \frac{E^* + E}{E_{\mathrm{W}} + m_{\mathrm{W}}} \, . \tag{102}$$

A rotated frame was now defined with a z^*-axis parallel to $\vec{p}_W$. The y^*-axis was then defined as,

$$\vec{y}^* = \vec{z} \times \vec{z}^* , \tag{103}$$

where $\vec{z}$ was parallel to the z-axis in the OPAL Master Reference System. Finally, the x^*-axis was defined by,

$$\vec{x}^* = \vec{y}^* \times \vec{z}^* , \tag{104}$$

so as to give a complete orthogonal right-handed set of axes.

The cosine of the polar angle of a fermion momentum vector in the new frame was given by,

$$\cos\theta^* = \frac{\vec{p}^* . \vec{z}^*}{|\vec{p}^*||\vec{z}^*|} . \tag{105}$$

The sine and cosine of the azimuthal angle of a fermion momentum vector in the new frame were given by,

$$\sin\phi^* = \frac{\vec{p}^* . \vec{y}^*}{|\vec{p}^*||\vec{y}^*|} \tag{106}$$

$$\cos\phi^* = \frac{\vec{p}^* . \vec{x}^*}{|\vec{p}^*||\vec{x}^*|} , \tag{107}$$

and the value of the azimuthal angle itself then followed from,

$$\phi^* = \arctan\left(\frac{\sin\phi^*}{\cos\phi^*}\right) , \tag{108}$$

where the appropriate solution for arctan was determined by the signs of $\sin\phi^*$ and $\cos\phi^*$.

D Supplementary figures

This appendix contains supplementary figures showing the angular distributions measured in the analysis and the form of the detector correction applied to the data. Section D.1 contains figures showing the angular distributions obtained from the data at each nominal centre-of-mass energy after correction for detector effects. Section D.2 contains figures illustrating the angular dependence of the efficiency and the efficiency-like scaling corrections at each nominal centre-of-mass energy, and section D.3 contains similar figures for the angular dependence of the purity.

D.1 Corrected Angular Distributions

Figures 50 to 54 show the measured angular distributions of the W bosons and their decay products at each of the eight nominal centre-of-mass energies after being corrected for the detector effects described in section 6.4.2.

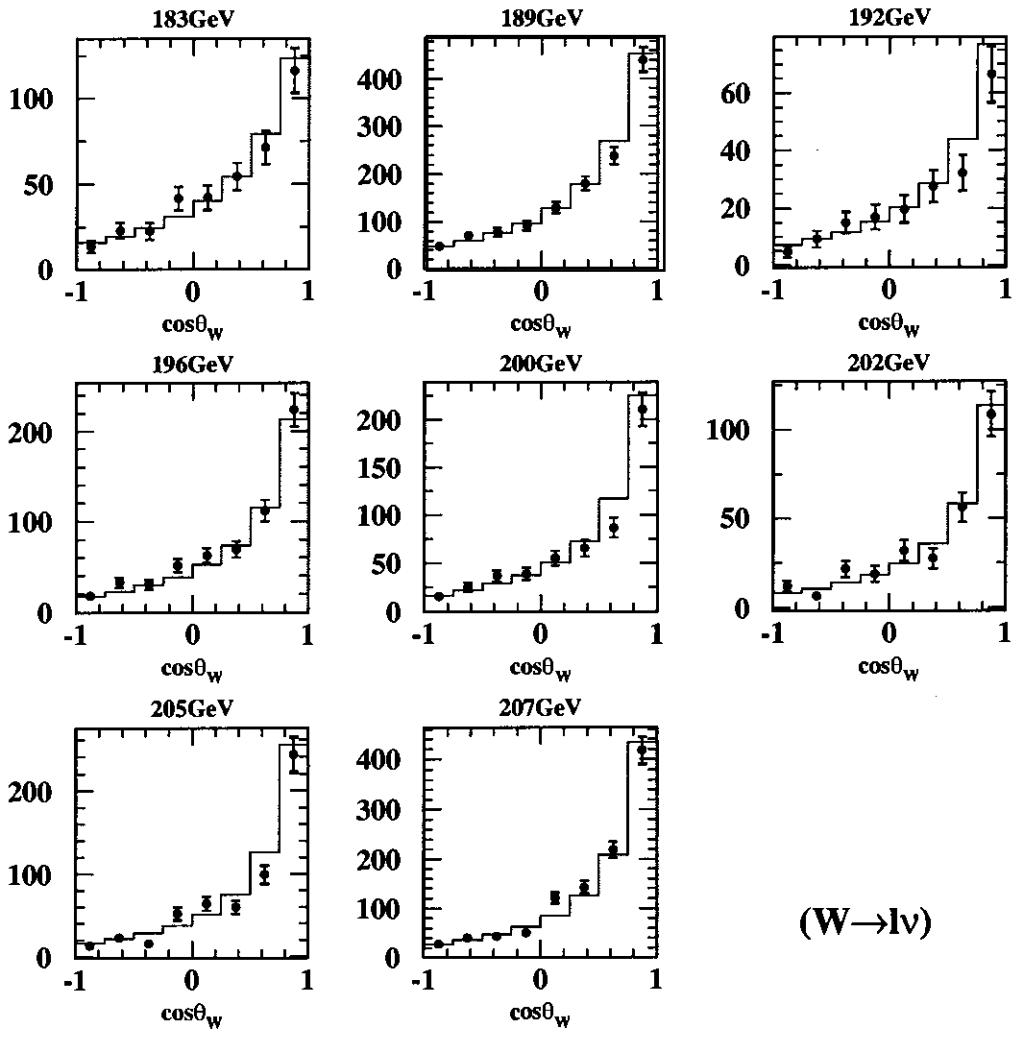

Figure 50: The measured $\cos\theta_W$ distributions obtained from the data at each nominal centre-of-mass energy following the detector correction. The points show the measured values from the data and the histogram shows the prediction from SM generator-level MC samples. The inner error bars represent the statistical uncertainties and the outer error bars represent the total uncertainties including systematic effects.

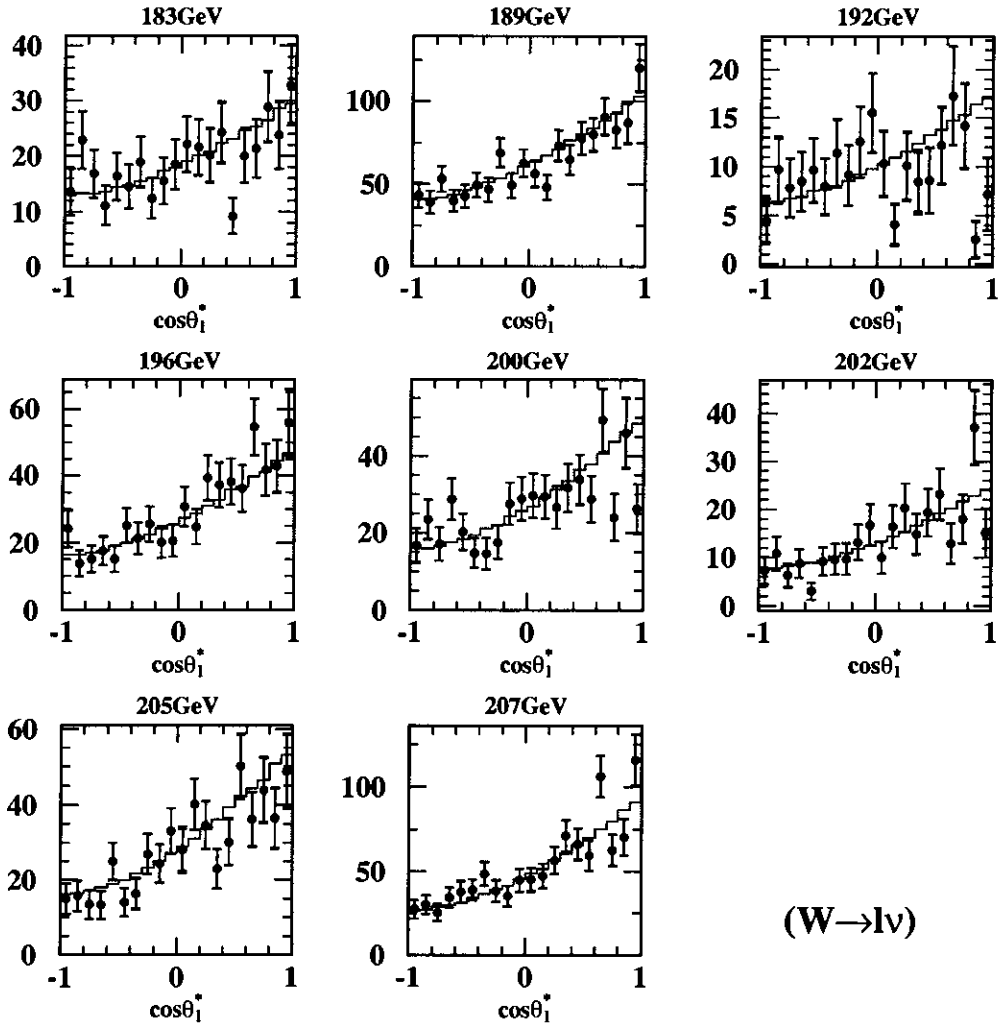

Figure 51: The measured $\cos\theta^*_\ell$ distributions obtained from the data at each nominal centre-of-mass energy following the detector correction. The points show the measured values from the data and the histogram shows the prediction from SM generator-level MC samples. The inner error bars represent the statistical uncertainties and the outer error bars represent the total uncertainties including systematic effects.

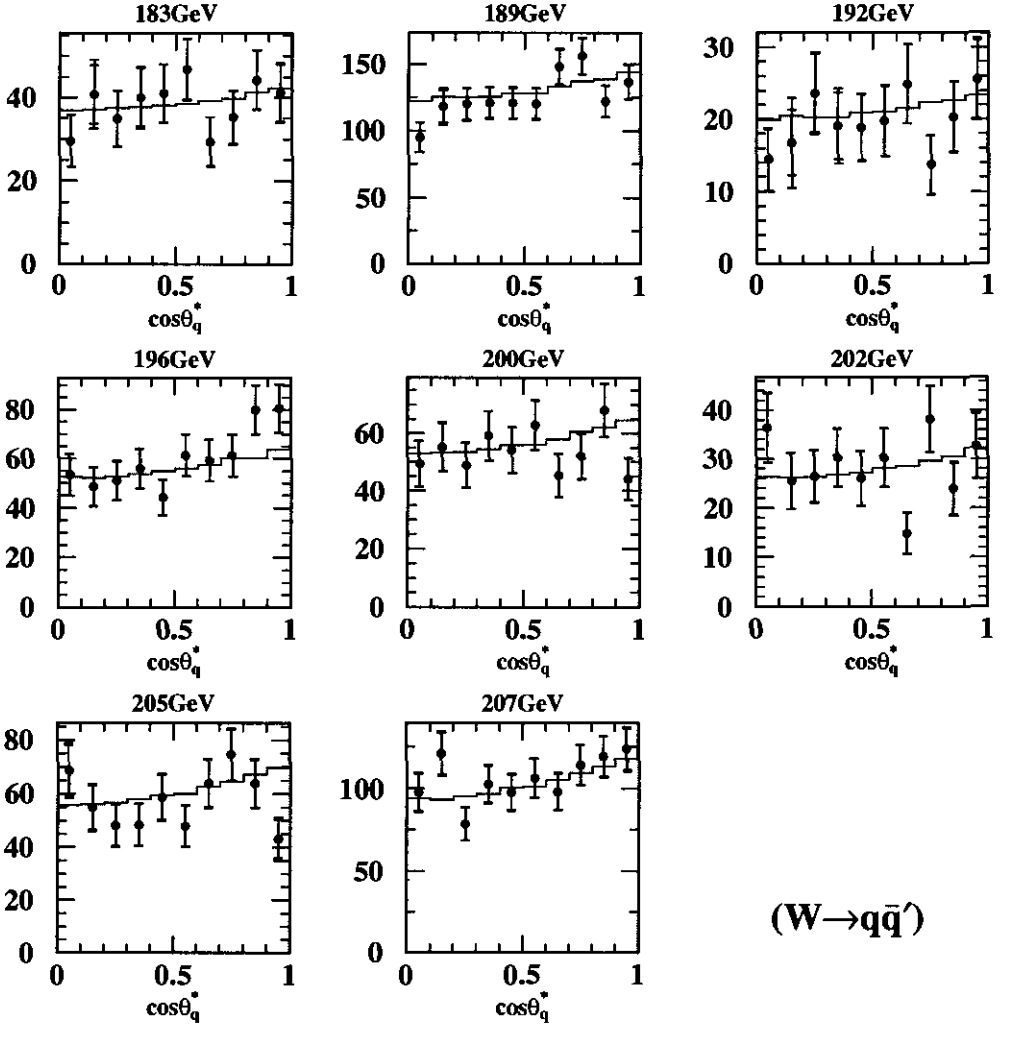

Figure 52: The measured $\cos\theta_q^*$ distributions obtained from the data at each nominal centre-of-mass energy following the detector correction. The points show the measured values from the data and the histogram shows the prediction from SM generator-level MC samples. The inner error bars represent the statistical uncertainties and the outer error bars represent the total uncertainties including systematic effects.

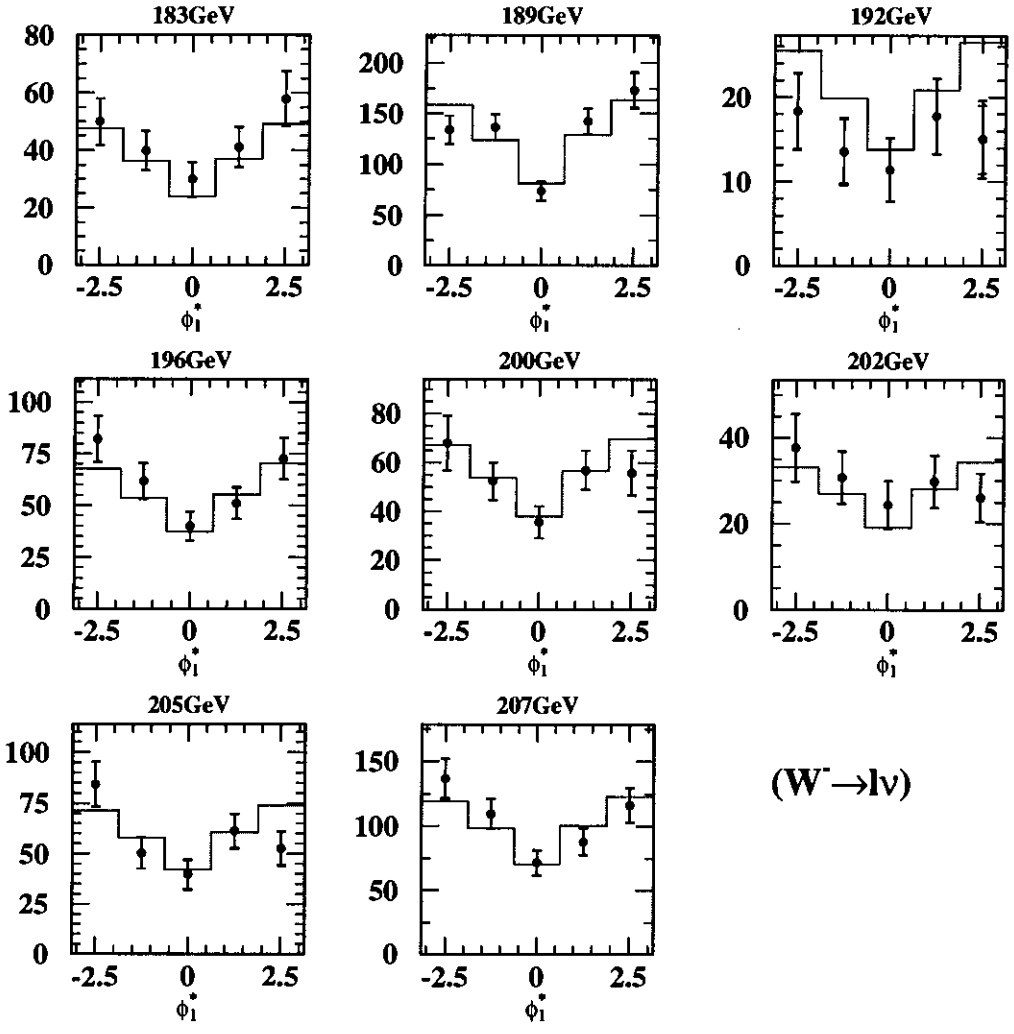

Figure 53: The measured ϕ_ℓ^* distributions from leptonic W^- decays obtained from the data at each nominal centre-of-mass energy following the detector correction. The points show the measured values from the data and the histogram shows the prediction from SM generator-level MC samples. The inner error bars represent the statistical uncertainties and the outer error bars represent the total uncertainties including systematic effects.

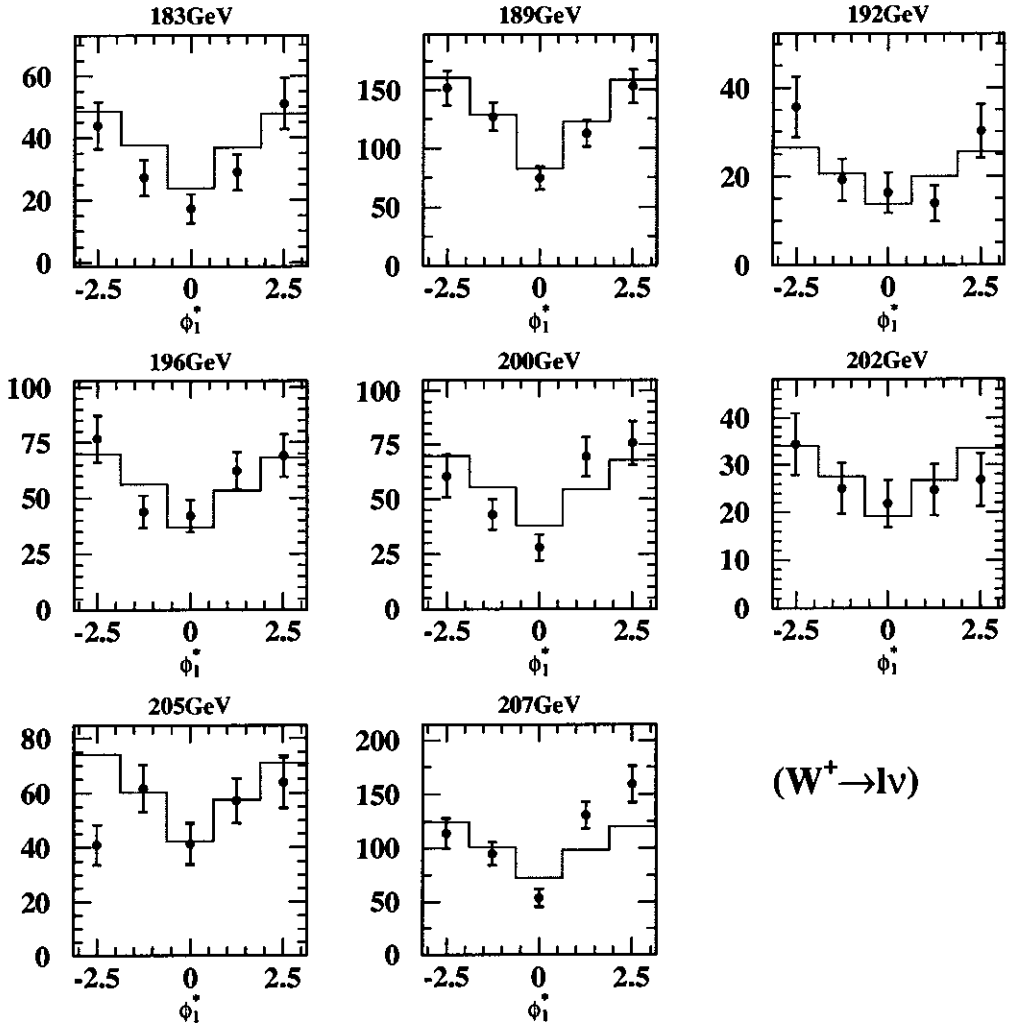

Figure 54: The measured ϕ_ℓ^* distributions from leptonic W^+ decays obtained from the data at each nominal centre-of-mass energy following the detector correction. The points show the measured values from the data and the histogram shows the prediction from SM generator-level MC samples. The inner error bars represent the statistical uncertainties and the outer error bars represent the total uncertainties including systematic effects.

D.2 Efficiency

The figures in this section show the variations in the efficiency of the signal selection defined in equation (75) of section 6.4.2 as a function of the W production and decay angles. Also shown are the variation in the efficiency-like scaling factor defined in equation (77) of section 6.4.2 as a function of the W production and decay angles. Figure 55 shows the $\cos\theta_{\mathrm{W}}$ dependence, figure 56 shows the $\cos\theta^*_\ell$ dependence and figure 57 shows the $\cos\theta^*_q$ dependence. The binning of the histograms corresponds to the binning of the detector correction used in evaluating the diagonal elements of the SDM.

Figure 59 and figure 58 show the $\cos\theta^*_\ell$ and ϕ^*_ℓ dependences respectively. The binning of the histograms corresponds to the binning of the detector correction used in evaluating the off-diagonal elements of the SDM. In all cases, the W^- and W^+ contributions have been combined.

An example of how the dependence on $\cos\theta^*_\ell$ of the efficiency and efficiency-like scaling factor varied between different bins in $\cos\theta_{\mathrm{W}}$ is shown in figure 60 using MC samples generated at a nominal centre-of-mass energy of 196 GeV. Figures 61, 62 and 63 show the same information for $\mathrm{q\bar{q}'}e\nu$, $\mathrm{q\bar{q}'}\mu\nu$ and $\mathrm{q\bar{q}'}\tau\nu$ signal events separately.

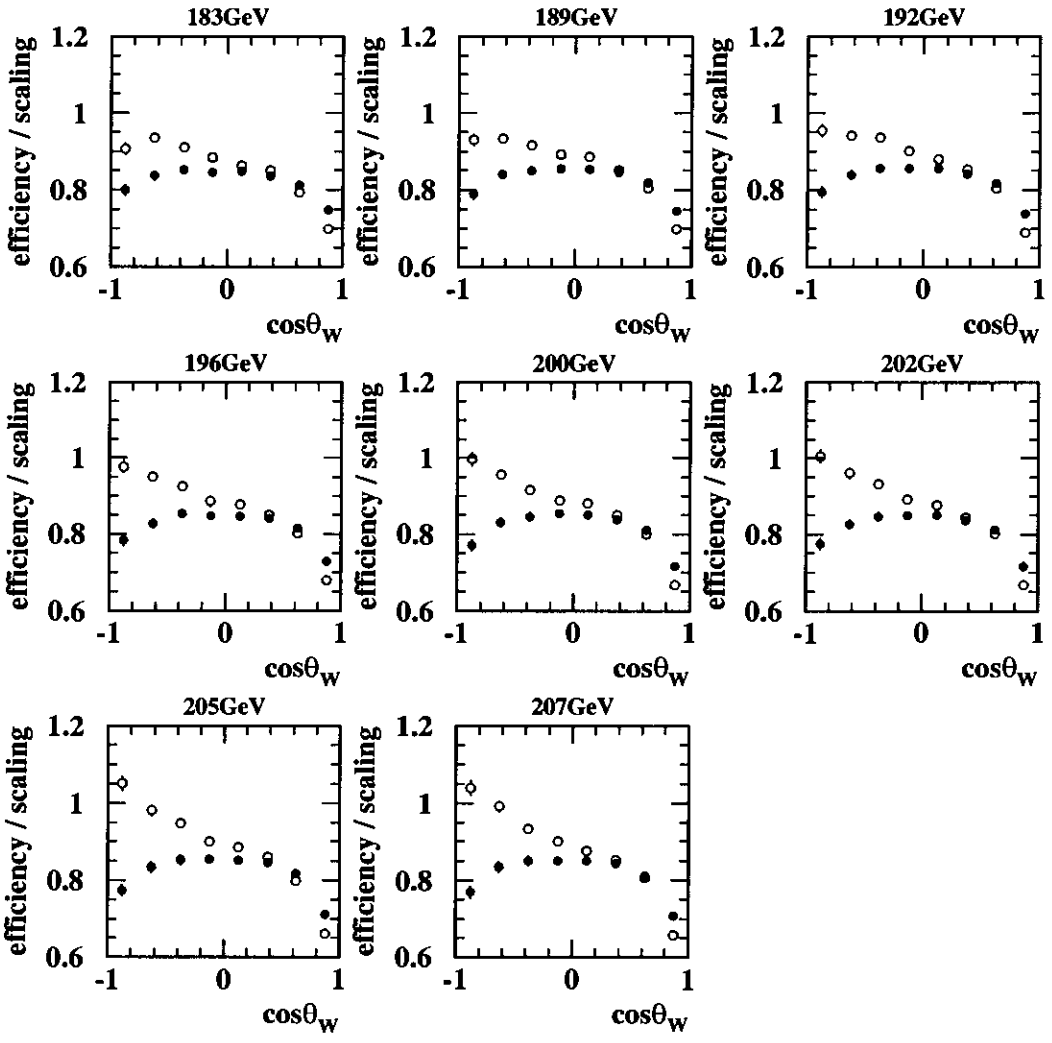

Figure 55: Efficiency calculated from MC samples of table 4 as a function of $\cos\theta_W$. The closed circles show the efficiency as defined in equation (75) and the open circles show the efficiency-like scaling correction defined in equation (77). The (small) error bars show the statistical error on the MC samples. The binning is the same as that used to parameterise the detector correction when measuring any element of the SDM.

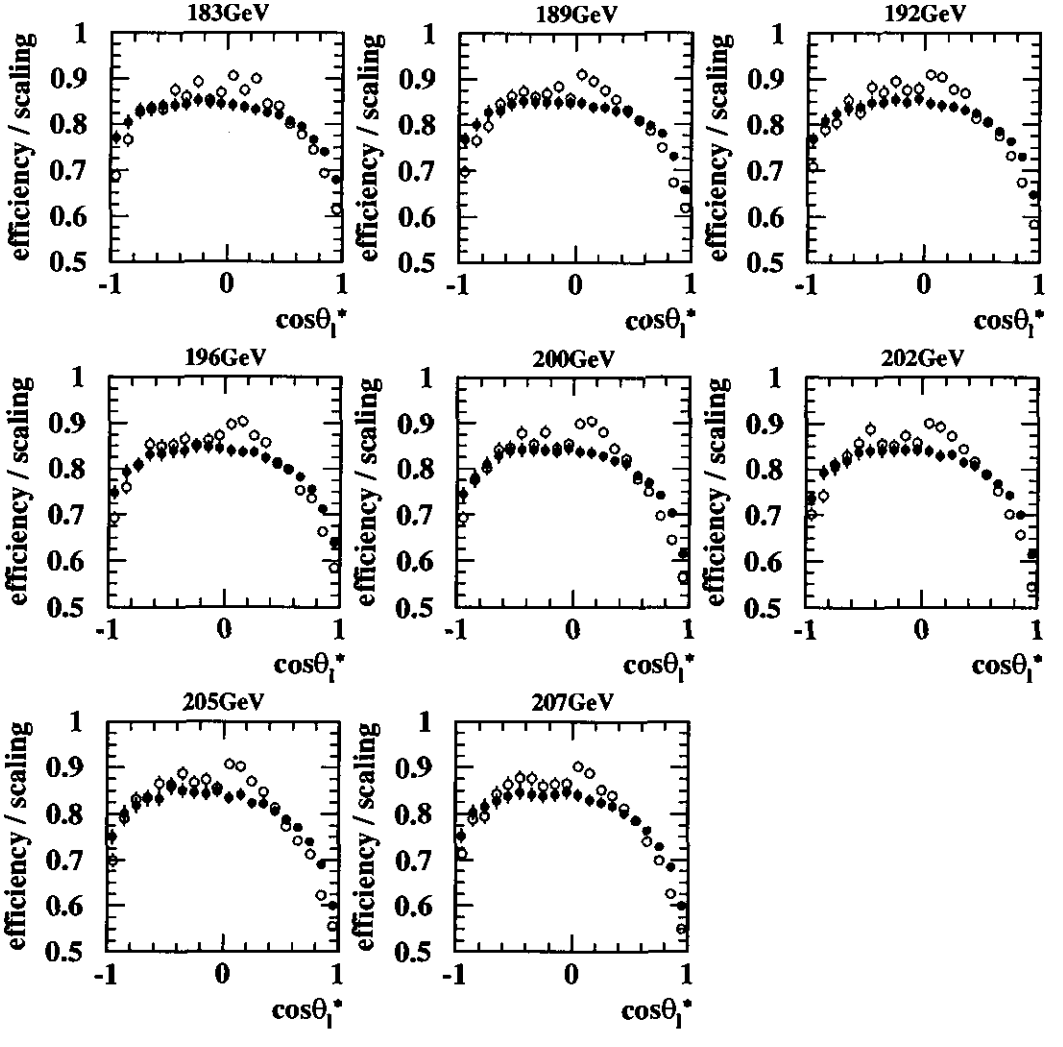

Figure 56: Efficiency calculated from MC samples of table 4 as a function of $\cos\theta^*_\ell$. The closed circles show the efficiency as defined in equation (75) and the open circles show the efficiency-like scaling correction defined in equation (77). The (small) error bars show the statistical error on the MC samples. The binning is the same as that used to parameterise the detector correction when measuring diagonal elements of the SDM for leptonically decaying W bosons.

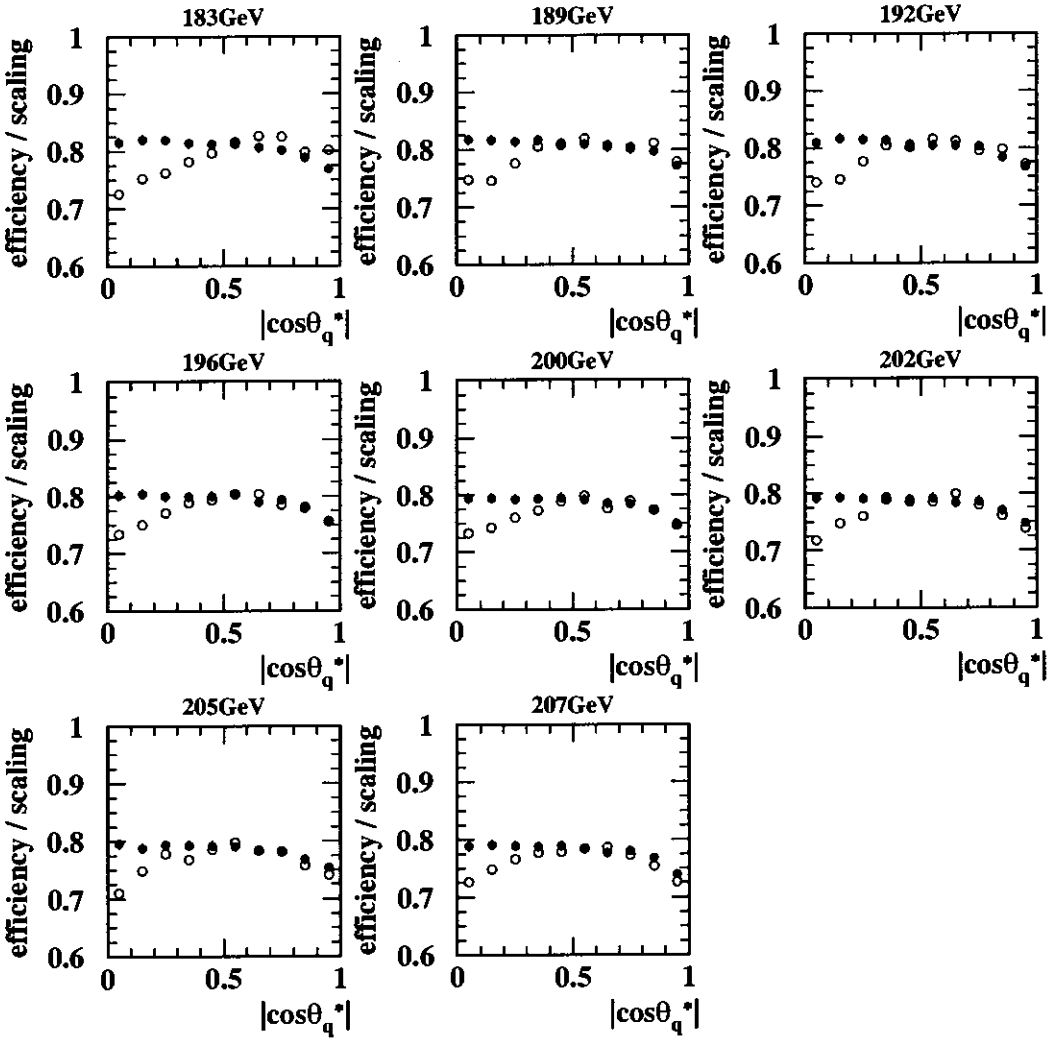

Figure 57: Efficiency calculated from MC samples of table 4 as a function of $\cos\theta_q^*$. The closed circles show the efficiency as defined in equation (75) and the open circles show the efficiency-like scaling correction defined in equation (77). The (small) error bars show the statistical error on the MC samples. The binning is the same as that used to parameterise the detector correction when measuring diagonal elements of the SDM for hadronically decaying W bosons.

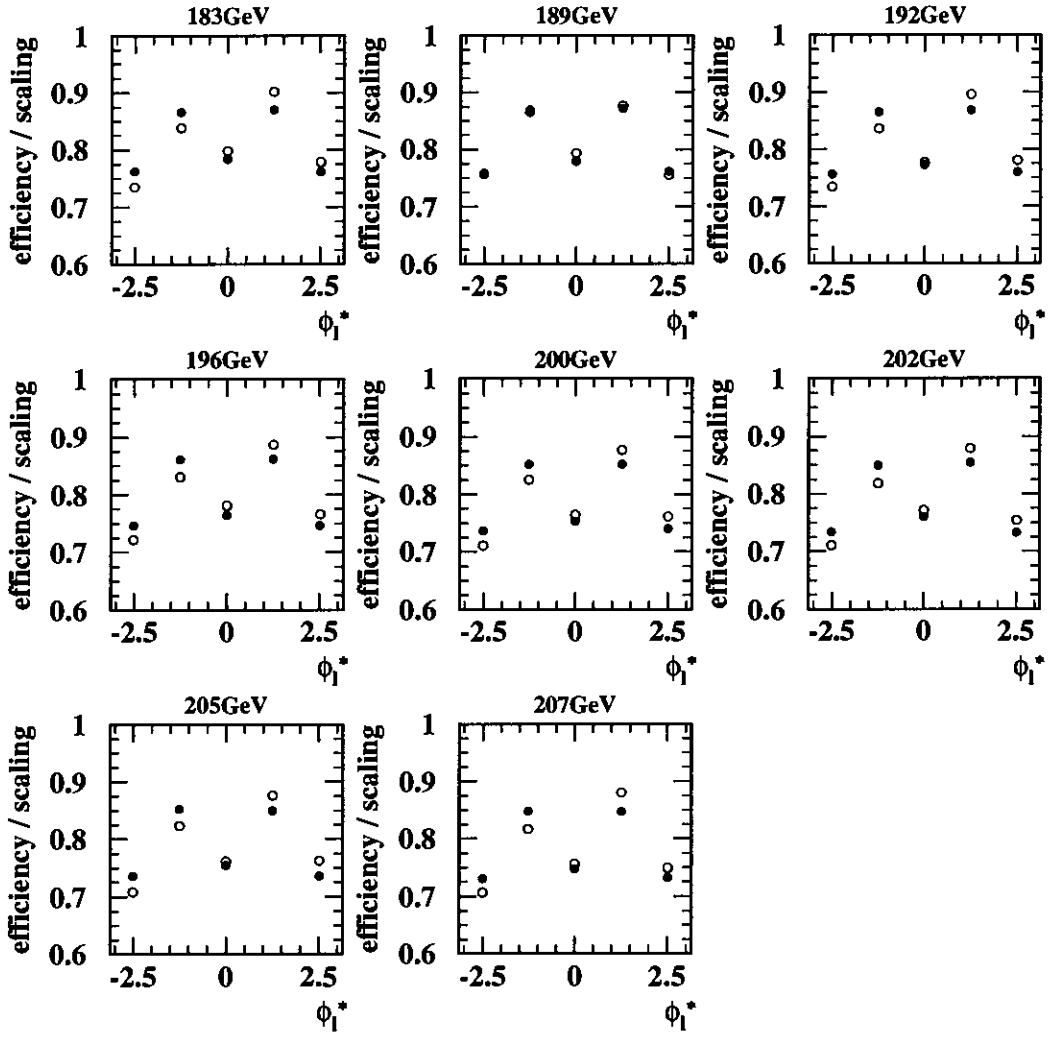

Figure 58: Efficiency calculated from MC samples of table 4 as a function of ϕ_ℓ^*. The closed circles show the efficiency as defined in equation (75) and the open circles show the efficiency-like scaling correction defined in equation (77). The (small) error bars show the statistical error on the MC samples. The binning is the same as that used to parameterise the detector correction when measuring off-diagonal elements of the SDM for leptonically decaying W bosons.

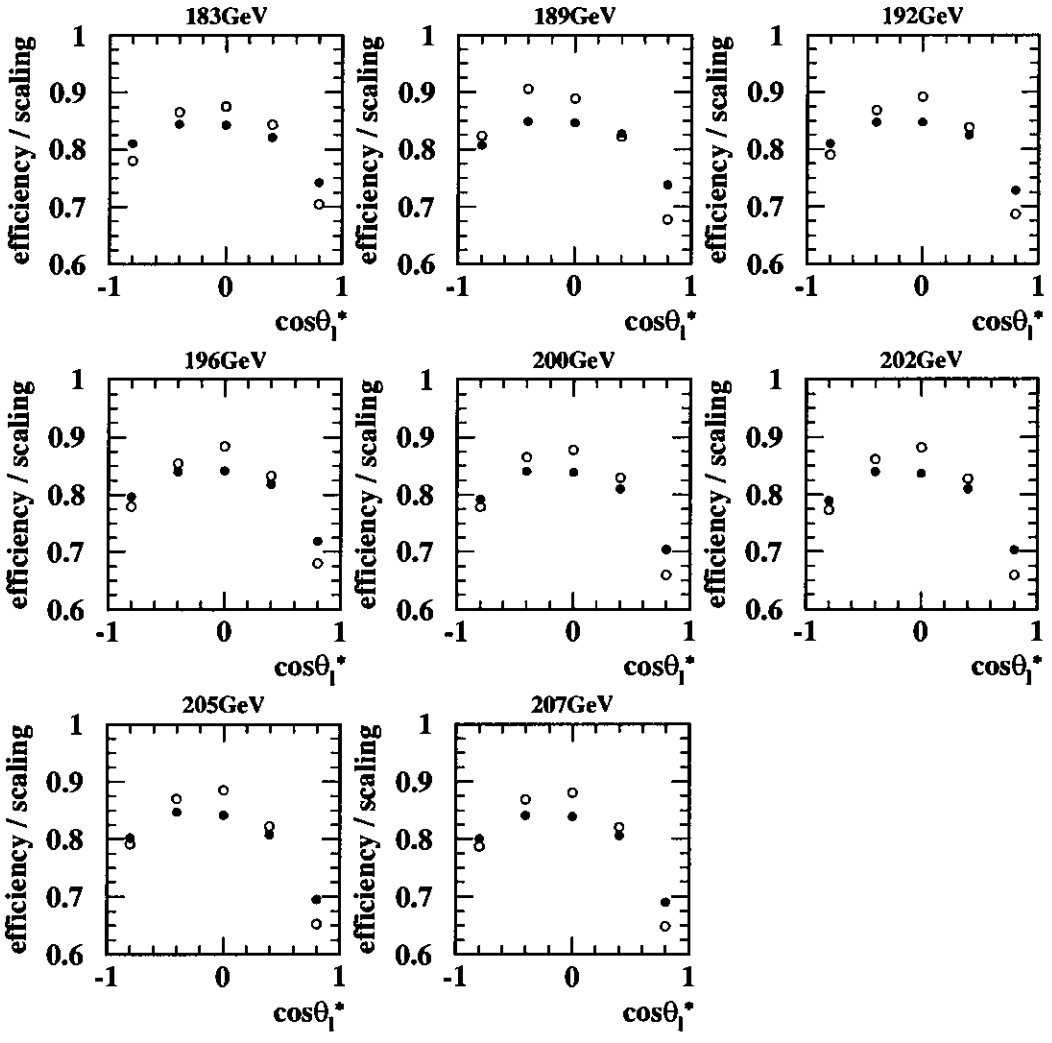

Figure 59: Efficiency calculated from MC samples of table 4 as a function of $\cos\theta_\ell^*$. The closed circles show the efficiency as defined in equation (75) and the open circles show the efficiency-like scaling correction defined in equation (77). The (small) error bars show the statistical error on the MC samples. The binning is the same as that used to parameterise the detector correction when measuring off-diagonal elements of the SDM for leptonically decaying W bosons.

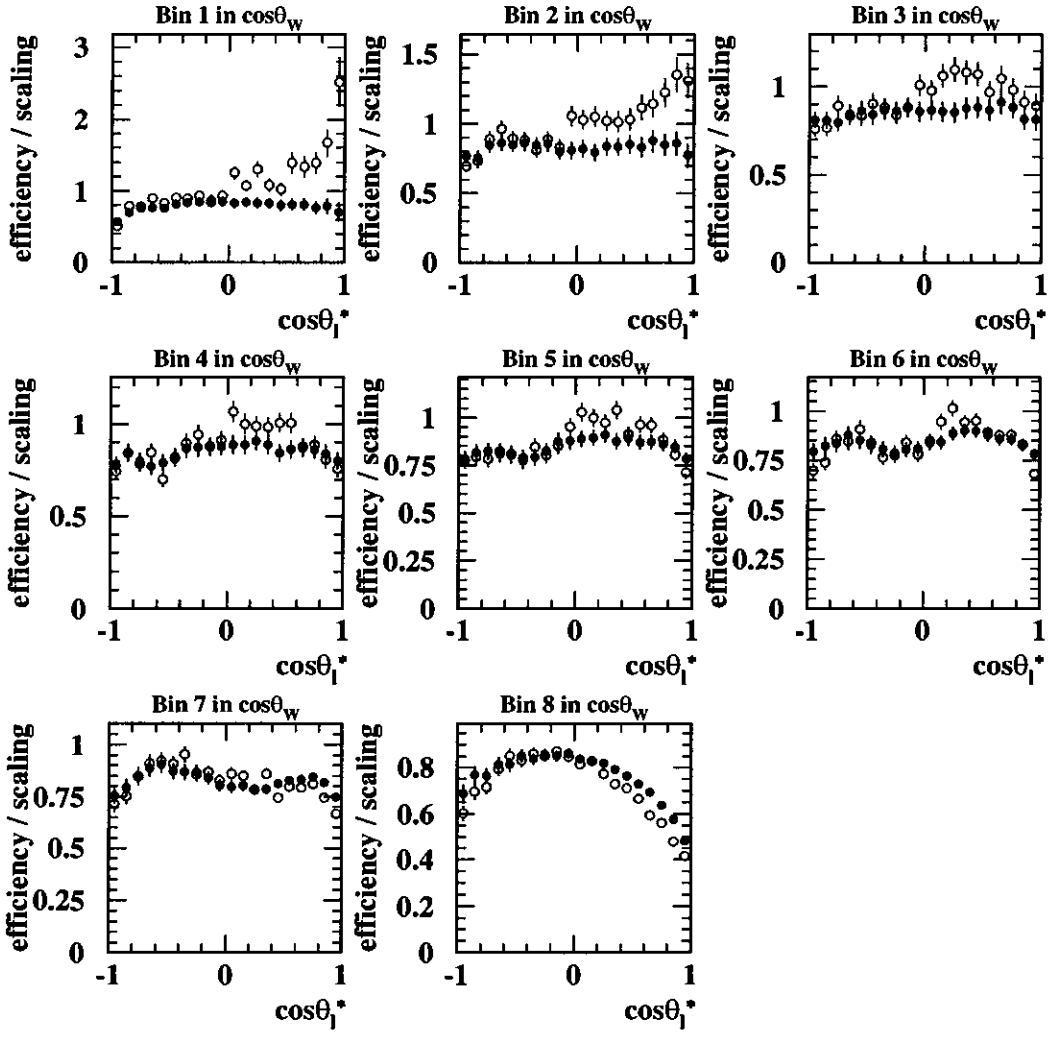

Figure 60: Efficiency calculated from MC samples of table 4 with a nominal centre-of-mass energy of 196 GeV as a function of $\cos\theta^*_\ell$ in slices of $\cos\theta_W$. The closed circles show the efficiency as defined in equation (75) and the open circles show the efficiency-like scaling correction defined in equation (77). The error bars show the statistical error on the MC samples. The binning is the same as that used to parameterise the detector correction when measuring diagonal elements of the SDM for leptonically decaying W bosons.

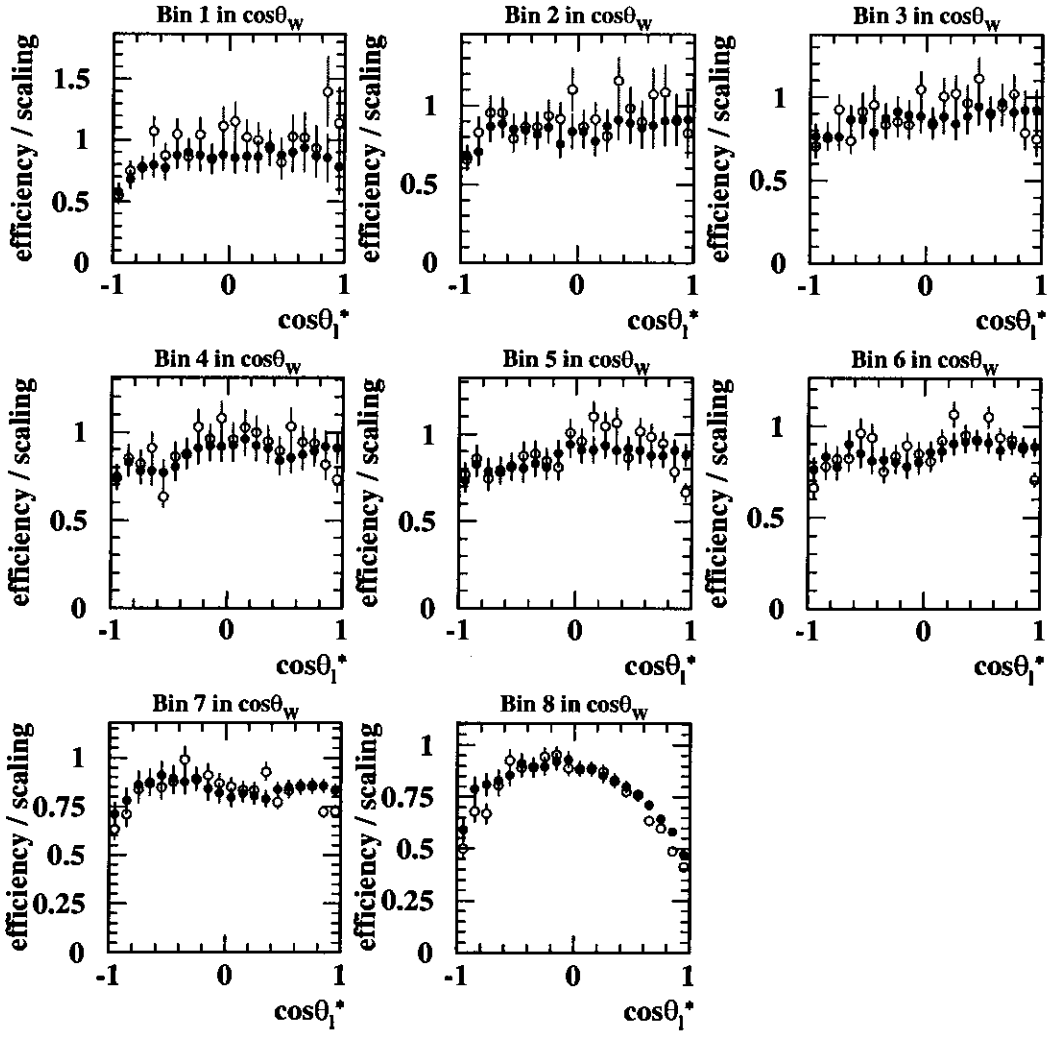

Figure 61: Efficiency for $q\bar{q}'e\nu$ signal events calculated from MC samples of table 4 with a nominal centre-of-mass energy of 196 GeV as a function of $\cos\theta_\ell^*$ in slices of $\cos\theta_W$. The closed circles show the efficiency as defined in equation (75) and the open circles show the efficiency-like scaling correction defined in equation (77). The error bars show the statistical error on the MC samples. The binning is the same as that used to parameterise the detector correction when measuring diagonal elements of the SDM for leptonically decaying W bosons.

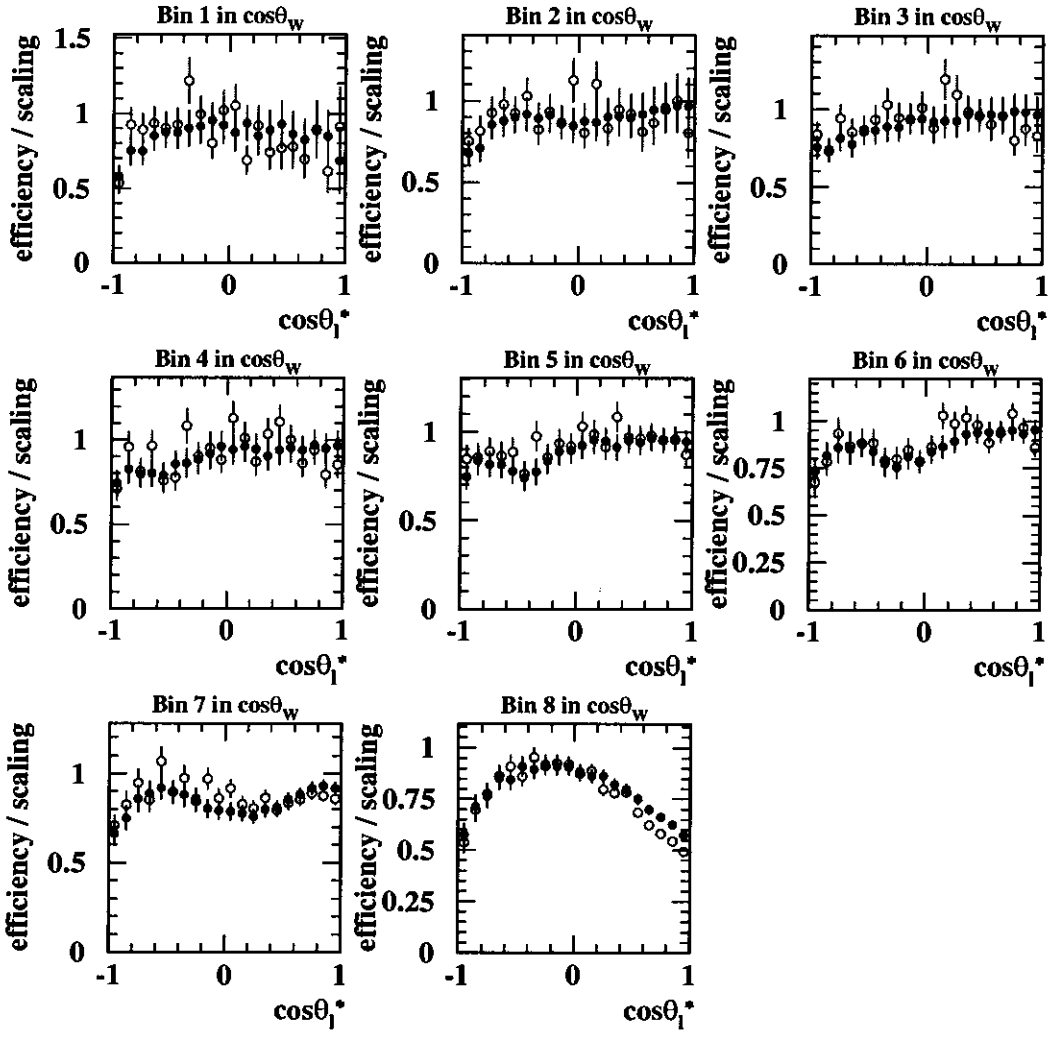

Figure 62: Efficiency for $q\bar{q}'\mu\nu$ signal events calculated from MC samples of table 4 with a nominal centre-of-mass energy of 196 GeV as a function of $\cos\theta_l^*$ in slices of $\cos\theta_W$. The closed circles show the efficiency as defined in equation (75) and the open circles show the efficiency-like scaling correction defined in equation (77). The error bars show the statistical error on the MC samples. The binning is the same as that used to parameterise the detector correction when measuring diagonal elements of the SDM for leptonically decaying W bosons.

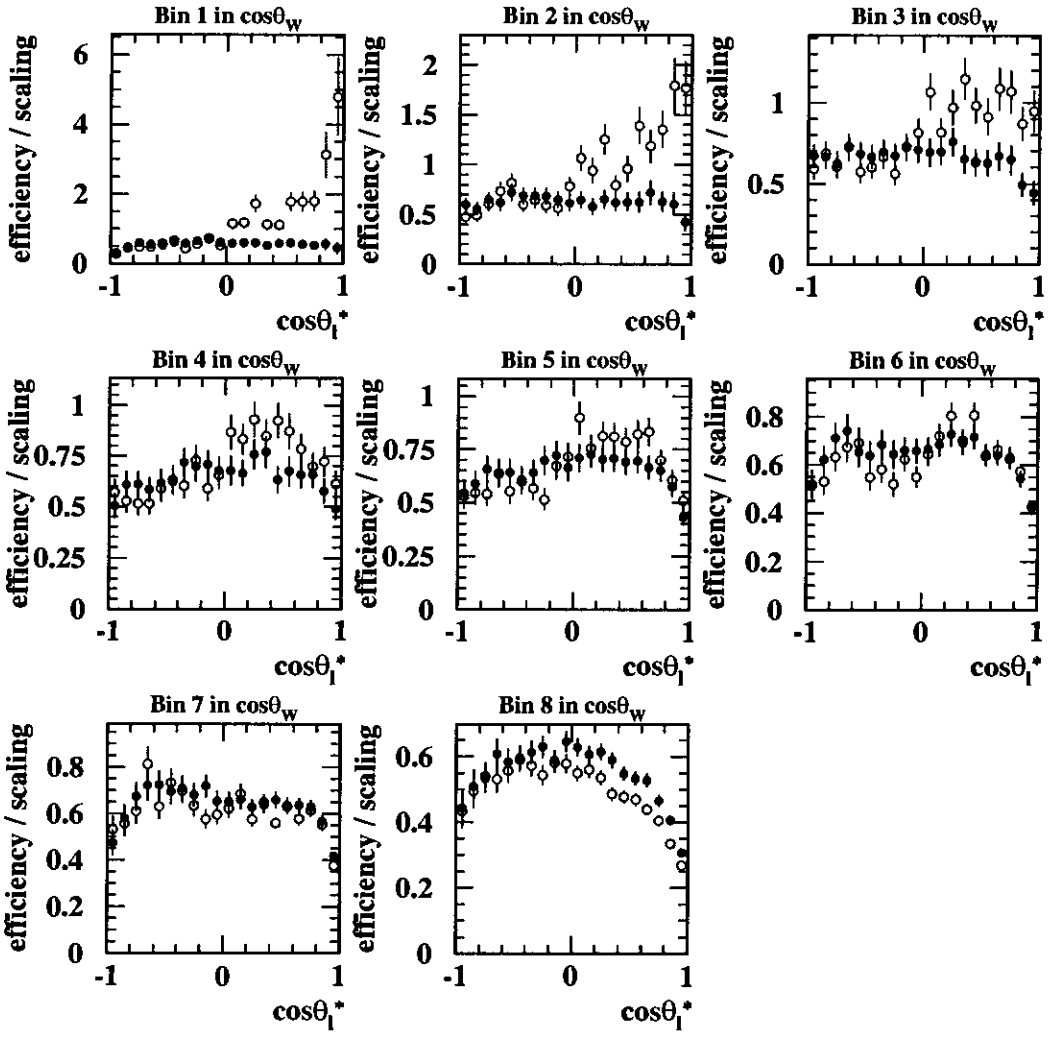

Figure 63: Efficiency for $q\bar{q}'\tau\nu$ signal events calculated from MC samples of table 4 with a nominal centre-of-mass energy of 196 GeV as a function of $\cos\theta_\ell^*$ in slices of $\cos\theta_W$. The closed circles show the efficiency as defined in equation (75) and the open circles show the efficiency-like scaling correction defined in equation (77). The error bars show the statistical error on the MC samples. The binning is the same as that used to parameterise the detector correction when measuring diagonal elements of the SDM for leptonically decaying W bosons.

D.3 Purity

The figures in this section show the variations in the purity of the signal selection defined in equation (76) of section 6.4.2 as a function of the W production and decay angles. Figure 64 shows the $\cos\theta_W$ dependence, figure 65 shows the $\cos\theta^*_\ell$ dependence and figure 66 shows the $\cos\theta^*_q$ dependence. The binning of the histograms corresponds to the binning of the detector correction used in evaluating the diagonal elements of the SDM.

Figure 68 and figure 67 show the $\cos\theta^*_\ell$ and ϕ^*_ℓ dependences respectively. The binning of the histograms corresponds to the binning of the detector correction used in evaluating the off-diagonal elements of the SDM. In all cases, the W^- and W^+ contributions have been combined.

An example of how the dependence on $\cos\theta^*_\ell$ of the purity varied between different bins in $\cos\theta_W$ is shown in figure 69 using MC samples generated at a nominal centre-of-mass energy of 196 GeV. Figures 70, 71 and 72 show the same information for $q\bar{q}'e\nu$, $q\bar{q}'\mu\nu$ and $q\bar{q}'\tau\nu$ signal events separately.

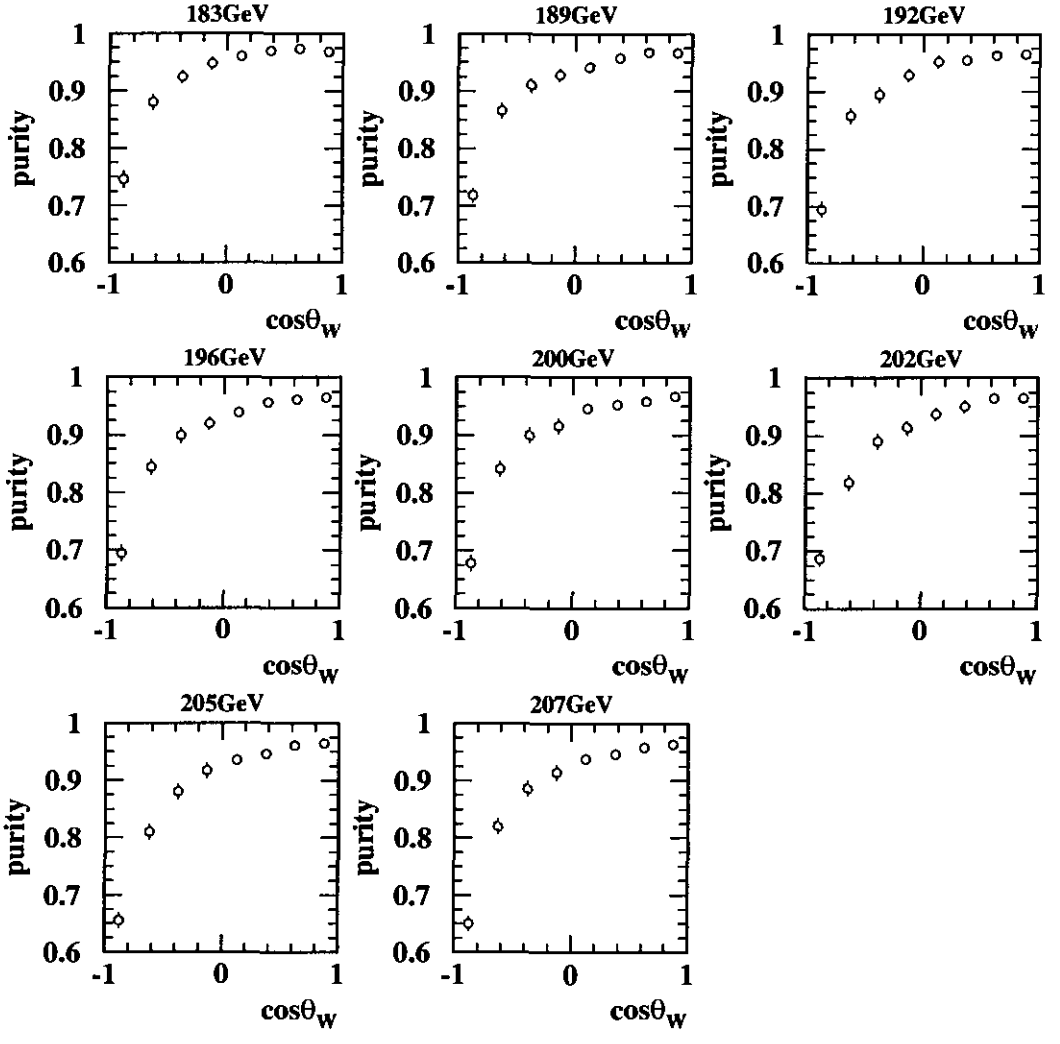

Figure 64: Purity calculated from MC samples of table 4 as a function of $\cos\theta_W$. The (small) error bars show the statistical error on the MC samples. The binning is the same as that used to parameterise the detector correction when measuring any element of the SDM.

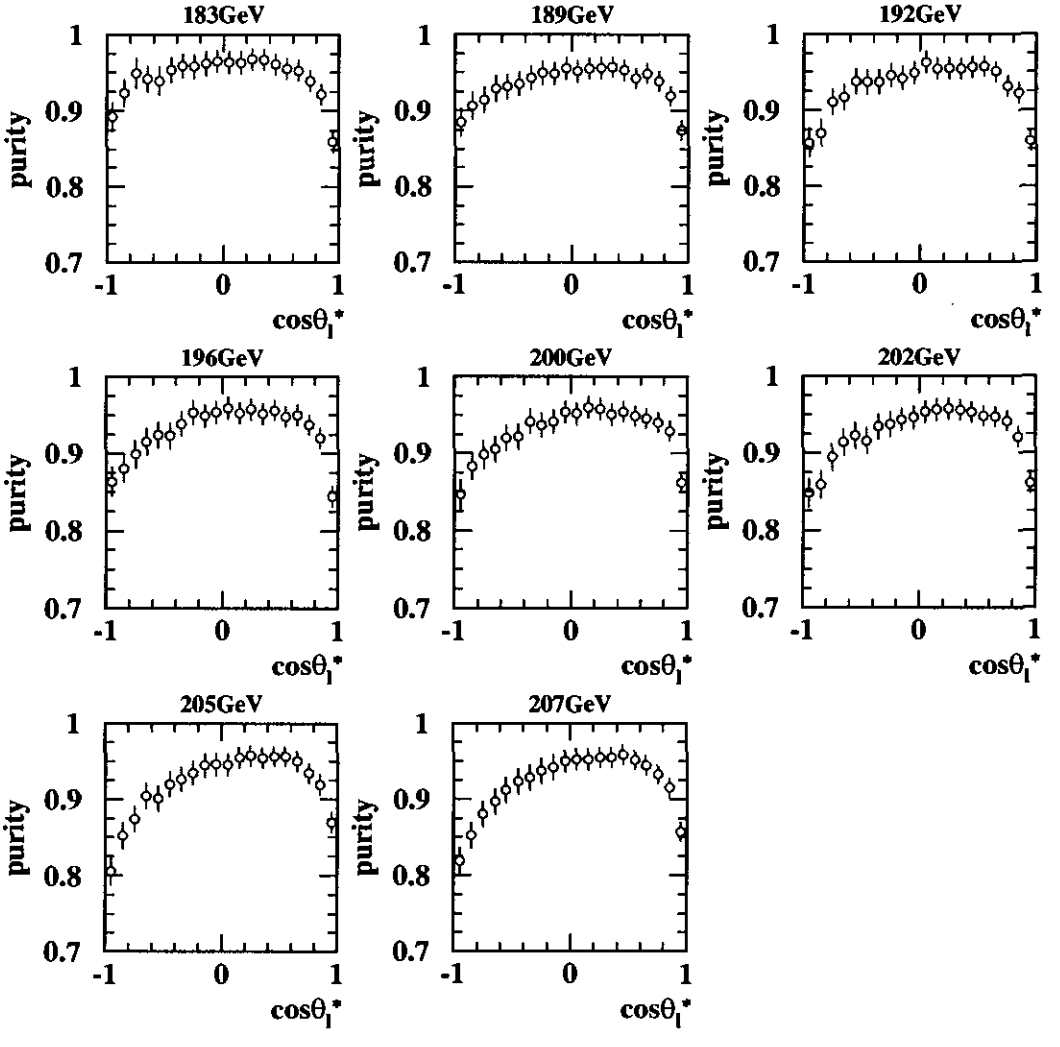

Figure 65: Purity calculated from MC samples of table 4 as a function of $\cos\theta^*_\ell$. The error bars show the statistical error on the MC samples. The binning is the same as that used to parameterise the detector correction when measuring diagonal elements of the SDM for leptonically decaying W bosons.

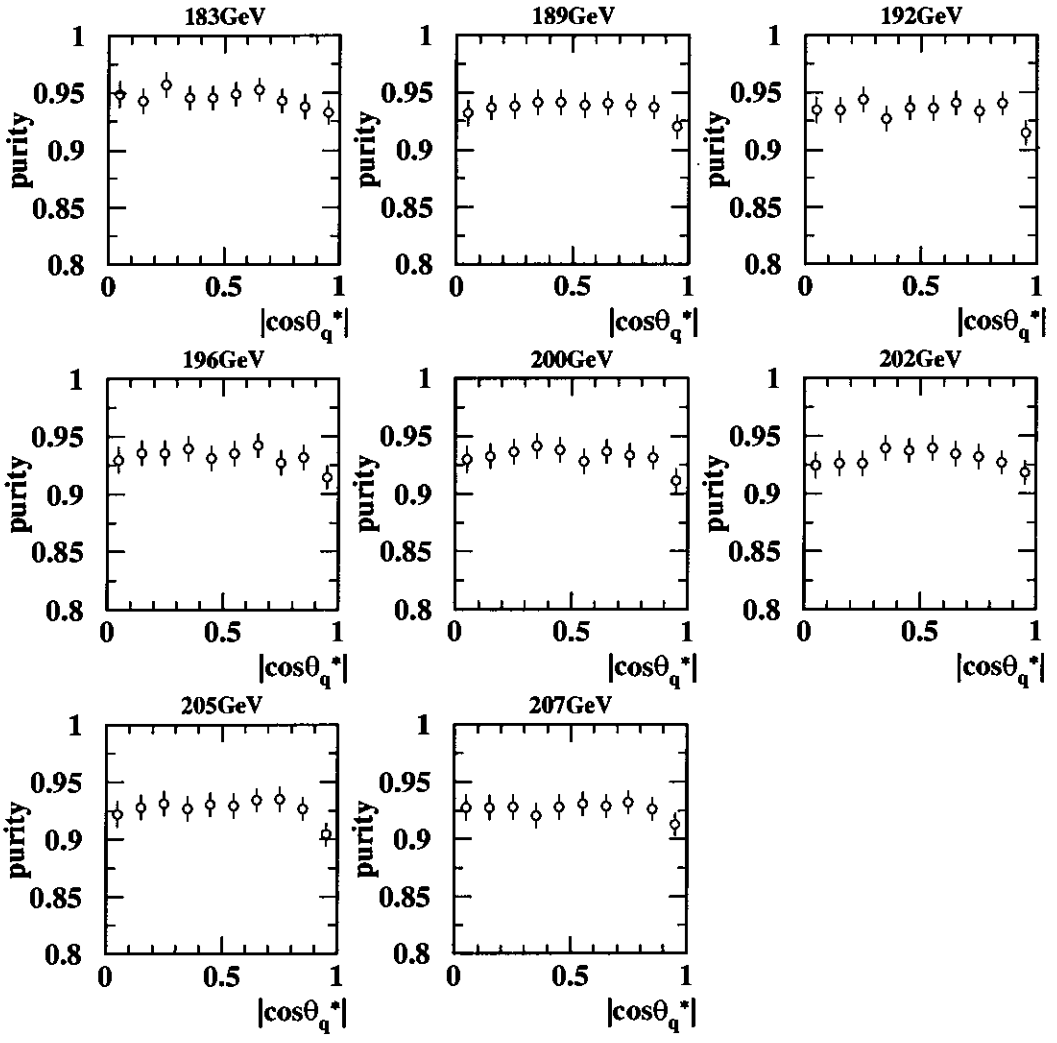

Figure 66: Purity calculated from MC samples of table 4 as a function of $\cos\theta_q^*$. The error bars show the statistical error on the MC samples. The binning is the same as that used to parameterise the detector correction when measuring diagonal elements of the SDM for hadronically decaying W bosons.

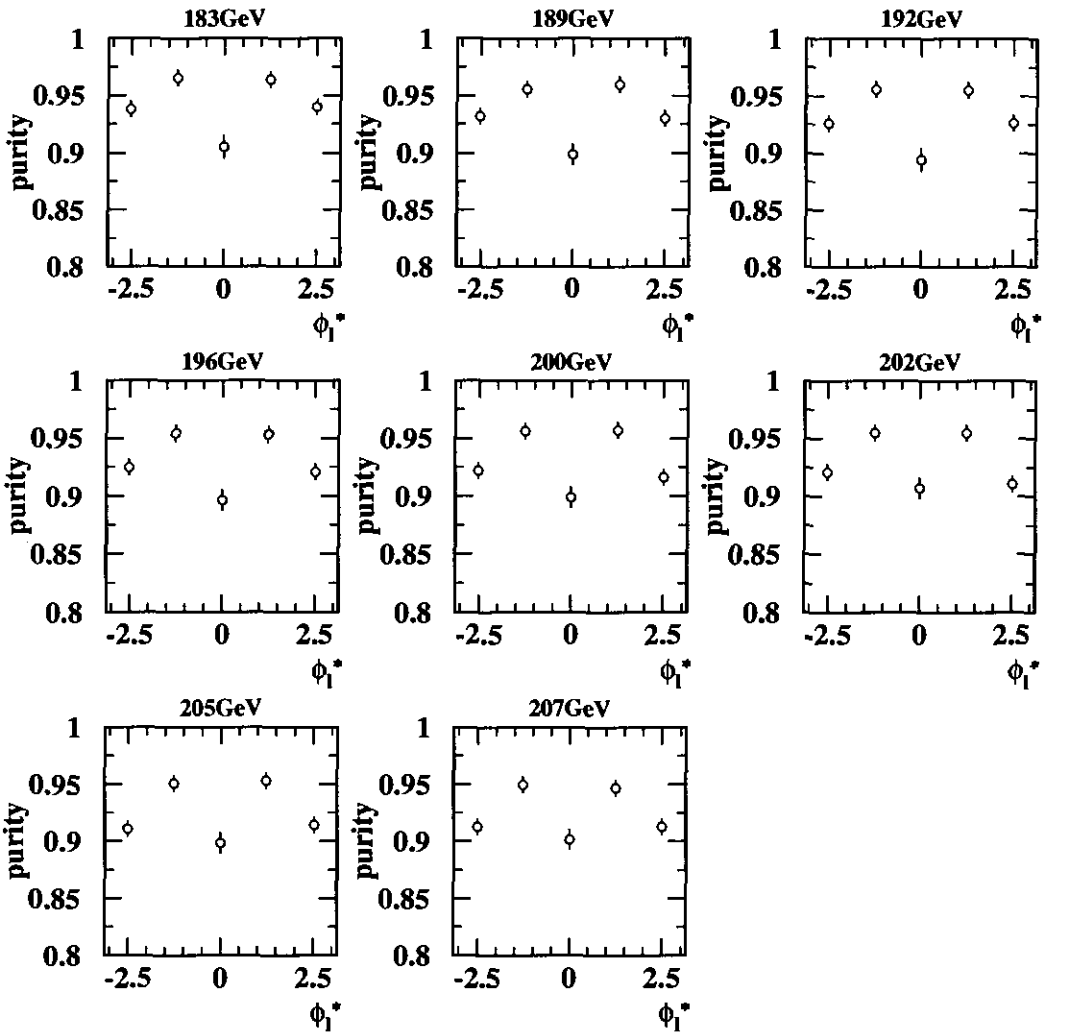

Figure 67: Purity calculated from MC samples of table 4 as a function of ϕ_ℓ^*. The error bars show the statistical error on the MC samples. The binning is the same as that used to parameterise the detector correction when measuring off-diagonal elements of the SDM for leptonically decaying W bosons.

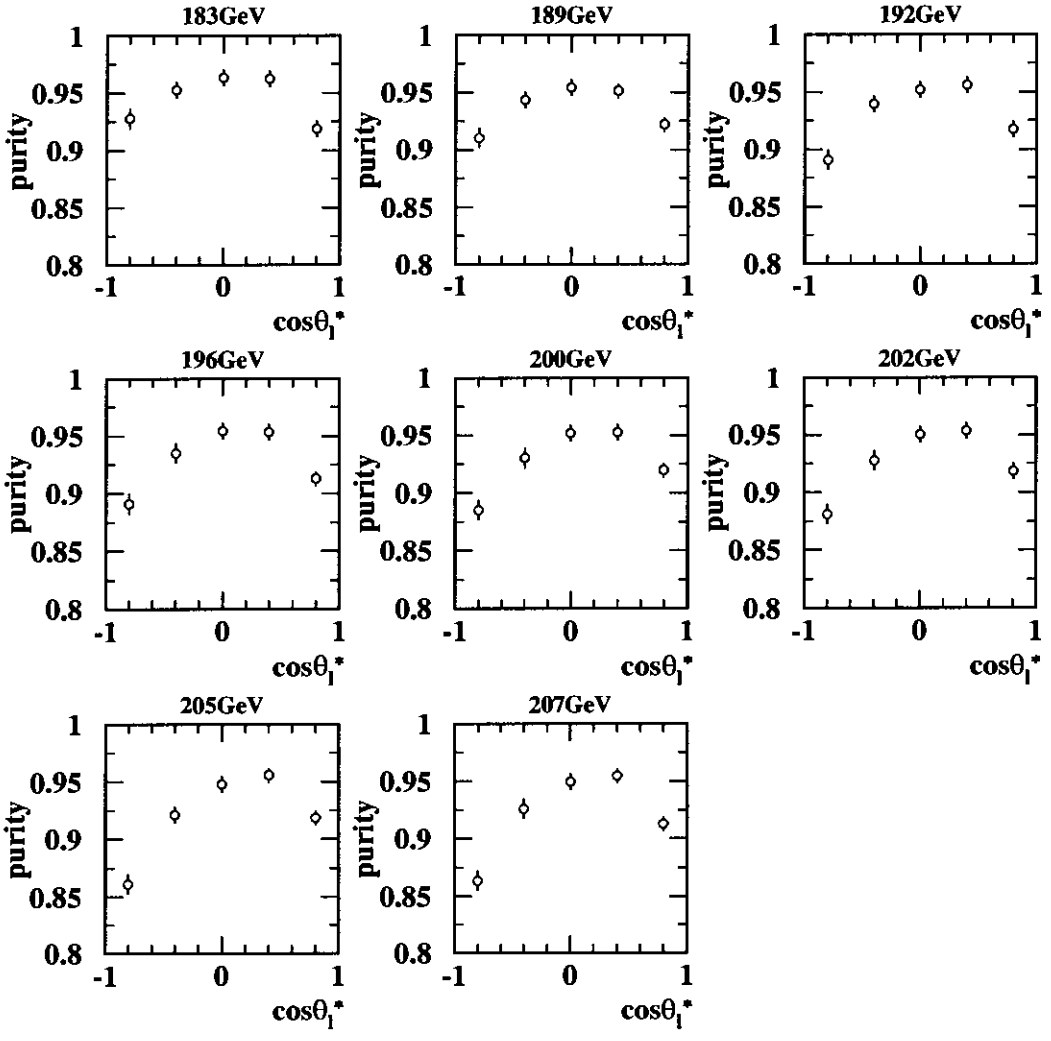

Figure 68: Purity calculated from MC samples of table 4 as a function of $\cos\theta_\ell^*$. The error bars show the statistical error on the MC samples. The binning is the same as that used to parameterise the detector correction when measuring off-diagonal elements of the SDM for leptonically decaying W bosons.

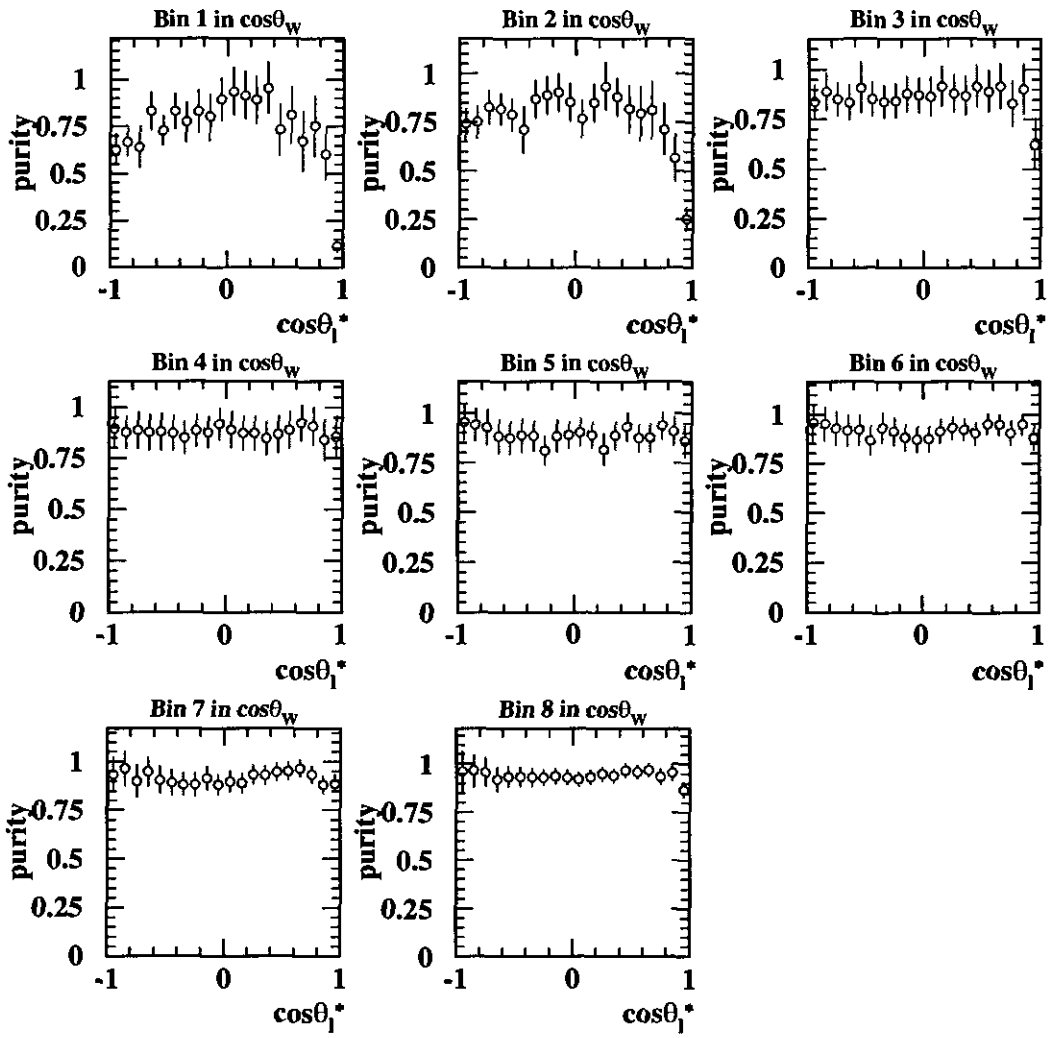

Figure 69: Purity calculated from MC samples of table 4 with a nominal centre-of-mass energy of 196 GeV as a function of $\cos\theta_\ell^*$ in slices of $\cos\theta_W$. The error bars show the statistical error on the MC samples. The binning is the same as that used to parameterise the detector correction when measuring diagonal elements of the SDM for leptonically decaying W bosons.

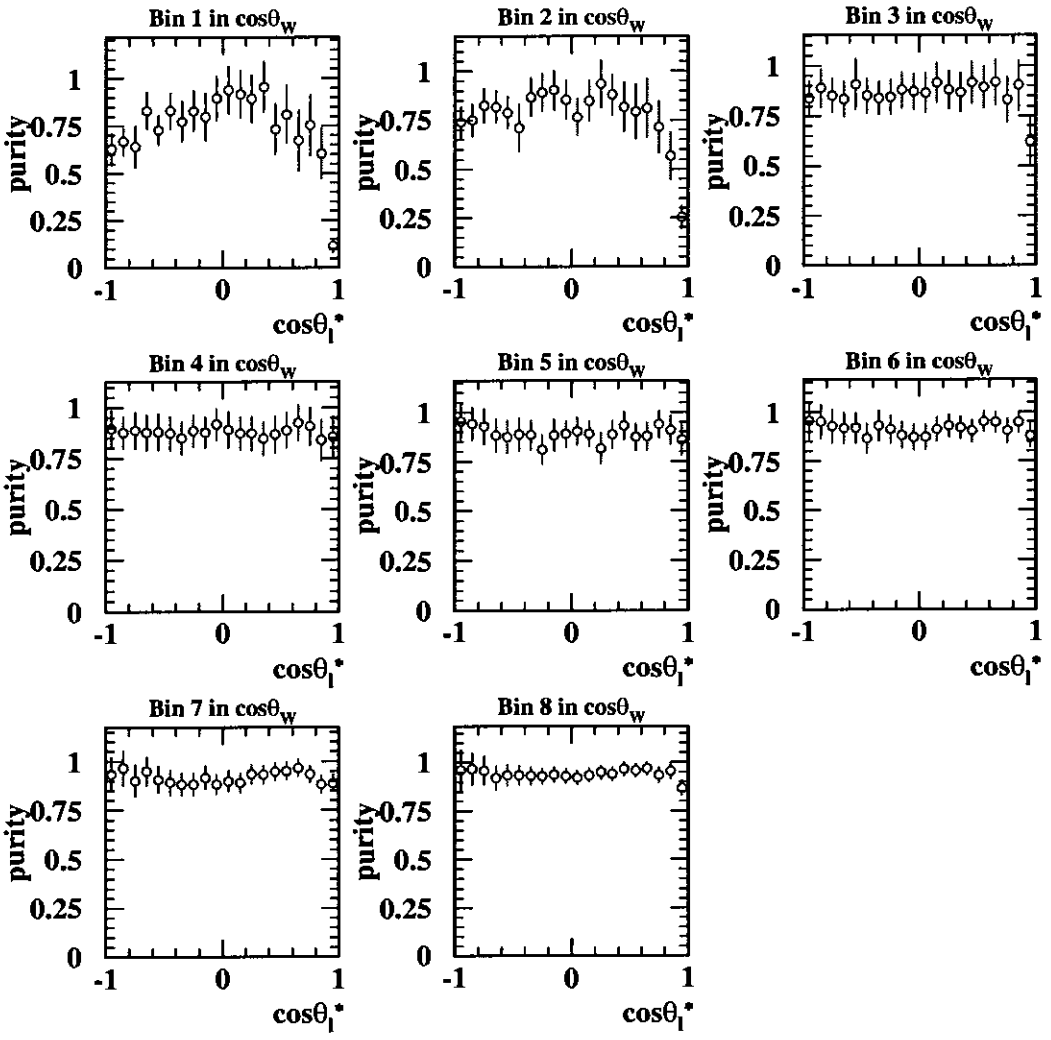

Figure 70: Purity for $q\bar{q}'e\nu$ signal events calculated from MC samples of table 4 with a nominal centre-of-mass energy of 196 GeV as a function of $\cos\theta_\ell^*$ in slices of $\cos\theta_W$. The error bars show the statistical error on the MC samples. The binning is the same as that used to parameterise the detector correction when measuring diagonal elements of the SDM for leptonically decaying W bosons.

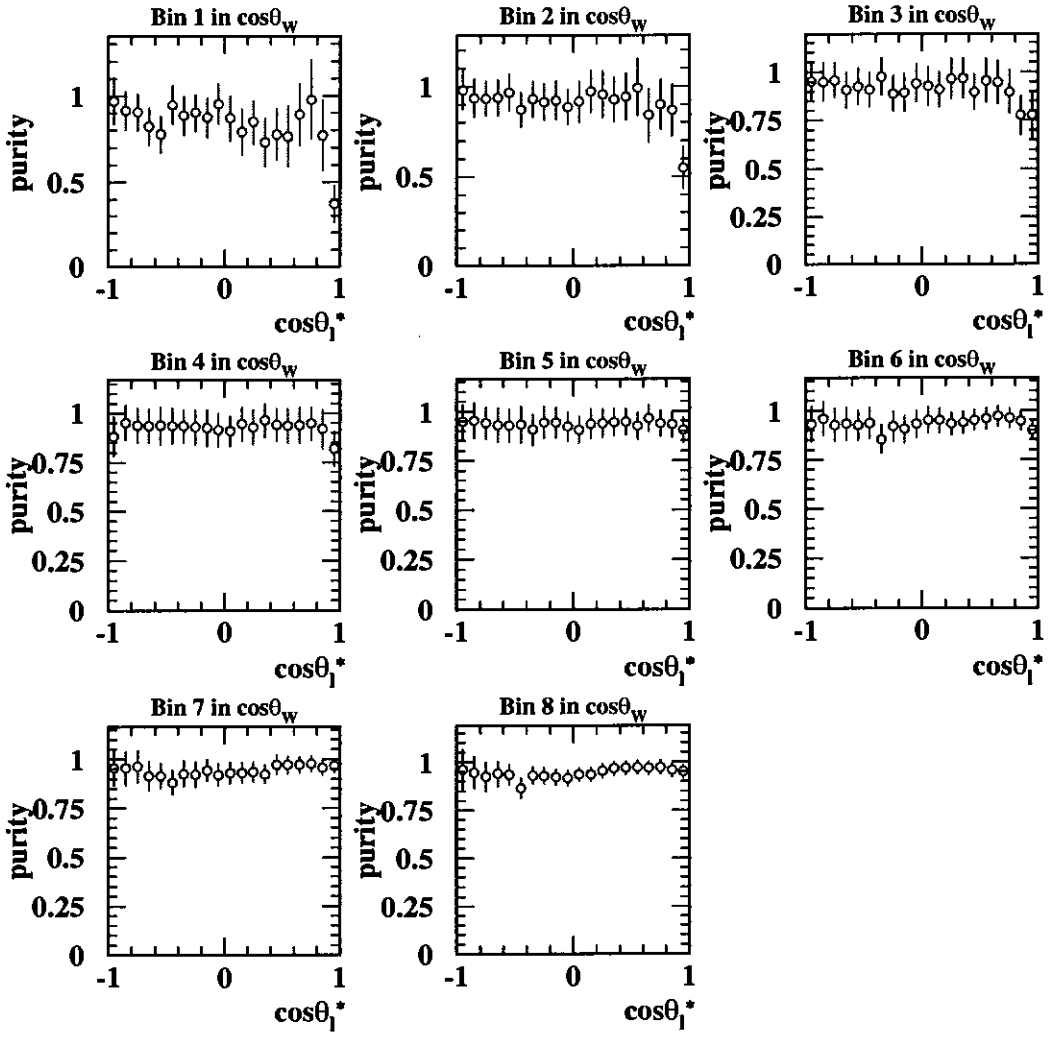

Figure 71: Purity for $q\bar{q}'\mu\nu$ signal events calculated from MC samples of table 4 with a nominal centre-of-mass energy of 196 GeV as a function of $\cos\theta^*_\ell$ in slices of $\cos\theta_W$. The error bars show the statistical error on the MC samples. The binning is the same as that used to parameterise the detector correction when measuring diagonal elements of the SDM for leptonically decaying W bosons.

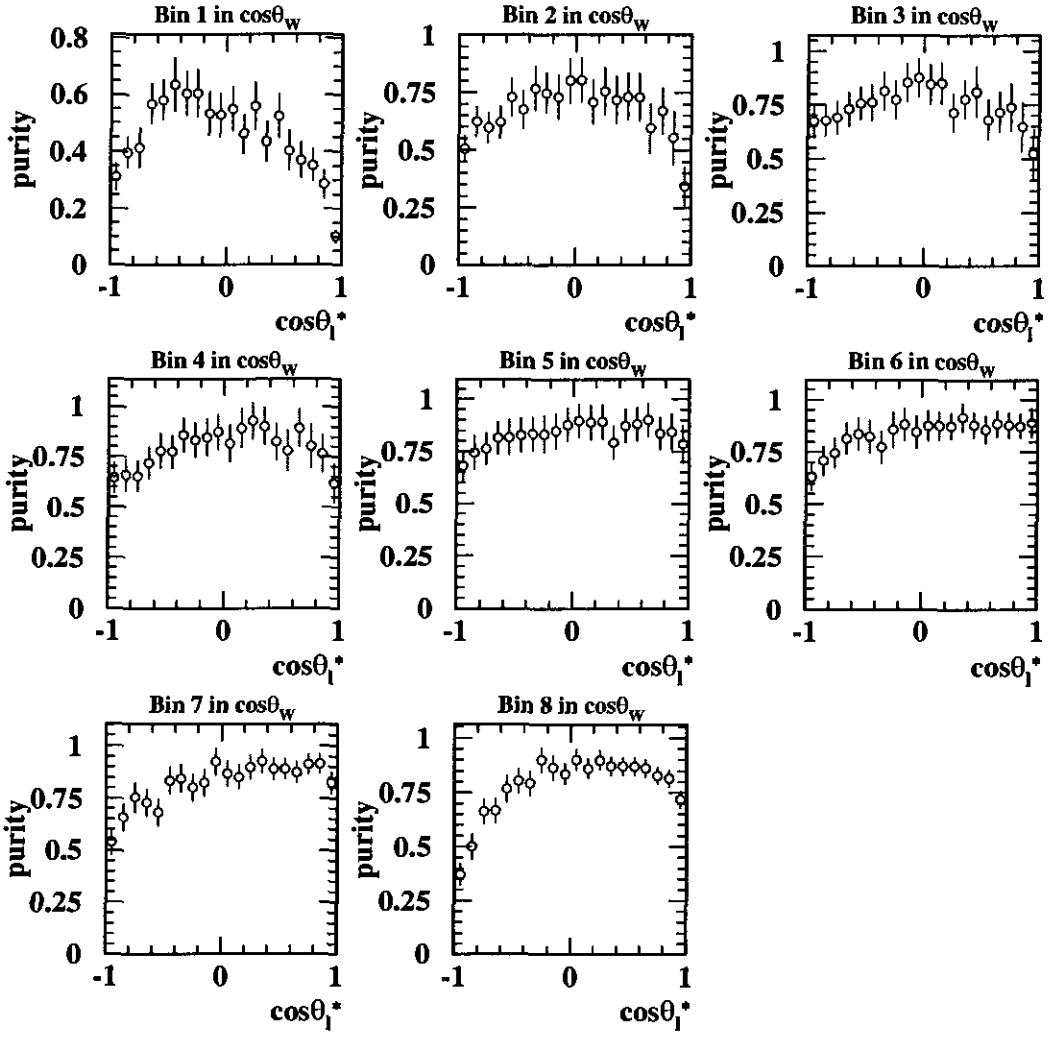

Figure 72: Purity for $q\bar{q}'\tau\nu$ signal events calculated from MC samples of table 4 with a nominal centre-of-mass energy of 196 GeV as a function of $\cos\theta^*_\ell$ in slices of $\cos\theta_W$. The error bars show the statistical error on the MC samples. The binning is the same as that used to parameterise the detector correction when measuring diagonal elements of the SDM for leptonically decaying W bosons.

E Unfolding

These notes on the detector correction used in the SDM analysis briefly summarise presentations made by the author of this thesis at OPAL plenary sessions and LEP W working group meetings in the years 2001 to 2003. The possibility of background events in the data and MC samples is ignored throughout this appendix in order to simplify the notation.

We are trying to construct statistical estimators, $\vec{\zeta}$, of the true binned angular distributions of the W bosons, $\vec{z}$, given the measured distributions from the detector, $\vec{d}$. The true distribution is divided into n_z bins which are referenced by the index 'τ' and the measured distribution is divided into n_d bins with are referenced by the index 'ρ'. The covariance matrix for the measured distributions is, D.

From Monte Carlo simulation it is straightforward to extract the smearing matrix (detector response), A, which satisfies equations (109) and (110). Equation (109) should be read as 'the number of events generated with true angles τ and reconstructed with measured angles ρ' divided by 'the number of events generated with true angles τ'.

$$A_{\rho;\tau} \equiv \frac{d_{\rho}^{(MC)} \cap z_{\tau}^{(MC)}}{z_{\tau}^{(MC)}} \tag{109}$$

$$\vec{d}^{(MC)} = A \,.\, \vec{z}^{(MC)} \tag{110}$$

The goal is to find an unfolding matrix (detector correction), C, which satisfies equation (111).

$$\vec{z}^{(MC)} = C \,.\, \vec{d}^{(MC)} \tag{111}$$

The estimators of the true data distributions are then given by equation (112).

$$\vec{\zeta^{(C)}} = C \,.\, \vec{d}^{(data)} \tag{112}$$

There are an infinite number of such matrices. The most obvious solution is to use A^{-1}. This is a mathematically valid solution but, in practice, it produces estimators with very large variances. Despite this, there are no unfolding matrices which can give estimators with smaller variances without also introducing a bias. This is a general result which can be derived analytically [93].

The SDM analysis presented in this thesis uses the same form of unfolding matrix as used in the previous SDM analysis [23] and many other HEP analyses. The matrix is required to be diagonal, which leads to the unique solution shown in equation (113). This unfolding matrix is sometimes referred to as a 'scaling' correction. It is similar, but not identical to, the reciprocal of the efficiency.

$$C_{\tau;\rho} = \begin{cases} \frac{z_\tau^{(MC)}}{d_\rho^{(MC)}} & \tau = \rho \\ 0 & \tau \neq \rho \end{cases} \tag{113}$$

This method is simple to implement because the estimators are uncorrelated but it is difficult to motivate theoretically.

Other unfolding matrices based on Bayes theorem [76] and the SVD regularised unfolding method [75] were also investigated during the development of the SDM analysis. Each of the unfolding matrices introduced approximately the same magnitude of bias into the estimators.

Apart from being mathematically unaesthetic, the only disadvantage of the scaling method is that the correlation matrix between $\cos\theta_W$ elements is not automatically produced as part of the analysis. In order to carry out a fit to the unfolded distribution it is always necessary to use the true inverse covariance matrix shown in equation (114) and not the inverse covariance matrix of the estimators shown in (115). Using equation (115) in place of equation (114) causes the errors on the fitted parameters to be underestimated.

$$Z^{-1} = A \,.\, D^{-1} \,.\, (A)^T \tag{114}$$

$$\left(Z^{(C)}\right)^{-1} = C^{-1} \cdot D^{-1} \cdot (C^{-1})^T \quad (115)$$

F The off-diagonal elements of the SDM

This appendix contains the measured luminosity-weighed average of the off-diagonal elements of the SDM. Figure 73 shows the results from the $W^- \to \ell^- \bar{\nu}_\ell$ decays and figure 74 shows the results from the $W^+ \to \ell^+ \bar{\nu}_\ell$ decays. The standard detector correction (parameterised by 8 bins in $\cos\theta_W$, 5 bins in $\cos\theta^*_\ell$ and 5 bins in ϕ^*_ℓ) was used in measuring the SDM elements. In addition, figure 75 shows the values of ρ_{+-} calculated using a detector correction parameterised by 8 bins in $\cos\theta_W$ and 20 bins in ϕ^*_ℓ with no binning in $\cos\theta^*_\ell$. This figure is included because the large type II bias in ρ_{+-} which arises when using the standard detector correction becomes negligibly small when using this alternative parameterisation (see section 6.5). The ρ_{+-} elements is the only element of the SDM whose projection operator is independent of $\cos\theta^*_\ell$. The systematic uncertainties on this detector correction were not evaluated, but the results show no significant deviations from those obtained using the standard detector correction. For completeness, sections F.1 and F.2 contain tables of the numeric values of the off-diagonal elements of the SDMs.

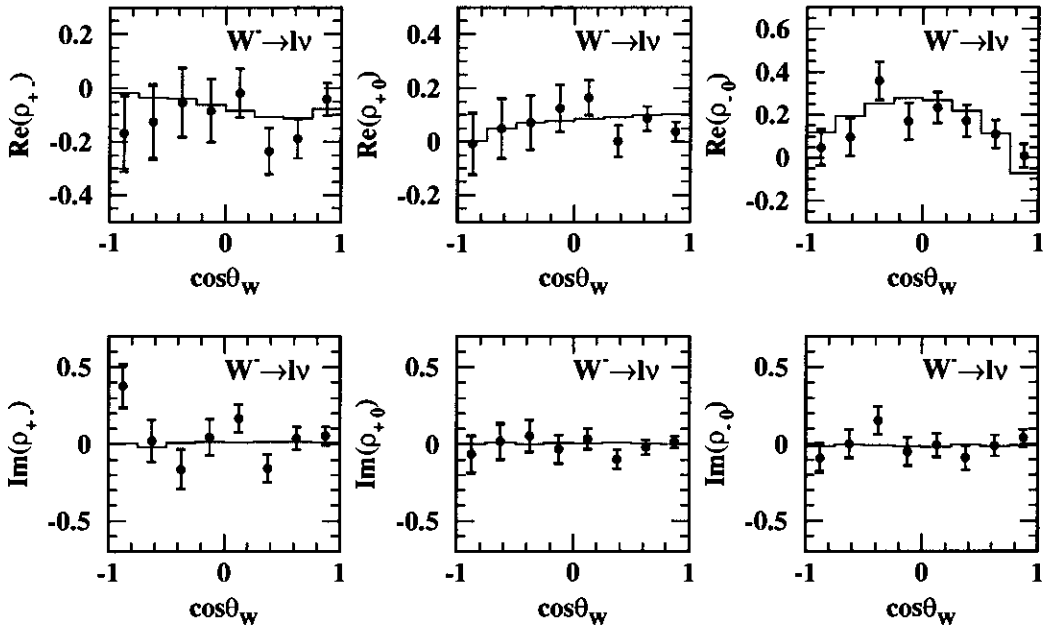

Figure 73: The off-diagonal elements of the SDM measured from the $W^- \to \ell^- \bar{\nu}_\ell$ decay mode. The points show the luminosity-weighted average of the values measured from the data at each centre-of-mass energy. The inner error bars show the statistical uncertainty on the data, and the outer error bars show the total uncertainty including the systematic uncertainty. The histogram shows the generator-level SM MC prediction.

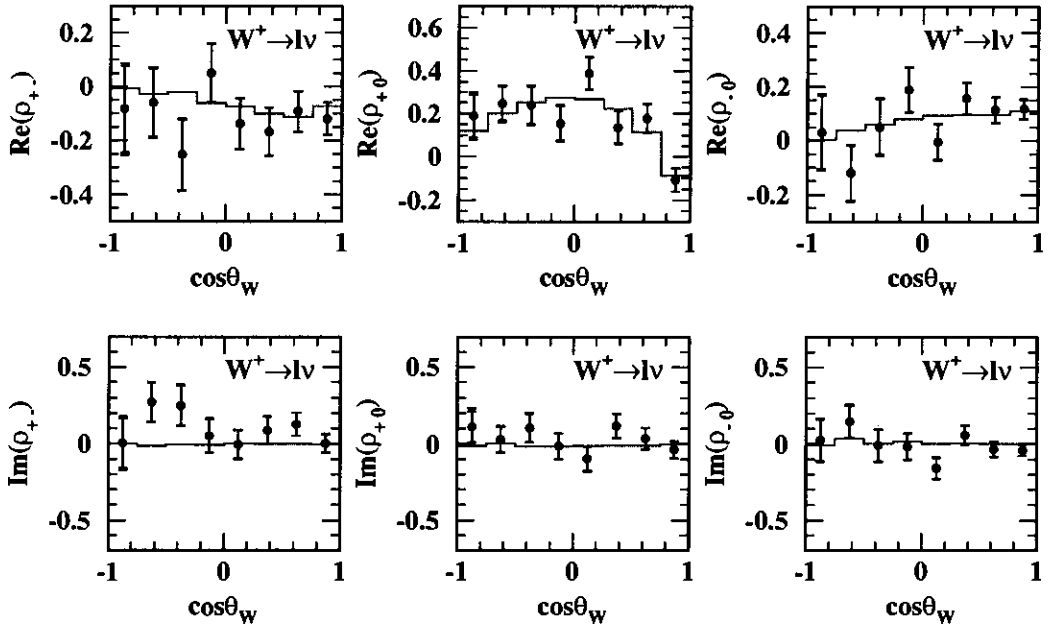

Figure 74: The off-diagonal elements of the SDM measured from the $W^+ \to \ell^+\bar{\nu}_\ell$ decay mode.The points show the luminosity-weighted average of the values measured from the data at each centre-of-mass energy. The inner error bars show the statistical uncertainty on the data, and the outer error bars show the total uncertainty including the systematic uncertainty. The histogram shows the generator-level SM MC prediction.

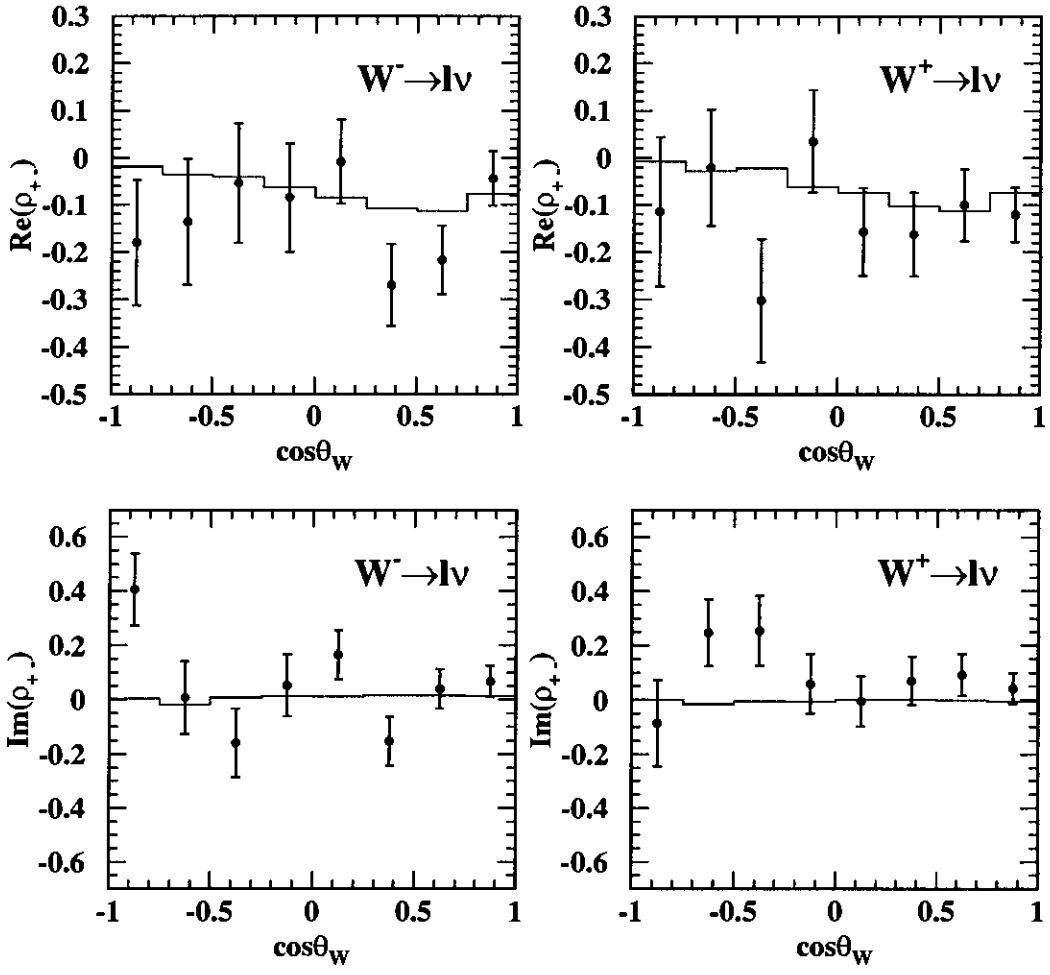

Figure 75: The off-diagonal elements of the SDM measured from the $W^- \to \ell^- \bar{\nu}_\ell$ and $W^+ \to \ell^+ \bar{\nu}_\ell$ decay modes using 20 bins in ϕ^*_ℓ. The points show the luminosity-weighted average of the values measured from the data at each centre-of-mass energy. The inner error bars show the statistical uncertainty on the data, and the outer error bars show the total uncertainty including the systematic uncertainty. The histogram shows the generator-level SM MC prediction.

F.1 Real Parts

$\cos\theta_W$	$Re\{\rho_{+-}\}$	s^{ρ}_{stat}	s^{ρ}_{sys}
-1.00 - -0.75	-0.167	0.135	0.053
-0.75 - -0.50	-0.127	0.134	0.046
-0.50 - -0.25	-0.054	0.128	0.032
-0.25 - 0.00	-0.084	0.116	0.024
0.00 - 0.25	-0.018	0.090	0.023
0.25 - 0.50	-0.236	0.087	0.017
0.50 - 0.75	-0.189	0.072	0.011
0.75 - 1.00	-0.042	0.061	0.010

Table 42: The luminosity-weighted average of the real part of ρ_{+-} measured from the $W^- \to \ell^- \bar{\nu}_\ell$ decay channel. s^{ρ}_{stat} denotes the statistical uncertainty and s^{ρ}_{sys} denotes the systematic uncertainty.

$\cos\theta_W$	$Re\{\rho_{+-}\}$	s^{ρ}_{stat}	s^{ρ}_{sys}
-1.00 - -0.75	-0.180	0.133	-
-0.75 - -0.50	-0.135	0.133	-
-0.50 - -0.25	-0.053	0.127	-
-0.25 - 0.00	-0.085	0.115	-
0.00 - 0.25	-0.008	0.090	-
0.25 - 0.50	-0.269	0.087	-
0.50 - 0.75	-0.217	0.073	-
0.75 - 1.00	-0.044	0.058	-

Table 43: The luminosity-weighted average of the real part of ρ_{+-} measured from the $W^- \to \ell^- \bar{\nu}_\ell$ decay channel using 20 bins in ϕ^*_ℓ. s^{ρ}_{stat} denotes the statistical uncertainty and s^{ρ}_{sys} denotes the systematic uncertainty.

$\cos\theta_W$	$Re\{\rho_{+-}\}$	s^{ρ}_{stat}	s^{ρ}_{sys}
-1.00 - -0.75	-0.083	0.161	0.056
-0.75 - -0.50	-0.059	0.125	0.038
-0.50 - -0.25	-0.254	0.130	0.033
-0.25 - 0.00	0.051	0.109	0.023
0.00 - 0.25	-0.138	0.093	0.019
0.25 - 0.50	-0.168	0.088	0.013
0.50 - 0.75	-0.093	0.075	0.011
0.75 - 1.00	-0.120	0.060	0.009

Table 44: The luminosity-weighted average of the real part of ρ_{+-} measured from the $W^+ \to \ell^+\bar{\nu}_\ell$ decay channel. s^{ρ}_{stat} denotes the statistical uncertainty and s^{ρ}_{sys} denotes the systematic uncertainty.

$\cos\theta_W$	$Re\{\rho_{+-}\}$	s^{ρ}_{stat}	s^{ρ}_{sys}
-1.00 - -0.75	-0.114	0.158	-
-0.75 - -0.50	-0.020	0.123	-
-0.50 - -0.25	-0.302	0.130	-
-0.25 - 0.00	0.035	0.109	-
0.00 - 0.25	-0.157	0.093	-
0.25 - 0.50	-0.163	0.089	-
0.50 - 0.75	-0.100	0.076	-
0.75 - 1.00	-0.120	0.058	-

Table 45: The luminosity-weighted average of the real part of ρ_{+-} measured from the $W^+ \to \ell^+\bar{\nu}_\ell$ decay channel using 20 bins in ϕ^*_ℓ. s^{ρ}_{stat} denotes the statistical uncertainty and s^{ρ}_{sys} denotes the systematic uncertainty.

$\cos\theta_W$	$Re\{\rho_{+0}\}$	s^{ρ}_{stat}	s^{ρ}_{sys}
-1.00 - -0.75	-0.008	0.113	0.036
-0.75 - -0.50	0.049	0.110	0.034
-0.50 - -0.25	0.072	0.101	0.020
-0.25 - 0.00	0.125	0.087	0.023
0.00 - 0.25	0.164	0.064	0.015
0.25 - 0.50	0.002	0.058	0.009
0.50 - 0.75	0.087	0.045	0.008
0.75 - 1.00	0.037	0.036	0.009

Table 46: The luminosity-weighted average of the real part of ρ_{+0} measured from the $W^- \to \ell^- \bar{\nu}_\ell$ decay channel. s^{ρ}_{stat} denotes the statistical uncertainty and s^{ρ}_{sys} denotes the systematic uncertainty.

$\cos\theta_W$	$Re\{\rho_{+0}\}$	s^{ρ}_{stat}	s^{ρ}_{sys}
-1.00 - -0.75	0.188	0.100	0.047
-0.75 - -0.50	0.246	0.080	0.033
-0.50 - -0.25	0.238	0.088	0.023
-0.25 - 0.00	0.154	0.079	0.027
0.00 - 0.25	0.387	0.073	0.018
0.25 - 0.50	0.135	0.075	0.012
0.50 - 0.75	0.176	0.067	0.011
0.75 - 1.00	-0.107	0.053	0.010

Table 47: The luminosity-weighted average of the real part of ρ_{+0} measured from the $W^+ \to \ell^+ \bar{\nu}_\ell$ decay channel. s^{ρ}_{stat} denotes the statistical uncertainty and s^{ρ}_{sys} denotes the systematic uncertainty.

$\cos\theta_W$	$Re\{\rho_{-0}\}$	s^{ρ}_{stat}	s^{ρ}_{sys}
-1.00 - -0.75	0.048	0.082	0.033
-0.75 - -0.50	0.096	0.085	0.024
-0.50 - -0.25	0.358	0.087	0.021
-0.25 - 0.00	0.170	0.084	0.025
0.00 - 0.25	0.233	0.071	0.017
0.25 - 0.50	0.173	0.073	0.013
0.50 - 0.75	0.110	0.065	0.010
0.75 - 1.00	0.009	0.054	0.014

Table 48: The luminosity-weighted average of the real part of ρ_{-0} measured from the $W^- \to \ell^- \bar{\nu}_\ell$ decay channel. s^{ρ}_{stat} denotes the statistical uncertainty and s^{ρ}_{sys} denotes the systematic uncertainty.

$\cos\theta_W$	$Re\{\rho_{-0}\}$	s^{ρ}_{stat}	s^{ρ}_{sys}
-1.00 - -0.75	0.031	0.136	0.039
-0.75 - -0.50	-0.119	0.102	0.027
-0.50 - -0.25	0.050	0.103	0.030
-0.25 - 0.00	0.189	0.083	0.022
0.00 - 0.25	-0.005	0.066	0.016
0.25 - 0.50	0.157	0.059	0.012
0.50 - 0.75	0.113	0.047	0.010
0.75 - 1.00	0.117	0.035	0.008

Table 49: The luminosity-weighted average of the real part of ρ_{-0} measured from the $W^+ \to \ell^+ \bar{\nu}_\ell$ decay channel. s^{ρ}_{stat} denotes the statistical uncertainty and s^{ρ}_{sys} denotes the systematic uncertainty.

F.2 Imaginary Parts

$\cos\theta_W$	$Im\{\rho_{+-}\}$	s^{ρ}_{stat}	s^{ρ}_{sys}
-1.00 - -0.75	0.378	0.135	0.059
-0.75 - -0.50	0.023	0.133	0.035
-0.50 - -0.25	-0.163	0.128	0.030
-0.25 - 0.00	0.045	0.115	0.029
0.00 - 0.25	0.167	0.090	0.021
0.25 - 0.50	-0.154	0.087	0.017
0.50 - 0.75	0.039	0.073	0.015
0.75 - 1.00	0.053	0.061	0.012

Table 50: The luminosity-weighted average of the imaginary part of ρ_{+-} measured from the $W^- \to \ell^- \bar{\nu}_\ell$ decay channel. s^{ρ}_{stat} denotes the statistical uncertainty and s^{ρ}_{sys} denotes the systematic uncertainty.

$\cos\theta_W$	$Im\{\rho_{+-}\}$	s^{ρ}_{stat}	s^{ρ}_{sys}
-1.00 - -0.75	0.005	0.162	0.067
-0.75 - -0.50	0.271	0.125	0.038
-0.50 - -0.25	0.249	0.130	0.037
-0.25 - 0.00	0.052	0.109	0.028
0.00 - 0.25	-0.004	0.093	0.022
0.25 - 0.50	0.089	0.089	0.018
0.50 - 0.75	0.127	0.075	0.013
0.75 - 1.00	0.003	0.060	0.012

Table 51: The luminosity-weighted average of the imaginary part of ρ_{+-} measured from the $W^+ \to \ell^+ \bar{\nu}_\ell$ decay channel. s^{ρ}_{stat} denotes the statistical uncertainty and s^{ρ}_{sys} denotes the systematic uncertainty.

$\cos\theta_W$	$Im\{\rho_{+-}\}$	s^{ρ}_{stat}	s^{ρ}_{sys}
-1.00 - -0.75	0.406	0.133	-
-0.75 - -0.50	0.008	0.132	-
-0.50 - -0.25	-0.163	0.127	-
-0.25 - 0.00	0.052	0.115	-
0.00 - 0.25	0.164	0.090	-
0.25 - 0.50	-0.153	0.087	-
0.50 - 0.75	0.039	0.073	-
0.75 - 1.00	0.068	0.058	-

Table 52: The luminosity-weighted average of the imaginary part of ρ_{+-} measured from the $W^- \to \ell^- \bar{\nu}_\ell$ decay channel using 20 bins in ϕ^*_ℓ. s^{ρ}_{stat} denotes the statistical uncertainty and s^{ρ}_{sys} denotes the systematic uncertainty.

$\cos\theta_W$	$Im\{\rho_{+-}\}$	s^{ρ}_{stat}	s^{ρ}_{sys}
-1.00 - -0.75	-0.086	0.159	-
-0.75 - -0.50	0.247	0.124	-
-0.50 - -0.25	0.254	0.129	-
-0.25 - 0.00	0.059	0.109	-
0.00 - 0.25	-0.005	0.093	-
0.25 - 0.50	0.069	0.089	-
0.50 - 0.75	0.091	0.077	-
0.75 - 1.00	0.041	0.058	-

Table 53: The luminosity-weighted average of the imaginary part of ρ_{+-} measured from the $W^+ \to \ell^+ \bar{\nu}_\ell$ decay channel using 20 bins in ϕ^*_ℓ. s^{ρ}_{stat} denotes the statistical uncertainty and s^{ρ}_{sys} denotes the systematic uncertainty.

$\cos\theta_W$	$Im\{\rho_{+0}\}$	s^{ρ}_{stat}	s^{ρ}_{sys}
-1.00 - -0.75	-0.066	0.114	0.050
-0.75 - -0.50	0.017	0.111	0.043
-0.50 - -0.25	0.053	0.102	0.030
-0.25 - 0.00	-0.033	0.089	0.027
0.00 - 0.25	0.034	0.066	0.021
0.25 - 0.50	-0.097	0.060	0.013
0.50 - 0.75	-0.019	0.048	0.008
0.75 - 1.00	0.013	0.037	0.010

Table 54: The luminosity-weighted average of the imaginary part of ρ_{+0} measured from the $W^- \to \ell^- \bar{\nu}_\ell$ decay channel. s^{ρ}_{stat} denotes the statistical uncertainty and s^{ρ}_{sys} denotes the systematic uncertainty.

$\cos\theta_W$	$Im\{\rho_{+0}\}$	s^{ρ}_{stat}	s^{ρ}_{sys}
-1.00 - -0.75	0.110	0.102	0.071
-0.75 - -0.50	0.027	0.083	0.035
-0.50 - -0.25	0.105	0.093	0.031
-0.25 - 0.00	-0.017	0.083	0.019
0.00 - 0.25	-0.099	0.077	0.022
0.25 - 0.50	0.117	0.078	0.017
0.50 - 0.75	0.033	0.069	0.014
0.75 - 1.00	-0.040	0.054	0.015

Table 55: The luminosity-weighted average of the imaginary part of ρ_{+0} measured from the $W^+ \to \ell^+ \bar{\nu}_\ell$ decay channel. s^{ρ}_{stat} denotes the statistical uncertainty and s^{ρ}_{sys} denotes the systematic uncertainty.

$\cos\theta_W$	$Im\{\rho_{-0}\}$	s^{ρ}_{stat}	s^{ρ}_{sys}
-1.00 - -0.75	-0.090	0.085	0.050
-0.75 - -0.50	0.001	0.090	0.030
-0.50 - -0.25	0.152	0.090	0.027
-0.25 - 0.00	-0.049	0.089	0.023
0.00 - 0.25	-0.007	0.075	0.017
0.25 - 0.50	-0.090	0.077	0.015
0.50 - 0.75	-0.011	0.067	0.012
0.75 - 1.00	0.040	0.055	0.017

Table 56: The luminosity-weighted average of the imaginary part of ρ_{-0} measured from the $W^- \to \ell^- \bar{\nu}_\ell$ decay channel. s^{ρ}_{stat} denotes the statistical uncertainty and s^{ρ}_{sys} denotes the systematic uncertainty.

$\cos\theta_W$	$Im\{\rho_{-0}\}$	s^{ρ}_{stat}	s^{ρ}_{sys}
-1.00 - -0.75	0.025	0.137	0.044
-0.75 - -0.50	0.145	0.103	0.045
-0.50 - -0.25	-0.010	0.104	0.030
-0.25 - 0.00	-0.017	0.083	0.029
0.00 - 0.25	-0.159	0.068	0.024
0.25 - 0.50	0.058	0.062	0.016
0.50 - 0.75	-0.034	0.050	0.010
0.75 - 1.00	-0.041	0.037	0.009

Table 57: The luminosity-weighted average of the imaginary part of ρ_{-0} measured from the $W^+ \to \ell^+ \bar{\nu}_\ell$ decay channel. s^{ρ}_{stat} denotes the statistical uncertainty and s^{ρ}_{sys} denotes the systematic uncertainty.